UNIVERSIDAD POLITÉCNICA DE MADRID
Escuela Técnica Superior de Ingenieros de Telecomunicación

Non-Contact Vital Signs Monitoring Using Millimeter-Wave Radar Technologies

D O C T O R A L T H E S I S

Submitted for the degree of Doctor by:

Elías Antolinos García
Máster Universitario en Ingeniería de Telecomunicación

Madrid, 2024


UNIVERSIDAD POLITÉCNICA DE MADRID
Escuela Técnica Superior de Ingenieros de Telecomunicación

Doctoral Degree in Tecnologías y Sistemas de Comunicaciones

Non-Contact Vital Signs Monitoring Using Millimeter-Wave Radar Technologies

D O C T O R A L T H E S I S

Submitted for the degree of Doctor by:

Elías Antolinos García
Máster Universitario en Ingeniería de Telecomunicación

Under the supervision of:
Dr. Jesús Grajal de la Fuente

Madrid, 2024

Title: Non-Contact Vital Signs Monitoring Using Millimeter-Wave Radar Technologies

Author: Elías Antolinos García

Doctoral Programme: Tecnologías y Sistemas de Comunicaciones

Thesis Supervision:

Dr. Jesús Grajal de la Fuente, Catedrático del Dpto. de Señales, Sistemas y Radiocomunicaciones, Universidad Politécnica de Madrid (Supervisor)

External Reviewers:

Thesis Defense Committee:

Thesis Defense Date:

This thesis has been partially supported by an FPU Fellowship granted by the Spanish Ministry of Education (FPU18/01525).

"It's the questions we can't answer that teach us the most.
They teach us how to think. If you give a man an answer,
all he gains is a little fact. But give him a question
and he'll look for his own answers."

Patrick Rothfuss, *The Wise Man's Fear*

Acknowledgement

Me gustaría aprovechar este espacio para expresar mi agradecimiento a todas las personas que, de una forma u otra, han contribuido al desarrollo de esta tesis. En primer lugar, agradezco a mi director, Jesús Grajal, por su paciencia y por toda la ayuda que me ha brindado desde que me uní al Grupo de Microondas y Radar, en 2018, hasta la finalización de este trabajo.

También quiero expresar mi gratitud al Ministerio de Educación, Cultura y Deporte por la concesión de la Beca de Formación de Profesorado Universitario (FPU), cuyo apoyo económico ha sido fundamental para la realización de esta tesis. Asimismo, agradezco a los diferentes proyectos de investigación que han cubierto los gastos adicionales derivados de este trabajo, incluyendo, entre otros, la financiación de publicaciones y la asistencia a conferencias.

No me quiero olvidar de todas las personas que han contribuido de forma directa en esta tesis, "ofreciéndose" voluntarias para colaborar en las campañas de medidas, a todos vosotros: gracias, de corazón.

Y como bien dice el refrán, "es de bien nacidos ser agradecidos", así que voy a extenderme un poco más, porque hay muchas personas que merecen un reconocimiento especial en esta tesis. Quiero comenzar agradeciendo a vosotros, quienes no solo habéis participado activamente en este trabajo, sino que también lo habéis vivido y sufrido conmigo: a mis compañeros y amigos del GMR, y en especial, a Randy, Nacho S., Nacho L., Fran, Marta y Fernando, ¡GRACIAS!

Y ya, por último, gracias a todos los que me habéis transmitido aliento y me habéis acompañado en esta montaña rusa de emociones. A mis padres, mi hermano, y a mi familia, que me han apoyado de forma incondicional siempre. Y al resto de amigos y compañeros de piso que me han hecho estos años mucho más fáciles: piratitas, surrealistas cobardes y telecos, una parte de esta tesis es vuestra.

Abstract

The advances in monolithic microwave integrated circuits have enabled the miniaturization and integration of radar systems into a wide range of devices. Consequently, these systems are currently utilized in diverse environments, including automotive, security, industrial, structural health monitoring, and even in biomedical and healthcare contexts. Indeed, the non-contact monitoring of human vital signs with radar has become an active research area in recent years. This has been further emphasized following the emergence of the COVID-19 pandemic and the increasing interest in home monitoring and telemedicine.

Traditionally, radars have been employed to measure the displacement of the chest wall due to breathing and heart movements. However, radar monitoring allows for the extraction of heartbeat and respiration, as well as the measurement of other biomarkers that can provide significant information in the detection of certain cardiovascular diseases. This Ph.D. thesis focuses on the feasibility of using radar technology for non-contact monitoring of vital signs. The initial section of the thesis examines radar technology with the objective of identifying the optimal configuration for this application. This includes a comprehensive comparison between the two main radar configurations used in the literature: continuous-wave and linear-frequency-modulated continuous-wave configurations.

The second part of this thesis examines the different vital signs and biomarkers that can be obtained using radar technology. It analyses different algorithms to determine the optimal signal processing for extracting some biomarkers from heart activity. Furthermore, a radar configuration to evaluate the carotid-femoral pulse wave velocity is presented, which is the gold standard for evaluating arterial stiffness.

Finally, the last part of this thesis addresses the challenges that must be overcome in order for radar technology to become a viable solution for vital sign monitoring in daily life scenarios. These challenges include multi-target monitoring scenarios, radar focusing and vital signs extraction during target movement. Furthermore, a real-time vital sign monitoring application has been developed, that allows the simultaneous monitoring of multiple targets in real-world scenarios. This application represents a preliminary prototype that can also be used for sleep-monitoring scenarios, as it is capable of detecting apnea periods. This represents a preliminary step towards obstructive sleep apnea monitoring.

Resumen

Los avances en circuitos monolíticos integrados de microondas han permitido la miniaturización e integración de los sistemas radar en una multitud de dispositivos. Esto ha posibilitado su uso en diversos campos, entre los que se incluyen la automoción, la seguridad, la industria, la monitorización de estructuras e incluso en entornos biomédicos y de salud. De hecho, la monitorización sin contacto de señales vitales con tecnología radar se ha convertido en un activo campo de investigación en los últimos años. Esto se ha visto impulsado por la emergencia sanitaria que supuso la pandemia del COVID-19 y el creciente interés en la monitorización domiciliaria y la telemedicina.

Tradicionalmente, los radares se han empleado para medir el desplazamiento del pecho provocado por los movimientos de la respiración y del corazón. Sin embargo, la monitorización radar permite extraer la señal de respiración y latido, y, además, medir otros biomarcadores que proporcionan información importante para la detección de ciertas enfermedades cardiovasculares. Esta Tesis Doctoral se centra en la viabilidad de utilizar la tecnología radar como herramienta para la monitorización sin contacto de señales vitales. La primera parte de esta tesis analiza la tecnología radar con el objetivo de identificar la configuración óptima para esta aplicación. Esto incluye una comparación en profundidad entre las dos configuraciones de radar más utilizadas en la literatura: los radares de onda continua y los radares de onda continua y frecuencia modulada.

La segunda parte de esta tesis analiza las distintas señales vitales y biomarcadores que pueden medirse con tecnología radar. En ella se analizan los distintos algoritmos para determinar el sistema de procesamiento óptimo para extraer algunos biomarcadores de la actividad cardíaca. Además, se presenta una configuración radar para monitorizar la velocidad de la onda del pulso desde la arteria carótida a la femoral, que es el estándar de referencia para evaluar la rigidez arterial.

Por último, esta tesis aborda los distintos desafíos que deben superarse con el objetivo de que la tecnología radar sea una solución viable para la monitorización de señales vitales en escenarios reales. Entre estos desafíos, se destacan la monitorización simultánea de distintas personas en el mismo escenario, el apuntamiento del sistema radar y la extracción de señales vitales cuando el blanco está en movimiento. Además, se ha desarrollado una aplicación para la monitorización en tiempo real de señales vitales de varias personas simultáneamente en escenarios reales. Esta aplicación es un prototipo preliminar que puede usarse para la monitorización del sueño, ya que es capaz de detectar episodios de apnea, y supone un primer paso hacia la monitorización de la apnea obstructiva del sueño.

Table of Contents

List of Figures

List of Tables

Abbreviations and acronyms

AWGN Additive White Gaussian Noise

ADC Analogical-Digital Converter

AE Absolute Error

ANS Autonomic Nervous System

AO Aortic Valve Opening

AoA Angle of Arrival

B Breathing

BCG Ballistocardiograph

BMI Body Mass Index

BP Blood Pressure

BR Breathing Rate

BSS Blind Source Separation

cfPWV Carotid-Femoral Pulse Wave Velocity

CRLB Cramér-Rao Lower Bound

CW Continuous-Wave

DACM Differentiate and Cross-Multiply

DSP Digital Signal Processing

ECG Electrocardiogram

EMD Empirical Mode Decomposition

FCC Federal Communications Commission

FFT Fast Fourier Transform

FoV Field of View

GPIO General Purpose Input Output

HB Heartbeat

HR Heart Rate

HRV Heart Rate Variability

HS Heart Sounds

IBI Inter-Beat Interval

ICA Independent Component Analysis

ICG Impedance Cardiogram

ICNIRP International Commission on Non-Ionizing Radiation Protection

IQ In-Phase & Quadrature

IMF Intrinsic Mode Function

LFMCW Linear-Frequency-Modulated Continuous-Wave

LoA Limits of Agreement

MAE Minimum Absolute Error

MIMO Multi-Input Multi-Output

MLE Maximum Likelihood Estimation

MMIC Monolithic Microwave Integrated Circuit

OSA Obstructive Sleep Apnea

PCB Printed Circuit Board

PCG Phonocardiogram

PFD Phase Frequency Detector

PSG Polysomnogram

PTT Pulse Transmit Time

PUT Person Under Test

PWV Pulse Wave Velocity

RBM Random Body Movement

RCS Radar Cross-Section

RSA Respiratory Sinus Arrhythmia

RVP Residual Video Phase

RX Receiver

SAR Synthetic Aperture Radar

SCG Seismocardiograph

SIMO Single-Input Multiple-Output

SISO Single-Input Single-Output

SNR Signal-to-Noise Ratio

STFT Short-Time Fourier Transform

TDM Time Division Multiplexing

TFM Task Force Monitor

TX Transmitter

UAV Unmanned Aerial Vehicle

UPM Universidad Politécnica de Madrid

VCO Voltage-Controlled Oscillator

WHO World Health Organization

WN White Noise

WT Wavelet Transform

Chapter 1

Introduction

The microwave and millimeter-wave bands are the regions of the electromagnetic spectrum between the radio and sub-millimeter waves, as shown in Fig. 1.1. The microwave band includes the frequencies in the range of 3 to 30 GHz, while the millimeter-wave band includes the frequencies in the range of 30 GHz to 300 GHz.

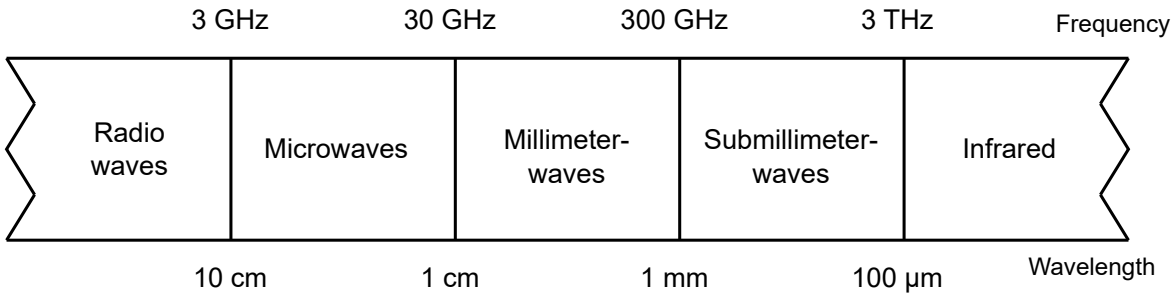

Figure 1.1: Region of the electromagnetic spectrum between the radio and infrared waves bands.

1.1 Overview and Radar Applications

The first use of the microwave and millimeter-wave bands dates back to the 1890s, when Hertz performed the first experiments to confirm the Maxwell's theory predicting the existence of radio waves. The first wavelengths generated by Hertz were produced with a spark-gap generator in the centimeter range [Wilt 84]. During that decade, following the methods used by Hertz, wavelengths detection were reported in the millimeter range by Bose [Rams 67].

However, it was not until World War II that the use of the microwave and millimeter-wave spectrum became of great interest due to the use of radar technology. At this time, radars were beginning to incorporate the latest developments in radio wave generation based on vacuum tube configurations, such as the klystron [Ginz 76] or the cavity magnetron [Boot 76]. During this period, the line of investigation was focused on moving to higher frequencies with the aim of obtaining better angular resolution and reduce the antenna size, so radars could be

more mobile [Jame 89]. The typical airborne radar operated in X-band and during the war there were developments in K-band (around 24 GHz) [Skol 62]. After the war, microwave and millimeter-wave research was focused on spectroscopy and conventional radio communications [Beri 46, Wart 77].

During the 1950s and 1960s experiments in both bands were widespread, highlighting radars at 70 GHz [Butt 81], high power sources extended upward to 120 GHz [Krol 54, Van 59], the research on new transmission lines and mixer diodes [Olin 84], radio astronomy [Hadd 58], communications [Sobo 84] and passive sensing systems [Cohn 63]. This development was slowed down by the advent of lasers in the mid-1960s, which took a large portion of the financing resources. Nevertheless, most of the research lines were resumed by the 1970s, when oscillators at 35 GHz started to become commercially available, because of the development of both Gunn and IMPATT diodes [Wilt 84].

These advances in solid-state devices and integrated circuits allowed the technology to be commercialized and used in other applications. Thus, although radar was motivated by military applications, radar technology has continued to develop in a variety of defense and civilian applications. Regarding military applications, radars have been used, for instance, in missile guidance systems [Maly 06], in airborne radar synthetic aperture systems for target recognition on the battlefield [Ream 93, King 16], or target tracking [Yan 22]. Indeed, the rapid advancement of unmanned aerial vehicles (UAVs) as combat weaponry has reaffirmed the critical role of radar technology as a detection mechanism for such dangers. Consequently, there is a pressing need to devise radars or sensors, enabling them not only to detect targets with minimal radar cross-section (RCS), but more importantly, to maintain continuous tracking of their trajectory over time [Farl 21, Zhan 23].

On the other hand, the use of radar also stands out in civil applications. Two major groups of radar applications can be distinguished. The first group is related to long-range radar monitoring, which involves tasks such as monitoring the Earth's surface [Amit 21], oceans, planetary observation [Pisa 21], and tracking natural phenomena like earthquakes, volcanoes, or landslides [Li 19b], standing out the interferiometric synthetic aperture systems (InSAR). Conversely, short-range applications, which encompass tasks like structural health monitoring [Arno 18], security [Ahme 21], industrial applications [Geig 19], automotive applications [Dokh 19], as well as biomedical and in healthcare contexts [Taba 21, Liu 21]. Fig. 1.2 depicts the interest in some of the aforementioned topics, which have been evaluated based on the number of publications in the Web of Science (WoS), considering articles, book chapters, reviews, letters, and patents.

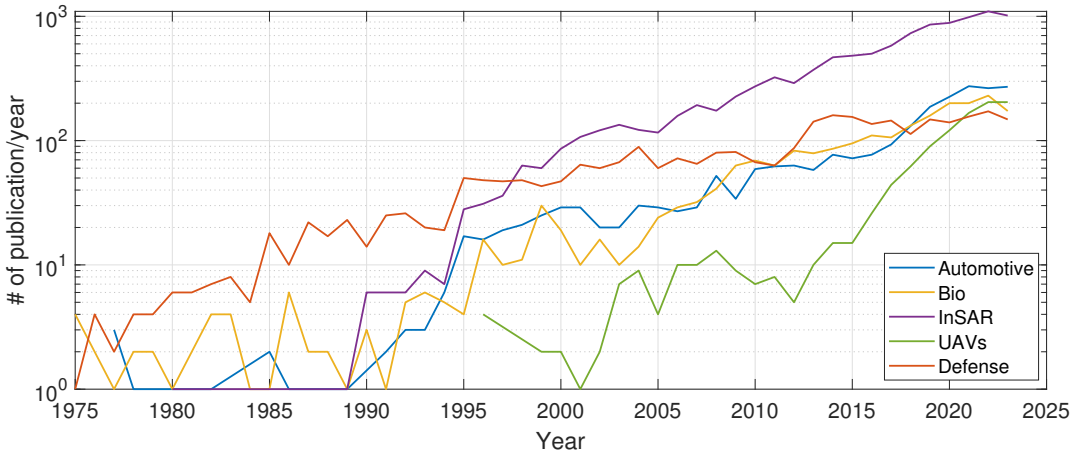

Figure 1.2: Number of publications (articles, book chapters, reviews, letters and patents) in WoS for some radar topics since 1975.

1.2 Healthcare Radar Applications

In the field of biomedical applications, there has been a growing interest in non-contact health monitoring techniques, including radar technology, over the past few decades. Demographic changes in recent decades point to an aging population as one of the main reasons. As stated by authors in [Amin 16], the worldwide elderly population is growing and is projected to increase to one billion in 2030. Consequently, investment in non-contact technology to assist the elderly can potentially extend their life expectancy while simultaneously reducing healthcare costs associated with elder care [Dark 08, Gurb 19, Le K 19]. Home monitoring and telehealth allow early detection of worsening conditions, which would decrease these costs by reducing the number of hospital admissions and bed days of care. Moreover, the recent pandemic caused by COVID-19 has once again highlighted the importance of this issue. Remote vital sign monitoring is of particular importance as it alleviates pressure on hospital resources, facilitates post-surgery monitoring, and enables early detection of health complications, thereby reducing hospital costs and the duration of care needed. Indeed, between 2007 and 2017, healthcare expenditure grew by almost 80% in Australia and by 50% in the USA [Worl].

Consequently, there are a number of healthcare applications where radar technology appears to offer a promising solution in the aforementioned scenarios. These applications, presented in Fig. 1.3, can be divided into two major groups:

- Human activity monitoring applications: These include applications that typically involve the monitoring of the Doppler and range-time signature of diverse body parts. For instance, it is possible to detect falls [Amin 16] or extract motor biomarkers from the micro-Doppler signature of the gait to detect diseases such as Parkinson's disease [Lope 23].
- Vital sign monitoring application: These include those that are directly related to vital sign monitoring and the biomarkers that can be extracted from them. For instance, the

direct monitoring of breathing and heart rates or the identification and classification of the different sleep stages.

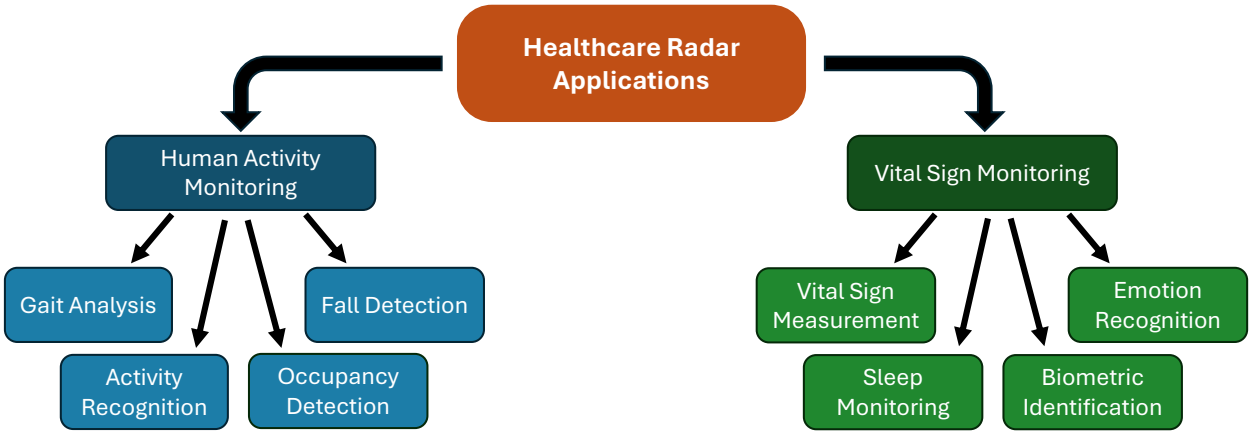

Figure 1.3: Principal healthcare applications of radar technology.

Fall detection

The topic of fall detection, and in particular, elderly fall detection, is a significant area of interest in healthcare scenarios, due to the aging population. Indeed, one in three elderly individuals over the age of 65 will fall each year, with this percentage rising for those residing in long-term care facilities [Amin 16]. Radar technology, combined with machine learning techniques, enables the identification of falls in individuals [Sadr 21, Yao 22].

Occupancy detection

Radar technology is also used to detect the presence of people in a location. Although the majority of these applications are focused on counting the number of people in a indoor environment for energy saving purposes (turning lights on/off, adjusting room temperature...) [Sant 18, Isla 23], it can also be used to locate trapped or injured people in post-disaster search and rescue applications [Shi 23].

Activity recognition

Radar technology is also used in activity recognition, specially because of its privacy protection. For this application, radar technology are also combined with deep learning techniques, where the range-Doppler information is analyzed to identify and classify the activity [Li 19a]. Within the activity recognition, there are applications focused on classifying large movements such as jumping, sitting or walking [Wang 21], and others focused on analyzing gestures such as monitoring food intake [Wang 24] or gestures for human-computer interaction [Lien 16].

Gait Analysis

The interest in home monitoring has increased the attention on gait analysis. Continuous monitoring of gait changes helps to assess recovery from physical injuries. It also enables early diagnosis of various diseases, including neurodegenerative diseases such as Parkinson's, and facilitates the study of disease progression to design appropriate treatment [Seif 19, Lope 23]. To this end, radar technology offers a non-contact solution that can analyze and separate the micro-Doppler signatures of different parts of the body, such as knees or feet.

Vital sign measurement
The primary application of radar for vital signs monitoring is the direct measurement of vital signs and the extraction of various biomarkers. This is the basis of other applications related to vital signs monitoring, which analyze respiratory and cardiac information for a more specific purpose. This thesis focuses on the development of radar technology and signal processing techniques for cardiorespiratory signal analysis and biomarker extraction.

Sleep monitoring
Sleep quality and quantity is another area of research where radar technology has gained significant interest. This field can be divided into two main categories: applications related to physiological disorders such as obstructive sleep apnea (OSA) and applications that assess sleep quality by identifying the different states of consciousness during wakefulness and the different sleep stages (REM, light, and deep sleep) [Toft 20, Park 24]. OSA diagnosis is confirmed with a polysomnogram (PSG), which requires the subject to be fully wired in a sleep center, causing discomfort and affecting the quality of sleep, and the final diagnosis [Kang 20, Lube 23]. The utilization of radar technology provides a non-contact monitoring solution that may result in a more convenient and potentially more accurate alternative.

Emotion recognition
Emotion recognition is a new field of study that has attracted much interest in the research community. Emotions have an impact on human life in aspects such as attention, cognition, or mental health. There are studies that use radar technology to identify emotions (joy, pleasure, sadness or anger) [Zhao 16, Gouv 20] or inferring a person's stress level [Ha 21]. These applications are based on analyzing the breathing and heart patterns of these emotions using machine learning techniques.

Biometric identification
Radar-based identity authentication using vital signs analysis is also an emerging research topic. Some research has shown that respiration-related biomarkers and cardiac signals can be used for personal authentication [Isla 21, Silv 24]. In addition, studies have shown that ECG signals can be used for this purpose due to their high inter-person variability [Melz 23]. Compared to other authentication systems, radar has the advantage of being non-invasive and non-contact.

Although all the above applications are related to human activities, it is important to emphasize that these applications are extended to animal monitoring. For example, it is of particular interest in livestock farming to make production more efficient and accurate by obtaining information on the animal's status [Yin 23]. In addition to the obvious advantage of non-contact monitoring, radar has the advantage of being able to monitor the vital signs of animals through their hair or fur [Saka 24].

1.2.1 Vital sign monitoring techniques

In addition to the aforementioned aging of the population and increase in life expectancy, it is important to note that a growing percentage of the population suffers from cardiovascular diseases [Kons 12]. The data provided by the World Health Organization (WHO) for the 2000-2019 period indicates that the causes of death globally are as illustrated in Fig. 1.4. This

figure shows that 40% of deaths are attributable to cardiorespiratory diseases, with nearly one-third being cardiovascular in nature. Ischemic heart disease represents the leading cause of global mortality, accounting for 16% of total deaths worldwide. In 2019, this resulted in 8.9 million deaths. Stroke and chronic obstructive pulmonary disease are the second and third leading causes of death, respectively, accounting for approximately 11% and 6% of total deaths [Worl 20]. Consequently, the ability to monitor cardiorespiratory activity is a key factor in the early detection of these conditions, allowing prompt intervention and treatment.

Conversely, the non-contact monitoring of cardiopulmonary activity has also gained attraction, representing a promising solution to overcome difficulties in certain scenarios where the use of traditional contact-based technologies is not feasible or desirable. Such scenarios include, for instance, sleep monitoring, monitoring of patients in a burn unit, post-surgery monitoring, and newborn infant monitoring [Bori 15, Anto 18, Tata 18]. This technology allows for remote control and monitoring without the need for a wired system. It provides a more comfortable situation for the patient, which in turn leads to more accurate diagnoses.

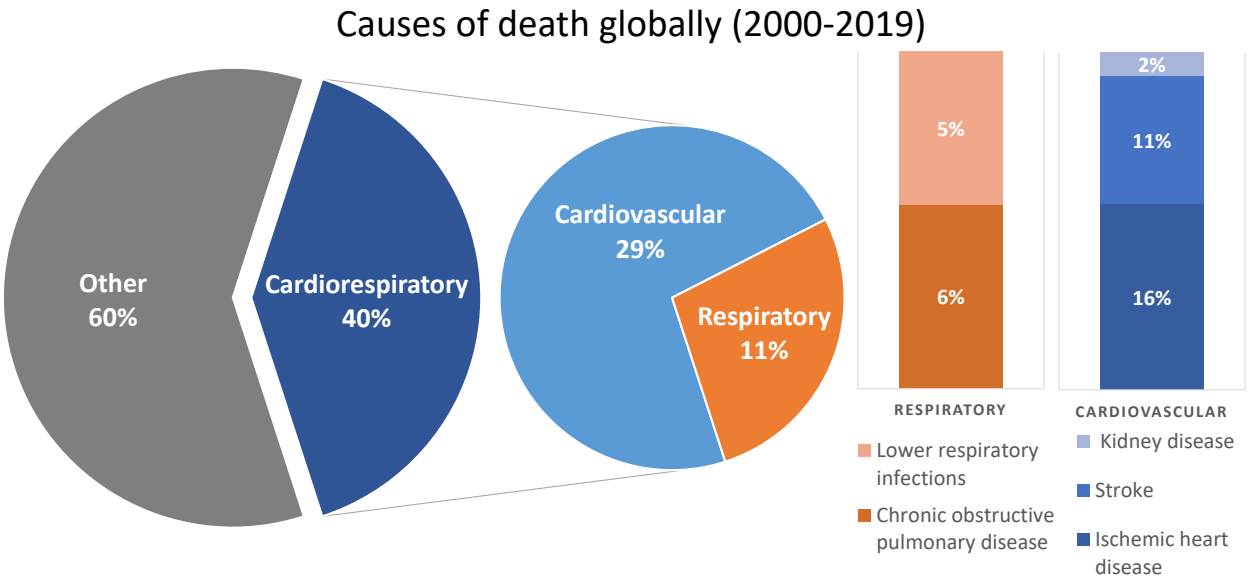

Figure 1.4: Causes of death globally reported by the WHO in the 2000-2019 period.

Cardiopulmonary activity monitoring is based on measuring one or more physiological effects of mechanical or electrical nature occurring in the heart, the lung, or both. The traditional cardiorespiratory monitoring techniques require contact or invasive interactions with the patient. Indeed, all the gold standard techniques used in vital sign monitoring require invasive or contact-based sensors, as shown in Fig. 1.5.

The gold standard technique for heart rate monitoring is the electrocardiogram (ECG). The ECG is a measure of the electrical changes of the heart over time, as a result of the muscle cells depolarization during each cardiac cycle [Viea 15], which are recorded through electrodes located at different body locations. Regarding to the respiratory rate, there is not a gold standard technique [Loug 18]. However, several reference standards have been

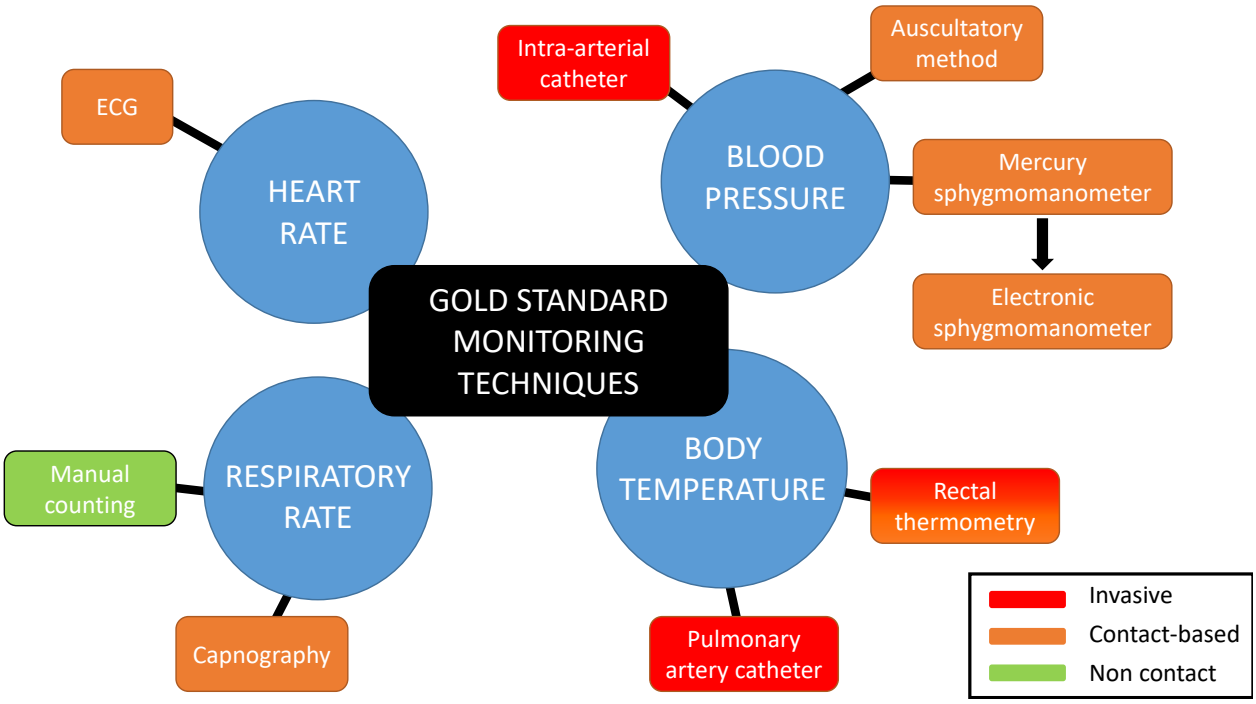

Figure 1.5: Gold standard for monitoring different vital signs: heart rate, blood pressure, respiratory rate and body temperature.

suggested, ranging from expert visual or auditory manual counting to video recordings with manual or automated extraction of respiratory rate, as well as the use of capnography, which is considered by many experts to be the gold standard [Anse 19]. The capnography method involves the measurement of the partial pressure of carbon dioxide (CO_2) in exhaled breath, expressed as the concentration of CO_2 over time [Krau 16].

On the other hand, the monitoring thorough an intra-arterial catheter is the gold standard technique for blood pressure monitoring. However, other noninvasive techniques are also widely used and can be considered as gold standard for BP monitoring, such as using ascultatory methods [Grim 16], or mercury sphygmomanometer [Oged 10]. Following the ban on mercury usage, electronic devices have largely replaced mercury sphygmomanometers.

However, the use of these contact sensors is neither possible nor desirable in many situations. To overcome this limitation, several non-contact-based devices have been developed for cardiorespiratory monitoring: video-based motion analysis methods [Wu 12], laser-based methods [Hong 97], thermal methods [Abba 11], or radar monitoring. Most of them are based on the body surface displacement caused by organ motion and deformation and fluid displacement caused by breathing and heartbeat as explained in [Brus 15]. The main characteristics of these non-contact monitoring techniques are listed in Table 1.1. This table also encompasses the ballistocardiograph (BCG) [Star 39] and the seismocardiograph (SCG) [Zane 91], which, although contact-based, are employed to monitor cardiorespiratory activity by analyzing chest wall motion. Nevertheless, they are not normally used in clinical environments due to lack of reliability, accuracy, and automatization [Bori 15]. The aim of this thesis is to to improve the understanding of radar technology as a monitoring and

diagnostic tool.

Table 1.1: Main characteristics and limitations of non-contact devices for cardiorespiratory monitoring.

Non-Contact Devices	Working Principle	Limitations
Laser-based	Method that measures chest displacement using light.	• Only capable of monitoring one subject at a time. • High cost.
Video motion monitoring	Method that films the displacement of the body surface.	• Sensitive to illumination. • Privacy.
Thermal-based	Method that measures temperature changes and allows a representation of the heartbeat and breathing.	• Sensitive to ambient temperature. • High cost.
Ballistocardiograph	Method that obtains the heartbeat and breathing due to repetitive movements of the human body, occurring because of acceleration of blood as it is ejected and moved in the vessels during the cardiac cycle.	• Artifacts due to target motion. • Complexity of the system: sensors and accelerometers. • It requires a direct mechanical coupling with the subject. • Only capable of monitoring one subject at a time.
Seismocardiograph	Method that measures the heartbeat and breathing due to the vibrations of the chest wall.	• Artifacts due to target motion. • High sensitivity owing to sensor location and accelerometer axes orientation. • It requires a direct mechanical coupling with the subject. • Only capable of monitoring one subject at a time.
Radar-based	Method that analyzes the displacement of different parts of the body caused by breathing and cardiac activities.	• Artifacts due to interfering movements resulting from target motion [1].

[1] Radar-tracking algorithms could be used to mitigate artifacts due to target motion.

Therefore, radar technology offers several advantageous features compared to the other techniques [Amin 17, Ahma 22]:

- Non-contact monitoring: Radars enable remote sensing capabilities, making it possible to monitor multiple targets without direct contact.

- High Accuracy: Radars are capable of detecting small displacements in the micrometer range, enabling precise monitoring.
- Day & Night Detection: Regardless of ambient light conditions, radar systems provide continuous monitoring for reliable day and night operation.
- Privacy-Preserving: Radar-based monitoring techniques facilitate privacy-preserving operations by collecting data without compromising sensitive information, ensuring confidentiality and compliance with privacy regulations.
- Portability: Radar sensing devices are designed to be portable, featuring low-power consumption and wireless interconnectivity, facilitating seamless integration into various monitoring setups and environments.
- Cost-Effectiveness: With the potential for scalability and network formation, radar sensors offer a cost-effective solution for short-range monitoring applications, with individual sensor nodes available at a low unit cost, making them suitable for large-scale deployments.

1.2.2 Radar for vital sign monitoring

The non-contact detection and monitoring of cardiopulmonary activity using radar technology has been known since 1975 [Lin 75]. However, until the late 1990s, when advances in technology enabled the integration of a radar on a single chip, rendering the technology compact, lightweight, mass-produced, and inexpensive [Li 17], it was not considered a viable option.

During the last two decades, studies have highlighted the numerous advantages of this method for cardiopulmonary activity monitoring, which make it an ideal technology for home monitoring or telemedicine: measurements from distances in the order of meters or even through walls are possible [Kun 00], accurate measurements independent of person orientation [Siyi 15], and unobtrusive measurements to the subject (no need for sedation or drugs, no need to stand still, and the subject can be fully clothed [Lee 14]), which means that regular daily activities can be performed while being measured. Indeed, the authors of [Bjar 04] conducted an analysis of the attenuation of eight common garment materials, including nylon, leather, wool, linen, denim, and silk, across a range of frequencies between 100 GHz and 1.2 THz. Their findings demonstrated that the attenuation was consistently below 3 dB across all frequencies until 350 GHz.

The main approach behind radar-based vital signs detection is the measurement of chest vibrations resulting from the mechanical effects of breathing and the cardiac cycle. Table 1.3 lists different approaches carried out for vital sign monitoring using continuous-wave (CW), frequency-modulated continuous-wave (FMCW) and ultra-wideband (UWB) radars.

Table 1.3: Vital sign monitoring with radar techniques.

Radar Technology	Frequency (GHz)	Reference Signal	Results	Additional Comments
CW [Droi 01]	1.892	Finger pulse sensor	Respiratory and heart rate	-
CW [Mass 09]	2.4	ECG and respiratory belt	HRV	Analysis of RSA effect
CW [Will 17]	24	Sphygmogram	Reconstructed pulse waveform	Correlation between radar output and sphygmogram measuring carotid, vein and ventricle pressure
CW [Dong 20]	24	ECG (Identifying cardiac events)	Respiratory and heart rate	Correlation between the radar output and the overall cardiac volume conducted through skin
CW [Petk 09]	228	ECG and respiratory belt	Respiratory and heart rate	Measurements up to 50 m
FMCW [Lee 18]	24.05–24.25	Piezoelectric finger sensor	Heart rate	Simultaneously heart rate detection of multiple subjects
FMCW [Ahma 18]	77–81	-	Respiratory and heart rate	Simultaneously vital sign detection of multiple subjects, uses MIMO
FMCW [Prat 19]	118.5–125.5	Respiratory belt and pulsioximeter	Respiratory and heart rate	-
UWB [Duan 18]	2.9–10.1	ECG	Respiratory and heart rate	Through the wall measurements
UWB [Laza 10]	3.1–10.6	ECG	Respiratory and heart rate	Analysis of breathing harmonics
UWB [Wang 19]	6.59–7.99	Respiratory belt and pulsioximeter	Reconstructed pulse waveform and rates	Distinguish between humans and animals

However, radar technology still has a number of challenges that need to be addressed to make it practical for real-world applications [Sing 21, Isla 22a, Fior 23]:

- There is no consensus or analysis to determine which radar configuration is better for vital signs monitoring.
- Radar technology has to deal with multi-subject monitoring scenarios, where it is necessary to isolate and separate the respiratory and cardiac information of each person.
- Radar technology has to handle the movement of the target, where it is necessary to track the subject's movement or cancel out random body movements that can interfere with vital sign extraction.
- Real-time implementation of this vital signs monitoring, since most of research is done offline.
- Further research is needed in the processing algorithms to separate and extract the respiration and heartbeat signals because of the need to deal with strong breathing harmonics and coupling between these signals.

1.2.3 Health concerns related to millimeter-wave radiations

The growing number of investigations into the applications of millimeter-waves (mmWaves) has prompted interest and concern regarding the potential biological safety implications [Wu 15]. Of particular concern is the potential for adverse health effects associated with prolonged human exposure to mmWave radiation [Sing 21].

Unlike ionizing radiation such as ultraviolet or X-rays, mmWave radiation does not have enough energy to reach the level necessary to remove an electron from an atom, which is three orders of magnitude greater [Rapp 19]. Therefore, mmWave radiation is considered harmless in terms of ionization risks. However, one concern that should be considered is the heating effect caused by the absorption of mmWave energy [Gand 86]. The effects of radio-frequency (RF) exposure are commonly studied using the specific absorption rate (SAR), which represents the RF power absorbed by a living body [Inte 23]:

$$SAR\left(\frac{W}{kg}\right) = \frac{d}{dt}\left(\frac{dW}{dm}\right) = \frac{\sigma|E|^2}{\rho} \tag{1.1}$$

where dW stands for the incremental energy dissipated in an incremental tissue mass (dm), σ denotes the tissue conductivity, E is the root-mean-square (rms) value of the electric-field strength dissipated in the tissue, and ρ stands for the tissue mass density.

Scientific inquiry into the biological effects and health risks of RF radiation commenced in the 1940s. In the 1960s, guidelines for limiting exposure to RF electromagnetic fields were established to safeguard against the known adverse health effects [Lin 16]. These guidelines are periodically revised and updated. Current guidelines impose basic restrictions and limits to prevent the heating effect of absorption of mmWave radiation from increasing skin temperature by more than 1^{o}C, which is considered a safe threshold [Inte 98]. For that purpose, the Federal Communications Commission (FCC) and International Commission on Non-Ionizing Radiation

Protection (ICNIRP) have standardized safe exposure limits for electromagnetic radiation at various frequency ranges [Inte 20]. For instance, Table 1.5 illustrates the fundamental limitations for electromagnetic field exposure across a range of frequencies, from 100 kHz to 300 GHz, as established by the ICNIRP. These restrictions vary depending on the specific body part being exposed. Additionally, the SAR limits are presented for two distinct exposure scenarios:

- Occupational exposure: It stands for the individuals who are exposed under controlled conditions associated with their occupational duties. These individuals are trained to be aware of potential RF electromagnetic field risks and have the capacity to implement measures to mitigate any adverse effects.
- General public exposure: It stands for the individuals of all ages and varying health statuses, including those who are more vulnerable or have limited knowledge or control over their exposure to electromagnetic fields.

Table 1.5: Electromagnetic field exposure restrictions from 100 kHz to 300 GHz, for averaging intervals ≥6 min [Inte 20].

Exposure scenario	Frequency range (GHz)	Average SAR	Local Head and Torso SAR	Local Limb SAR	Local S_{ab} (W/m^2)
Occupational	0.0001 – 6	0.4	10	20	-
	6 – 300	0.4	-	-	100
General public	0.0001 – 6	0.08	2	4	-
	6 – 300	0.08	-	-	20

* SAR limits are provided in (W/kg).
[1] Whole-body average SAR is to be averaged over 30 min.
[2] Local SAR in to be averaged over a 10-g cubic mass.
[3] S_{ab}, which stands for the absorbed power density, provides a measure of the power absorbed in tissue that closely approximates the superficial temperature rise. Local S_{ab} is to be averaged over a square 4-cm^2 surface area of the body. Above 30 GHz, an additional constraint is imposed, such that exposure averaged over a square 1-cm^2 surface area of the body is restricted to two times that of the 4-cm^2 restriction.

By focusing on human exposure to radar technology, it can be compared to an element that is used constantly in our daily lives, such as a cell phone. The power of the signal transmitted by a commercial radar is 1000 times lower than the maximum power of a cell phone [Wan 14], which makes this technology safer in comparison[1].

It is also noteworthy that, at this time, there are more reports of the beneficial effects than detrimental effects from low-level exposure to mmWave radiation. Indeed, several researchers have indicated that mmWave radiation (42.2 GHz in [Loga 06], 50-80 GHz in [Bene 09] and 61.22 GHz in [Radz 04]) has been effective in inhibiting tumor growth.

[1]Indeed, following the radar equation [Skol 80] with the radars used in this thesis (Tables 2.1 and 2.2 from Section 2.1), the minimum distance between the radar and the person to ensure the local value of *Sab* is 1.4 cm for the 134 GHz radar, 4.45 cm for the 24 GHz radar, and 2.96 cm for the 77 GHz radar.

Moreover, several works have also reported that mmWaves can enhance the human immune system [Roja 98, Maka 05, Zhad 11]. Nevertheless, it is essential to ascertain whether these experiments can be replicated by independent researchers.

1.3 Thesis Motivation and Objectives

This thesis describes the feasibility of using radar technology for non-contact monitoring of vital signs. The work contributes to the technological development in the areas of non-contact vital signs monitoring and radar signal processing through the items summarized below:

1. Analysis of radar technology for vital signs with the aim of identifying the optimal configuration for cardiorespiratory monitoring.
    - Comprehensive comparison of LFMCW and CW radar configurations carried out at different operating frequency bands (24 and 134 GHz).
    - Development of a radar phase extraction algorithm to deal with FFT bin target migration and FFT bin phase distribution.
2. Analysis of the different vital signs and biomarkers that can be obtained from the radar acquired target displacement signal.
    - Analysis of the heart sounds for improving cardiac activity monitoring.
    - Analysis of the optimal signal processing algorithm to evaluate the extraction of the heart rate variability sequence.
    - Development of a radar configuration to evaluate the measurement of the carotid-femoral pulse wave velocity.
    - Initial development and testing of a real-time cardiorespiratory activity monitoring application using radar.

1.4 Thesis Organization

Aside from the introduction carried out in Chapter 1, the thesis is divided into three additional chapters. The organization is as follows:

- Chapter 2 discusses the hardware and software tools used for vital signs and biomarker extraction. It focuses on the radar system and its fundamentals. An analysis of the optimal radar configuration for this application is also presented.
- Chapter 3 describes the different signals and biomarkers obtained with radar techniques, such as breathing and heart rate, heart rate variability or pulse wave velocity. An analysis of the extraction of heart rate variability sequences at different body locations is also presented.
- Chapter 4 addresses some of the challenges that still need to be overcome to bring this sensor technology into real-world applications. Challenges such as the radar physiological

sensing in multi-target scenarios, the body motion tracking and cancellation, and real-time monitoring are covered.

- Chapter 5 summarizes the conclusions drawn from the work performed and some of the future lines of research that could be pursued for the remote analysis of vital signs.
- The Appendixes supplement the information in the previous chapters. These pages present, for instance, an analysis of the optimum operating frequency band for CW and LFMCW radar configurations, an analysis of the various sources of noise found in radar systems, and the effect of IQ imbalance on radar phase extraction. Finally, they describe some of the metrics employed throughout this thesis.

1.5 Publications

The results obtained from the development of this thesis have been published in the following journals and international conferences:

- **E. Antolinos** and J. Grajal, "Improving Vital Signs Monitoring in Real-World Environments with W-Band Phased-Array Radars," *IEEE Transactions on Microwave Theory and Techniques*, (submitted for publication).
- I. Sardinero-Meirás, I. E. López-Delgado, **E. Antolinos**, F. N. Pérez-Fernández, M. Ferreras, L. Pérez-Eijo, M. Arias, B. González-Valdés and J. Grajal, "From mmWave Radar Nodes to Multistatic Arrays: Design Considerations and Applications," *2024 18th European Conference on Antennas and Propagation (EuCAP)*, pp. 1–5, Glasgow, United Kingdom, Mar. 2024.
- I. Sardinero-Meirás, **E. Antolinos**, I. E. López-Delgado, M. Gómez-Bracamonte, J. Fernández-Martínez, L. Pérez-Eijo, M. Arias, B. González-Valdés and J. Grajal, "Portable Low-Cost Millimeter-Wave Radar Node for Short-Range Applications," *2023 European Radar Conference (EURAD)*, pp. 460–463, Berlin, Germany, Sept. 2023.
- **E. Antolinos**, F. N. Pérez-Fernández and J. Grajal, "Pulse Wave Velocity Monitoring Using A mmWave Radar Network," *2023 IEEE MTT-S International Microwave Biomedical Conference*, pp. 85–87, Leuven, Belgium, Sept. 2023.
- **E. Antolinos** and J. Grajal, "Comprehensive Comparison of Continuous-Wave and Linear-Frequency-Modulated Continuous-Wave Radars for Short-Range Vital Sign Monitoring," *IEEE Transactions on Biomedical Circuits and Systems*, Vol. 17, No.2, pp. 229–245, Apr. 2023.
- I. E. López-Delgado, **E. Antolinos**, I. Sardinero-Meirás, M. Gómez-Bracamonte, J. D. Arias-Londoño, E. Luque-Buzo, F. Grandas, J. I. Godino-Llorente and J. Grajal, "mm-Wave wireless radar network for early detection of Parkinson's Disease by gait analysis," *2023 IEEE Radar Conference (RadarConf23)*, pp. 1–6, San Antonio, TX, USA, May 2023.
- **E. Antolinos**, F. García-Rial, C. Hernández, D. Montesano, J. I. Godino-Llorente and J. Grajal, "Cardiopulmonary Activity Monitoring Using Millimeter Wave Radars,"

Remote Sensing, Vol. 12, No. 14, pp. 2265, Jul. 2020.

The results of the thesis have also been published in the following national conferences:

- **E. Antolinos**, F. N. Pérez-Fernández and J. Grajal, "Non-Invasive Monitoring of Arterial Stiffness with mmWave Radar," *URSI 2024 Cuenca XXXIX Simposium Nacional de la Unión Científica Internacional de Radio*, Cuenca, Spain, Sept. 2024.
- I. Sardinero-Meirás, I. E. López-Delgado, **E. Antolinos**, F. N. Pérez-Fernández, M. Ferreras, L. Pérez-Eijo, M. Arias, B. González-Valdés and J. Grajal, "Towards mmWave Multistatic Arrays: A 120 GHz Phased-Array Imaging Radar," *URSI 2024 Cuenca XXXIX Simposium Nacional de la Unión Científica Internacional de Radio*, Cuenca, Spain, Sept. 2024.
- I. E. López-Delgado, **E. Antolinos**, I. Sardinero-Meirás, M. Gómez-Bracamonte, J. D. Arias-Londoño, E. Luque-Buzo, F. Grandas, J. I. Godino-Llorente and J. Grajal, '"Gait analysis with a wireless radar network for early detection of Parkinson's Disease," *URSI 2023 Vigo XXXVIII Simposium Nacional de la Unión Científica Internacional de Radio*, Cáceres, Spain, Sept. 2023.
- I. Sardinero-Meirás, **E. Antolinos**, I. E. López-Delgado, M. Gómez-Bracamonte, J. Fernández-Martínez, L. Perez-Eijo, M. Arias, B. Gonzalez-Valdes and J. Grajal, "Compact Low-Cost Millimeter-Wave Radar Sensor for Short-Range Applications," *URSI 2023 Vigo XXXVIII Simposium Nacional de la Unión Científica Internacional de Radio*, Cáceres, Spain, Sept. 2023.
- **E. Antolinos**, F. García-Rial, C. Hernández, D. Montesano, J. I. Godino-Llorente and J. Grajal, "Vital sign monitoring using a 122 GHz FMCW-Radar," *URSI 2021 Vigo XXXVI Simposium Nacional de la Unión Científica Internacional de Radio*, Vigo, Spain, Sept. 2021.

1.6 Research Projects Involved

The work performed during this thesis has been partially or fully funded by the following national research projects or grants:

- **Ministerio de Ciencia e Innovación**: "*Cribado y monitorización del párkinson usando biometrías basadas en tecnología RADAR (PD-RADAR)*", TED2021-131688B-I00, 2022-2024.
- **Ministerio de Ciencia e Innovación**: "*Radar multiestático en bandas milimétricas para generar imágenes dinámicas 3D en campo cercano: Sensor (MultiScan-UPM)*", PID2020-113979RB-C21, 2021-2024.
- **Ministerio de Ciencia, Innovación y Universidades**: "*Comunicaciones con transceptores en MIMO LTE-A/mmW para servicios avanzados en transporte de alta movilidad*", TEC2017-87061-C3-1-R, 2019-2021.
- **Ministerio de Educación y Formación Profesional**: "*Desarrollo de sistemas radar*

en bandas milimétricas para la detección de señales vitales", Programa de Ayudas para la Formación de Profesorado Universitario 2018, FPU18/01525, 2019-2023.

Chapter 2

Vital Sign Monitoring Tools

This thesis focuses on non-contact monitoring of vital signs by analyzing cardiorespiratory mechanical activity. Achieving this by measuring skin displacement caused by cardiac and respiratory activity, using radar technology. This cardiorespiratory activity is also acquired with external sensors used as references to measure the radar system's performance. This chapter presents the hardware tools used in the study, including the radar sensor and external devices used as reference. Moreover, it details the signal processing carried out to the target displacement, R(t), which is acquired with the radar. The purpose of this signal conditioning stage is to isolate the displacement caused by respiratory and cardiac activities, using denoising algorithms and techniques for signal separation, in order to prepare $R(t)$ for the vital sign and biomarkers extraction. This overview is shown in Fig. 2.1.

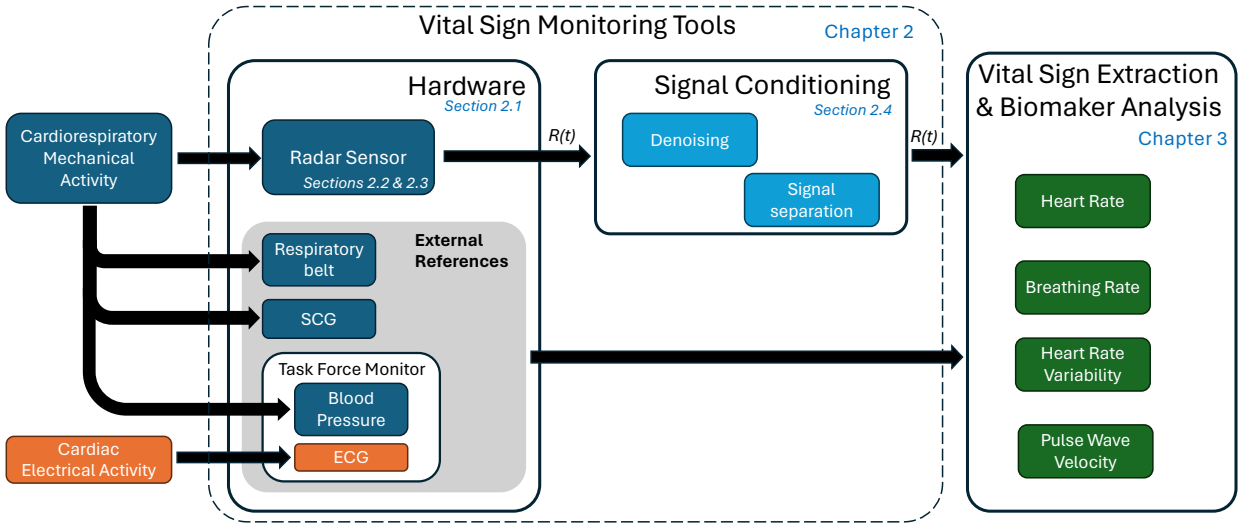

Figure 2.1: Hardware and signal processing overview for non-contact vital sign monitoring.

Thus, the chapter is structured into the following sections:

- Section 2.1 outlines the hardware tools employed, encompassing both the radar system and the devices utilized as references for monitoring respiration and heartbeat activities.

- The radar fundamentals are presented in Section 2.2. It also includes the signal processing algorithm chain employed for extracting the target displacement.
- The choice of the optimum radar waveform configuration is carried out in Section 2.3.
- Section 2.4 introduces the signal conditioning tools that are used to prepare the displacement signal for the vital signs and biomarker extraction. It presents techniques for denoising and signal separation, focusing on spectral analysis, empirical mode decomposition (EMD) and wavelet transform.

2.1 Monitoring Hardware

This section details the hardware setups used in this work:

- A radar sensor. Among the different radar sensors used, two stand out: a radar sensor based on a linear-frequency-modulated continuous-wave (LFMCW) radar fabricated by Silicon Radar [Sili 22], and a commercial radar kit manufactured by Texas Instruments [Texa 20c].
- An external device used as reference. For instance, the Task Force Monitor [CNSy 23], which is used for acquiring the ECG or the blood pressure waveform, or the Zephyr BioHarness 3.0 [Zeph 12], which is a respiratory belt used to measure the chest motion caused by the respiratory activity.

Thus, the general measurement setup will consist of a radar sensor and an ECG, which represents the gold standard for the measurement of cardiac activity. Additional reference sensors may be used in some experiments. The measurement setup diagram is shown in Fig. 2.2.

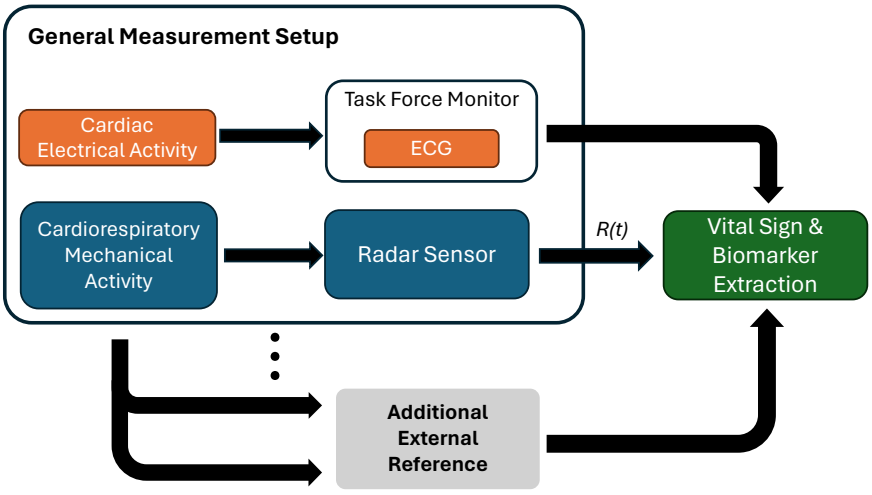

Figure 2.2: General measurement setup scheme used for vital sign extraction.

2.1.1 Radar sensor

2.1.1.1 Silicon Radar

The main radar sensor used is based on a LFMCW radar fabricated by Silicon Radar [Sili 22]. The device itself is based on a 8 x 8 mm^2 monolithic microwave integrated circuit (MMIC) transceiver. Research related to this sensor and its previous versions may be found throughout the literature [Paul 17].

In order to better fit the desired application, the commercial version of the radar baseband board has been modified. These modifications allow to use the radar sensor at two frequencies (24 and 134 GHz) only by exchanging the MMIC board, and in CW or LFMCW configurations. The assembled radar module is presented in Fig. 2.3. The main modifications have been the replacement of the commercial radar's microcontroller and baseband boards with custom-made PCBs. The system architecture is common for both operating configurations, and its diagram is presented in Fig. 2.4.

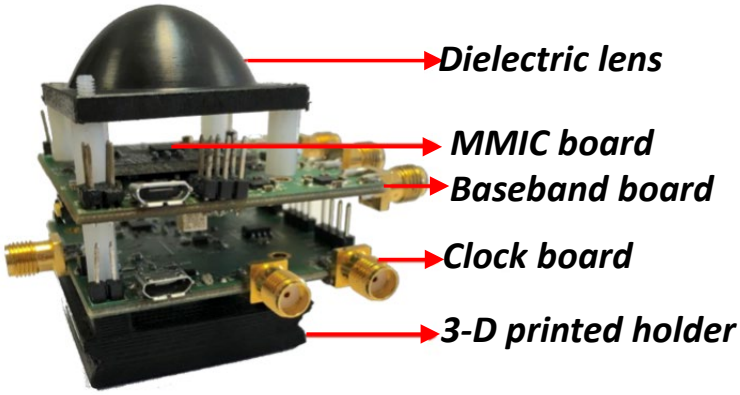

Figure 2.3: Photograph of the 134 GHz radar global assembly with the MMIC located below the dielectric lens.

The radar system consists of:

- A commercial MMIC board fabricated by Silicon Radar. Two MMIC boards have been used, one operating at 134 GHz and the other at 24 GHz. The difference in architecture between both boards is indicated in Fig. 2.4, each board has its specific voltage-controlled oscillator (VCO). In the 134 GHz board, the VCO frequency is 67 GHz and it is doubled to 134 GHz.
- A baseband board, which controls the MMIC and conditions the I/Q signals. This board includes the microcontroller (μC), the Phase Frequency Detector (PFD) and the I/Q filters:
  - The PFD used is the ADF4159 from Analog Devices [Anal 14]. It can be configured to perform a frequency sweep, controlling the swept bandwidth, the duration and the linearity of the frequency sweep. Thus, it allows to configure the transmitted waveform, and, therefore, if the radar is operating in CW or LFMCW configuration without changing the hardware architecture. The reference oscillator used to feed

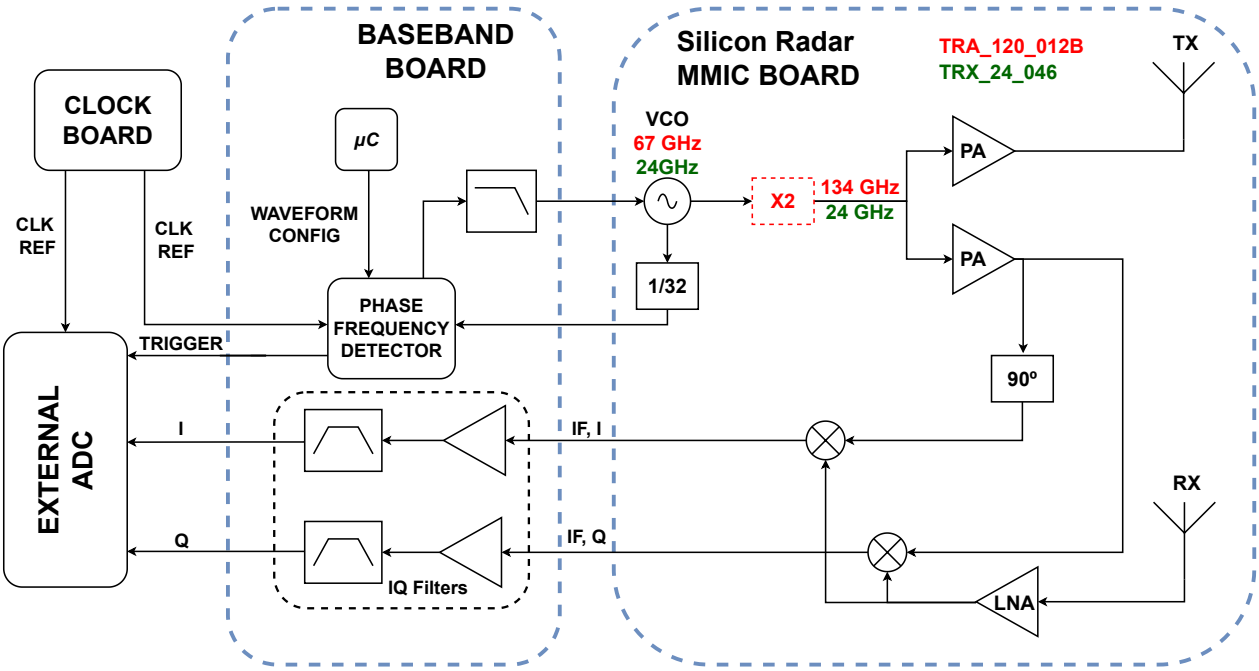

Figure 2.4: Diagram of the radars RF and baseband architectures. The baseband board is common for both frequencies: 24 and 134 GHz. The architecture differences between the MMIC boards are represented in red, for the 134 GHz radar, and in green, for the 24 GHz radar.

the PDF has also been replaced and is now located on the clock board. It provides less phase noise and improves dynamic range.

  - The commercial microcontroller has been replaced by the Attiny-167 [Atme 14], a 8-bits microcontroller with 14 GPIO pins available. The commercial LFMCW radar's transmission was limited to intervals managed by its microcontroller. These intervals included off-time between clusters of LFMCW sweeps to allow for on-board signal processing and USB-to-PC data transmission, which would hinder continuous cardiopulmonary measurements. In the present version, all processing is offloaded to a PC, allowing continuous LFMCW operation. The replacement of the microcontroller also improves waveform configurations, allowing for finer bandwidth and sweep time selections. This has enabled proper alignment of sweep flyback times, and triggering of the ADC's sampling using an end-of-ramp signal. Both improvements create better synchronized waveform generation and sampling, reducing the error in the measurements.

  - I/Q filters. The analog filters applied to the in-phase and quadrature signals have been modified to be low-pass filters, allowing CW configuration. The cutoff frequency is 2 MHz.

- A clock board distributes the clock reference. The reference oscillator allocated in this board is a 80 MHz oscillator from the ABLNO series [Abra 22], from ABRACOM. This frequency can be divided with a programmable divider by powers of 2 from 2 to 16.

Thus, the ADC sampling frequency can vary from 5 MHz to 80 MHz.

- An external ADC. The external ADC used is the model PCI-9846 from ADLINK [ADLI 14], with 16 bits, 4 channels, and a configurable sampling frequency up to 40 MS/s.

More information about the hardware architecture can be found in [Garc 19]. The main radar characteristics are summarized in Table 2.1 and a photograph of the radar modules can be seen in Fig. 2.5.

Table 2.1: Main characteristics of the radar modules used.

Characteristic	**Radar 134 GHz**	**Radar 24 GHz**
Model	*TRA_120_045*	*TRX_024_046*
Central Frequency (GHz)	134	24.6
Output Power (dBm)[1]	−3	4
Bandwidth (GHz)	20 (max)	3.6 (max)
Sweep Time	12 μs to 18 ms	12 μs to 18 ms
Antenna type	Dipole	6x4 Patch array
Beamwidth	15°(E) 40°(H)	25°(E) 15°(H)
Antenna Gain	6 dB	16 dB
Beamwidth (with the lens)[2]	4°(E) 4°(H)	-
Lens Gain	12 dB	-
Board dimensions (cm)	5x5	8x5

[1] Without antennas.

[2] The use of dielectric lens allows a narrower focusing. Lens are only used with the 134 GHz radar.

Besides these characteristics, the radar's phase stability is critical for vital sign monitoring. It represents the random distance displacement caused by phase shifts in the received signal when the radar is focused on a static target. As the target is static, any registered phase shifts in the received signal must be due to atmospheric variations or the sensor's own phase noise. Therefore, this parameter can be interpreted as minimum displacements that can be measured with the radar. Distance displacements with a corresponding phase shift lower than the sensor's phase stability cannot be accurately measured.

The phase stability of the 134 GHz radar is presented in Fig. 2.6 and has been measured by pointing the radar to a static metal plate. This measurement has been carried out using the radar in LFMCW configuration, with a sweep time of 1 ms and a bandwidth of 6 GHz, which is a standard configuration for this kind of application. The signal processing to extract this target displacement is detailed in Section 2.2.2.

As will be detailed in Chapter 3, the heart's activity causes chest displacement in the range of tenths of millimeters, which is two to three orders of magnitude above the radar's phase stability. Therefore, this radar is able to monitor these movements.

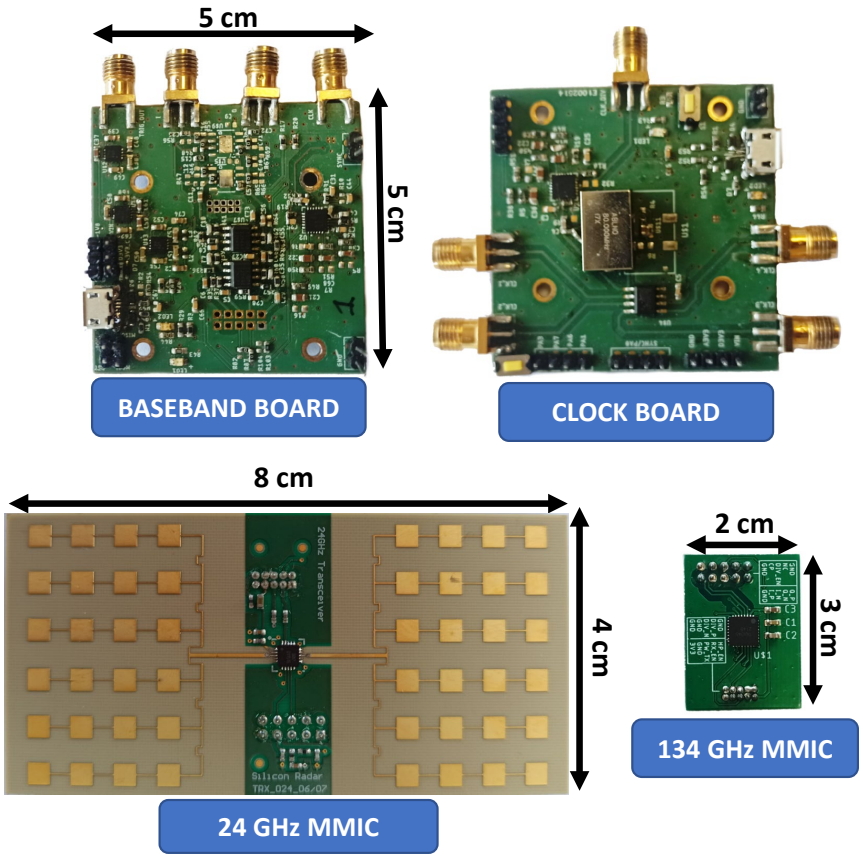

Figure 2.5: Boards for the 134 and 24 GHz radars. From top to bottom: the baseband and clock boards, which are common for both frequencies, the 24 GHz and the 134 GHz MMIC boards.

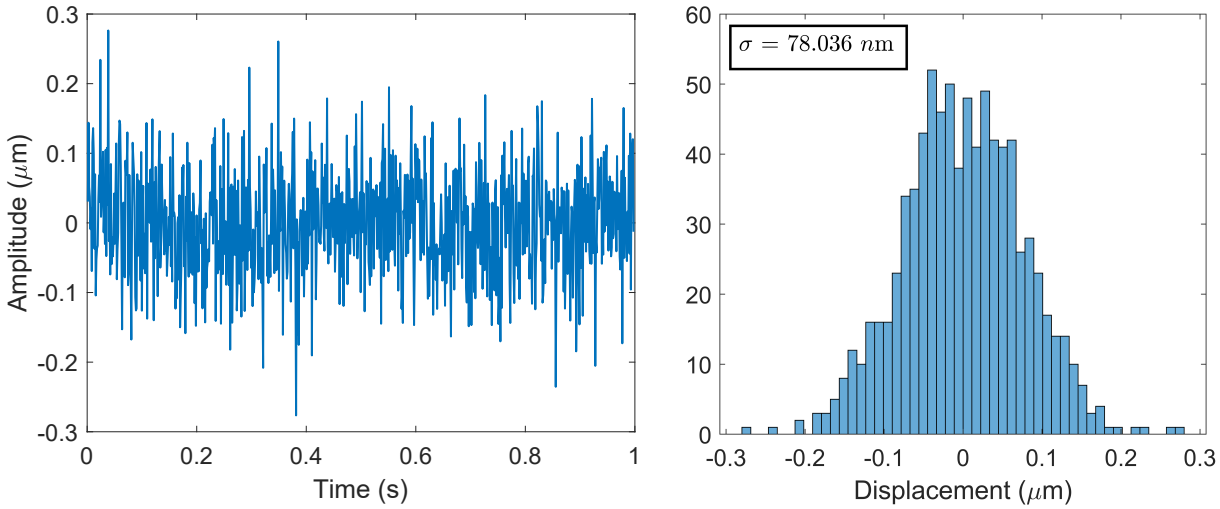

Figure 2.6: Target displacement of the radar sensor measuring a static target. Histogram of the phase stability distribution for a 10-seconds measurement.

2.1.1.2 Texas Instruments

The AWR2243 is a commercial single-chip FMCW transceiver developed by Texas Instruments for automotive applications. This chip implements 3 transmitters and 4 receivers which operate in the 76 to 81 GHz band, being able to operate in multiple-input multiple-output (MIMO) configuration. A MIMO radar can be conceptualized as a SIMO (single-input multiple-output) radar of $N = N_{Tx} \cdot N_{Rx}$ receiving antennas, where N_{Tx} and N_{Rx} represent the number of transmitting and receiving antennas, respectively [Robe 04].

Two evaluation board that uses this radar chip are used:

- AWR2243BOOST [Texa 20b]. This device is a standalone board which integrates the AWR2243 radar sensor. This platform allows raw capture of ADC data from the radar front end. Data is acquired using the DCA1000 board [Texa 18], a capture card that interfaces with the Texas Instrument radar and allows real-time data transfer to a PC via 1 Gbps Ethernet. However, it is important to note that this is carried out using the UDP protocol, which may lack the reliability required for certain applications.
- AWR2243 Cascade [Texa 20a]. This solution (MMWCAS-RF-EVM) is based on the AWR2243 chip, where 4 chips are cascaded together using a 20 GHz local oscillator to operate synchronously, allowing support for up to 12 transmitters and 16 receivers. Thus, it improves the SNR and angular resolution of the single-device system. This board must be paired with the mmWave cascaded imaging radar DSP evaluation module (MMWCAS-DSP-EVM [Texa 20d]) for capturing and storing the data.

Photographs of the aforementioned devices are shown in Fig. 2.7, and their main parameters are listed in Table 2.2.

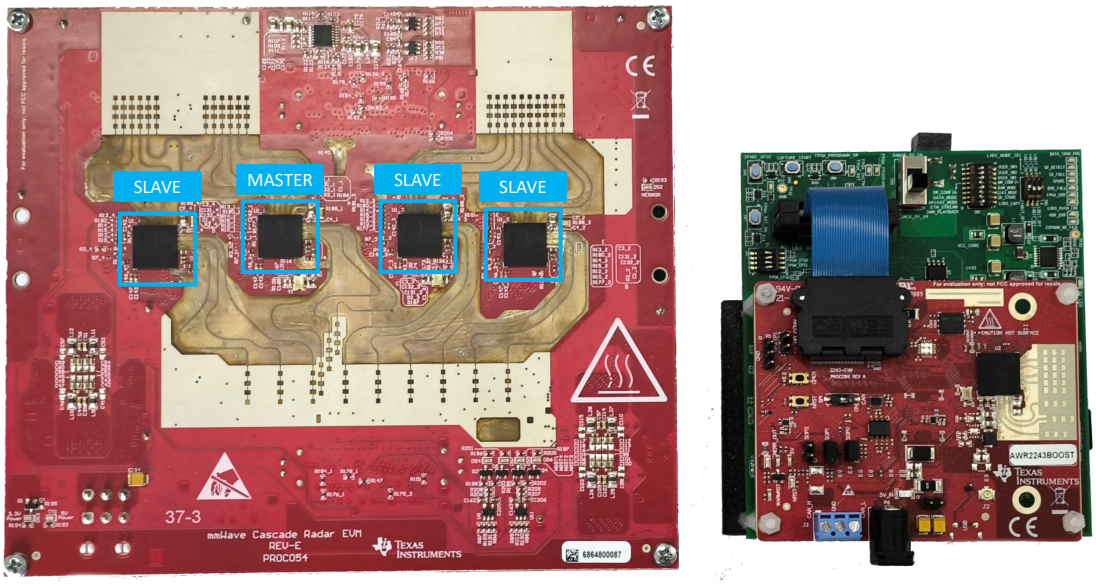

Figure 2.7: Boards for the AWR2243 radars. From left to right: the AWR2243 Cascade device, where the 4 chips are identified, and the AWR22431BOOST with the DCA1000 board.

Table 2.2: Main characteristics of the radar modules used.

Characteristic	*AWR2243*
Number Tx	3^B 12^C
Number Rx	4^B 16^C
Frequency (GHz)	76 – 81
Output Power (dBm)[1]	13
Sweep Time	13 μs to 5 ms
Sampling frequency	2 kHz - 45 MHz
Antenna type	Patch array
Board dimensions (cm)	8x7^B 16x14^C

^{B} AWR2243BOOST. ^{C} AWR2243 Cascade.

[1] Per chip and without antennas.

These radars can be configured in time division multiplexing (TDM) mode. This mode entails the transmission of a chirp by each transmit antenna during a non-overlapping slot of time. This provides orthogonality in time, allowing the receiving antennas to separate the echoes from each transmit antenna [Bech 17]. An example of the TDM-MIMO sequence transmitted is illustrated in Fig. 2.8. In this example, the transmitted chirps are grouped in loops, which are repeated K times inside a frame.

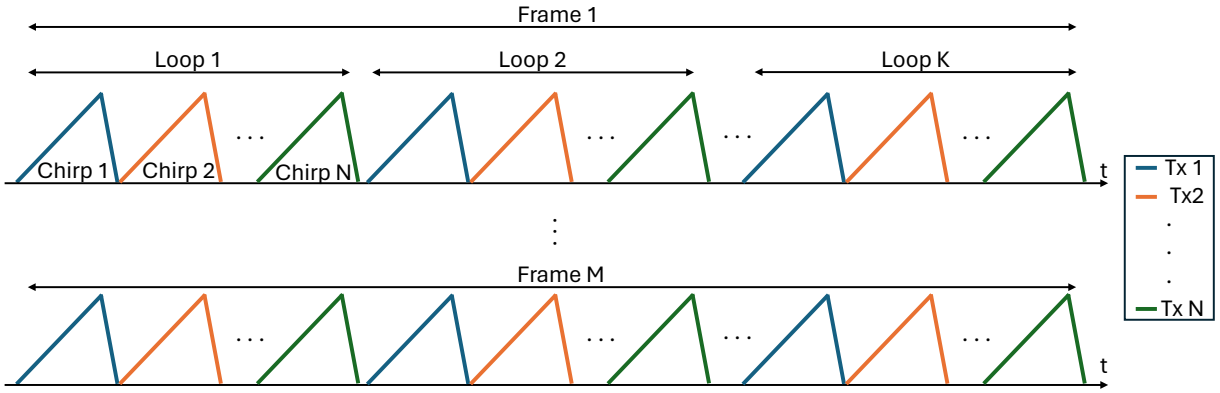

Figure 2.8: Example of a TDM-MIMO sequence transmitted with the radar.

Furthermore, MIMO systems can be characterized by a virtual array constructed by the convolution of the locations of the transmit and receive antenna locations [Li 08]. This TDM-MIMO configuration enables the formation of a larger virtual array with enhanced angle resolution compared with a conventional phased array [Broo 85]. The radar angle resolution for a uniform linear array is determined by the following expression [Mail 17]:

$$\Delta\theta_{3dB}(rad) \simeq 0.89\frac{\lambda}{Nd\ cos(\theta)} \tag{2.1}$$

where N represents the number of virtual channels, d is the distance between them, and θ is the beam pointing direction. Table 2.3 shows the azimuth angle resolution that can be achieved with the aforementioned radars. Moreover, Fig. 2.9 shows a diagram of the equivalent virtual array obtained with the AWR2243BOOST, where Tx 1 and Tx 3 are used for azimuth resolution and Tx 2 is used for elevation resolution.

Table 2.3: Azimuth angle resolution enhancement for the AWR2243BOOST and AWR2243 Cascade.

	# Rx elements	Angle resolution (°)	# Virtual elements	Angle resolution (°)
AWR2243BOOST	4	25.50	8[1]	12.75
AWR2243 Cascade	16	6.37	86[2]	1.19

[1] This radar has 12 virtual antennas, but only 8 give azimuth information.

[2] This radar has 192 virtual antennas, but only 86 give azimuth information.

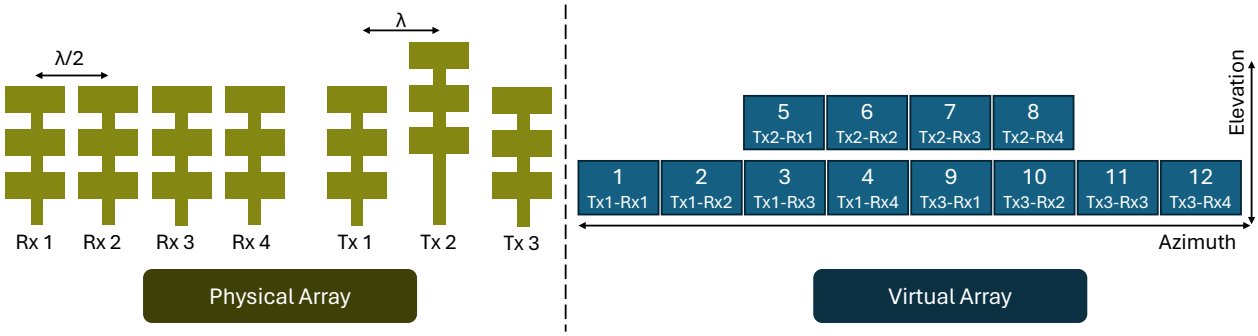

Figure 2.9: Diagram of the physical antenna array and its equivalent virtual array for the AWR2243BOOST.

Furthermore, these radars allow analog beamforming, where the phase of each transmitter channel is configured to steer the beam towards a specific direction. The transmitters of these radars utilize phase shifters with a resolution of 6-bits, which allows for the configuration of phase resolution of 5.625° [Texa 20a]. However, the problem with performing beamforming by hardware is that the beam steering is fixed, and the system cannot adapt to changes without reconfiguring the phase shifters.

2.1.1.3 Commercial radar solutions overview

The growing interest in the use of radar in industrial (∼60 GHz band) and automotive (∼77 GHz band) applications has resulted in a wide variety of radar solutions available on the market. Table 2.4 shows a comparison between some of the commercial radar versions available.

Table 2.4: Commercial mmWave radar sensors.

Product	Frequency (GHz)	# Tx	# Rx	TX Power (dBm)[1]	Antenna	Manufacturer
TR2_060_095 [Sili 23b]	56.1 – 66	1	2	6*	External	Silicon Radar
T4R4_060_096⋆ [Sili 23a]	55.9 – 66.4	4	4	5*	External	Silicon Radar
TRA_120_045 [Sili 20]	113.9 – 134.1	1	1	-3	On-chip	Silicon Radar
TRA_120_067 [Sili 23d]	119.3 – 125.8	1	1	-3	External	Silicon Radar
TRA_240_091 [Sili 23c]	222.5 – 267.5	1	1	2	On-chip	Silicon Radar
BGT24ATR11 [Infi 13]	24 – 24.25	1	1	9	External	Infineon
BGT24ATR12 [Infi 14]	24 – 24.25	1	2	9	External	Infineon
BGT60UTR11AIP [Infi 23b]	57.4 – 63	1	1	5	External	Infineon
BGT60ATR24C [Infi 23a]	58 – 62	2	4	4	External	Infineon
AWRL6432⋆ [Texa 24]	57 – 64	2	3	14	External	Texas Instruments
AWR6x43⋆ [Texa 22b]	60 – 64	3	4	12	External	Texas Instruments
AWR1x43⋆ [Texa 22a]	76 – 81	3	4	12	External	Texas Instruments
AWR1x42⋆ [Texa 21]	76 – 81	2	4	12	External	Texas Instruments
TEF810x [NXP 19]	76 – 81	3	4	11.5+	External	NXP
TEF82xx [NXP 20]	76 – 81	3	4	13.5	External	NXP
RAA270205 [Rene 22]	76 – 81	4	4	19	External	Renesas
STRADA431 [STMi 19]	24 – 24.25	1	3	13	External	STMicroelectronics

[1] Without antennas.

* Simulated power.

+ Output power of 12 dBm (76-78 GHz) and 11 dBm (78-81 GHz).

⋆ This product can be found as integrated final solutions, with antennas and acquisition unit.

2.1.2 External reference devices

2.1.2.1 Accelerometer ADXL335

The device is the ADXL335 from Analog Devices [Anal 10]. This sensor can measure the static acceleration of gravity and the dynamic acceleration resulting from motion or vibration. It is a 3-axis accelerometer, with a full sensing range of $\pm 3g$ and a sensitivity of 300 mV/g. An image of the ADXL335 board can be found in Fig. 2.10.

Unlike the rest of the reference devices presented in this section, this is the only one that shares nature with the radar system, since both measure a signal with a mechanical origin. For the analysis carried out in this thesis, only the normal axis to the surface is analyzed, which corresponds to the movement direction acquired with the radar. Moreover, the ADXL335 has an analog low-pass filter with a cutoff frequency of 50 Hz.

From a medical point of view, the signal obtained with this device is equivalent to that obtained with a seismocardiogram (SCG), which measures the accelerations and chest's vibrations caused by the heart motion. For convenience, from here on, the ADXL335 is will be referred to as *SCG sensor*.

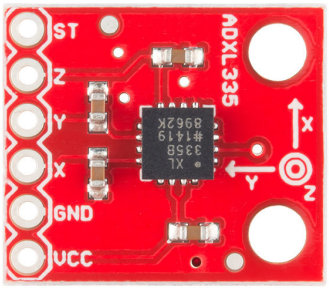

Figure 2.10: External accelerometer ADXL335 board from Analog Devices.

2.1.2.2 Task Force Monitor

The Task Force Monitor (TFM) developed by CNSystems [CNSy 23] is used as an additional reference for the vital signs monitoring, since it can synchronously measure electrocardiogram (ECG), blood pressure (BP) and impedance cardiogram (ICG). Figs. 2.11 and 2.12 show a photograph of the device and its software interface, respectively. This image present the TFM front face, where the connections with the elements applied to the patient to perform the measurements are located:

- The silver (metallic) connectors allow the connection of the compressed air outlets for the continuous and oscillometric blood pressure measuring devices.
- The green one connects to the continuous blood pressure measuring device.
- The red one connects the ECG cable.
- The yellow one connects the ICG.
- The black one is an external input port that allows the user to connect other equipment.

The purpose of this external input port is to be able to synchronize a signal from an external source with the rest of the signals.

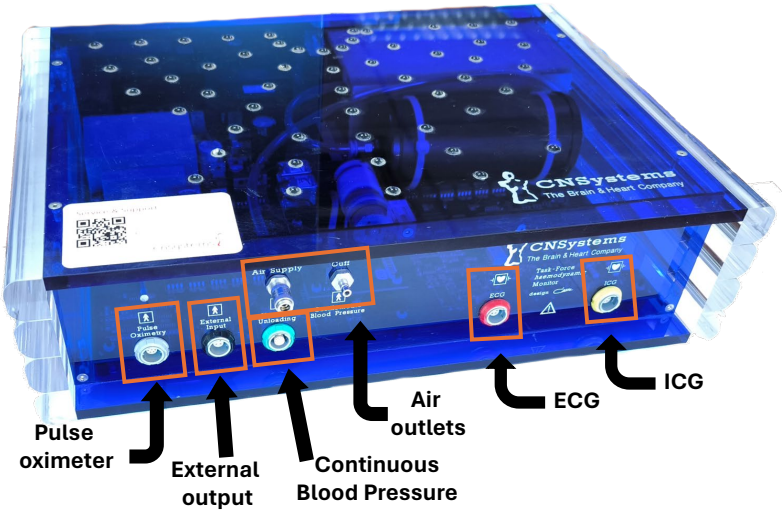

Figure 2.11: Front view of the Task Force Monitor with the different connectors.

Figure 2.12: Main window of the application to analyze and visualize the measurements.

The radar sensor and the TFM are synchronized using a gold-code sequence [Sche 20], which is generated in the clock board of the radar, and it is digitalized simultaneously in the TFM (using the external input) and in the radar's external ADC. In this thesis, only the ECG signal is used.

Focusing on the 3-lead ECG acquired with the TFM, it is obtained according to two classic methods [AlGh 12]: the three standard derivations of Einthoven (identified in the application as ECG I, ECG II, and ECG III) and the three derivations of Goldberger (identified as aVR, aVL, and aVF). Each of these derivations is in a position of the Einthoven triangle, as

represented in Fig. 2.13. Einthoven's are the classic cardiac derivations of the electrocardiogram. They record the potential difference between two electrodes located at different extremities. On the other hand, the Goldberger derivations (also called monopolar derivations of the extremities) record the potential difference between a theoretical point in the center of the Einthoven triangle, with a value of 0, and the electrode of each limb.

In this work, the first and second Einthoven derivations are chosen for the ECG measurements.

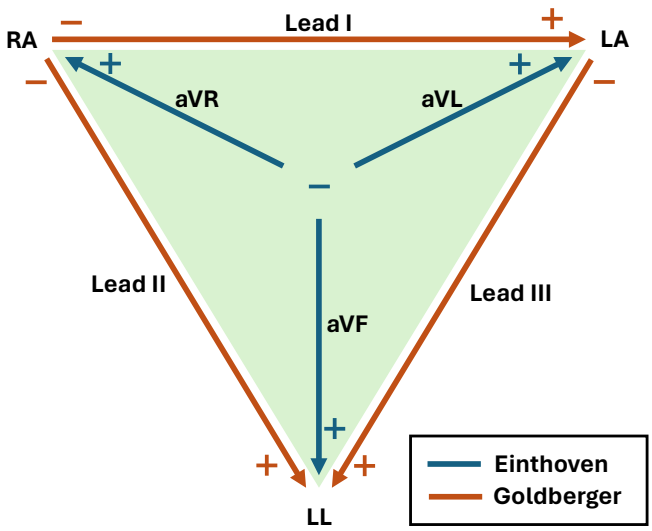

Figure 2.13: Graphical representation of ECG leads: Einthoven leads in orange and Golderbergs leads in blue. RA, LA, and LL represent the right arm, left arm, and left leg, respectively.

2.1.2.3 Zephyr BioHarness 3.0

The Zephyr BioHarness 3.0 chest band serves as a telemetry device for physiological monitoring [Zeph 12]. It is designed for the monitoring of adults in various settings, including the home, workplace, and alternative care environments. The chest band comprises a strap that goes around the chest and an electronic device. It is equipped with a series of sensors that capture various physiological signals. These sensors consist of a 1-lead ECG, a three-axis accelerometer, a skin temperature thermistor, and a capacitive sensor for respiration motion. Thus, this device enables users to capture heart rate, respiratory rate, acceleration, activity level, and body posture. It is able to stream these data wirelessly via Bluetooth. A photograph of the Zephyr BioHarness can be found in Fig. 2.14.

The Zephyr BioHarness has been widely validated through the literature, where it has been used, mainly, in sportive scenarios. In a recent systematic review [Naza 18], the authors reported that the Zephyr BioHarness 3.0 device provides reliable and accurate measurements of heart rate in various contexts. The review also emphasized its strong agreement with gold standard measurements, consistent with findings reported in other validation studies. The study in [Kim 12a] also validated the respiration rate of this device by comparing it with a portable cardiopulmonary breath-by-breath gas exchange analyzer during exercise.

Figure 2.14: Photograph of the Zephyr BioHarness 3.0.

This reference device has been used, mainly, for acquiring the respiration information, see Section 3.2.1. However, it has also been used to monitor the ECG in multi-target scenarios or in scenarios where the target should not be limited by the length of TFM's ECG cables.

2.2 Radar Fundamentals

The radar sensor, as was previously introduced in Section 2.1, can work in CW and LFMCW configurations. Therefore, before detailing the signal processing tools used in this thesis, it is important to introduce the basic principles on which CW and LFMCW configurations are based. This section also presents the different parameters to consider when configuring the radar. It also describes the steps of the algorithms used to obtain the target displacement in each radar configuration and the signal conditioning. It also includes an analysis to determine which is the optimal radar configuration.

2.2.1 Radar working principle

This section introduces the working principles of CW and LFMCW radars. The complete mathematical formulation is detailed in Appendix A.

2.2.1.1 CW Radar

The working principle of non-modulated CW is based on transmitting a single-tone signal, which is reflected by the target. A replica of the transmitted signal is mixed with the received echoes, obtaining the beat signal. The ideal CW transmitted signal can be defined with the following expression:

$$s_{tx}(t) = A\exp(j(2\pi f_0 t + \phi)) \tag{2.2}$$

where f_0 is the transmitted frequency and ϕ is the initial phase. The received signal for a point scatterer at a range $R(t)$ can be expressed as:

$$s_{rx}(t) = A\sigma s_{tx}\left(t - \frac{2R(t)}{c}\right) \tag{2.3}$$

where σ is the reflection coefficient of the target and $\frac{2R(t)}{c}$ is the round trip delay, being c, the light velocity. After the IQ demodulation and filtering processes, the radar baseband signal can be expressed as:

$$s_b(t) = A_b \exp\left(j\frac{4\pi f_0 R(t)}{c}\right) \tag{2.4}$$

where A_b is the signal amplitude. Thus, the displacement information is contained in the phase of $s_b(t)$.

2.2.1.2 LFMCW radar

Analougsly to CW radars, the working principle of LFMCW is based on transmitting a linear frequency modulated RF signal. Under the "stop and go assumption" [Carr 95], which states that the target does not change its position during the radar sweep time, the beat signal for a point-scatterer at a range $R(\tau)$ (where τ is the so-called slow time[1]) can be formulated as:

$$s_b(t,\tau) = \sigma \exp(j(2\pi f_b(\tau)t + \phi(\tau) + \phi_2(\tau))) \tag{2.5}$$

The beat signal follows a sinusoidal waveform with a frequency known as beat frequency $f_b(\tau) = \frac{2B}{T \cdot c}R(\tau)$, $\phi(\tau) = 4\pi f_0 R(\tau)/c$, and $\phi_2(\tau) = -\frac{4\pi B R^2(\tau)}{T \cdot c^2}$, where f_0 is the initial frequency transmitted, B is the bandwidth, and T is the sweep time. $\phi_2(\tau)$ represents the residual video phase (RVP) [Carr 95], which is found to be negligible and can be ignored, since it is proportional to $1/c^2$. These parameters are shown in Fig. 2.15.

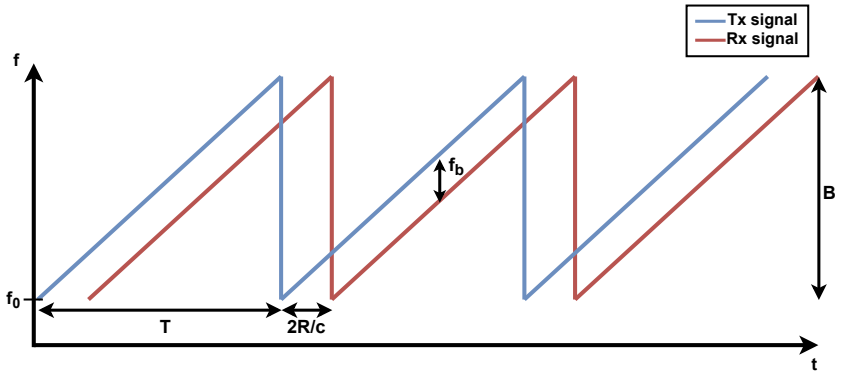

Figure 2.15: Working principle of LFMCW radars. B stands for the transmitted bandwidth, f_0 is the initial frequency transmitted, T is the repetition period and $2R/c$ is the round-trip delay.

2.2.2 Radar signal processing

This section details the signal processing steps required to extract the target displacement from the I and Q signals acquired with the radar. The algorithm steps for CW and LFMCW radar configurations are shown in Fig. 2.16.

[1]Mathematically, the slow time can be expressed as $\tau_i = i \cdot T$, with $i \in \mathbb{Z}$, so it is a sampled version of the fast time t, which is defined in the interval $[0, T]$.

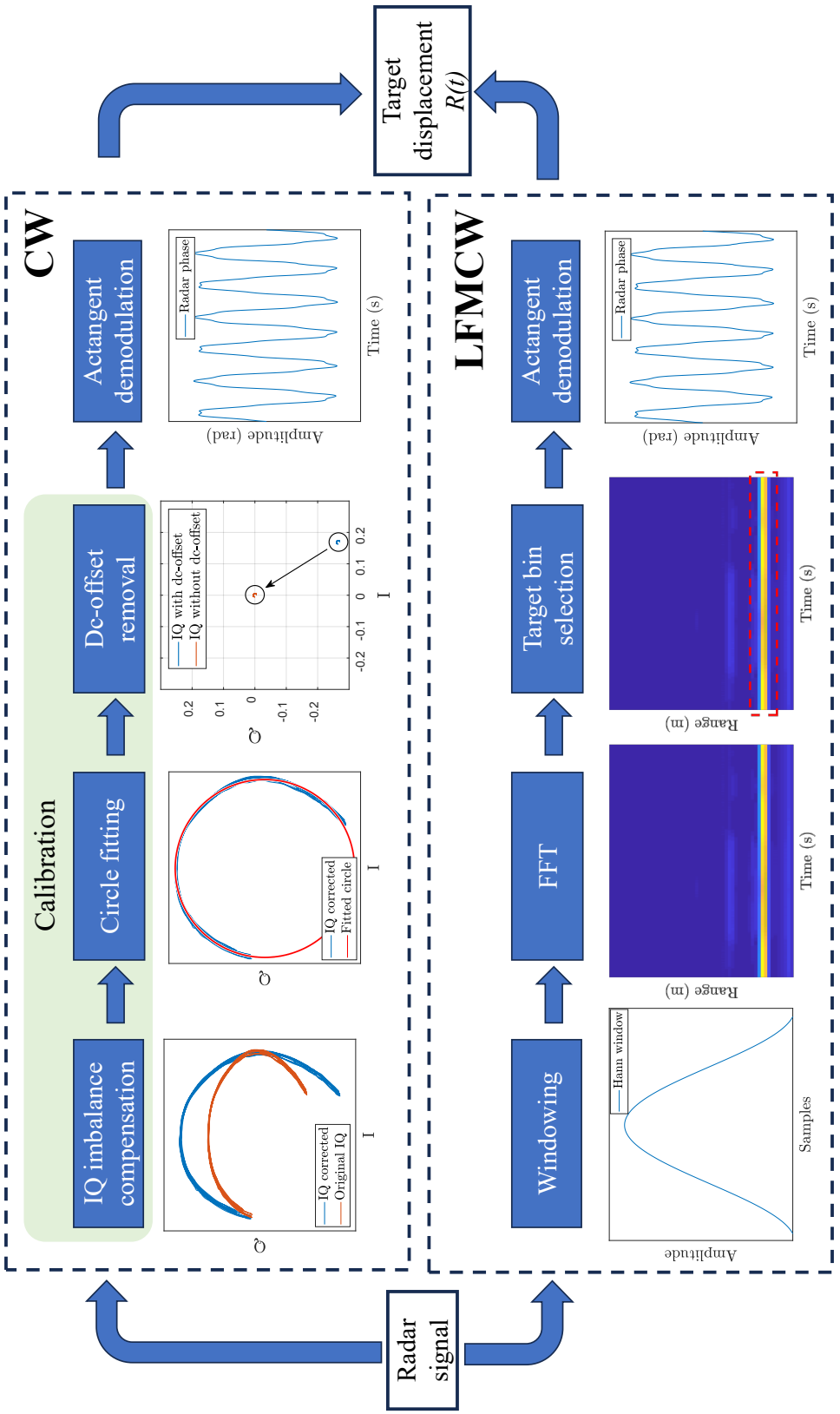

Figure 2.16: Flowchart with the processing steps to obtain the target displacement in CW and LFMCW configurations.

2.2.2.1 CW

First of all, a third-order Butterworth low-pass filter with a cutoff frequency of 100 Hz is applied to the I and Q signals to reduce the noise. A calibration is then required to compensate for the IQ imbalances in the CW configuration, the impact of this calibration is described in Section 2.3.2. Then, the arctangent demodulation is used to estimate the signal phase, as showed in [Kay 93], the arctangent is the maximum likelihood estimator (MLE) for this case. Then, the displacement is calculated as:

$$\Delta R(t) = \frac{unwrap\{\phi(t) - \phi(t_0)\} \cdot c}{4\pi \cdot f_o} \tag{2.6}$$

where $\phi(t_0)$ is the initial phase at $t = t_0$. Phase must be unwrapped because it takes values between $-\pi$ and π.

2.2.2.2 LFMCW

In the LFMCW configuration, no calibration is needed, as showed in Appendix B. First of all, a Hann window is applied to the in-phase and quadrature signals to enhance the dynamic range. After that, an FFT is performed to identify the range where the target's beat frequency is located. Then, the FFT is clipped in the predefined range, with the aim of isolating the target from interfering objects in the radar's field of view. After that, for each ramp, the phase is computed at the beat frequency, which is calculated as the maximum of the FFT in the range previously calculated.

Analogously to the CW case, the arctangent is the MLE for estimating the signal phase. Finally, the displacement calculation is carried out. The displacement signal has the following expression:

$$\Delta R(\tau) = \frac{unwrap\{\phi(\tau) - \phi(\tau_0)\} \cdot c}{4\pi \cdot f_0} \tag{2.7}$$

where $\phi(\tau_0)$ is the initial phase.

With the aim of solving the unwrapping limitations, most of researchers use the extended differentiate and cross-multiply (DACM) algorithm proposed in [Wang 14b], which has showed to provide more robust and accurate demodulation results. Nevertheless, this algorithm does not deal with the phase changes that are caused by the range migrations. The target can change between range bins of the FFT along the time. A new technique that combines the phase and frequency information from the range bin to extract the displacement information is presented in Appendix B.2.1. The target displacement is then determined using the following equation:

$$\Delta R(\tau) = \frac{(\phi(\tau) - \phi(\tau_0)) + \frac{\pi L f_{bin}(\tau)}{f_s}}{\frac{4\pi f_0}{c} + \frac{2\pi BL}{f_s T c}} \tag{2.8}$$

It is important to note that LFMCW processing is performed once per sweep time, unlike CW processing which is carried out per each sample time. Therefore, the extracted displacement, denoted as R, is downsampled by the sweep time ($f_s^{LFMCW} = f_s^{CW}/T$).

2.2.3 Optimal parameter selection

From the previous sections, it can be observed that there are some parameters that can be configured in the radar system, such as the waveform, the frequency working band, bandwidth or sweep time. The analysis to determine which radar configuration is optimal between CW or LFMCW configurations is performed in the next section. Notwithstanding, there are other parameters that can be configured and should be taken into account. Ones are common for both configurations, such as the working frequency band or the system sampling frequency, and other are specific parameters, such as the sweep time and bandwidth in LFMCW configuration.

The previous sections have shown that various parameters in the radar system can be modified, such as waveform configuration, frequency working band, bandwidth, and sweep time. The next section will analyze the optimal radar configuration.

2.2.3.1 Working frequency band

Based on the radar baseband expressions, Eqs. 2.4 and 2.5, it can be concluded that increasing the working frequency enhances the measurement accuracy, since, at high frequencies, small displacements result in significant phase changes, ΔR: $\Delta\phi \propto f_0 \cdot \Delta R$.

Notwithstanding, there are studies which indicate that an optimal carrier frequency exists maximizing the detection sensitivity in Doppler radars [Li 07, Gu 13], stating that the working frequency band can be increased up to the lower region of the Ka-band to improve detection accuracy. But these studies are limited to the CW case, not analyzing the impact of using LFMCW configuration. Moreover, they analyzed vibrational amplitudes that do not coincide with the ranges of breathing and heartbeat amplitudes reported in the literature [Bori 15], and limit their analysis to frequencies up to 40 GHz.

An analysis of the optimum transmitted frequency has been carried out in Appendix C, where, it is concluded that there is not an optimum frequency for vital sign monitoring, as each frequency is only optimal for a specific vibrational amplitude. However, using higher working frequencies is the most convenient. Simulations show that using higher frequencies improves the detection of lower amplitude vibrational motions.

Nevertheless, increasing the working frequency increases the attenuation [Skol 80], so a balance must be struck between the operating frequency and the attenuation that can be supported by the application (short-distance applications are not power-limited). Besides that, with higher frequencies, small displacements result in significant phase changes, antennas reduces their size and beamwidths get narrower [Bala 16]. Additionally, the anatomical properties of the body also play a role in choosing the radar working frequency. The dielectric properties of the human body tissues have been estimated along the millimeter-wave band [Chah 11], where it was concluded that the reflection from the body tissues is stronger at higher frequencies, since the complex dielectric constant decreases with frequency.

2.2.3.2 Sampling frequency

Despite the sampling frequency is not directly a parameter of the radar configuration, it is present in all radar systems. The sampling frequency required in each system depends on its waveform configuration. It is highlighted in [Lu 11] that LFMCW radars are not as efficient as CW radars because they need to sample the target position at higher frequencies than the fundamental vibration frequency to be measured.

However, recent advances on technology bring solutions to these issues. For instance, low-cost commercial microcontrollers embed analog-to-digital converters that can operate at sampling frequencies in the range of 5-10 MS/s, with resolution of 12-16 bits. With these microcontrollers and typical configurations in LFMCW radars, such as sweep time of 1 ms and bandwidth of 3 GHz, these radars can measure targets up to 250 m. Thus, sampling frequency is not longer a limitation in selecting the best radar configuration for vital sign monitoring. For instance, using the previous radar configuration, a sampling frequency of 100 kHz is enough for measurements up to 5 meters.

2.2.3.3 LFMCW parameters

There are other parameters that can be configured in LFMCW radars: bandwidth and sweep time. The bandwidth determines the radar's ability to separate targets by distance, which follows the next expression: $\Delta R = c/2B$, being ΔR the distance resolution.

On the other hand, the sweep time determines the maximum Doppler frequency that can be measured. As was previously stated with the "stop and go assumption", the target is measured once each sweep time, assuming that it does not change during this period. Thus, the target is "sampled" at 1/T, and the maximum Doppler frequency is 1/2T. Using smaller sweep times allows measurement of higher Doppler frequencies, at the cost of sacrificing SNR, since decreasing T results in a shorter integration time. Therefore, a trade-off has to be found:

- From a radar performance point of view, the ratio B/T should be chosen to place the beat frequency outside the phase noise region. More details about the phase noise impact can be found in Appendix E. Fig. 2.17 illustrates the phase noise region, showing that the beat frequency should be greater than 10 KHz to avoid being in the noisy region.
- From a vital sign monitoring perspective, certain signals require a minimum sampling rate to avoid losing significant information. According to the authors in [Task 96], the optimal range for heart rate variability (HRV) analysis should be between 250 and 500 Hz, or higher. Commercial ECGs are typically sampled at 1000 Hz [Kwon 18]. Therefore, in order to extract the vital signs with a minimum signal rate of 500 Hz, the sweep time must be shorter than 2 ms. This is because LFMCW radars obtain one sample of information per chirp, resulting in a signal rate of 1/T.

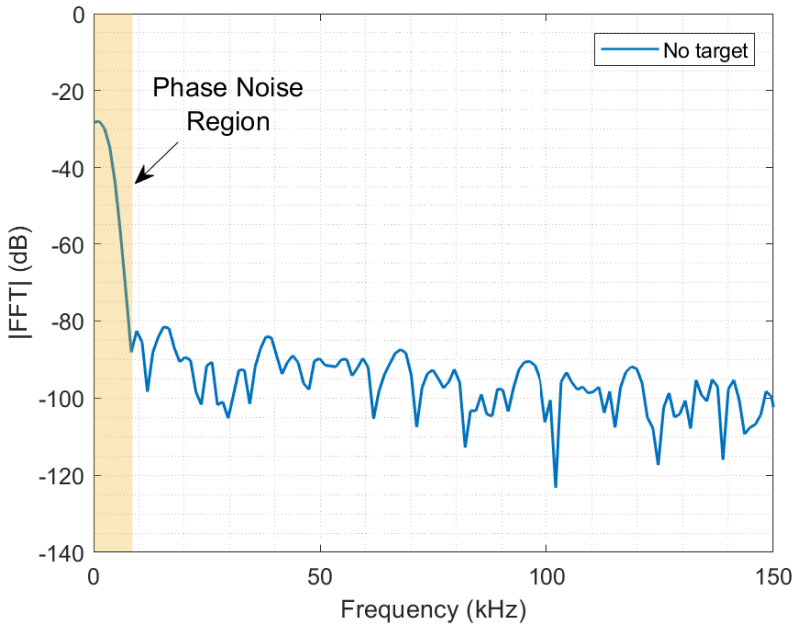

Figure 2.17: Spectrum of the radar signal without any target to identify the phase noise region, using the 134 GHz radar from Silicon Radar.

2.3 Best Waveform Configuration

This section presents a comparison between CW and LFMCW radars to determine which one suits better for vital sign monitoring. Among the most used radar configurations for cardiopulmonary monitoring, it stands out the Doppler or CW radar [Lube 02, Will 17], the LFMCW radar [Wang 14a, Ahma 18] and the impulse radar [Ren 16]. The use of impulse radar is not as extended due to its high power requirements and more complex system architecture [Gu 16].

Although there is an extensive bibliography focusing on the comparison between CW and LFMCW radars for healthcare applications [Li 13, Gu 16, Muño 17, Kebe 20, Isla 22b], it is not clear which radar configuration offers the best solution. A qualitative comparison of mono- and multi-mode architectures for short-range continuous-wave radars is presented in [Gu 16], where they state that CW radars have a higher sensitivity to small vibrations than LFMCW radars, while LFMCW configuration allows the separation of echoes from different targets, but they do not provide a quantitative comparison of both configurations.

It is a fact that CW architecture is simpler than LFMCW one, however, LFMCW configuration presents improvements compared to the previous one:

- LFMCW radars can retrieve range information (Eq. 2.5), allowing target separation. This feature makes it possible to remove unwanted interferences from clutter [He 17] and simultaneous multi-target monitoring.
- LFMCW radars are more robust than CW radars against low-frequency noise, because

the beat frequency can be kept away from this frequency range.

- LFMCW radars are more robust than CW radars against IQ imbalances and dc-offset.

The last two points are further developed below.

2.3.1 Noise impact

In radars where the received signal is mixed with a replica of the transmitted signal, such as CW and LFMCW radars, the beat frequency should be kept away from the low-frequency noisy range to guarantee a robust performance. Fig. 2.18 shows the main noise sources affecting this type of systems: thermal noise, phase noise and flicker noise. Additionally, the low-frequency spectrum is often not clean due to other effects, such as the direct antenna coupling from the TX to the RX [Stov 92]. The noise impact is higher in CW radars because two main reasons:

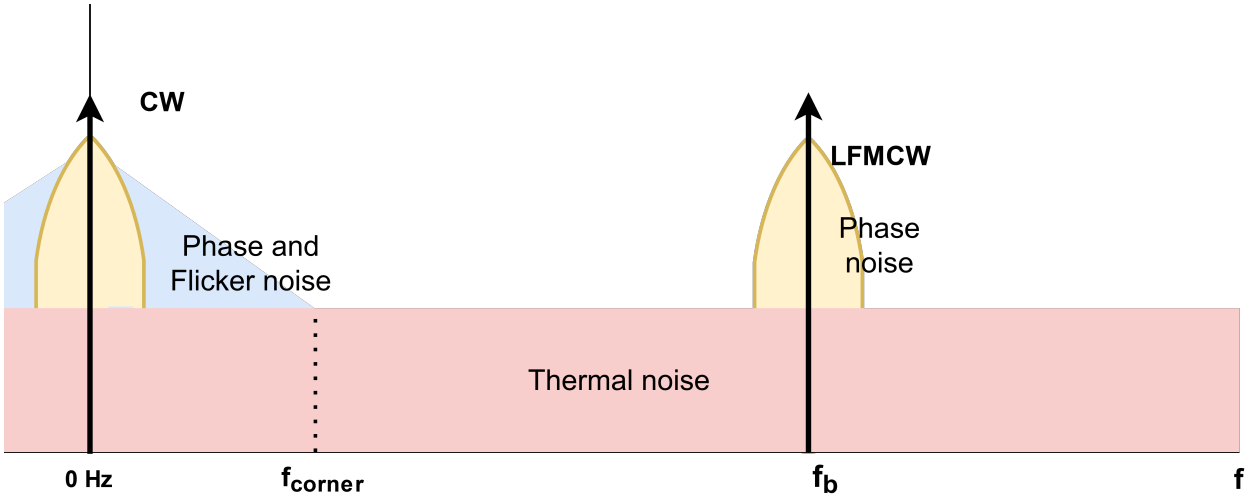

Figure 2.18: Noise impact on CW and LFMCW configurations. It shows the main sources of noise affecting a radar system: thermal noise, phase noise and flicker noise.

- Noise distribution. CW radars are affected by all the noise sources, as shown in Fig. 2.18. On the other hand, in LFMCW radars, the beat frequency can be adjusted to separate it from the noise sources present around 0 Hz. In fact, it can be placed at higher frequencies where impact of flicker noise is lower than thermal noise.
- Processing. The signal estimation is performed in CW radar sample by sample, while in LFMCW configuration is performed in each sweep time by a filterbank of N filters implemented via an N-FFT. Thus, LFMCW has an estimation improvement of N, where $N = f_s \cdot T$, f_s is the sampling frequency and T the sweep time. This can be shown in Eqs. 2.9 and 2.10 from Appendix D, which represent Cramér-Rao lower bounds (CRLB) for CW and LFMCW estimations, respectively. This can also be seen in the CRLB bounds presented in Fig. 2.19.

$$var(\hat{R}) \geq \left(\frac{c}{4\pi f_0}\right)^2 \frac{\sigma^2}{2A^2} \tag{2.9}$$

$$var(\hat{R}) \geq \left(\frac{c}{4\pi f_0}\right)^2 \frac{\sigma^2}{2A^2} \frac{1}{N + \frac{B(N-1)}{f_0} + \frac{B^2(2N-1)(N-1)}{6Nf_0^2}} \tag{2.10}$$

where A^2/σ^2 is the signal-to-noise ratio of the complex signal, f_0 is the carrier frequency, f_0 is the radar initial frequency transmitted, B is the transmitted bandwidth and N is the signal length, in samples.

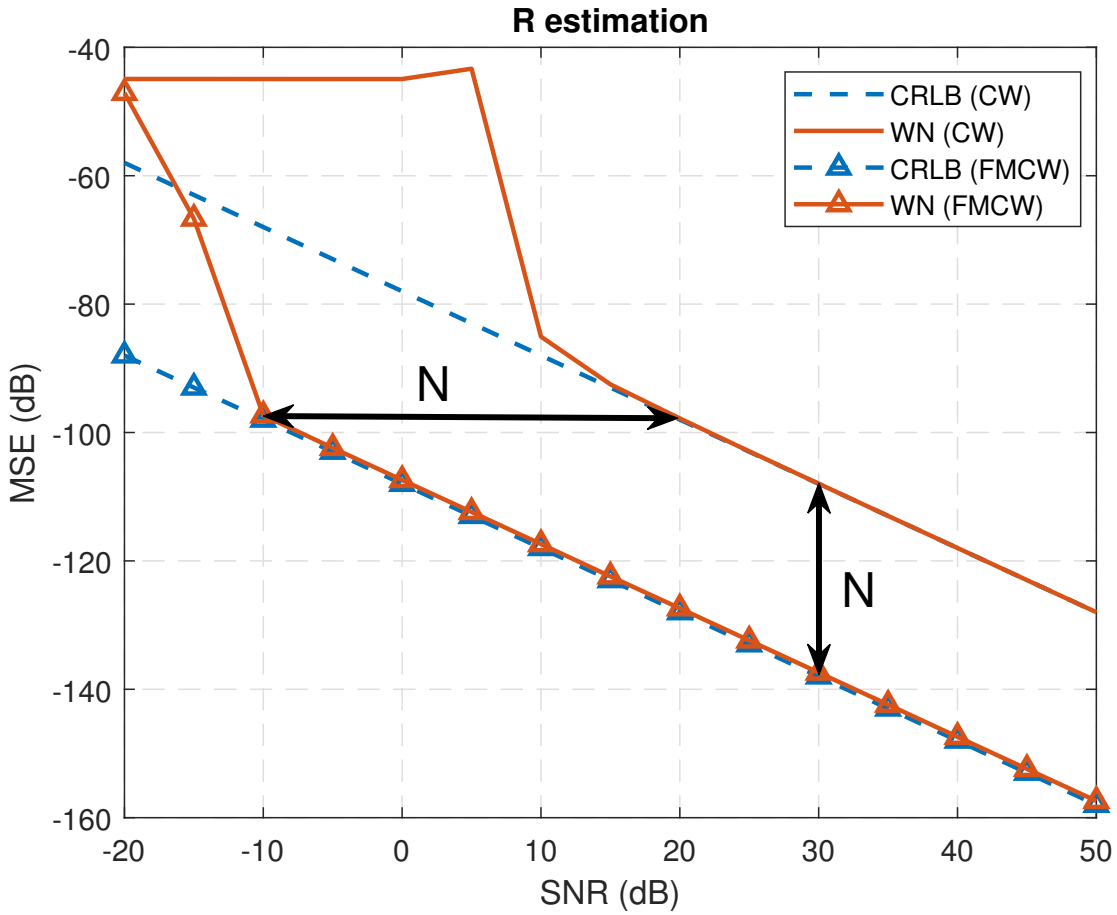

Figure 2.19: Displacement estimation with thermal noise for the CW and FMCW configurations. Example with N=1000 samples, which implies an improvement of 30 dB in the R estimation and in the SNR. Simulation: 1000 iterations.

A more detailed analysis of the noise sources and impact in CW and LFMCW radars can be found in Appendix E.

2.3.2 IQ imbalance impact

In CW radars, before using the in-phase and quadrature signals to obtain the target displacement, a calibration process is carried out to compensate the amplitude and phase mismatches, and dc-offsets [Hu 13]. The analysis of the errors introduced due to imbalances and dc-offsets is detailed in Appendix B.

The amplitude and phase imbalances do not change significantly over time, since they are mainly generated by hardware imperfections, so these imbalances can be easily calibrated using compensation methods [Park 20]. However, the dc-offset also comes from reflections from stationary objects around the target [Park 07]. Thus, the correction needs to be run at the beginning of a new measurement each time the environment changes.

The amplitude and phase imbalances provoke that the joint plot of I and Q signals forms an ellipse instead of a circumference. Thus, the ellipse fitting estimation method in [Sing 13] is applied. Once the fitting ellipse is defined, the Gram–Schmidt's technique [Chur 81] is applied to compensate and correct the imbalances. After that, the Pratt's method [Prat 87] is performed to obtain the best-fit circle so as to obtain the circle center, i.e., the dc-offset. The IQ imbalance compensation is shown in Fig. 2.20. After the dc-offset removal, the arctangent demodulation is carried out to obtain the target's displacement. The calibration process is challenging when the I/Q components do not complete a closed circle, since the estimation of the center of an arc is more prone to errors than the center estimation of a circle, as will be shown in Section 2.3.3 (Figs. 2.24 and 2.26).

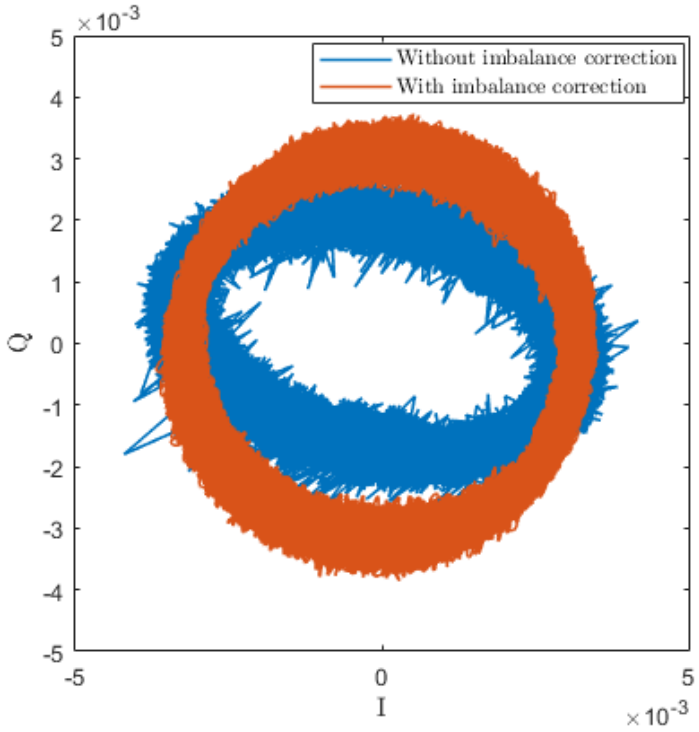

Figure 2.20: IQ imbalance correction example. It shows the IQ signals before the calibration -in blue- and after the calibration -in red-.

On the other hand, unlike in CW radars, LFMCW radars do not require a calibration process, as detailed in Appendix B. The IQ imbalances have a greater impact in the dc-component, which is filtered out in LFMCW. Moreover, if these imbalances remain constant over time, they can be omitted without affecting the overall outcome.

2.3.3 Experimental verification

Some experiments have been carried out to determine which waveform configuration provides the best results for vital signal extraction. In order to perform this comparison, a commercial baseband board from a 134 GHz radar has been modified to operate indistinctly in CW or LFMCW configurations, as was detailed in Section 2.1.1.1. This modifications allow to use the same baseband board with two different front-ends: one at 134 GHz and other at 24 GHz. The analysis is carried out at 134 GHz and the findings are confirmed with the 24 GHz radar. The performance of both configurations have been tested in two different scenarios. The first scenario involved the emulation of the chest wall displacement by measuring the periodic displacements of the membrane of a woofer. In the second scenario, the radars analyzed the chest displacement of a person to acquire their cardiorespiratory activity. Two experiments were performed in this second scenario, one with the 134 GHz radar to compare the CW and LFMCW configurations. The conclusions were confirmed with a second experiment using a 24 GHz radar, proving their independence from the radar frequency band. An overview of the different experiments carried out is shown in Fig. 2.21.

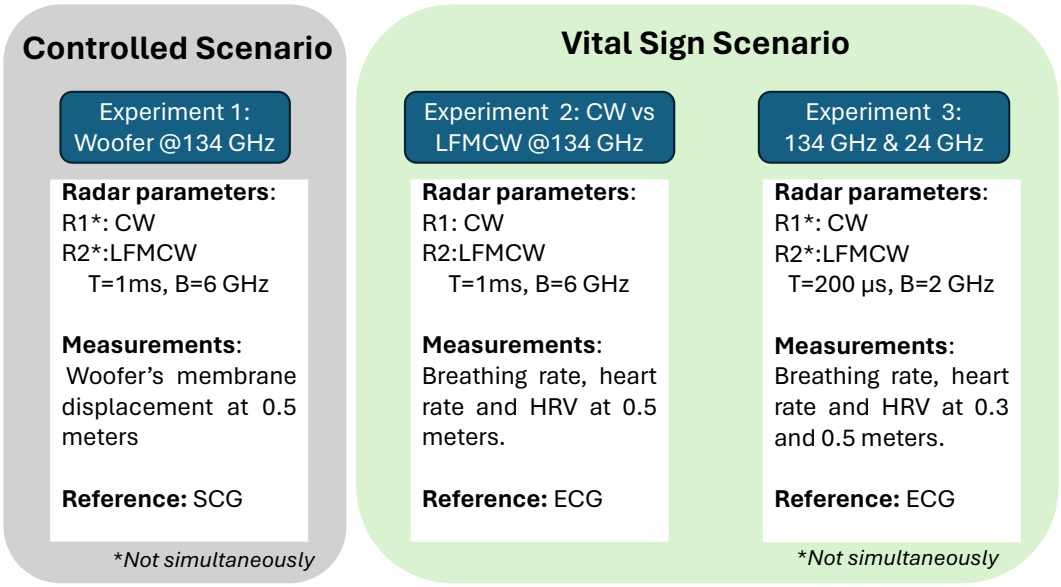

Figure 2.21: Overview of the different experiments carried out to determine which is the best waveform configuration.

The radar signals are sampled at a frequency of 10 MHz. The signal processing outlined in Section 2.2.2 is applied to each configuration to extract the radar displacement. The displacement signals obtained from the radars are downsampled to a frequency of 1 kHz for synchronization with the references obtained from the SCG and the TFM.

Comparison metrics

In order to compare the performance of CW and LFMCW configurations, two main comparison have been carried out:

- Signal waveform: The displacement measured with the radar is compared with the

displacement signal derived from the SCG sensor to quantify which radar configuration reproduces more accurately the waveforms. This comparison is evaluated by using the Russell's error measure [Russ 97], which is explained in Appendix F.1.

- Fiducial points: The radar's performance is evaluated to determine which radar can extract vital signs more accurately. The comparison is performed by comparing the HRV sequence extracted from the radar with the HRV sequence extracted from the ECG. The HRV sequence is explained in more detail in Chapter 3.3.2.

2.3.3.1 Controlled scenario

Experiment 1

The analysis is carried out by comparing the woofer membrane displacement measured with the SCG and the radar. The radar is placed 0.5 m away from a commercial woofer which is excited with a known waveform, as can be shown in Fig. 2.22. The field of view (FoV) at this distance is a circle of 3.5 cm in diameter. To emulate a vital sign monitoring scenario, the woofer is excited with three different waveforms. One emulates the chest displacement due to breathing motion, another emulates the chest displacement due to heart motion, and the last one emulates the chest displacement due to both activities. The frequency and amplitude of the emulated displacements are selected according to the ranges provided by authors in [Bori 15]. The resulting waveforms are:

- Waveform 1: A sinusoidal displacement of 0.2 Hz and 2 mm of amplitude, which emulates the breathing signal.
- Waveform 2: A sinusoidal displacement of 0.9 Hz and 0.2 mm of amplitude, which emulates the heartbeat in apnea condition.
- Waveform 3: The sum of the previous 2 signals, which emulates the cardiorespiratory signal.

For each waveform, the membrane displacement is captured with the radar operating in CW and LFMCW configurations, and these signals are compared with the SCG used as ground truth. The radar measures displacement information, while the SCG retrieves acceleration information. Both signals are analyzed (displacement and acceleration) since they have useful information, as will be explained in Section 3.2. Thus, two approaches are employed to compare the radar signals acquired:

- The first approach compares displacement information. Therefore, the SCG signal is double integrated to obtain the displacement information from the acceleration, and the resulting waveform is compared with the radar signal.
- The second approach compares acceleration information. Hence, the radar signal is double differentiated to obtain the acceleration information from the displacement, and this signal is compared with the data from the SCG.

The integration and derivation steps are carried out in the frequency domain with the whole length of the signals. Table 2.5 shows the Russell's error obtained for the comparison of each waveform.

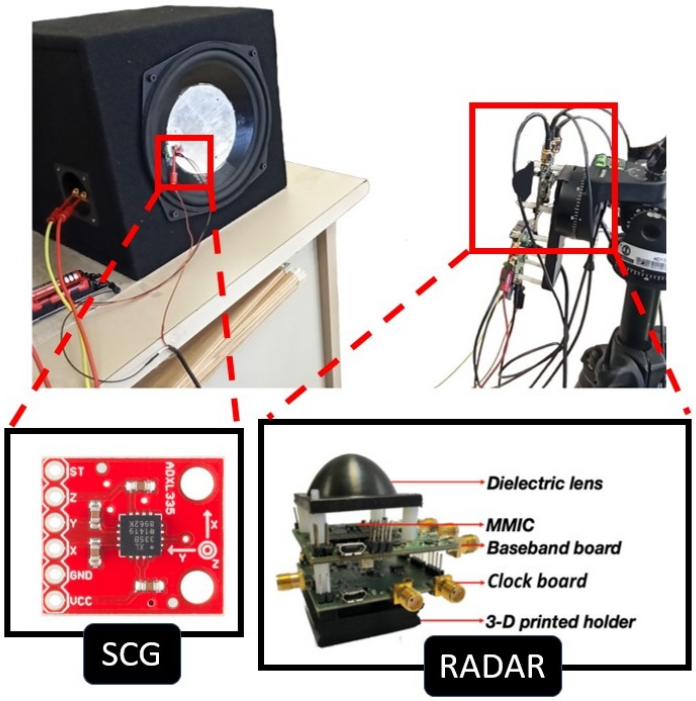

Figure 2.22: Experiment 1: the woofer membrane displacement is measured with an SCG and a radar placed at 0.5 m from the target, simultaneously.

Moreover, the extraction of the heartbeat signals from the cardiorespiratory signal has been also emulated. A band-pass filter is applied from 0.8 to 50 Hz to *Waveform 3* so as to extract the emulated heartbeat waveform. The extracted waveform is compared with the integrated SCG, which has also been filtered using the same filter (it is displayed in Table 2.5 as *Waveform 3 - HB*).

Table 2.5: Experiment 1: LFMCW vs CW under a controlled scenario.

	LFMCW		CW	
	$\int\int_{SCG}\, dt^2$	$\frac{d^2}{dt^2}_{Rad}$	$\int\int_{SCG}\, dt^2$	$\frac{d^2}{dt^2}_{Rad}$
Waveform 1	0.0375	0.2295	0.0319	0.4910
Waveform 2	0.0623	0.2665	0.4882	1.077
Waveform 3	0.0354	0.1079	0.0324	0.2397
Waveform 3 - HB	0.0723	0.2834	0.0730	0.5742

Russell's error obtained for the first approach ($\int\int_{SCG}\, dt^2$) and the second approach ($\frac{d^2}{dt^2}_{Rad}$) for each waveform. *Waveform 3 - HB* is the result of band-pass filtering *Waveform 3* to emulate the heartbeat waveform extraction.

The comparison of the different waveforms can be shown in Figs. 2.23, 2.24 and 2.25. These figures show both approaches: top figures represent waveforms for displacement and bottom figures represent acceleration waveforms.

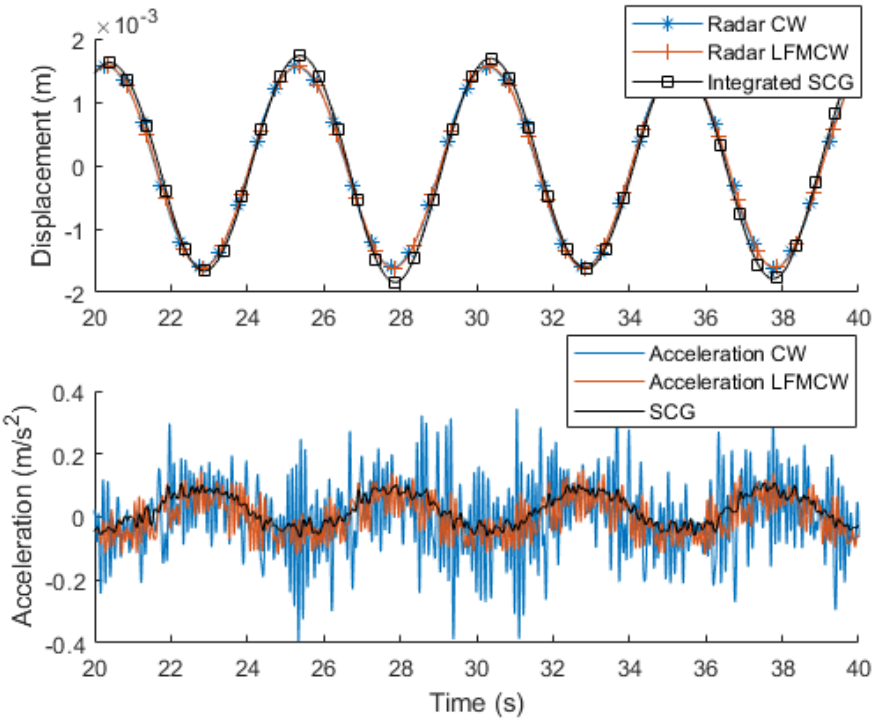

Figure 2.23: *Waveform 1* case: Comparison between the radar signal acquired using CW, LFMCW and the reference SCG.

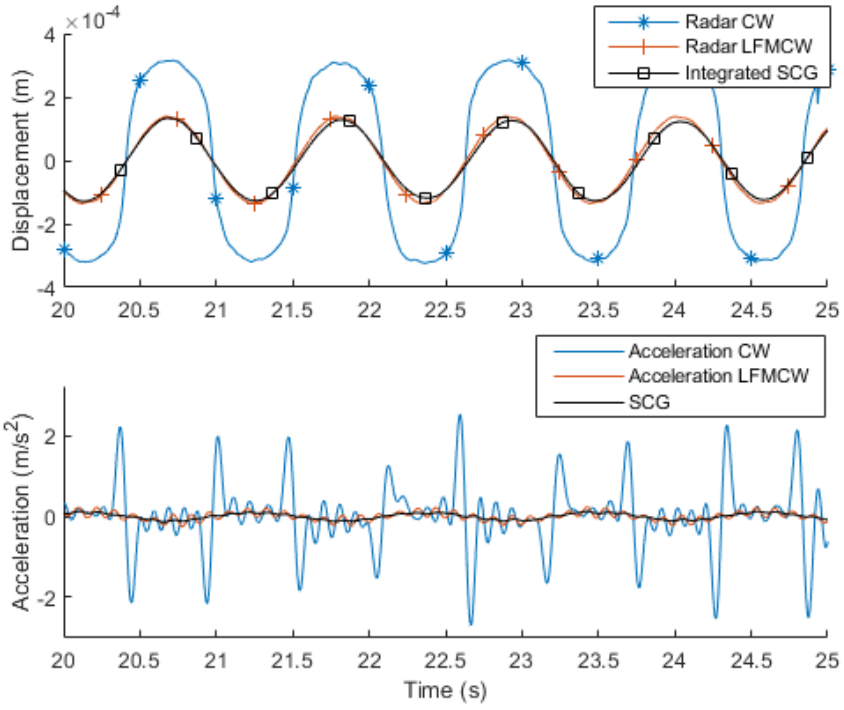

Figure 2.24: *Waveform 2* case: Comparison between the radar signal acquired using CW, LFMCW and the reference SCG.

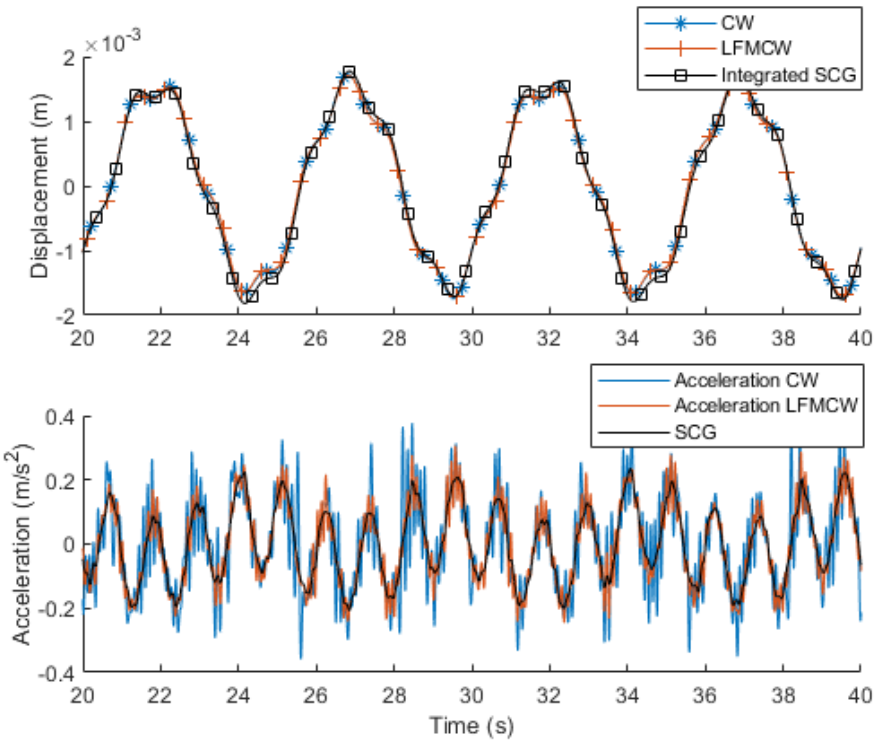

Figure 2.25: *Waveform 3* case: Comparison between the radar signal acquired using CW, LFMCW and the reference SCG.

Regarding the comparison carried out with the first approach (displacement analysis), results reflect that both configurations extract accurate results. Table 2.5 shows that the differences between both radar configurations are minimum for the *Waveform 1* and *Waveform 3* cases. However, these results show larger differences in *Waveform 2*, this is caused by a non accurate imbalance correction in CW configuration. As was stated in [Muño 17] that CW was more sensitive to small vibrations, it is also highly dependent on a good calibration. In *Waveform 2* case, the displacement signal to be measured (0.2 mm) is significantly smaller than the wavelength (2.2 mm). At 134 GHz, a vibration movement of 0.2 mm of amplitude covers, approximately, 20% of the I/Q circle, as displayed in Fig. 2.26.

The calibration process is challenging when the I/Q components do not complete a closed circle, and the phase extraction is not accurate, as is displayed in Fig. 2.24. Since the circle is not complete, the center estimation is not accurate and the dc-offset cannot be removed efficiently. Therefore, the error measured with the radar operating in CW is significantly higher. Notwithstanding, there are studies in the literature that address this issue, for instance, the authors from [Park 20] propose a CW radar with four-phased local oscillator signals to generate multiarcs, which enhances the center estimation but requires a more complex architecture.

Fig 2.25 shows the multi-component waveform, whose shapes can be compared with the traditional cardiorespiratory waveform. Additionally, this study analyzes the frequency spectra of the displacement signal obtained using radar in both CW and LFMCW modes. Fig. 2.27

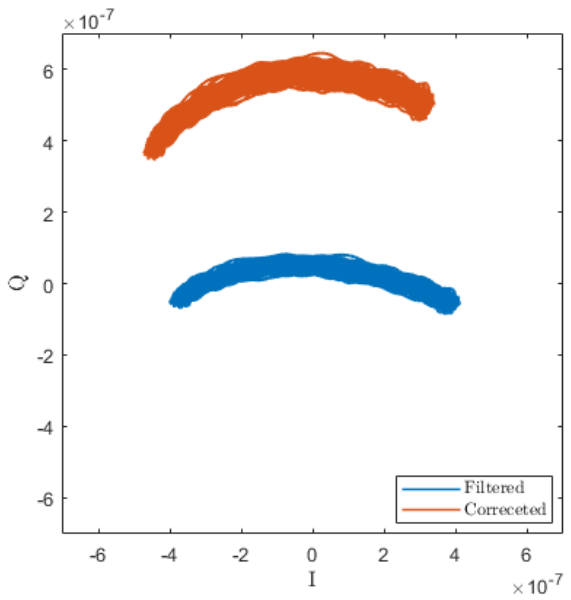

Figure 2.26: IQ imbalance correction for *Waveform 2*. It shows the IQ plot after noise filtering -in blue- and after the imbalance calibration -in red-.

displays the frequency components of *Waveform 3*, which includes fundamental frequencies at 0.2 and 0.9 Hz, as well as their harmonics. As anticipated, the double differentiation process amplifies the noise, this double differentiation is equivalent to multiplying the spectrum by $(j\omega)^2$. Besides, it can be observed that the spectra obtained in the CW configuration are noisier than those obtained in the LFMCW configuration.

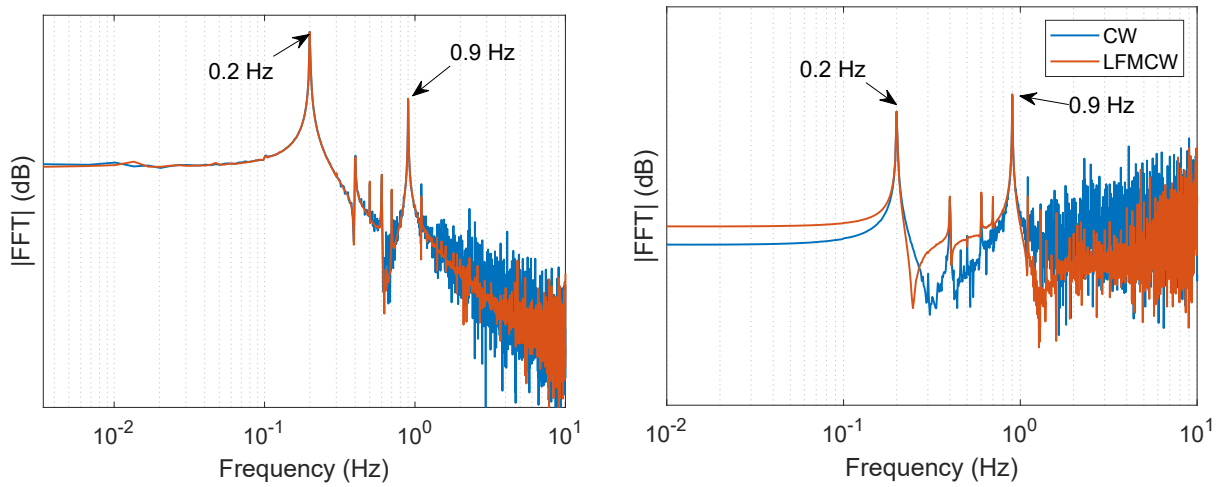

Figure 2.27: Radar signals acquired in CW and LFMCW for *Waveform 3*. From left to right: spectra of the displacement signals, and spectra of the acceleration signals.

Regarding the second approach (acceleration analysis), the comparison carried out in Table 2.5 between the acceleration signal from the radar and the SCG signal shows that LFMCW radar

performs better than CW radar. This fact can be seen at a glance in Figs. 2.23 and 2.25: the signals obtained from the CW radar are noisier. As previously stated, the higher noise present in CW is amplified due to the double differentiation, which acts as a high-pass filter.

2.3.3.2 Vital sign scenario

Experiment 2
The first experiment carried out in this scenario is performed by measuring the vital signs of a person under test (PUT)[2] with the two radars simultaneously: one operates in CW, while the other operates in LFMCW. The PUT is lying down in supine position and the radar setup is focusing with normal incidence on its chest at 0.5 m. Both radars are placed adjacently in order to point to the same chest region, as shown in Fig. 2.28. However, due to the narrow beamwidth, the FoV of both radars do not overlap, as displayed in Fig. 2.29. The FoV at 0.5 m is, approximately, a circle with a diameter of 3.5 cm.

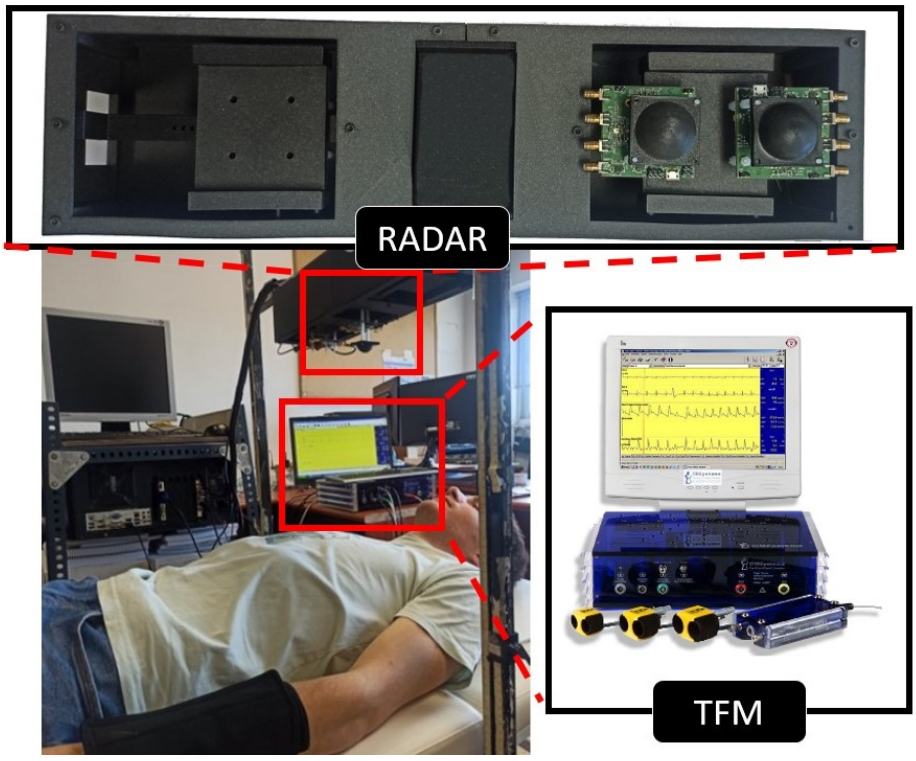

Figure 2.28: Vital sign scenario setup. The radar is oriented perpendicular to the subject, who is lying down in supine position at 0.5 m from the radar. The reference signals are acquired with the Task Force Monitor.

The chest surface curvature causes differences in the radar reflection. In order to remove uncertainties resulting from different incidence, the experiment is divided into two stages:

[2]It is important to emphasize that for this and all experiments conducted throughout this thesis, informed consent was obtained from all subjects involved in these experiments.

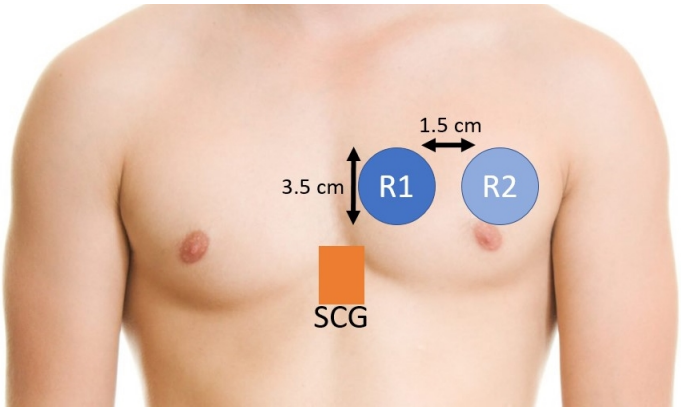

Figure 2.29: FoV covered with each radar and SCG placement.

- First stage: the radar pointing to R1 operates in CW, while the radar pointing to R2 operates in LFMCW.
- Second stage: the radar pointing to R1 operates in LFMCW, while the radar pointing to R2 operates in CW.

Four different measurements have been analyzed, two from each stage. In these measurements, the PUT is asked to breath normally for 120 seconds. The SCG is placed on the xiphoid process, located in the inferior segment of the sternum [Taeb 19]. Moreover, the ECG is measured with the Task Force Monitor. An example of the different vital signs that can be measured with radar, which will be detailed in Chapter 3, is displayed in Figs. 2.30 and 2.31. These vital sign waveform have been obtained using both radar configurations simultaneously.

In this scenario, the accuracy extracting the different vital signals is studied. The breathing rates are compared between radars, while the heart rates are also compared with the reference ECG. The HRV sequence extracted with each radar is compared with the HRV one computed from the ECG. The HRV error is calculated as the mean of the absolute value of the difference between both HRV sequences. The HRV sequence extraction is thoroughly explained in Section 3.3.2.

The results are displayed in Table 2.6. It shows, for each measurement:

- The radar configuration (CW or LFMCW).
- The breathing rate (BR)[3].
- The heart rate measured with ECG (HR_{ref}) and radar (HR_{rad}).
- The mean absolute error between the HRV sequences obtained with the ECG and the HRV sequence extracted with the radar. This metric is described in Appendix F.2. It is denoted as $MAE^{HB}_{\{HRV\}}$ if it is extracted from the heartbeat waveform, and as $MAE^{Acc}_{\{HRV\}}$ if it is computed from the acceleration signal.

[3]The breathing rate was obtained by selecting the maximum peak of the radar FFT. The BR has not been measured with a reference device.

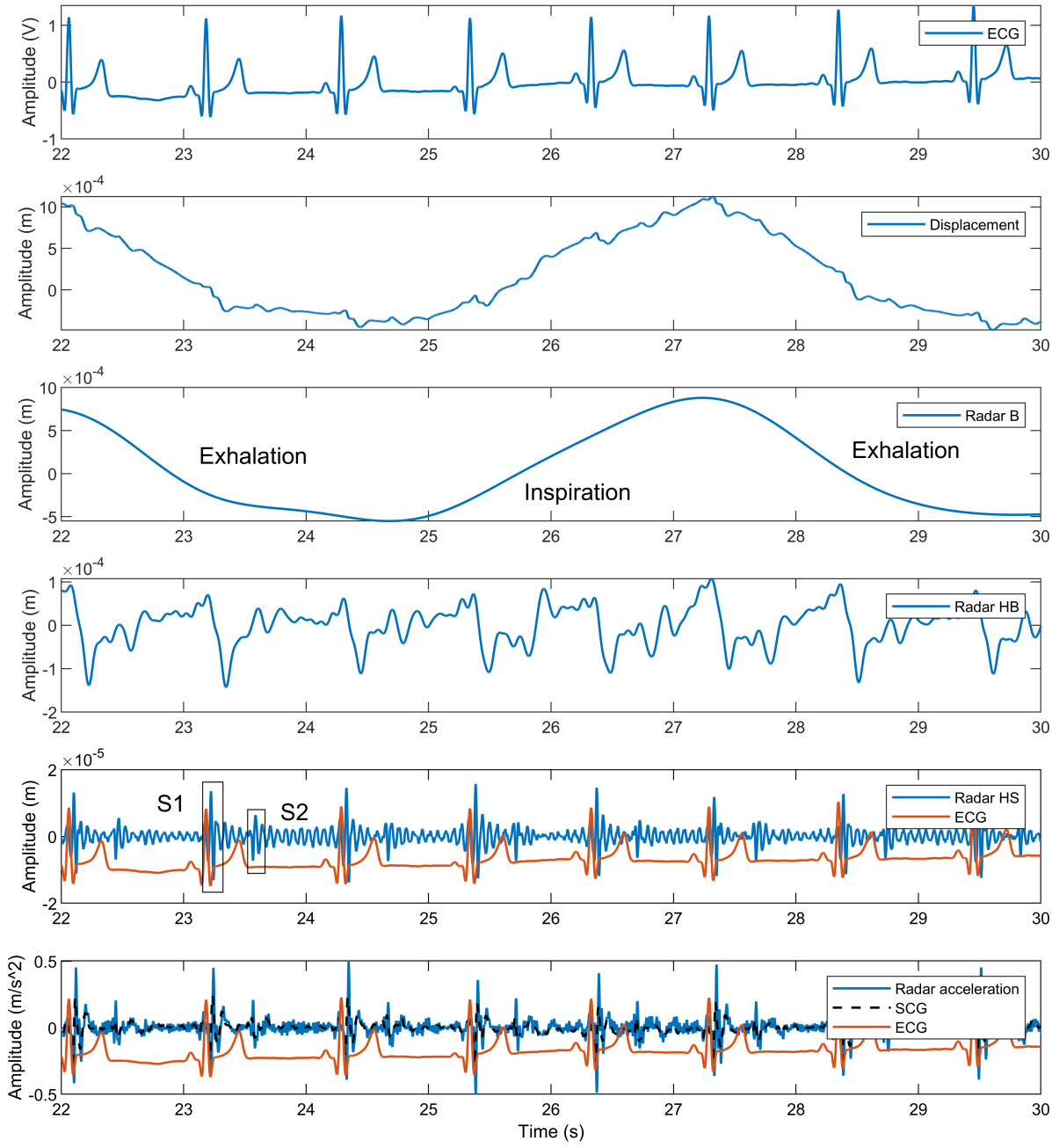

Figure 2.30: Comparison between the signals that can be acquired with the LFMCW radar and the reference sensors. From top to bottom: ECG signal, raw radar signal, breathing signal (Radar B), heartbeat signal (Radar HB), heart sound signal (Radar HS), and acceleration signal (Radar acceleration).

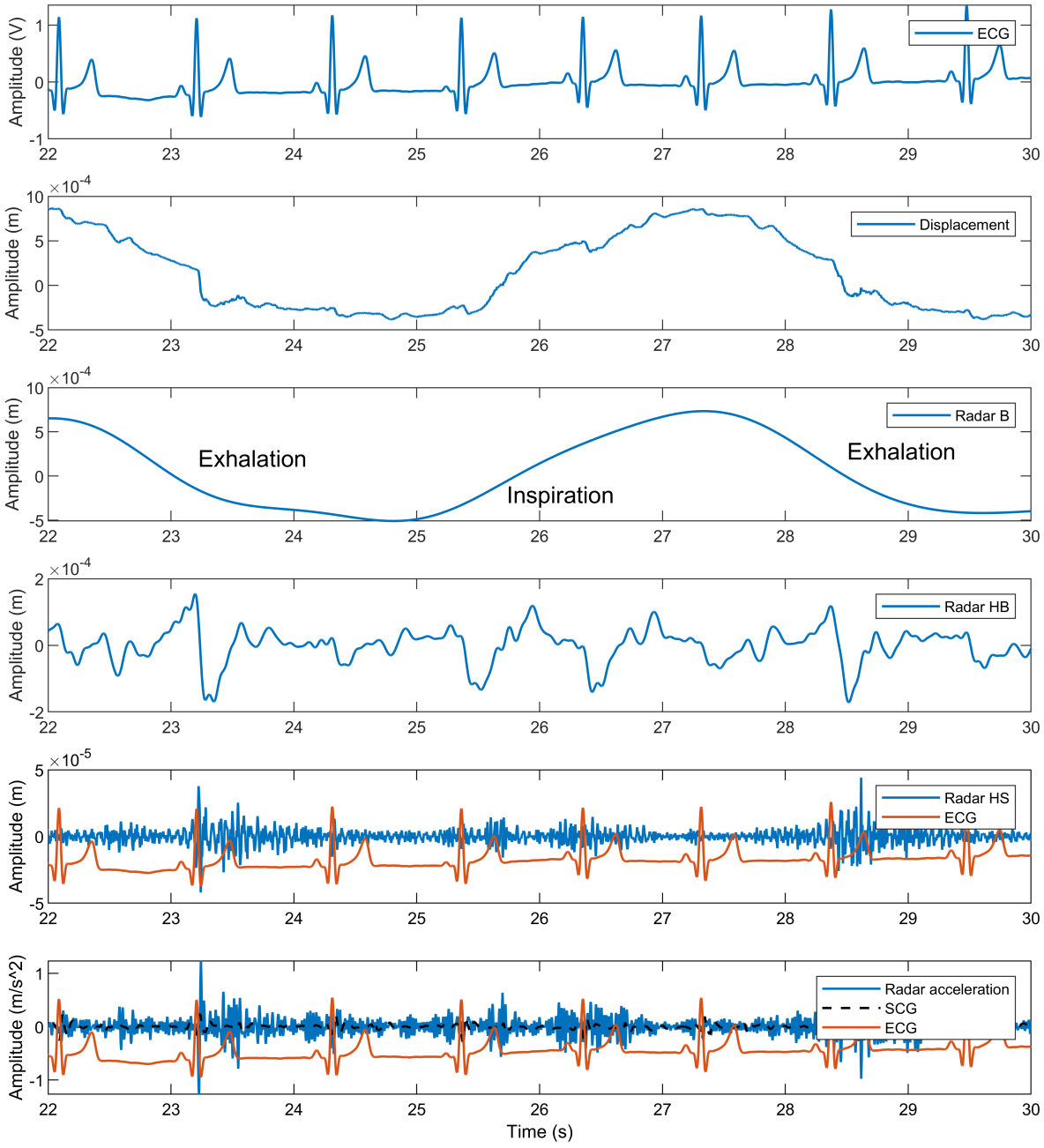

Figure 2.31: Comparison between the signals that can be acquired with the CW radar and the reference sensors. From top to bottom: ECG signal, raw radar signal, breathing signal (Radar B), heartbeat signal (Radar HB), heart sound signal (Radar HS), and acceleration signal (Radar acceleration).

Table 2.6: Experiment 2: LFMCW vs CW in a vital sign scenario at 0.5 meters with the 134 GHz radar.

	R1					
	Mode	**BR (breaths/min)**	**HR$_{ECG}$ (bpm)**	**HR$_{rad}$ (bpm)**	**MAE$^{HB}_{\{HRV\}}$ (ms)**	**MAE$^{Acc}_{\{HRV\}}$ (ms)**
Meas. 1	CW	11.0	60.5	60	10.38	17.57
Meas. 2	CW	14.5	56.5	56.2	2.24	7.87
Meas. 3	LFMCW	13.0	57.6	57.6	2.77	0.61
Meas. 4	LFMCW	11.5	58.6	58.6	2.34	0.53
	R2					
	Mode	**BR (breaths/min)**	**HR$_{ECG}$ (bpm)**	**HR$_{rad}$ (bpm)**	**MAE$^{HB}_{\{HRV\}}$ (ms)**	**MAE$^{Acc}_{\{HRV\}}$ (ms)**
Meas. 1	LFMCW	11.0	60.5	60.6	5.55	0.63
Meas. 2	LFMCW	14.5	56.5	56.5	6.26	0.65
Meas. 3	CW	13.0	57.6	57.1	7.82	14.21
Meas. 4	CW	11.5	58.6	58.6	6.78	16.16

BR: Breathing rate (radar). HR$_{ECG}$: Heart rate (ECG). HR$_{rad}$: Heart rate (radar). MAE$^{HB}_{\{HRV\}}$: Mean absolute error between HRV$_{HB}$ and HRV$_{ECG}$. MAE$^{Acc}_{\{HRV\}}$: Mean absolute error between HRV$_{Acc}$ and HRV$_{ECG}$. The measurements with the same numbering are carried out simultaneously.

Results obtained in the vital sign scenario confirm the conclusions extracted in the previous controlled scenario. Both radar configurations are capable of extracting general metrics, such as breathing and heart rates. The same breathing rate, and almost the same heart rate compared to ECG (reference) are obtained with errors below 1% for both configurations.

However, there are differences between the two configurations for the HRV sequence extraction. LFMCW has a performs better in extracting the HRV, especially from the acceleration chest displacement. This is more challenging in CW radar since the noise content at higher frequencies tends to mask the signal details.

Fig. 2.32 shows the histogram of the error distribution for one of the measurements, allowing for a comparison of the performance of both configurations. The results confirm that LFMCW outperforms CW. Moreover, Fig. 2.32a shows that the errors obtained when the HRV sequence is extracted from the heartbeat waveforms are more scattered (larger standard deviation) than when the acceleration signal is used. These results clearly show the improvement of using the radar acceleration instead of the heartbeat waveform in the HRV sequence extraction. This procedure is only possible with the LFMCW radar (see Fig. 2.30 and 2.31) because the information is not masked by noise. In addition, the ability to extract acceleration information from the radar signal improves the identification of important cardiac events as will be described in Chapter 3. These include events such as aortic opening, which facilitates the extraction of HRV sequences [Tadi 15].

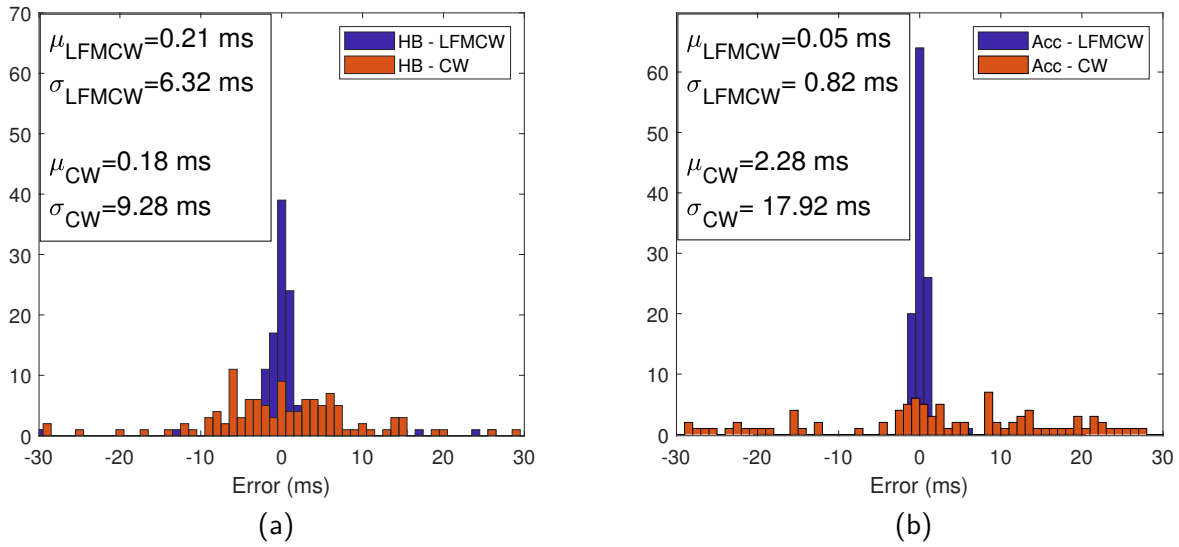

Figure 2.32: (a) Error of HRV sequence measured with the ECG and the HRV sequence computed from the heartbeat waveform in CW and LFMCW configurations. (b) Error of HRV sequence extracted from the radar acceleration in LFMCW and the ECG.

Additionally, Fig. 2.33 shows that even if the best HRV extraction method for each configuration is chosen, LFMCW presents the best extraction results.

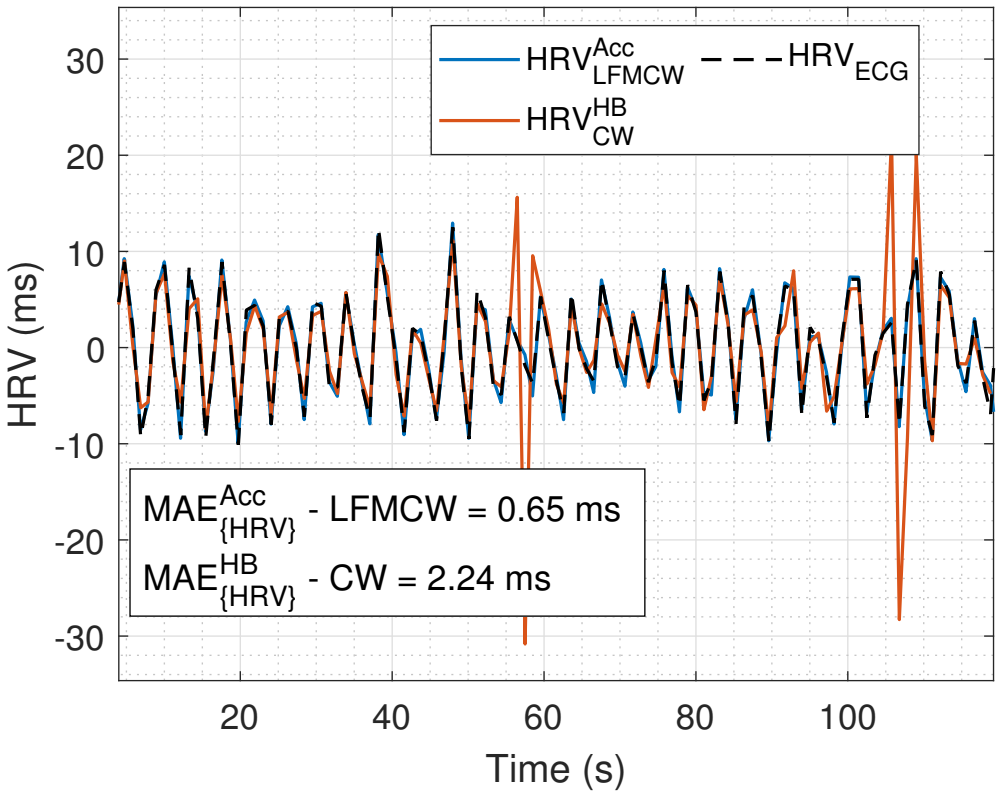

Figure 2.33: Comparison between the HRV sequence extracted from the ECG -in black-, the radar operating in LFMCW -in blue-, and the radar operating in CW -in red-. These data belong to *Measurement 2*.

Experiment 3

A second experiment is carried out to confirm the findings at 134 GHz. In this experiment, the vital signs of a target, which is lying down in supine position in front of the radar, are measured with the 24 GHz radar. However, as was detailed in Section 2.1.1.1, the antenna beamwidth of this MMIC board is broader than the one at 134 GHz, so the FoV covered is larger. With the aim of covering a body chest area similar to the previous experiment, the PUT is measured at 0.3 and 0.5 meters. The FoV at these distances is 15.5 x 8.4 cm^2 and 25.9 x 14 cm^2 at 0.3 and 0.5 meters, respectively, so it covers R1 and R2 regions simultaneously. Focusing is an important matter in this analysis because some studies show how the heart wave shape changes depending on the area measured [Will 17]. However, the area covered with the 24 GHz MMIC at these distances is still comparable with the heart size (12 x 8 cm [Moha 16]).

On the other hand, the parameters used to configure the 24 GHz LFMCW radar are different from the previous experiment, due to the bandwidth at 24 GHz is limited to 3.6 GHz. With the aim of having a beat frequency comparable with *Experiment 2* ($f_b \simeq 20$ kHz), the radar has been configured to transmit a bandwidth of 2 GHz and the sweep time has been set to 200 μs. In order to compare these results with those obtained in Table 2.6, the PUT has

also been measured with the 134 GHz radar using the same configuration parameters. The measurements carried out at 134 GHz have been performed pointing at R1.

Results are presented in Table 2.7, which follows the same structure than Table 2.6. Results obtained with the 24 GHz MMIC board prove that the conclusions reached previously do not depend on the radar working frequency:

- LFMCW configuration is better to extract the HRV.
- Results do not depend on the distance, while the FoV is still comparable with the heart size.

On the other hand, measurements at 0.5 meters with the 134 GHz MMIC board show that the results do not depend on the sweep time selected or the transmitted bandwidth, since they are comparable to those presented in Table 2.6 (errors of the same order of magnitude).

Therefore, despite both radar configurations are capable of extracting and measuring vital signs with high performance, the use of LFMCW radar over CW is recommended. Using the same hardware architecture, LFMCW configuration allows the extraction of more cardiac information and with higher accuracy.

Moreover, LFMCW configuration allows to measure not only the vital signs of one subject, but also monitor several subjects simultaneously, as will be detailed in Section 4.1, allowing its tracking and providing location information. These characteristics are basic for rescue-working and telehealth scenarios [Gurb 19, Le K 19].

2.3.3.3 Conclusions

The comprehensive comparison carried out also in this chapter between continuous-wave (CW) and frequency-modulated continuous-wave (LFMCW) radar configurations reflects that, although both radars can extract general metrics, such as breathing and heart rates, detailed information can only be extracted in LFMCW radars. It is explained that CW radar performance is more affected by low frequency noise, making challenging or unfeasible the extraction of heart sounds or the desired fiducial points from the acceleration signal. Moreover, this causes that the HRV sequence extraction is more accurate in LFMCW radars, since it can be computed from the acceleration signal. It has also be highlighted that CW radars, unlike LFMCW radars, are highly dependent on calibration. Besides, LFMCW configuration allows multi-target monitoring simultaneously, which is essential in assisting living monitoring environments.

Table 2.7: Experiment 3: 24 GHz vs 134 GHz in a vital sign scenario.

	24 GHz MMIC						
	Dist. (m)	**Mode**	**BR (breaths/min)**	**HR$_{ECG}$ (bpm)**	**HR$_{rad}$ (bpm)**	**MAE$^{HB}_{\{HRV\}}$ (ms)**	**MAE$^{Acc}_{\{HRV\}}$ (ms)**
Meas. 5	0.3	LFMCW	11.2	63.8	63.8	7.41	1.29
Meas. 6	0.3	CW	12.3	61.5	61.5	17.24	18.48
Meas. 7	0.5	LFMCW	14.5	57.1	57.1	10.32	1.37
Meas. 8	0.5	CW	12.3	61.5	59.3	15.76	17.60
	134 GHz MMIC						
	Dist. (m)	**Mode**	**BR (breaths/min)**	**HR$_{ECG}$ (bpm)**	**HR$_{rad}$ (bpm)**	**MAE$^{HB}_{\{HRV\}}$ (ms)**	**MAE$^{Acc}_{\{HRV\}}$ (ms)**
Meas. 9	0.5	LFMCW	15.7	53.7	53.7	10.18	1.33
Meas. 10	0.5	CW	12.3	58.2	58.2	15.16	19.8

BR: Breathing rate (radar). HR$_{ECG}$: Heart rate (ECG). HR$_{rad}$: Heart rate (radar). MAE$^{HB}_{\{HRV\}}$: Mean absolute error between HRV$_{HB}$ and HRV$_{ECG}$. MAE$^{Acc}_{\{HRV\}}$: Mean absolute error between HRV$_{Acc}$ and HRV$_{ECG}$.

2.4 Signal Conditioning

This section describes the different signal processing techniques used to prepare the signal displacement for the vital sign and biomarker extraction. It focuses on the different techniques than can be used for denoising and for separating the skin wall displacement associated with the respiratory activity from that associated with the heart activity. These techniques can be divided into three main groups:

- Frequency-domain techniques: spectral analysis and classic filtering.
- Time-domain techniques: EMD.
- Time-frequency domain techniques: wavelet transform and short-time Fourier Transform (STFT) analysis.

2.4.1 Frequency-domain techniques

These techniques have been traditionally employed in the analysis of vital signs. These methods involve the examination of signals in the frequency spectrum, breaking down these signal into its constituent frequencies. Despite the limitations of this approach, the application of frequency-domain techniques continues to be fundamental in analyzing vital signs obtained via radar.

2.4.1.1 Spectral analysis

The Fast Fourier Transform (FFT) is primarily used to convert a signal from the time domain into the frequency domain. After transforming the signal into the frequency domain, the FFT can reveal the frequency components present in the original signal. Some of these peaks correspond to specific frequencies associated with physiological activities [Li 06]. Therefore, this technique has primarily been used to determine breathing and heart rates by identifying the maximum peak in the frequency range where these signals are expected. This technique is particularly useful when dealing with physiological signals that exhibit periodic patterns, as it assumes that the analyzed signals are stationary.

Fig. 2.34 displays the spectra of the ECG signal and the radar displacement. The radar spectrum exhibits peaks that correspond to respiratory and heart activities. The peaks that correspond to heart activity coincide with those obtained from the ECG spectrum.

However, due to the dynamic nature of the breathing and heart patterns, these frequencies can vary along the time, making difficult to identify the peak or peaks related to the breathing and heart rates. This phenomenon is illustrated in Fig. 2.35, in which the target's heart rate oscillates between 60 and 70 bpm, exhibiting two dominant frequencies. However, the temporal evolution cannot be determined through this technique. Additionally, the accuracy of heart rate estimation may be affected by the harmonics of the breathing waveform or intermodulation products [Morg 09]. This is because these harmonics, can either overlap or be in close proximity to the peak associated with the heart rate, potentially exhibiting greater power. Fig. 2.35 shows the breathing and heartbeat frequency components identified using the FFT analysis.

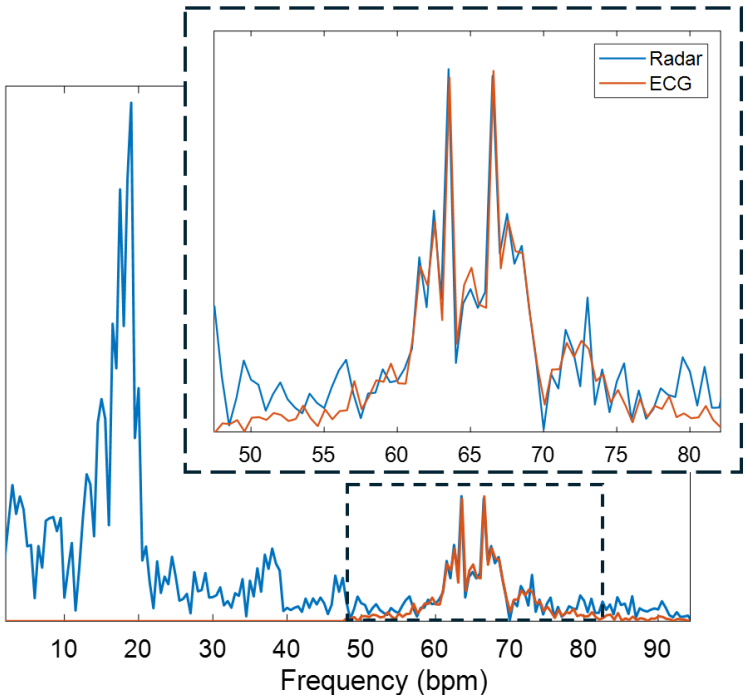

Figure 2.34: Comparison between the radar displacement and the ECG spectra.

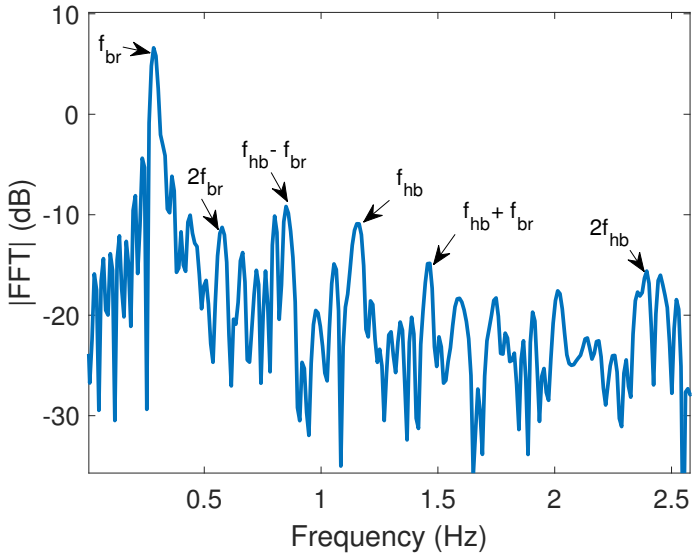

Figure 2.35: Breathing and heartbeat harmonics identified in a vital sign spectrum.

2.4.1.2 Classic filtering

This technique is the most used processing algorithm for breathing and heartbeat waveforms separation. It involves isolating a specific frequency range of interest that corresponds to the aforementioned signals. Traditionally, band-pass filters, such as 4th-order Butterworth filters, are used to extract the desired signals [Lohm 02]. Figs. 2.36 and 2.37 show an example of

this technique, where a band-pass filter has been applied to the radar signal, being able to separate the heartbeat waveform from the breathing signal.

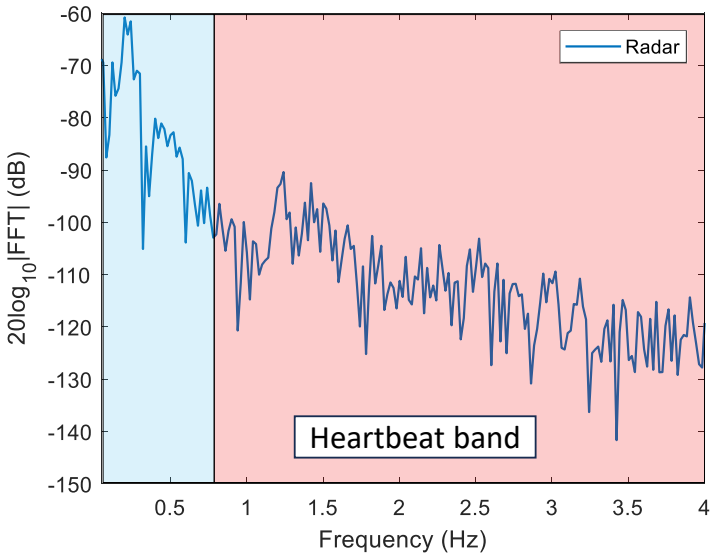

Figure 2.36: Chest displacement spectrum acquired with the radar where the regions for band-pass filtering are identified: breathing band –in blue– and heartbeat band –in red–.

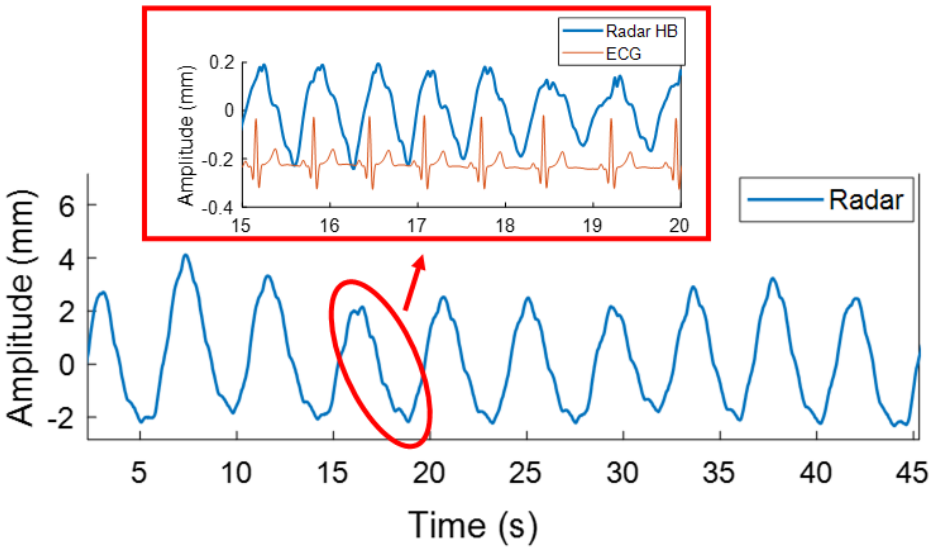

Figure 2.37: Heartbeat waveform extraction using the classic filtering approach.

This technique present some limitations, since it cannot separate signals which overlap in frequency. For instance, there are breathing harmonics inside the frequency range which is defined for the heartbeat extraction. With the aim of dealing with this issue, some approaches have been developed to cancel or attenuate the breathing harmonics in the heartbeat frequency range, for instance, the use of notch filters [Lv 21].

2.4.2 Time-domain techniques

Time-domain techniques are also utilized for analyzing vital signs. Unlike frequency-domain techniques, they do not require any transformation and allow for easy tracking of signal variations over time, as these signals are non-stationary.

2.4.2.1 Empirical Mode Decomposition (EMD)

EMD techniques are widely used in literature for decomposing nonlinear and non-stationary signals in diverse fields such as structural health monitoring, biomedical, or geophysics [Kara 10, Wang 12, Barb 20]. This concept was firstly introduced by Norden E. Huang in [Huan 98]. The author describes a process to decompose a signal in modes, that are denominated "intrinsic mode function" (IMF)[4]. It is important to highlight that the EMD is a *data driven* method and not a model driven method. This means that the method varies according to the input signal. This technique presents some limitations. By definition, every IMF must have only one frequency component. However, sometimes one IMF contains several frequencies components. This phenomenon, known as "mode mixing", can be separated in two groups:

- Closely spaced components. Authors in [Rill 08] state that the relation between the amplitude and frequencies of the different components that made up the signal are crucial to the EMD mode mixing problem. They define that EMD cannot separate two components which frequency ratio (f_2/f_1) is above 0.67, and amplitude ratio (a_2/a_1) is greater than 0.5, where $f_1 > f_2$.
- Intermittency. This could result from interference caused by noise, signals related to specific events, or other causes.

To alleviate the mode mixing, specially the generated due to intermittency, noise-assisted techniques such as ensemble EMD (EEMD) [Wu 09], complementary EEMD [Yeh 10], and complete ensemble empirical mode decomposition with adaptive noise (CEEMDAN) [Colo 14], have been proposed. These methods performs EMD over an ensemble of signals with additive white Gaussian noise (AWGN). However, these methods present new problems: the IMFs contain some residual noise and different realizations of the signal with AWGN can produce a different number of modes. These methods do not solve the mode mixing caused by closely spaced spectral components. Fig. 2.38 shows the three possible outcomes of EMD: effective component separation, poor separation resulting in two modes that are not accurate, and no separation[5].

[4]These IMFs are defined under two main features:

- The difference between the number of zero-crossings and minima is not greater than one: $|\#Minima - \#ZeroCrossing| \leq 1$
- It has a zero mean value of the envelope outlined by the local minima and the envelope defined by the local maxima.

[5]In the no separation case, only one IMF is obtained.

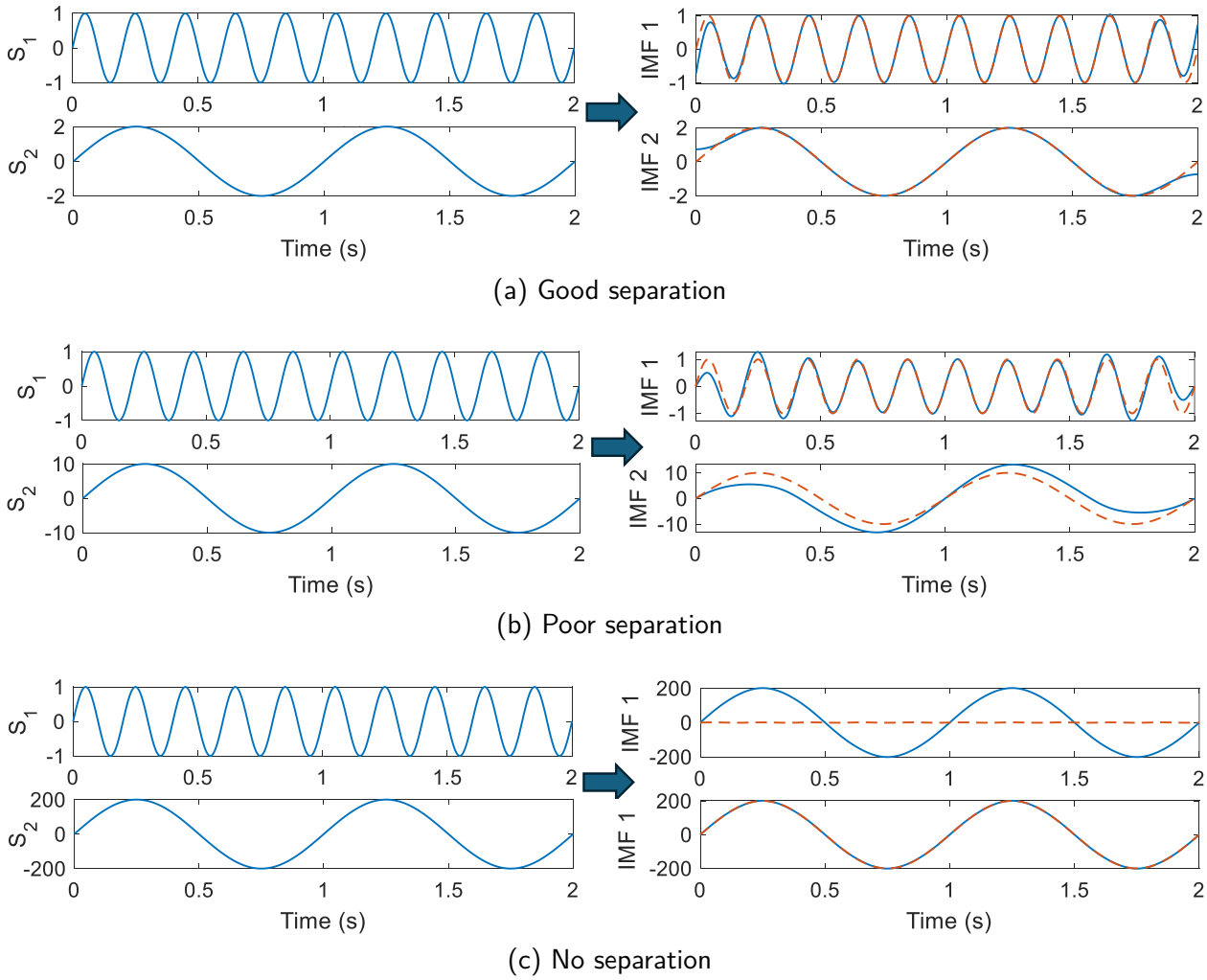

Figure 2.38: EMD decomposition analysis. (a) Good separation: frequency ratio of 0.2 and amplitude ratio of 2. (b) Poor separation: frequency ratio of 0.2 and amplitude ratio of 10. (c) No separation: frequency ratio of 0.2 and amplitude ratio of 200.

Thus, it is important to understand how the limitations of EMD could affect to the vital sign monitoring scenario. As was previously introduced, and is going to be detailed in Chapter 3, the cardiorespiratory signal has been widely analyzed in literature, knowing in detail the amplitude and frequency ranges of breathing and heartbeat waveforms. Thus, it is possible to identify the cases where EMD can effectively separate these two signals. Fig. 2.39 reproduce the mode mixing boundary map from [Rill 08], showing in yellow the regions where the two components are badly separated with EMD, and, in red, the normal ratios where the breathing and heartbeat waveforms are found. Moreover, the breathing and heartbeat waveforms vary its frequency over the time, while the IMFs are supposed to be monofrequency signals.

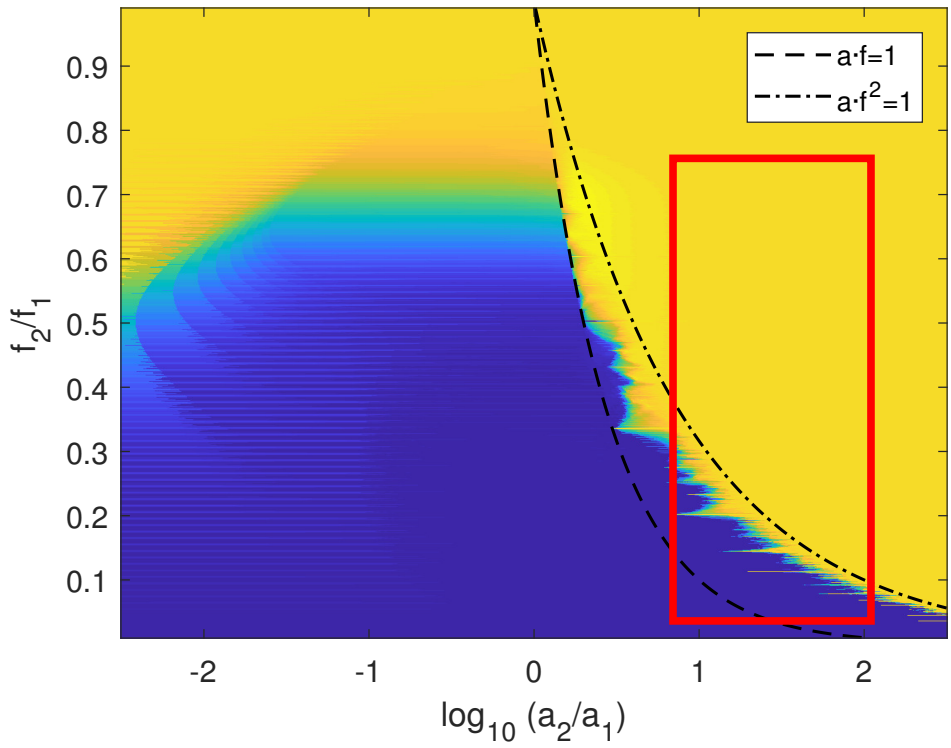

Figure 2.39: Mode mixing boundary conditions map. It includes the critical curves defined by [Rill 08] ($a \cdot f = 1$ and $a \cdot f^2 = 1$). The red rectangle stands for the vital sign region. Bad separation region –in yellow–.

It can be concluded that this technique is not suitable for separating vital signs. However, the amplitude and spectral content of the generated IMFs can be analyzed to eliminate those that fall outside the predefined range of the vital sign that will be extracted. This allows for noise reduction and the removal of baselines which can be caused by interfering body motions.

Figs. 2.40 and 2.41 present an example of the application of EMD technique in vital sign analysis. The analyzed signal in Fig. 2.40 represents the chest wall displacement of a target in apnea condition. The first IMFs are low-frequency components that may be related to unwanted body motions. Subsequent IMFs contain information about the signal under test, such as IMF 4 – 7, while the 8th and 9th IMFs are noisy modes. Fig. 2.41 shows the resulting waveform after eliminating these unwanted modes.

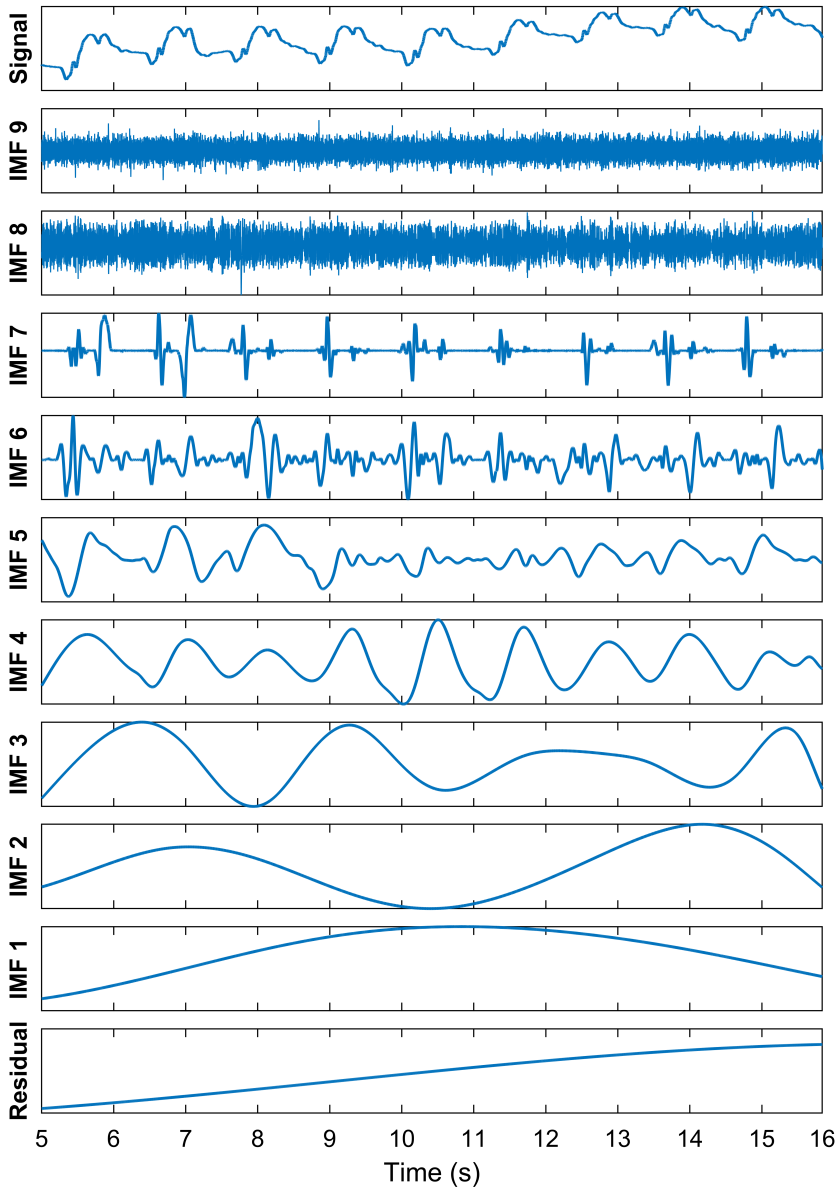

Figure 2.40: Intrinsic mode functions extracted from the radar signal using the EMD method.

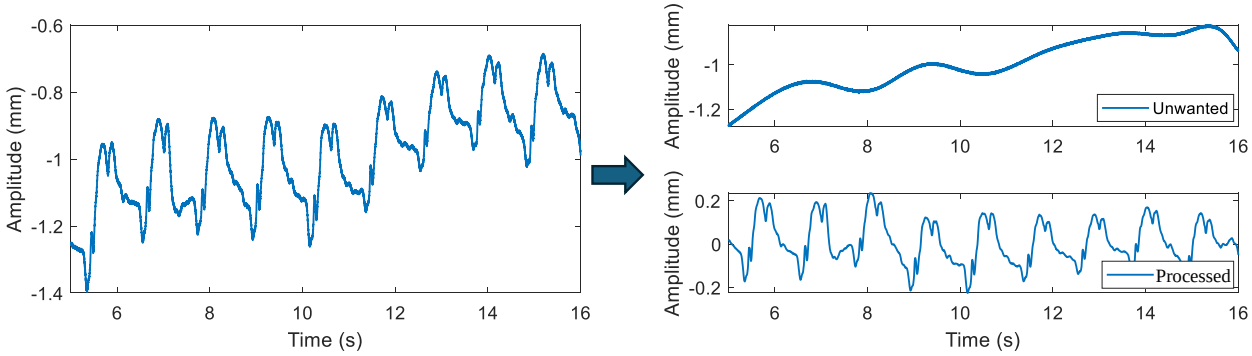

Figure 2.41: Signal processing using EMD. Unwanted modes: Residual mode, IMFs 1–3, 8 and 9.

2.4.3 Time-frequency domain techniques

Time-frequency signal processing represents an innovative approach to signal processing, introducing methods, techniques and systems that exploit two natural variables simultaneously: time and frequency. This departure from traditional signal processing approaches, which are often based exclusively on time or frequency, bringing a new perspective to signal analysis and interpretation. It gives an indication of how the frequency content of a signal changes with time, especially when signals are non-stationary. In this section, we explore two approaches: Short-Time Fourier Transform (STFT) and wavelet analysis.

2.4.3.1 Short-Time Fourier Transform

The STFT is a signal processing technique for analyzing the frequency of a signal over time. Unlike the FFT, which provides frequency information about the total duration of the signal, the STFT divides the signal into smaller overlapping segments and performs the Fourier transform of each segment individually. Considering a signal $s(t)$, and a real, even window centered in $t = \tau$, $w(t - \tau)$, the STFT can be defined by the following equation [Boas 15]:

$$S(t, f) = \int_{-\infty}^{\infty} s(t)w(t - \tau)e^{-j2\pi f\tau}d\tau \tag{2.11}$$

However, this technique has a main limitation: the time and frequency resolution of the STFT is limited by the window's width function and cannot be optimized at the same time. A wider window will allow a better frequency resolution, while a narrow window will allow a greater temporal resolution

The spectrogram stands for the squared magnitude of the STFT. Fig. 2.42 shows an example of the spectrogram of a breathing waveform where episodes of normal breathing, apnea, fast and deep breathing can be distinguished. With the aim of achieving a finer frequency resolution, a wider window length is required. In this case, to obtain a 0.1 Hz resolution, a window of 10 seconds is needed. However, this leads to a poor temporal resolution, resulting in a broadening of the frequency response of each episode and not being able to observe the transitions between the different frequencies.

However, it is possible to observe changes in the fundamental breathing frequency over time. A traditional FFT would not be able to provide this capability, as shown in Fig. 2.42, since it assumes the signal to be stationary. It would display distinct frequency components and incorrectly identify the component with the highest power (located at 0.2 Hz and corresponding to the final 20 seconds of the measurement, which represents deep breathing) as the subject's respiratory frequency.

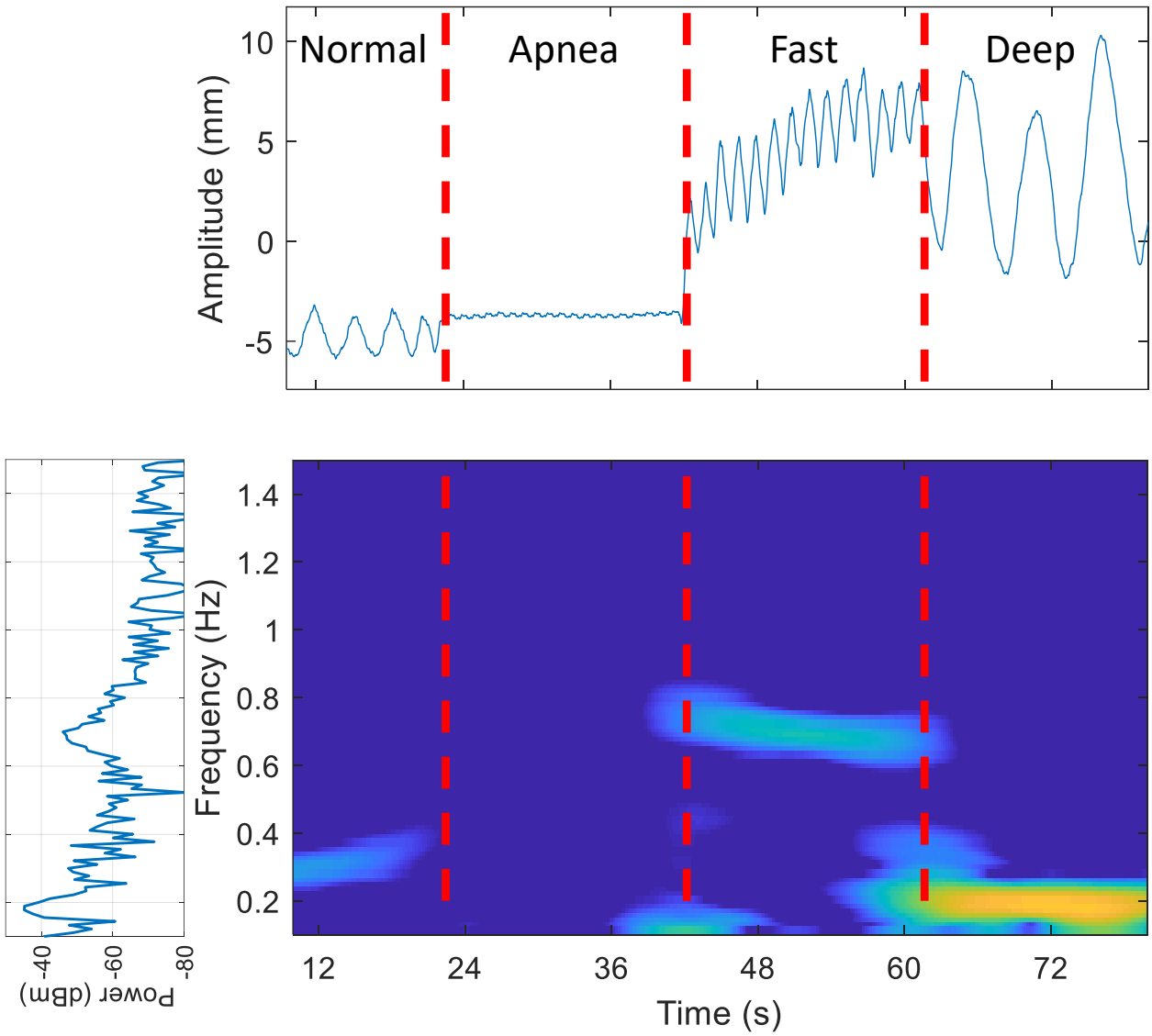

Figure 2.42: Spectrogram of the breathing signal acquired with the radar: differentiating normal breathing, apnea, fast, and deep breathing episodes. Spectrogram parameters: Hann window, 99% overlap, and 0.1 Hz of frequency resolution.

2.4.3.2 Wavelet analysis

Another approach to estimate the spectrum of signals that vary over time is the application of time-scale analysis, achieved through the utilization of wavelet transform (WT) [Mall 99]. The WT can be conceptualized as the representation of a signal by projecting it onto a set of basis functions. In contrast with STFT, which uses a fixed window function, not being able to optimize time and frequency resolution at the same time, the WT uses multiresolution windows that change the position and scaling of the mother wavelet so as to overcome the STFT limitations. Thus, WT can capture short-duration, high-frequency components, and

long-duration, low frequency components. The WT of a signal $s(t)$, using a mother wavelet function $\Psi(t)$, can be defined as [Mall 99]:

$$Ws(\tau, a) = \int_{-\infty}^{\infty} s(t) \frac{1}{\sqrt{a}} \Psi^* \left(\frac{t-\tau}{a} \right) dt \tag{2.12}$$

where the wavelet is dilated with a scale parameter a, and translated by τ. Analogously to the spectrogram, the square magnitude of the WT is also utilized and is referred to as scalogram. The scalogram of the same breathing signal used for computing the spectrogram in the previous section is displayed in Fig. 2.43. Unlike the spectrogram, the scalogram has a higher frequency and time resolution, being able to follow all the frequency variations and the time instants where they are produced. However, it is usually represented with a logarithmic representation in the frequency axis, thus, higher frequencies are spread in Fig. 2.43.

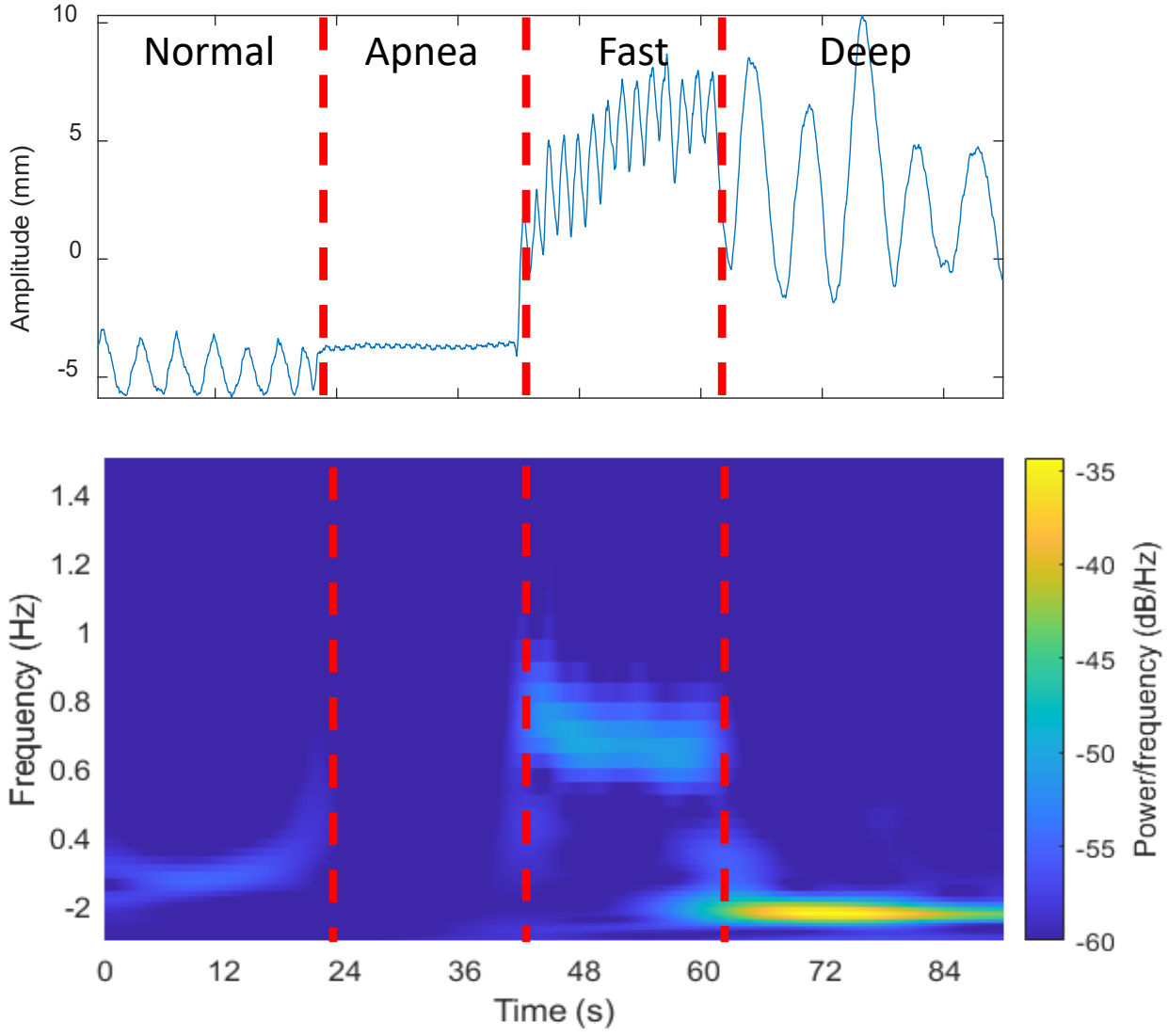

Figure 2.43: Scalogram of the breathing signal acquired with the radar: differentiating normal breathing, apnea, fast, and deep breathing episodes. Scalogram parameters: Morse wavelet, symmetry of 3, and time-bandwidth product of 60.

However, wavelet analysis faces a significant challenge: the selection of an optimal wavelet. There is no a systematic way of identifying which is the optimal wavelet basis. For the vital sign scenario, the best wavelet choice can vary depending on the specific vital sign being analyzed (heart rate, respiratory rate, heart sounds,...). Although different authors have used wavelet analysis for vital sign estimation, there is no a study, neither a consensus of which wavelet basis is desirable for each vital sign study. An analysis of which wavelet suits better for our application is carried out in Appendix G.

Chapter 3

Comprehending Cardiovascular Dynamics: Radar Signal Analysis

This chapter describes and analyzes the different signals and biomarkers that can be obtained, using radar techniques from the mechanical signals caused by the cardiorespiratory activity. The target displacement measured by radar is separated into different signals before extracting the different biomarkers: displacement caused by breathing activity (breathing waveform), displacement caused by cardiac activity (heartbeat waveform), and displacement associated with heart sounds. In addition, the acceleration of the heartbeat waveform is calculated to extract some biomarkers, such as heart rate variability (HRV) or pulse wave velocity (PWV). An overview of the aforementioned vital sign and biomarkers is presented in Fig. 3.1.

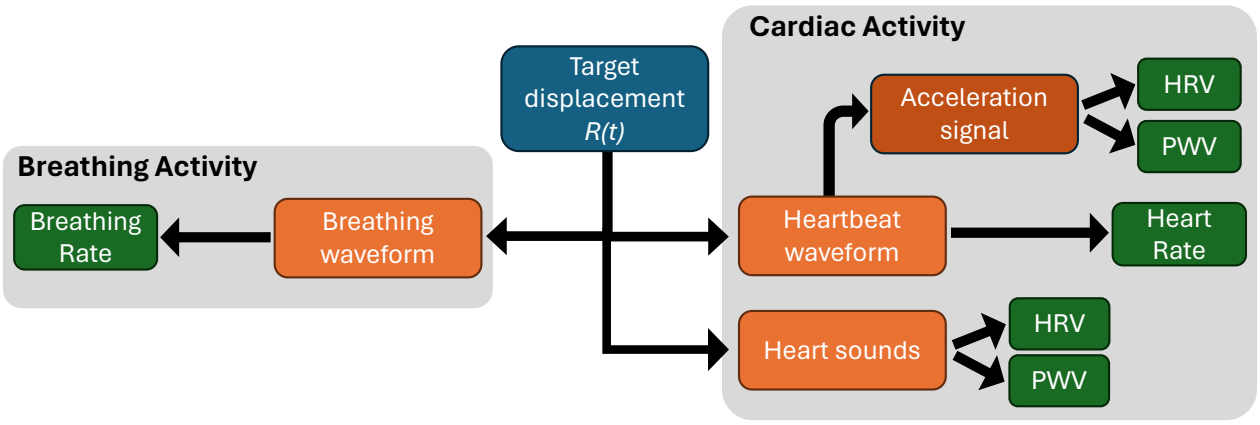

Figure 3.1: Overview of the different vital signs and biomarkers which are analyzed from the target displacement acquired with the radar.[1]

The sections in this chapter are organized as follows:

- Firstly, Section 3.1 provides an overview of the breathing and heart motion fundamentals,

[1]It is important to note that HRV and PWV can also be obtained from the heartbeat waveform. However, better results have been obtained using the heart sounds and the acceleration signal.

focusing on the heartbeat dynamics and the events generated in each phase.

- After introducing the cardiac cycle, Section 3.2 analyzes the different signals that can be obtained from the target displacement signal measured with the radar, including breathing and heartbeat waveforms and heart sounds.
- Section 3.3 details the different vital signs and biomarkers extracted from the signals described in Section 3.2.
- After that, Section 3.4 examines the influence of breathing activity on the heartbeat waveform for heart information extraction. This analysis utilizes the dataset of ten subjects, where the skin displacement is monitored with a radar simultaneously at the carotid, chest and wrist locations. Moreover, it explores heart parameter extraction using higher-order heart harmonics at different locations.
- The heart rate and heart rate variability sequences are analyzed for the aforementioned dataset in Section 3.5, so as to find the optimum body location to extract these parameters. In addition, the extraction performance in two long-time measurements is presented.

3.1 Respiratory and Cardiac Physiology

3.1.1 Respiratory mechanics

The main function of the respiratory system is the oxygen and carbon dioxide exchange process which takes place inside the lungs. During respiration, muscles contract, causing air to flow in and out of the lungs and resulting in displacement of the thoracic cage [Ishr 23]. Two main phases can be distinguished in this process:

- Inspiration. During this phase, the diaphragm, which is the main respiratory muscle, descends into the abdominal cavity, the volume inside the lungs increases and the air can flow into the them.
- Expiration. This phase happens when the pressure inside and outside the lungs is equal. In this moment, the air starts to flow out the lungs, while the diaphragm relaxes and moves back, reducing the chest volume.

It is important to highlight that, due to the anatomy of the rib cage and sternum, respiratory motion is not uniform throughout the entire thoracic cage. Being differentiated two main movements [Arth 19] (shown in Fig. 3.2):

- "Pump-handle": It refers to the upward and forward motion of the upper ribs and sternum along the sagital plane.
- "Bucket-handle": It refers to the lower ribs movement in the lateral dimension.

Thus, the chest surface motion associated with the breathing is the combination of the neck, abdominal and rib cage movements. Being the largest motion produced in the sternum area. The displacement of the chest wall due to breathing has been reported to range between 4 and 12 mm [Bori 15].

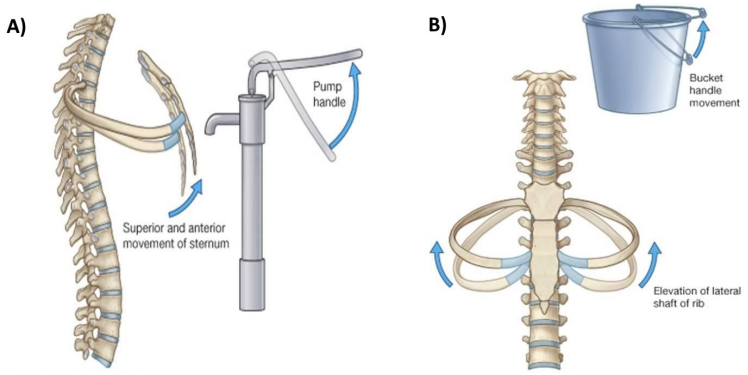

Figure 3.2: Rib motions due to breathing from [Drak 09]. a) The "pump-handle" motion. b) The "bucket-handle" motion.

3.1.2 Cardiac mechanics

The primary function of the heart is to distribute blood throughout the body. Through its contractions, it generates sufficient pressure to initiate blood flow. This motion, inside the thoracic cavity, causes a displacement in the chest surface. The greatest motion takes place at the apex and its maximum amplitude is below 0.5 mm [Bori 15]. The heart is located beneath the sternum and its partially overlapped by the lungs. Thus, the maximum chest displacement can be measured between the fourth and fifth intercostal space.

Anatomically, the heart consists of four chambers: two atria (upper chambers) and two ventricles (lower chambers). The right atrium receives deoxygenated blood from the body through the superior and inferior vena cavae, while the left atrium receives oxygenated blood from the lungs via the pulmonary veins. The atria contract to push blood into the ventricles. The right ventricle pumps deoxygenated blood to the lungs through the pulmonary artery, while the left ventricle pumps oxygenated blood to the rest of the body through the aorta. Fig. 3.3 shows a diagram with the aforementioned heart structures.

Taking a deep insight into the heart dynamics, it is important to highlight that the heart cycle involves a combination of mechanical and electrical processes [Bett 13]. Mechanically, as has been previously stated, the heart experiences rhythmic contractions and relaxations, driving the circulation of blood throughout the body. Electrically, the heart is guided by electrical impulses that regulate the timing and coordination of cardiac contractions, ensuring the synchronized pumping action necessary for blood circulation. This electrical response is traditionally measured with the ECG. The phases of the heart cycle, and the electrical and mechanical events of the heart are illustrated in Fig. 3.4.

The first event represented in Fig. 3.4 shows the state where the atria and ventricles are relaxed and the atrioventricular valves (mitral and tricuspid) are open. In this phase, the atria are depolarized (P wave), initiating atrial muscle contraction. This process causes an increase in blood inflow to the ventricles. Simultaneously, the vibration of the ventricular wall during atrial contraction produces the fourth heart sound, S4.

Following atrial contraction, ventricular depolarization occurs (QRS complex). At this stage, the atrioventricular valves close, preventing the backflow to the atria, and the semilunar valves

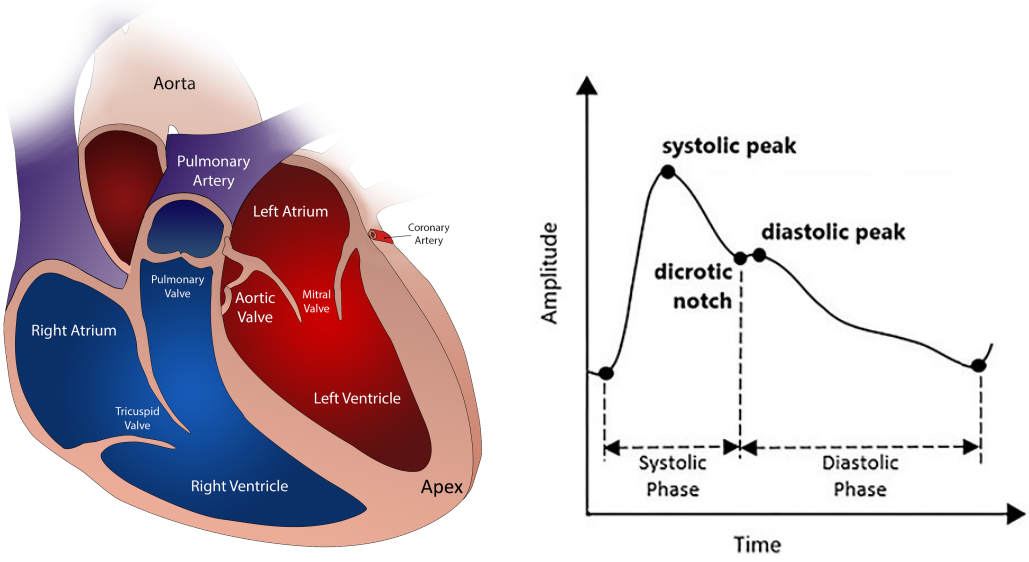

Figure 3.3: From left to right: Diagrammatic section of the heart, where the main cavities and valves are identified. Typical heartbeat pulse that can be measured using photoplethysmography [Subo 22].

(pulmonary and aortic) open. The closure of the atrioventricular valves produces the first heart sound, S1. This sound may be split, since there is a 40 ms delay between mitral and tricuspid valve closure. During the interval between the closure of the atrioventricular valves and the opening of the semilunar valves, ventricular pressure undergoes a rapid increase due to the absence of blood ejection. Ejection occurs when intraventricular pressure exceeds that of the aortic and pulmonary arteries, leading to valve opening. Following this, ventricular repolarization initiates (T wave). Leading to a ventricular pressure reduction.

When ventricular pressure decreases, the aortic and pulmonary valves close abruptly, resulting in the second heart sound, S2. The closure of these valves is associated with a slight backflow of blood into the ventricles, which produces the dichrotic notch, which can be seen in Fig. 3.3. During this phase, ventricular pressure decreases. The atrioventricular valves subsequently open, and the ventricles begin to fill passively while remaining in a relaxed state. Although this process is typically silent, there are instances when the third heart sound, S3, becomes audible. This sound may be attributed to the tension of the chordae tendineae, which are the structures which connect the heart wall muscles with the tricuspid and mitral valves. The third heart sound is often audible in children and may indicate a pathology in adults [Bett 13].

Notwithstanding, the cardiac motion study is not limited to the chest displacement due to the heart contractions [Bori 15]. The skin surface also moves due to pressure changes in the blood vessels, specially, at locations where the arteries are near the skin surface. The main superficial arteries include the carotid artery in the neck, the brachial and radial arteries in the arms, and the femoral and tibial arteries in the legs. In contrast, veins have much thinner walls compared to arteries due to the lower pressure of blood flow. Thus, veins contain less elastic tissue and are not as distensible as arteries. It is also important to highlight that the

skin surface motion from blood flow is strongly influenced by several factors, such as how close is the artery to the heart, the size of the artery, and the age of the subject [Bori 15]. Several studies [Gand 10, Laur 20] have showed that arterial wall rigidity increases with age, resulting in reduced arterial wall flexibility and skin surface motion.

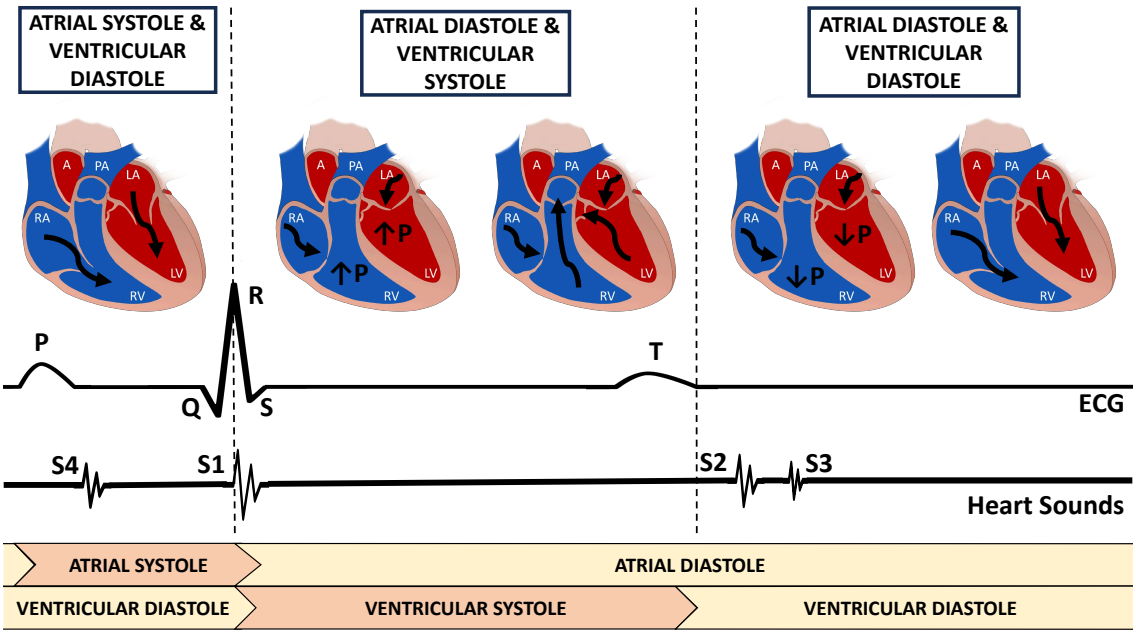

Figure 3.4: Heart cycle phases. In the heart diagram, the aorta (A), the pulmonary artery (PA), the right and left atria (RA and LA, respectively), and the right and left ventricles (RV and LV, respectively) are identified. P represents the pressure within the cavity.

3.2 Radar-Based Cardiovascular Monitoring: Signals and Interpretation

The literature has extensively analyzed the cardiorespiratory signal, allowing for a comprehensive characterization of its components. It is worth noting that the heartbeat signal usually displays a fundamental frequency ranging from 0.9 to 3 Hz (equivalent to 54 to 180 beats per minute), while the breathing signal typically falls within the range of 0.1 to 0.7 Hz (equivalent to 6 to 42 breaths per minute).

Thus, the frequency ranges mentioned above can be used to extract the waveforms of breathing and heartbeat over time. Recent studies suggest that information related to specific cardiac events can also be measured by analyzing higher frequencies, such as the heart sounds [Will 18].

A brief overview of the various vital signs that can be monitored using radar technology, and which will be addressed in this section, is shown in Fig. 3.5. This figure illustrates the raw radar displacement of the chest, the breathing and heartbeat waveforms, the heart sounds and the acceleration of the chest. The aforementioned signals have been acquired with the 134 GHz LFMCW radar, pointing towards the chest, and the Task Force Monitor (TFM),

which is used for extracting the ECG. The chest acceleration is also measured with the SCG. The breathing, heartbeat, and heart sounds have been obtained through the use of fourth order Butterworth band-pass filters within the specified frequency range[2] [Bori 15, Xia 18], as illustrated in Fig. 3.6. In addition, the radar acceleration has been obtained through double differentiation of the chest displacement data acquired. Further details regarding the signal processing employed for the extraction of these signals will be provided along this section.

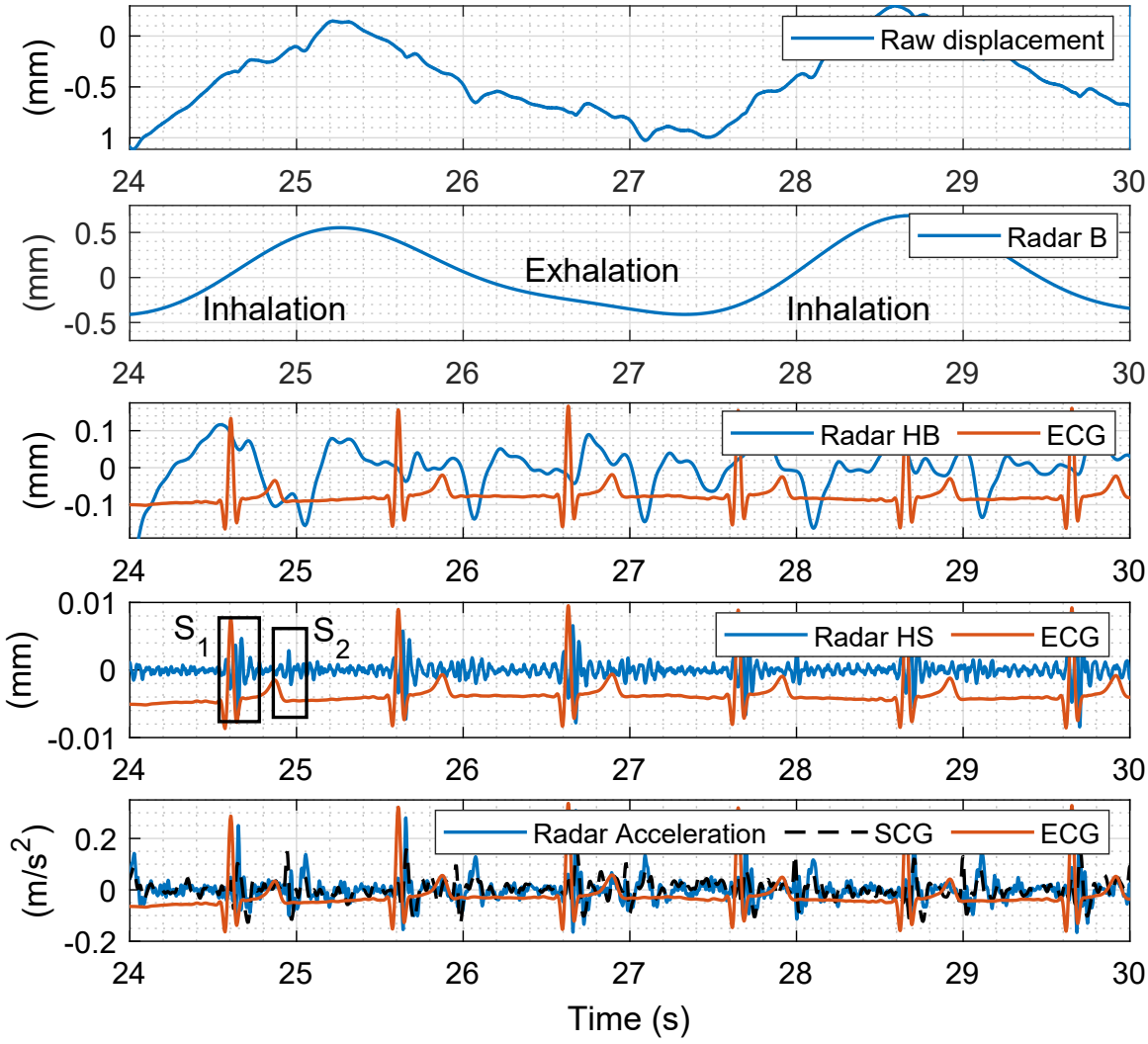

Figure 3.5: Comparison between the signals that can be acquired with radar and the reference sensors (ECG and SCG). From top to bottom: raw radar displacement signal, breathing signal (Radar B), heartbeat signal (Radar HB), heart sound signal (Radar HS), and acceleration signal (Radar acceleration).

[2]HB filtered from 0.8 to 3 Hz, HS from 10 to 30 Hz and radar acceleration from 0.8 to 50 Hz.

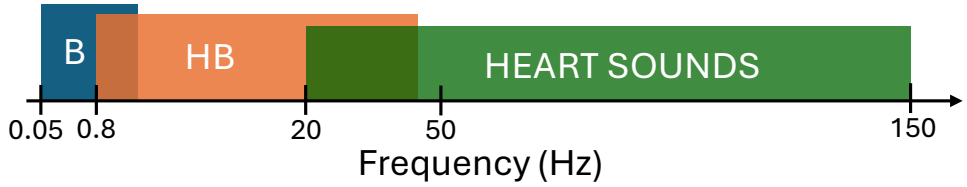

Figure 3.6: Bandwidths for the different vital signals to be extracted with a radar: breathing waveform (B), heartbeat waveform (HB) and heart sounds (HS).

3.2.1 Breathing waveform

The breathing and heartbeat signals can be separated analyzing the frequency bands shown in Fig. 3.6. This can be achieved through linear filtering or wavelets. Figs. 3.5c and 3.5d show examples of the waveforms for breathing and heartbeat that were extracted using radar. These waveforms were obtained using 4th-order Butterworth band-pass filters.

The breathing waveform has practically the same shape that the radar signal displacement, since the breathing amplitude is approximately 10 times higher than the heartbeat signal [Bori 15]. Fig. 3.7 shows the breathing waveform obtained from the radar signal and its high correlation with the chest wall displacement obtained using the Zephyr BioHarness reference. The differences between the two waveforms can be attributed to discrepancies in the methodology employed for their acquisition, given that the reference uses a capacitive sensor.

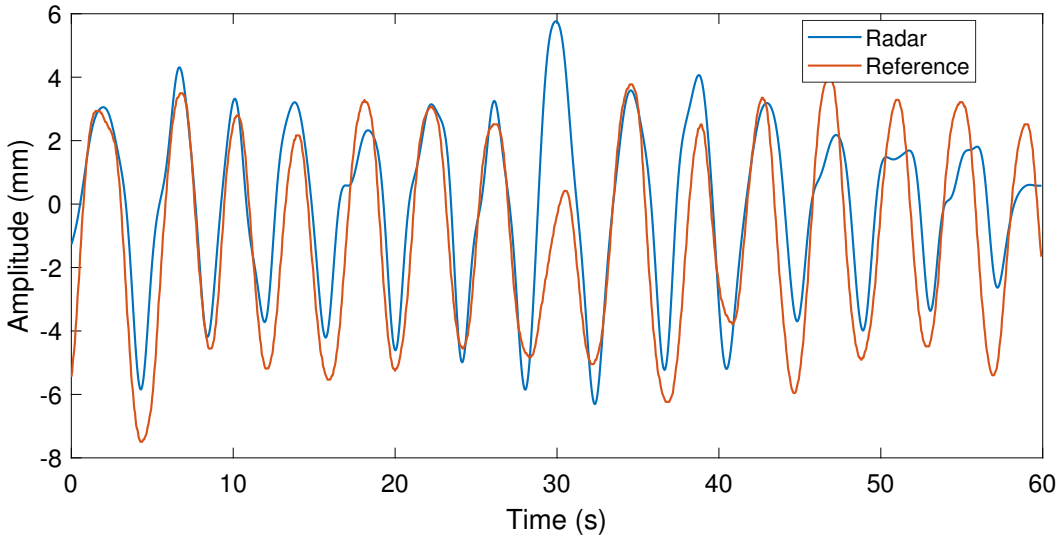

Figure 3.7: Breathing waveform extracted with the radar compared with the reference signal obtained from the Zephyr BioHarness 3.0 sensor.

[2]Note that the heartbeat and acceleration signals are limited to 50 Hz due to hardware limitations of the SCG, which is used as a reference for comparison.

Thus, in scenarios where the subject remains still, anomalies in respiration, such as apnea episodes or sudden changes in breath rate, can be observed directly by inspecting the raw radar signal. These phenomena are illustrated in Fig. 3.8, where an apnea and hyperventilation episodes have been forced and captured with the radar setup, and can be identified at a glance.

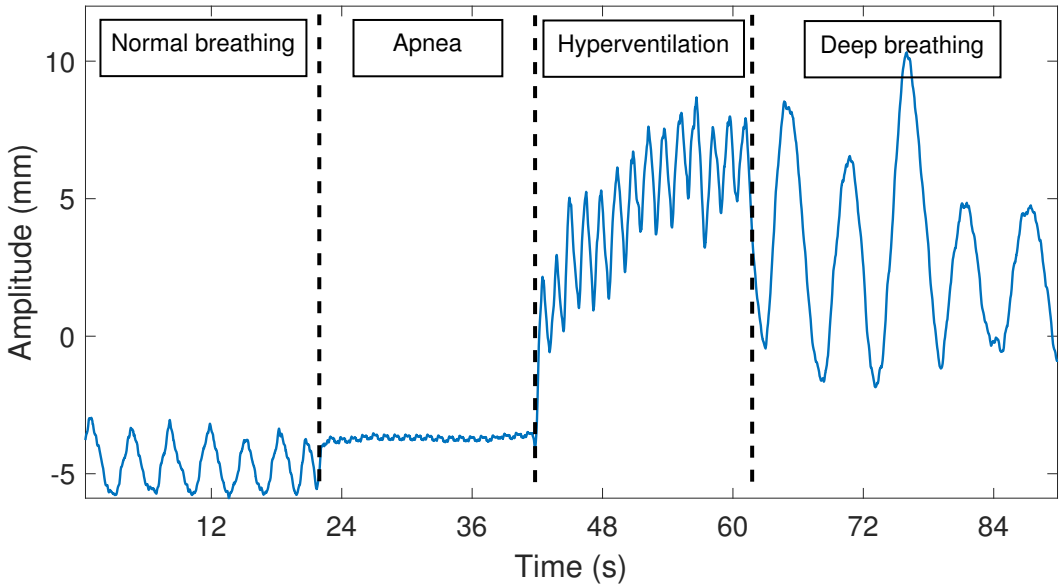

Figure 3.8: Displacement signal acquired with the radar setup in LFMCW configuration. From left to right: normal breathing, apnea, hyperventilation and deep breathing time intervals.

3.2.2 Heartbeat waveform

On the other hand, the heartbeat waveform can be retrieved with band-pass linear filtering. In this work, the heartbeat waveform is defined in the frequency range from 0.8 to 50 Hz, in order to compare it with the data extracted from the SCG. From this signal, some cardiac parameters, such as the dynamic heart rate and the HRV sequence, can be calculated.

In addition, it is important to highlight that the shape of the heartbeat waveform varies significantly depending on where it is measured, as was stated in [Will 17]. This fact is shown in Fig. 3.9, where the heartbeat waveform has been measured simultaneously at different locations: carotid, chest and femoral, and they have been compared with the pressure waveform obtained by photoplethysmography with the TFM. Observing these results and the ones extracted in [Serm 03, Beta 14, Open 16, Will 17], it can be concluded that the heartbeat waveform extracted with the radar is highly correlated to the arterial pressure waveform. Being this pressure waveform widely used for monitoring and cardiac disease diagnosis [Vasa 02, Espe 14, Roma 14].

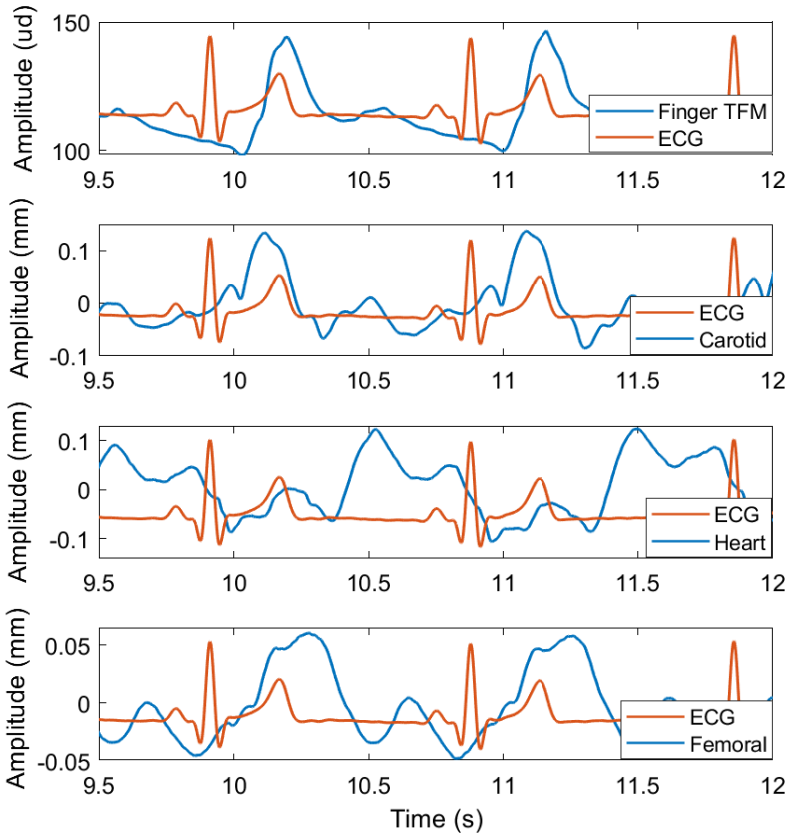

Figure 3.9: Comparison between the heartbeat waveform extracted from different locations. From top to bottom: finger –using the TFM–, carotid –using radar–, heart –using radar–, and femoral –using radar–.

On the other hand, as was introduced in Section 3.3.1, there is an interaction between respiratory and heart activities. Due to this, a first scenario has been analyzed in which a subject has been asked to hold his breath. The aim is to eliminate the coupling of breathing on the heartbeat and to analyze the latter in isolation. Therefore, a 22-year-old male subject has been monitored in apnea condition, the subject was lying down at 0.2 m from the radar set-up, where the radar is focused on the subject's chest. The distance was chosen to reduce the field of view of the radar to a region which mostly (FoV[3]of 10 cm^2) belongs to the heart location [Vinc 13]. The resulting waveform and the reference ECG are shown in Fig. 3.10.

Additionally, Fig. 3.10b illustrates that the key points in the heartbeat waveform, which provide important diagnostic information, can be identified. This is consistent with the typical shape presented in [Gedd 91] or in Fig. 3.3. The radar sequence presents the prototypical shape of the arterial pulse waveform measured with invasive catheters or applanation tonometry [Van 01], which is composed of a forward and backward wave. The forward wave represents the traveling wave generated by contraction of the left ventricle of the heart, while the reflected wave is the traveling wave generated by reflection from peripheral arteries [Vari 12].

[3] $FoV \approx Beamwidth \cdot R$, where R is the target range. The use of the lens allows a narrower focusing, as stated in Section 2.1.1.1.

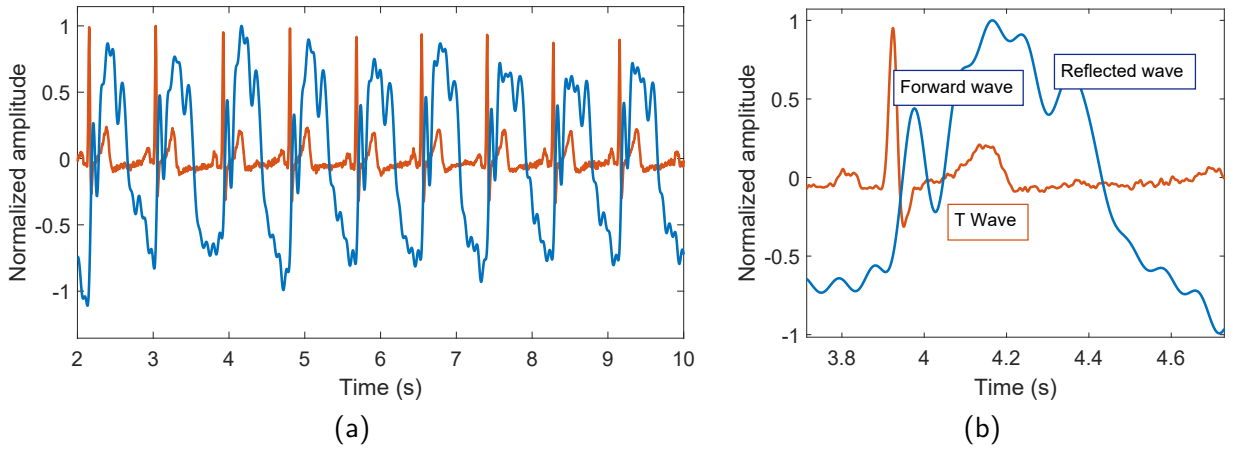

Figure 3.10: Heartbeat waveform and reference ECG. (**a**) Full sequence extracted from a subject holding his breath. (**b**) Zoom of one pulse of the heartbeat waveform.

On the other hand, Fig. 3.11 shows a more realistic scenario: a 22-year-old male is lying down, breathing normally, and the radar is positioned at a distance of 1 m from the subject.

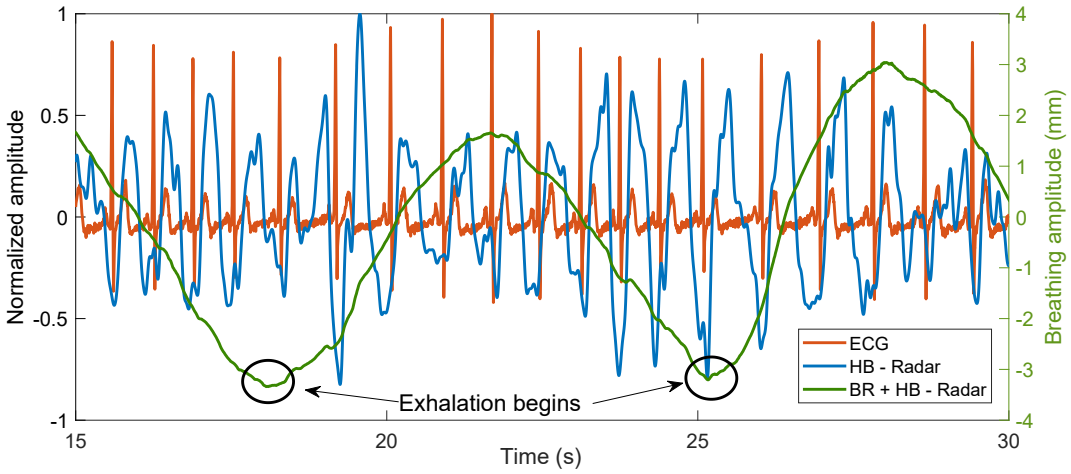

Figure 3.11: Heartbeat waveform extracted from a breathing subject. It also shows the displacement acquired with the radar, which contains the breathing and heartbeat signals.[4]

It shows in green the chest displacement obtained with the radar, where the heartbeat overlays the breathing waveform, which is the dominant component due to a 10:1 amplitude ratio between both signals. Thus, the chest displacement roughly corresponds with the breathing signal. Moreover, the normalized heartbeat (in blue) and the reference ECG (in red) are also displayed. These results indicate that respiratory activity causes distortion in the heartbeat waveform, as the heartbeat waveform differs between succesive beats, unlike in Fig. 3.10. However, the synchrony between the ECG and the heartbeat waveform remains.

[4]Note that negative displacements correspond to movements in which the target approaches the radar, which coincides with the inhalation process.

Additionally, Fig. 3.11 shows that the breathing directly modulates the heart rate: exhalations increase the pulse periods, whereas inhalations decrease the pulse periods. These effects were anticipated and have been extensively analyzed in the literature [Mukh 15, Janb 18]. Indeed, this phenomenon is referred to as respiratory sinus arrhythmia (RSA), which is discussed in greater detail in Section 3.3.2. RSA provides evidence that there is a coupling between respiration and the heartbeat.

The effect of RSA in the heart rate (HR) is measurable using radar techniques, and that the HR can be extracted regardless of the subject's position. Thus, a experiment is carried out where a 22-year-old male is measured in a lying down position with the radar focused on either to the chest (anterior view) or to the back (posterior view). These scenarios are analyzed when the person is breathing or during apnea. Then, the HR calculated from the ECG is compared to the HR obtained from the radar measurement (rHR). During breathing, the HR is compared with the breathing waveform to observe how the breathing affects the heart rate. The extracted sequences are shown in Figs. 3.12 and 3.13.

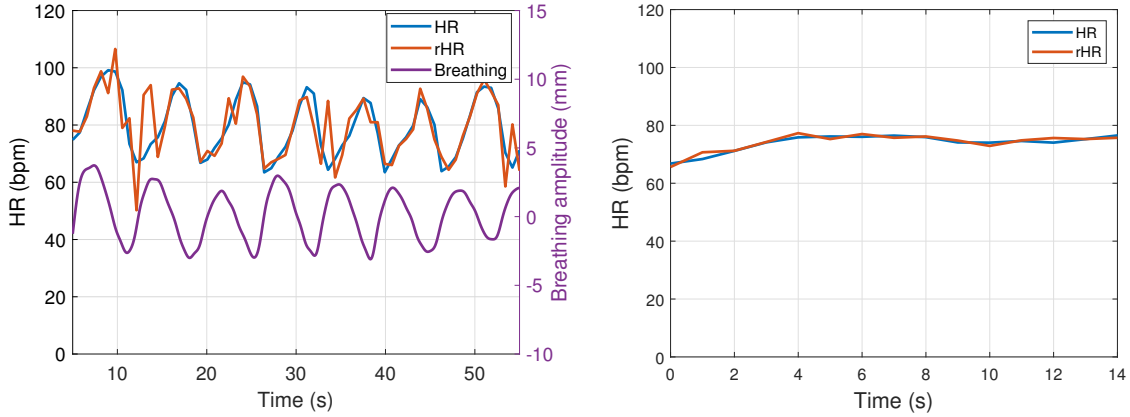

(a) Breathing subject (b) Subject holding his breath

Figure 3.12: HR sequences measured extracted from the ECG and the radar (anterior view).

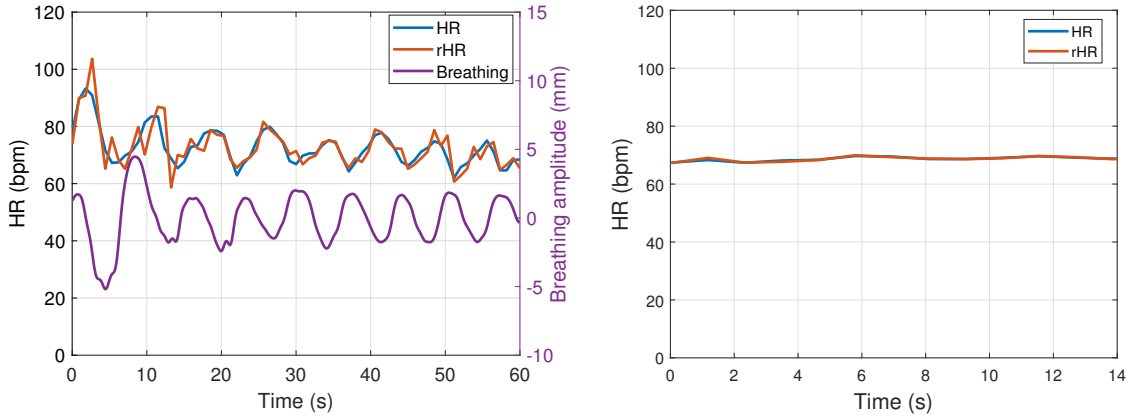

(a) Breathing subject (b) Subject holding his breath

Figure 3.13: HR sequences measured extracted from the ECG and the radar (posterior view).

These results confirm that HR and HRV can be successfully extracted from different locations. Furthermore, Figs. 3.12a and 3.13c reproduce the correlation between HR and the breathing signal found by H. Kobayashi [Koba 98]. On the other hand, in the apnea scenario, the heart rate remains stable as it is not affected by breathing.

3.2.2.1 Acceleration signal

Some cardiac events can be better identified after a previous preprocessing of the radar signal. Because the radar signal acquired has displacement information of the chest, the double differentiation of this signal provides information on acceleration. This acceleration signal has the same nature as the signal provided by an SCG, therefore, some characteristics events, such as the aortic valve opening (AO), the mitral valve closing (MC), the aortic valve closing (AC), or the mitral valve opening (MO) shown in [Dehk 19] can be identified. Fig 3.14 displays a comparison between the SCG reference and the acceleration signal extracted from the radar, allowing for identification of the aforementioned events.

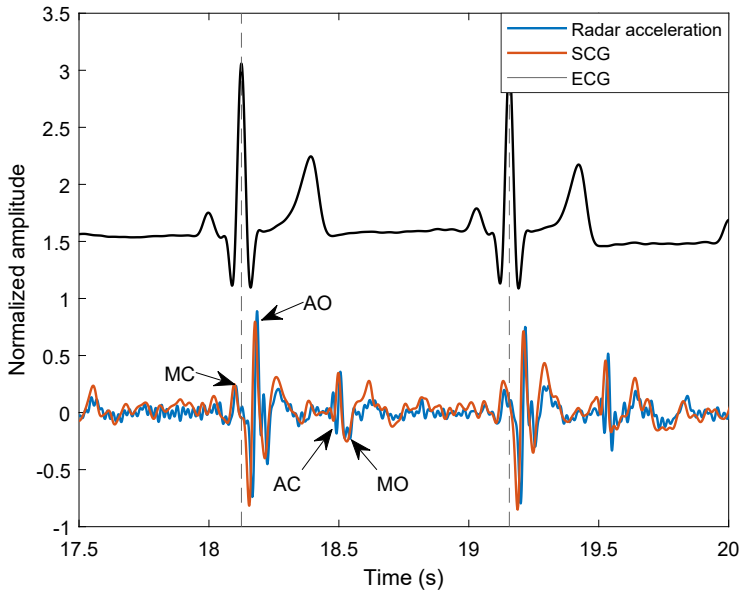

Figure 3.14: Comparison between the radar double differentiation and the SCG signal. Locations of ECG R-peaks are marked with dashed lines.

Regarding the frequency content, authors in [Mazl 09, Xia 18] analyzed the similarities between the SCG signal and the radar acceleration, stating that a high correlation was obtained analyzing the frequency range below 35 Hz. However, [Taeb 17] shows that there is SCG information above 40 Hz related to valve closure. The radar acceleration signal is analyzed in the 0-50 Hz frequency range, since the reference SCG used is limited to this band. Moreover, a spectral analysis of the SCG signal is presented in Fig. 3.15.

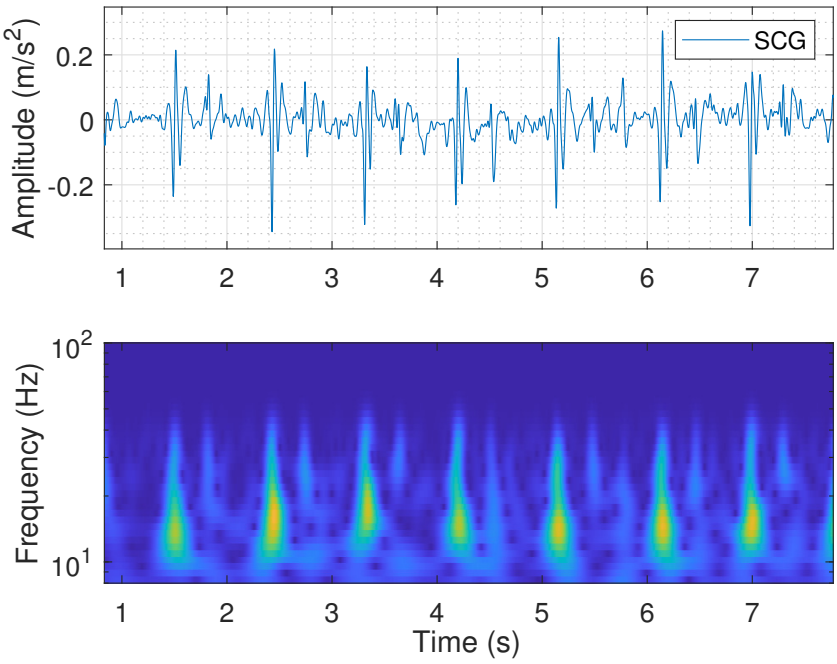

Figure 3.15: Time-frequency analysis of the SCG waveform acquired from the subject's chest.[5]

On the other hand, it should be emphasized that double differentiation is a noisy process. So, in scenarios with low SNR, the vital sign analysis through the skin surface's acceleration could be extremely challenging. For instance, CW radars have difficulties in the extraction of the acceleration signal. As was explained in Section 2.3, the impact of the low-frequency noise is higher in CW radars, which can mask these fiducial points in the extracted signals.

3.2.3 Heart sounds

The vibrations resulting from the aperture and closing of the different valves, which are highly correlated with the heart sound waveform obtained with the phonocardiograph [Will 18], can also be obtained from the radar signal. The shape of the heart sound signal obtained from the radar strongly correlates with the heart sound signal measured with the PCG (see Fig. 1 in [Dehk 19]), which shows the first and second heart sounds (S1 and S2, respectively).

As was explained at the beginning of this chapter, the first heart sound occurs directly after the R-peak of the ECG signal, and it is result of the closure of the atrioventricular valves. On the other hand, the second heart sound is a result of the sudden closure of the aortic and pulmonary valves. The spectrum of heart sound signals have been analyzed in the literature, and the main information of its components its placed in the 20-150 Hz range [Arno 84, Amit 09, Will 18]. The amplitude of S1 is higher than S2, so detecting this heart sound is easier than S2. However, it has to be also highlighted that the heart sounds can be modulated due to the breathing. During inhalation, the S1 decreases its intensity, whereas the

[5]If not specified, scalograms are computed using a Morse wavelet with a symmetry of 3 and a time-bandwidth product of 60.

S2 increases its amplitude [Amit 09]. The extraction and identification of the different heart sounds from the radar signal was previously addressed in [Will 18], which utilized a hidden semi-Markov model to detect heart sounds in both phonocardiograph and radar data. Authors in [Shi 20] provide a dataset to analyze the heart sounds extraction using a six-port-based radar system at 24 GHz, the radar signal are synchronized with two external references: an ECG and a PCG. Fig. 3.16 shows the high correlation between the heart sounds extracted with the radar and the PCG, using a measurement of the mentioned dataset.

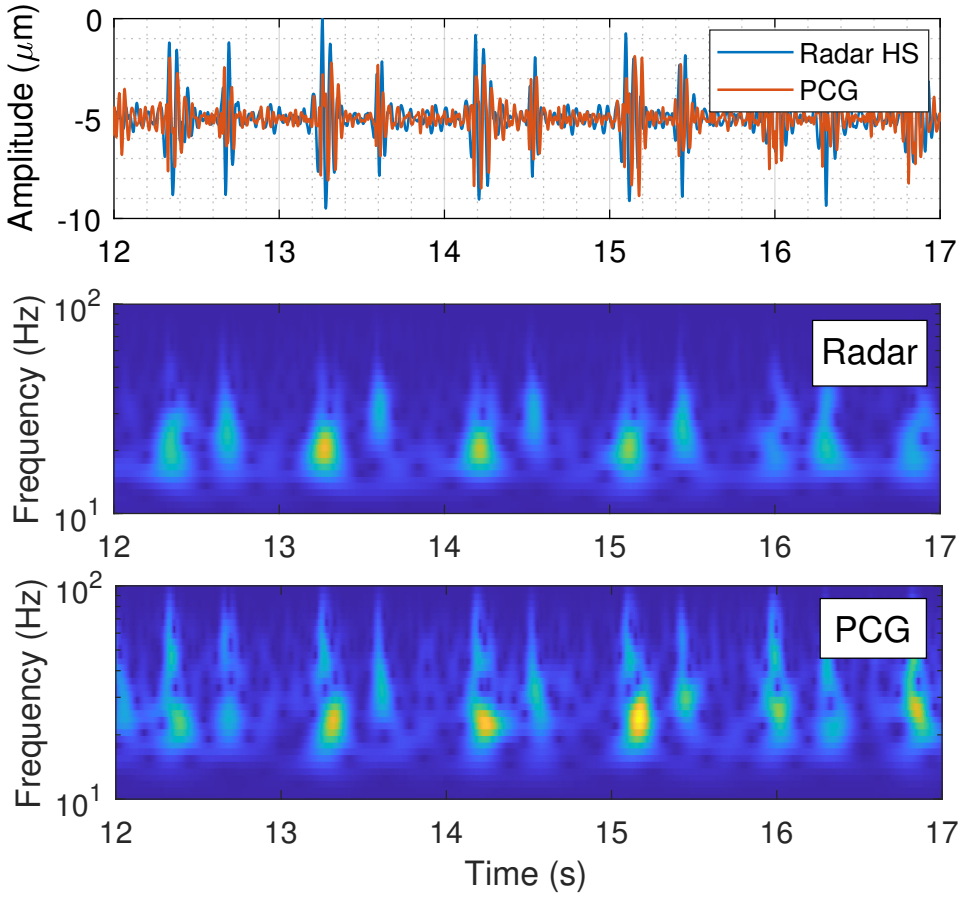

Figure 3.16: Comparison between the heart sounds extracted with the radar and the reference PCG. From top to bottom: the heart sounds waveforms, the scalogram of the radar heart sounds, and the scalogram of the PCG signal.

The morphology of heart sounds also differs based on the location of measurement. For instance, when heart sounds are measured at the carotid artery, the amplitude of S2 may be comparable to or even larger than S1 [Chan 13]. This is because the semilunar valves, which produce S2, are closer to the measurement point than the ventricular muscles responsible for S1. This phenomenon is displayed in Fig. 3.17, where the heart sounds have been measured simultaneously with two radars focused on the carotid and to the chest. Since S2's amplitude at the carotid location is comparable to that of S1, S1 identification may be challenging as it

is no always the loudest heart sound in each pulse.

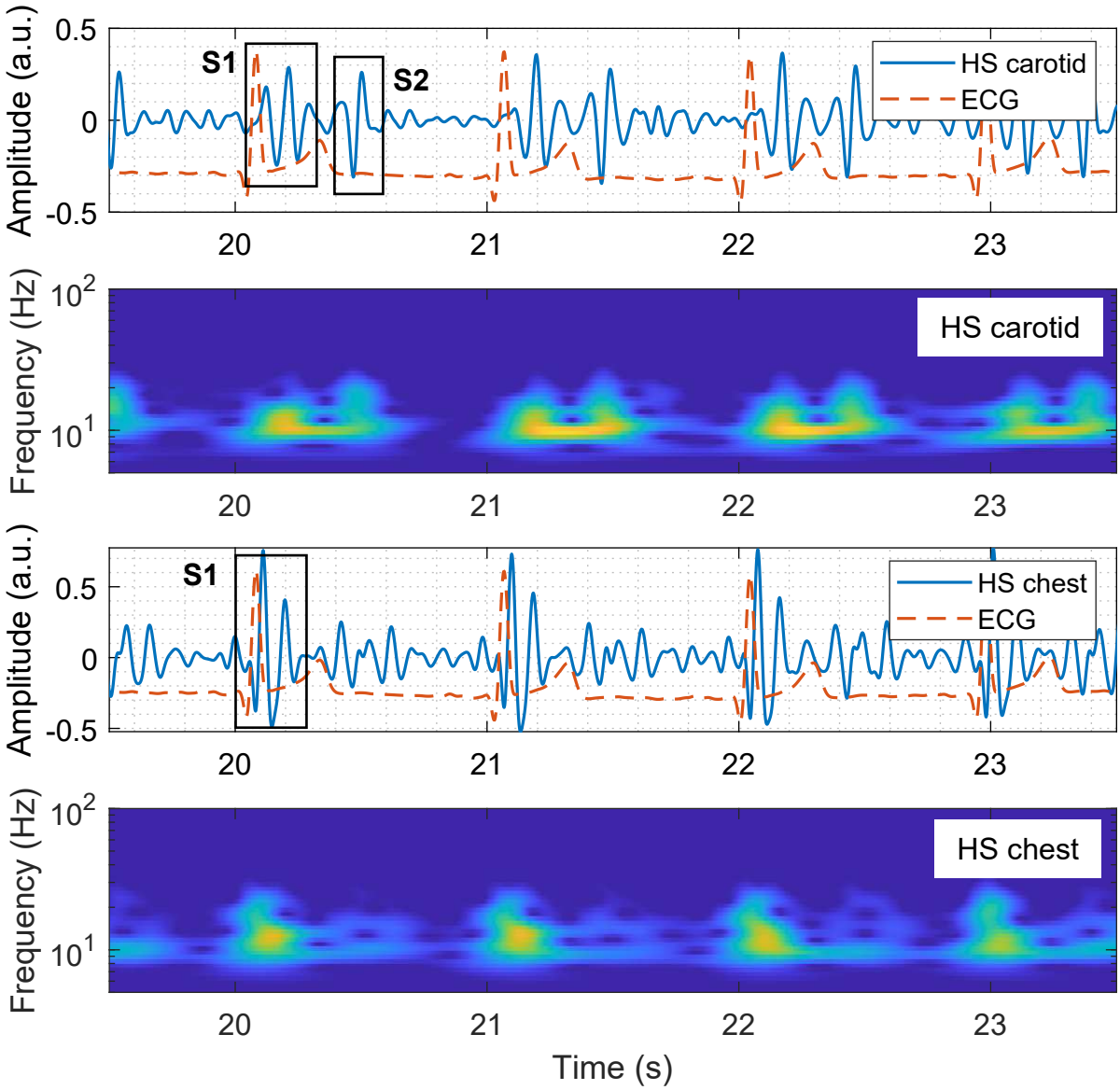

Figure 3.17: Comparison between the heart sounds extracted with the radar simultaneously at different locations. From top to bottom: the heart sounds waveforms focused on the carotid, its scalogram, the heart sounds waveform focused on the chest, and its scalogram.

It is important to note that while the literature indicates that the majority of the information contained within the heart sounds can be found within a frequency range from 20 Hz to 150 Hz (from 16 Hz in [Shi 20]), our experience has demonstrated that filtering from 10 Hz to 30 Hz has resulted in more accurate S1 extraction. The time-frequency analysis in Fig. 3.17 confirms that the components associated with the different heart sounds, especially S1, have spectral content around 10 Hz.

Moreover, it has to be noted that the scalograms of the heart sounds in Figs. 3.16 and 3.17 have a huge similarity with the scalogram of the radar acceleration displayed in Fig. 3.15. Indeed, there is a strong correlation between the chest acceleration measured with the radar and heart sounds. Authors in [Heck 82] state that the signal measured with a phonocardiograph represents a transformation (second derivative) of the pressure pulse, being both waveforms representations of the same phenomenon. This relationship is illustrated in Fig. 3.18, where the chest acceleration is compared with the heart sounds waveform.

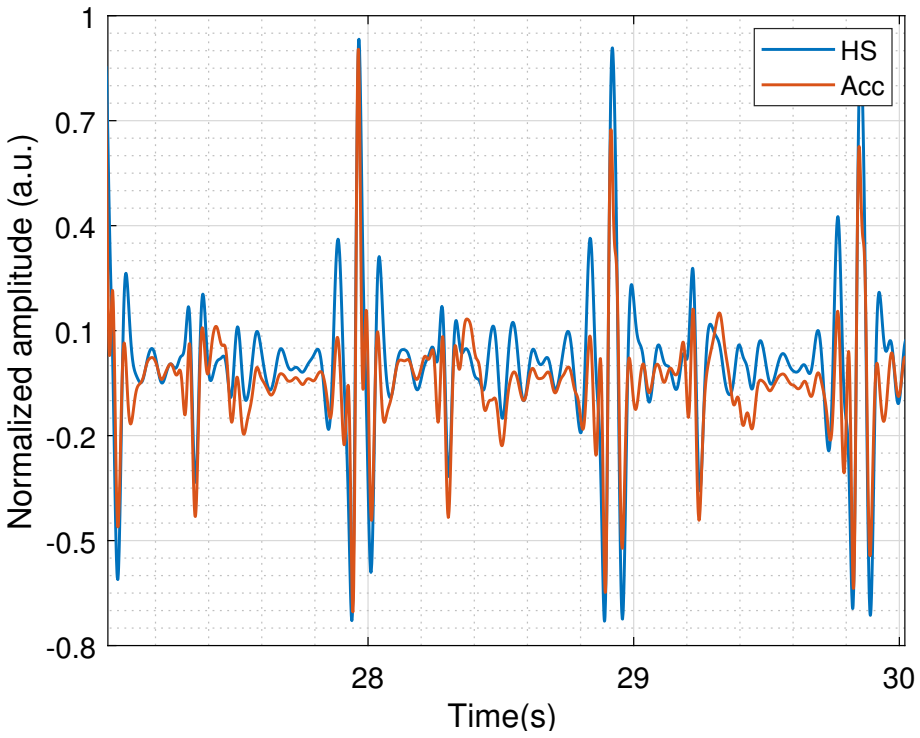

Figure 3.18: Comparison between the heart sounds and the chest acceleration obtained with the radar.

3.3 Vital Signs and Biomarkers

This section describes the different vital signs and biomarkers that can be obtained using radar technology. It focuses on breathing and heart rates, breathing and heartbeat waveforms, heart sounds, heart rate variability and pulse wave velocity. It should be emphasized that the results presented in this section have been obtained under favorable conditions, which means that the subjects were asked to remain as still as possible in order to reduce interference and potential inaccuracies caused by undesired motions. The robustness of vital sign extraction in more challenging scenarios is addressed in Chapter 4.

3.3.1 Breathing and heart rates

The primary parameters extracted in vital sign studies conducted using radar technology are the breathing and/or heart rates. These rates are traditionally obtained by performing a Fast Fourier Transform (FFT) to the radar displacement signal and looking for the fundamental components in the aforementioned frequency ranges [Petk 09, Wang 13b]. However, with this technique, the time information, which is useful for clinical diagnosis, is lost. These rates can be obtained dynamically using time-frequency analysis techniques or analyzing the breathing and heartbeat waveforms in the time domain. This is exemplified in Figs. 3.19 and 3.20.

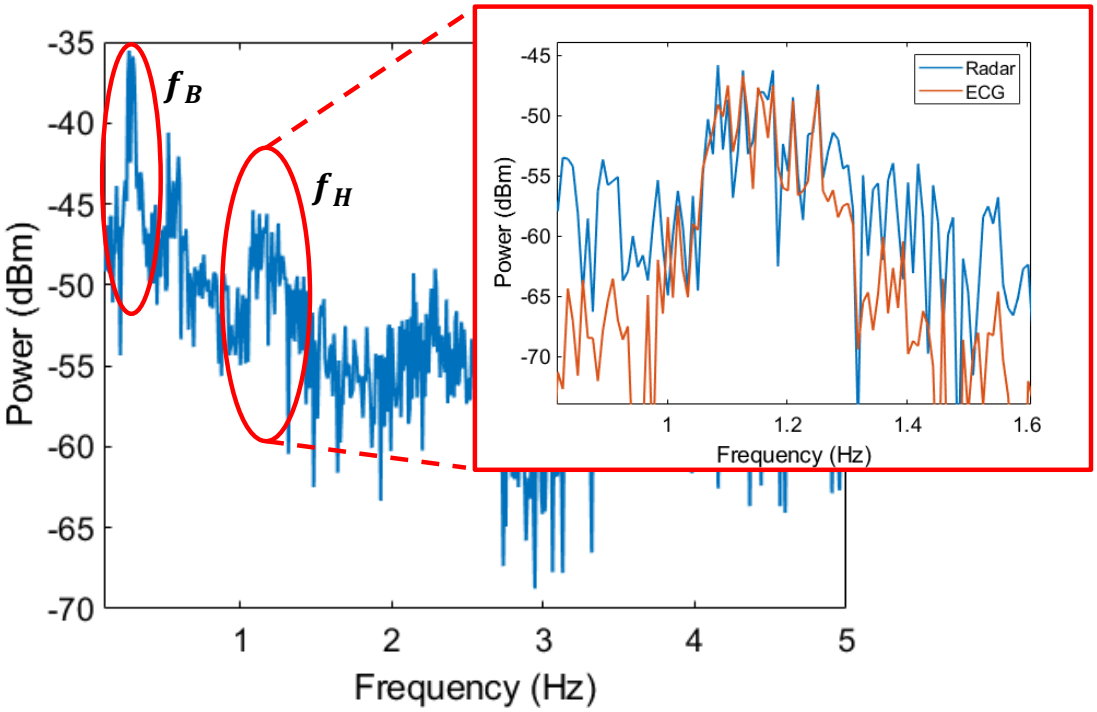

Figure 3.19: Spectrum of the radar displacement signal. The regions where the breathing and heartbeat fundamental frequencies are identified. The heartbeat frequency region is zoomed and compared with the reference ECG spectrum.

The initial figure shows the radar displacement spectrum after applying the FFT. Although frequency components related to the respiration and heartbeat signal are visible, it is not possible to precisely determine breathing and heart rates from the radar spectrum or the reference ECG spectrum. This is due to the fact that the frequency content of the signals varies over time, and the FFT lacks the time resolution to detect these changes. On the other hand, Fig. 3.20 shows the spectrogram of the same radar displacement signal, where the breathing and heart rates can be identified, observing its evolution along the measurement time. Moreover, harmonics and intermodulation products of these two frequencies can be observed. The presence of intermodulation products (the $f_B + f_H$ term, in this case) highlights the coupling between the respiration and heartbeat signals. This coupling suggests that the two systems are not isolated from each other and should not be studied separately ignoring this interaction.

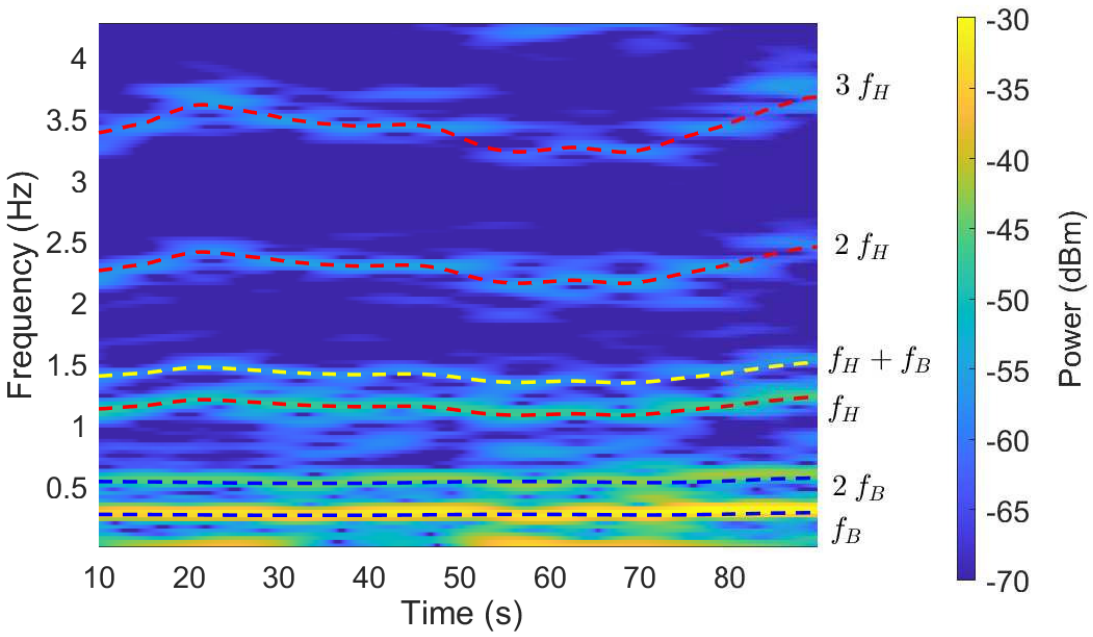

Figure 3.20: Spectrogram of the radar displacement signal. The breathing and heartbeat fundamental frequencies are identified, as well as some harmonics and intermodulation products of them.

3.3.2 HRV

The heart rate variability (HRV) is widely used as a noninvasive tool to assess the autonomic nervous system (ANS) activity, being used as a biomarker of some disorders, such as sleep apnea, sudden cardiac death, diabetic neuropathy, or stress [Khan 09, Tere 12, Tsao 13, Kang 16, Schw 20].

The concept behind the HRV was first introduced by Stephen Hales in 1733 [Hale 33], when he noticed a variation in the arterial blood pressure and time length between beats during the respiration cycle of horses. However, it was not until 1847 when this phenomenon was documented by Carl Ludwig [Ludw 47], stating an increase in the heart rate during inhalation and a decrease during exhalation. Nowadays, this is known as respiratory sinus arrhythmia (RSA). Fig. 3.21 illustrates the heart rate variation due to the breathing process, where it can also be observed the ECG amplitude modulation due to the breathing [Mukh 15]. Moreover, it shows how during inhalation the subject chest volume increases, reducing the distance between the radar setup and the region measured, which is represented with negative amplitude values. The existing correlation between the HRV and the breathing signal was previously analyzed by H. Kobayashi in [Koba 98], where the HRV was computed from the ECG and the breathing signal was acquired with a spirometer. Additionally, the HRV and RSA provide diagnostic capabilities to identify respiratory disorders such as central sleep apnea, chronic obstructive pulmonary disease or asthma, and refine diagnostic procedures [Lehr 97, Giar 04, Citi 11, Lee 14].

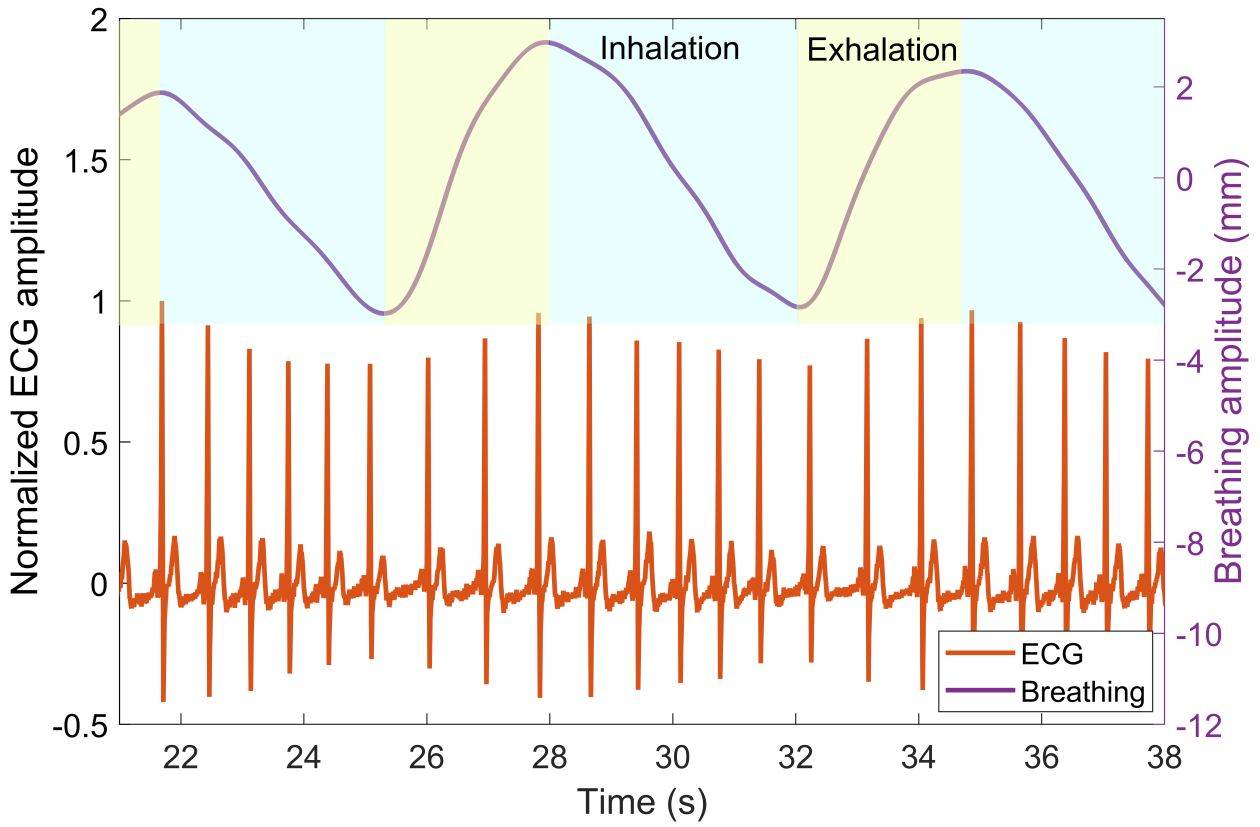

Figure 3.21: Breathing waveform extracted with the 134 GHz radar set-up compared with its reference ECG. The inhalation and exhalation processes are illustrated.

Therefore, this phenomenon further illustrates something that has been introduced throughout this chapter, which is the undeniable interaction of respiration on heartbeat, underscoring the intricate relationship between respiratory and cardiac dynamics. This leads us to reject the simplifications proposed at the beginnings of radar vital sign analysis [Li 10], which suggested that a person's chest displacement could be modeled as:

$$x(t) = A_B \sin(2\pi f_B t) + A_H \sin(2\pi f_H t) \tag{3.1}$$

where A_B and A_H are the breathing and heartbeat amplitudes, and f_B and f_H are the breathing and heartbeat fundamental frequencies.[6]

RSA is state-dependent and can be influenced by factors such as breathing pattern, sleep-wake cycles, psychological stress, physical activity, and age [Eckb 83]. It has been reported that the maximum RSA can be achieved when the subject breaths at their resonant frequency, which typically occurs at a slower breathing rate of around 6 breaths per minute [Lehr 13].

[6]The chest wall's displacement should be modeled as:

$$x(t) = A_B \sin(2\pi f_B t) + A_H \sin(2\pi f_H t + \beta \sin(2\pi f_B t)) \tag{3.2}$$

where the heartbeat waveform is defined as a FM signal, whose frequency is modulated by the breathing waveform in proportion to the term β, which is associated with the RSA phenomenon.

At this resonant frequency, there is maximal coherence between respiratory and heart rate variability, leading to the most pronounced RSA effect.

This biometric is calculated measuring the time difference between successive heart beats intervals, which are referred in literature as inter-beat intervals (IBIs), as can be shown in Fig. 3.22 ($\text{HRV}(i) = \text{IBI}_i - \text{IBI}_{i-1}$). Thus, it is necessary to identify characteristic points to extract the HRV accurately from the radar signal. These time intervals have been extracted from the ECG, the heartbeat waveform and the chest wall's acceleration following the next procedure:

- The time intervals used to calculate the HRV sequence from the ECG are obtained by measuring the time difference between R-peaks extracted using the Pan and Tompkins algorithm [Pan 85]. The Pan-Tompkins algorithm is robust and efficient, making it a popular choice for QRS detection in most clinical and research applications.
- The IBI extraction from the heartbeat waveform is more challenging. As has been presented in Section 3.2.2, the heartbeat waveform is irregular and can vary even between successive heartbeats, so identifying these characteristic points it is not a trivial task. In this thesis, the IBIs have been calculated by measuring the distance between minima, as displayed in Fig. 3.23. Additionally, the minimum distance between consecutive minima is restricted to be greater than $1/(2f_{hb})$, where f_{hb} is the heartbeat fundamental frequency.
- On the other hand, the post-processing carried out on the acceleration signal calculation improves the cardiac information extraction. Therefore, the HRV sequence can be computed with higher accuracy from these signals. The time intervals used to calculate the HRV sequence from the acceleration signal are extracted by measuring the distance between maxima applying the same restriction previously detailed. These maxima do not match the time instants selected in the heartbeat waveform to compute the HRV. As mentioned above, the maxima from the acceleration radar correlate with the aortic opening (AO) that can also be observed in the SCG. This is displayed in Fig. 3.14.

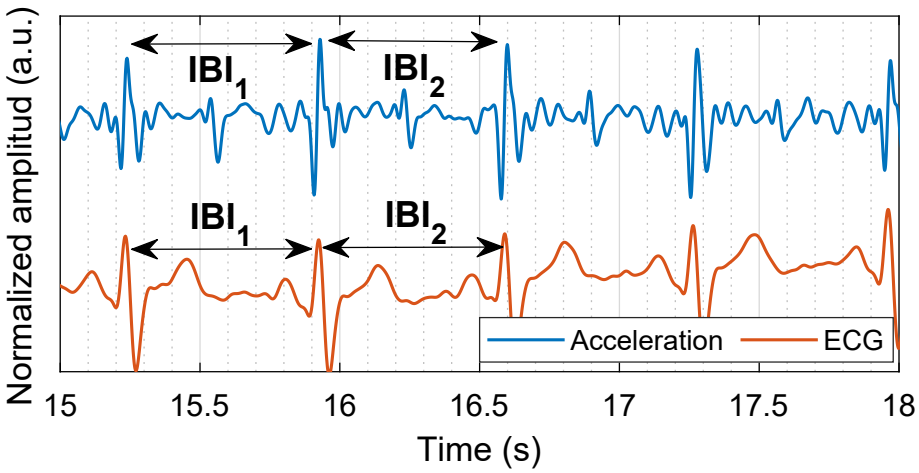

Figure 3.22: Example of the IBI extraction from the acceleration signal and the ECG.

The HRV sequence extracted from the heartbeat waveform (displacement signal) is label as HRV_{HB}, while the HRV extracted from the acceleration signal is label as HRV_{Acc}. An example of the HRV extraction using the heartbeat waveform and the chest wall's acceleration is displayed in Figs. 3.23 and 3.24. This was done to illustrate the effect of noise and interferences in the HRV extraction using the heartbeat waveform.

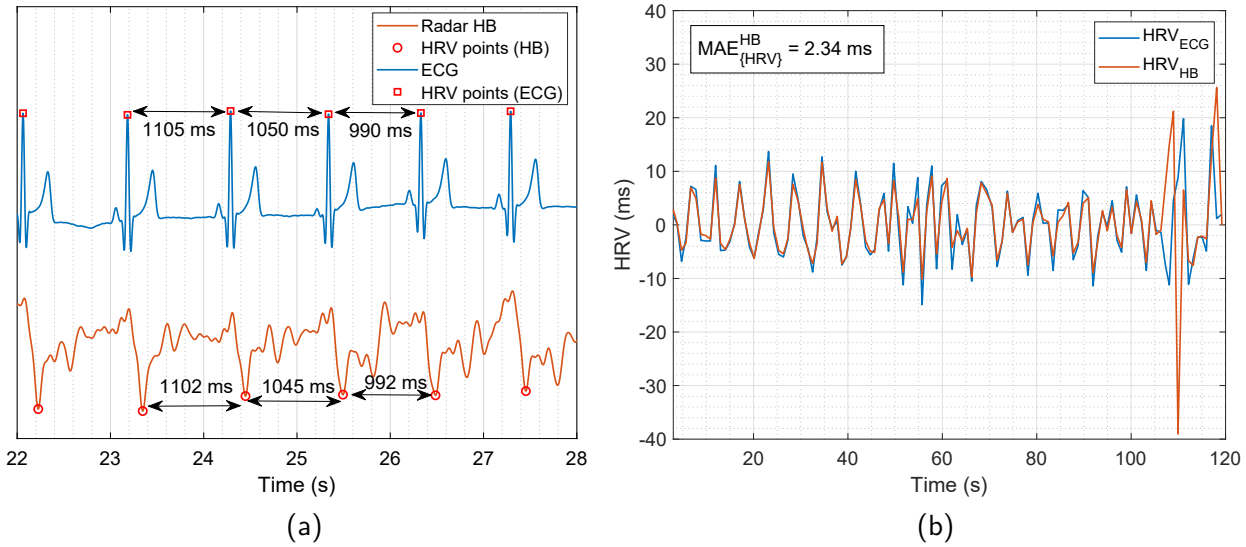

Figure 3.23: HRV sequences comparison. (a) Point identification for HRV sequence extraction. (b) The HRV sequence extracted from the heartbeat signal is compared with that one computed from the ECG, with a mean absolute error of 2.34 ms.

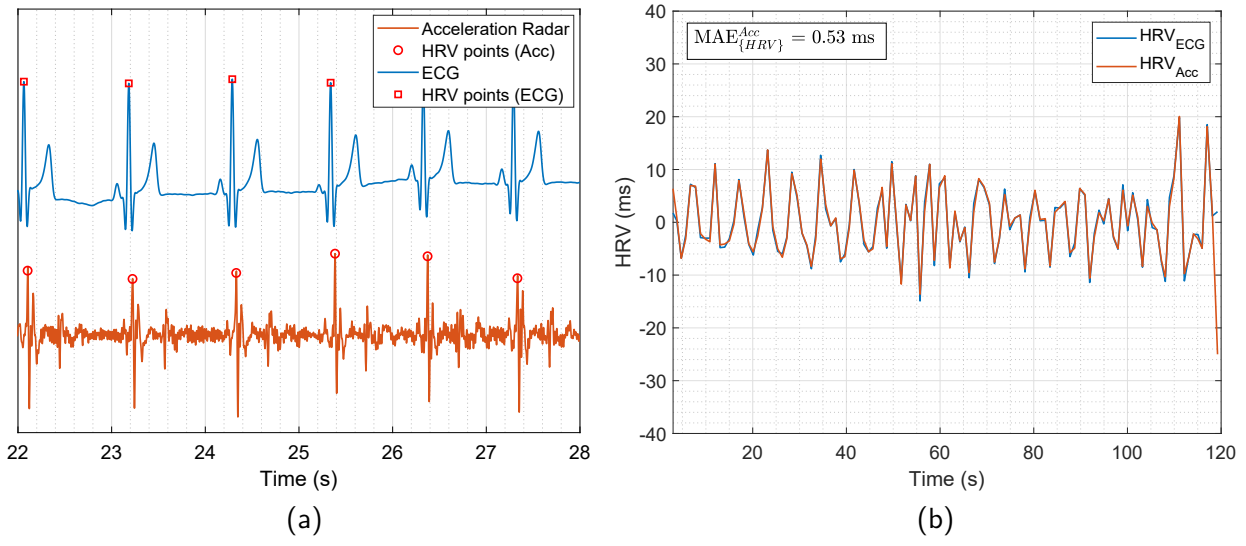

Figure 3.24: HRV sequences comparison. (a) Point identification for HRV sequence extraction. (b) The HRV sequence extracted from the acceleration signal is compared with that one computed from the ECG, with a mean absolute error of 0.53 ms.

Thus, these figures show that extracting the HRV sequence from the acceleration signal provides better results than using the heartbeat signal. Indeed, the time instants (radar AO) are easily identifiable, as is shown in Fig. 3.24a, allowing an easier HRV sequence extraction.

3.3.2.1 HRV analysis

Heart rate variability analysis has emerged as a vital tool in cardiology due to its noninvasive nature, ease of measurement, and provision of prognostic information for patients with heart disease. HRV serves as a valuable tool for assessing the function of the autonomic nervous system, particularly in diabetic and post-infection patients, enabling investigation into both sympathetic and parasympathetic activity [Raje 06]. Regarding HRV analysis, two major approaches are distinguished: time-domain and frequency-domain measurements. These metrics are typically calculated for either 24-hour or short-term (approximately 5 minutes) measurements. Although the same formulas are used for both types of measurements, they are not directly comparable, as their physiological meaning could vary [Kuus 16]. For instance, short-term HRV measurements are generated by the relationship between sympathetic and parasympathetic branches, baroreceptor reflex or RSA. While the 24-hour measurements, which is the "gold standard" for clinical HRV assessment, are affected by the sleep cycle, circadian rhythms, metabolism or body temperature [Shaf 17].

Frequency-domain measurements

These measurements estimate the distribution of absolute or relative power into four frequency bands: ultra-low-frequency (ULF), very-low-frequency (VLF), low-frequency (LF) and high-frequency (HF) [Shaf 17].

- ULF band: This band encompasses the frequency range below 0.003 Hz and requires a 24-hour measurement.
- VLF band: This band is contained within the frequency range of 0.0033 Hz to 0.04 Hz. It requires a minimum recording period of 5 minutes, but best results are obtained in 24-hour measurements. The power within VLF band shows a stronger association with all-cause mortality compared to both LF and HF power.
- LF band: This band mainly reflects the baroreceptor activity during resting conditions, and it is located within the 0.04-0.15 Hz frequency range. It requires a minimum measuring time of 2 minutes.
- HF power: This band contains the frequency range above 0.15 Hz. It reflects parasympathetic activity and the HR variations due to the respiratory cycle. It requires a minimum measuring time of 1 minute.

Time-domain measurements

These measurements quantify the variability of the inter-beat intervals (IBIs). The main metrics are [Shaf 17]:

- SDNN: Represents the standard deviation of the IBIs of normal sinus beats. SDNN is more accurate when calculated over 24-hour recordings than during short-term measurements, being the "gold standard" for medical stratification of cardiac risk in

24-hour measurements.

$$SDNN(ms) = \sqrt{\frac{1}{N-1}\sum_{i=1}^{N}(RR_i - \overline{RR})^2} \tag{3.3}$$

where RR_i represents the i-th IBI.

- RMSSD: Represents the root mean square of successive differences between normal heartbeats. This parameter provides a better assessment of RSA. It is correlated with the HF power.

$$RMSSD(ms) = \sqrt{\frac{1}{N-1}\sum_{i=1}^{N-1}(RR_{i+1} - RR_i)^2} \tag{3.4}$$

- pNN50: This metric shows the percentage of adjacent normal intervals that differ each other more than 50 ms. It is correlated with the RMSSD.

$$pNN50(\%) = \frac{\#|RR_{i+1} - RR_i|_{>50ms}}{N-1} \times 100 \tag{3.5}$$

A time-domain analysis of the the HRV sequence extracted with radar is presented in Section 3.5, with a comparison to the HRV obtained with an ECG.

3.3.3 Pulse Wave Velocity

PWV is widely used as an indicator of arterial stiffness and has been shown to predict mortality from cardiovascular disease, ischaemic heart disease, stroke and atherosclerosis [Till 07]. Moreover, it has been showed that PWV is inversely related with blood pressure (BP) and can be used for an indirect estimation of this indicator [Gesc 12]. Carotid-femoral pulse wave velocity (cfPWV) is considered the "gold standard" for measuring aortic stiffness [Till 07]. PWV can be monitored with invasive methods such as pressure catheter recordings or with electromechanical solutions which require direct contact with the patient's tissue [Pere 15]. It has been reported that these probes require to be placed over the widest pulsation area and require support from solid structures such as the bones, being uncomfortable for the patient. Additionally, there are other non-invasive techniques which monitor the time delay, which is also known as pulse transit time (PTT), between two different locations using electrocardiograms and photoplethysmograms, piezoelectric pressure transducers or sphygmomanometers, but all of them requires direct contact with the subject [Pere 15].

To perform this analysis, the heartbeat information has to be measured simultaneously at different locations. Thus, this study is carried out using a radar network which is composed by three 134 GHz radar nodes, that are synchronized using an external clock. The ECG acquired using the Task Force Monitor is used as reference.

The PTT measures from the radar and the TFM are calculated following the signal processing flow presented in Fig. 3.25. The PTTs from the radar signals are obtained as the difference between the R-peak from the ECG and the first maxima of the acceleration signal of each pulse, which was shown that was related with the heart sound S1.

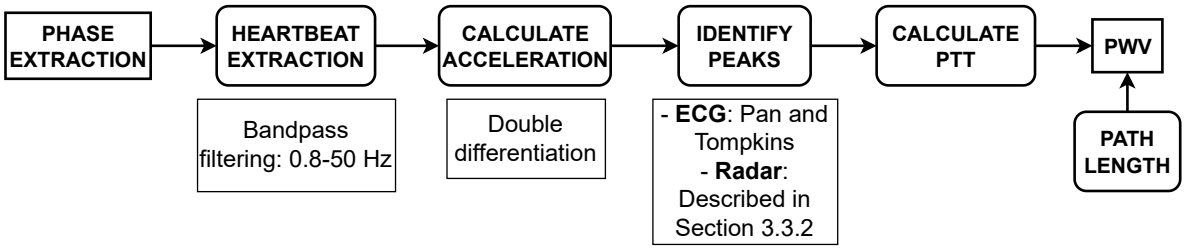

Figure 3.25: Signal processing flow followed to obtain the PWV measurement with the radar.

The IBI extraction is carried out following the same procedure described in the HRV analysis. The identification of these points are exemplified in Fig. 3.26, where it is noticeable the delay in the maxima of each signal with respect to the R-peak. This is due to the path that each heartbeat travels from the heart through the arteries. Once the ECG and the radar points are identified, the PTT is calculated as the time difference between them.

It is important to highlight that a double differentiation is a noisy process, thus, the noise present is magnified, as stated in Section 2.3. Despite that, extracting the time intervals in this signals yields better results than using the heartbeat waveform, as concluded in Section 3.3.2.

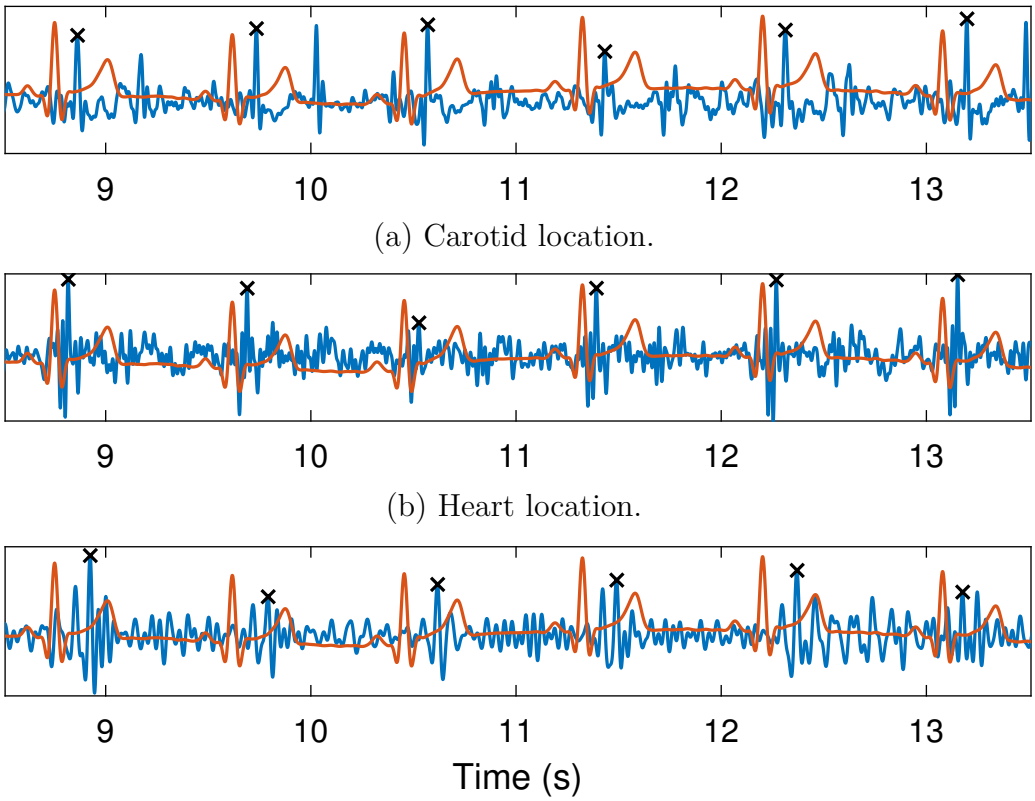

(a) Carotid location.

(b) Heart location.

(c) Femoral location.

Figure 3.26: Temporal instants obtained from the acceleration signals acquired with the radar (after double differentiation) compared with the ECG reference.

The radar setup used is displayed in Fig. 3.27. The three radars are focused on the region of interest (carotid, heart or femoral) at a distance of 0.3 m. The person-under-test is a healthy 27 years male, which has been monitored four times in intervals of 60 s.

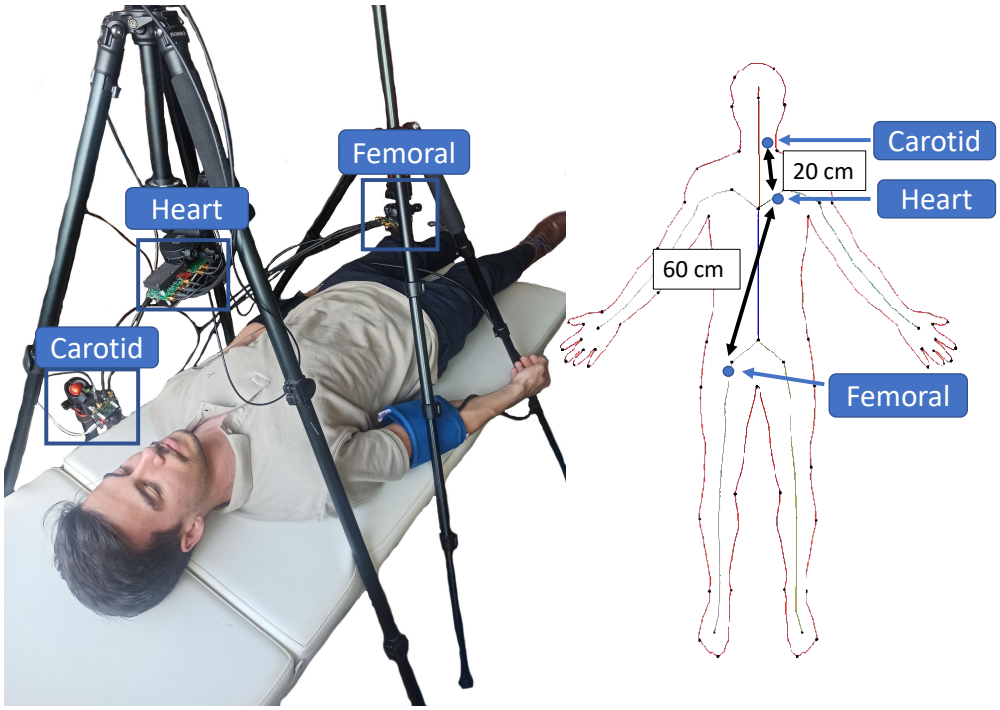

Figure 3.27: Experimental radar setup. Body diagram with the radar focusing regions and the estimated path distance between the different measuring points. The distances have been measured using a tape measure on the surface of the body.

The PTTs obtained are displayed in Fig. 3.28. This figure shows that the PTT measurements are consistent for each location, thus, it proves that the pulse delay can be calculated using radar techniques. It also shows how the delay is greater in the locations that are further from the heart location, as was expected. With these data it is possible to calculate the PWV, estimating the pulse travel path, as indicated in Fig. 3.27.

Thus, knowing the delay between the heartbeat measured in the carotid, the one measured in the femoral, and the distance between these two points, the carotid-femoral PWT (cfPWV) is calculated and represented in Fig. 3.29. The cfPWV has a mean value of 6.75 m/s and a standard deviation of 1.07 m/s which is within the margins defined in the literature for a healthy male which is under 30 years old [Refe 10]. It is important to clarify that these measurements are based on a gross estimation of blood vessel length, so further analysis is required with medical experts.

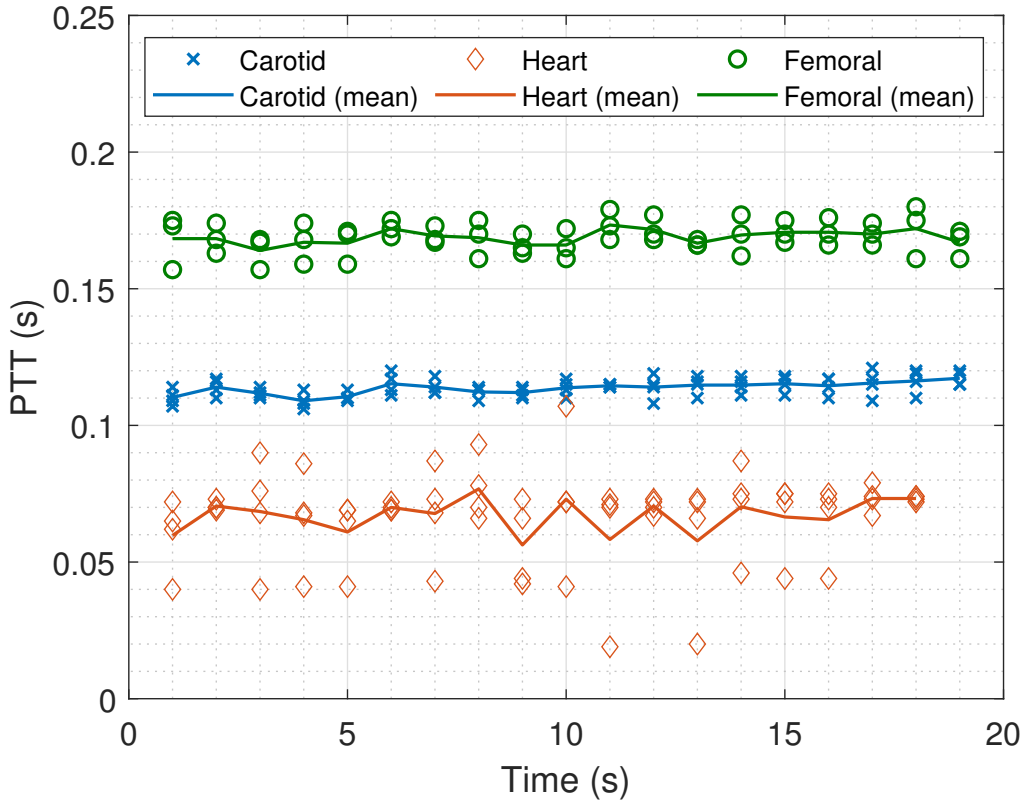

Figure 3.28: PTT measurements calculated for each location: carotid -in blue-, heart -in red- and femoral -in green-. Solid lines represent the mean of the four measurements carried out.

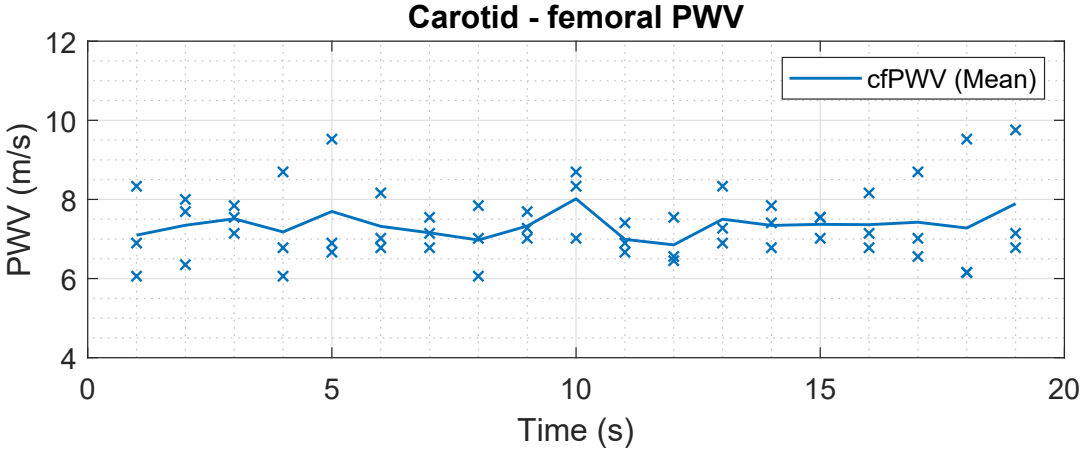

Figure 3.29: Results of cfPWV measurement obtained with the radar setup measuring an under 30 years old healthy male, with a mean of 6.75 m/s and a standard deviation of 1.06 m/s.

3.4 Impact of Breathing Activity on Cardiac Activity Extraction

Traditionally, breathing and heart activities are monitored by focusing on the radar to the target's chest. However, this chapter has showed that there is a clear interaction between these two activities. It is evident that the higher interaction between them is going to take place in the chest region, since the displacement of the rib cage is caused by breathing and heart activities. Nevertheless, this does not imply that the respiratory signal cannot be measured in other locations. However, the displacement resulting from breathing activity is more pronounced in the chest region, and this activity is recorded with greater intensity in this area. Consequently, some authors propose that more accurate heart rate monitoring can be achieved when measuring from the back, as the interference from respiration is reduced [Wang 13a, Vinc 13, Herz 22].

This section presents an analysis of the impact of respiration on the extraction of cardiac information from different body locations. To this end, two experiments have been conducted. Firstly, an experiment is carried out where six different targets (three males and three females) are simultaneously monitored from the chest and the back. On the other hand, other body locations are also explored. For that reason, a second experiment is conducted where the carotid, chest, and wrist of a single target are simultaneously analyzed.

3.4.1 Chest and back location analysis

The objective of this experiment is to determine which is the best location to monitor the heart activity, since, as previously stated, some researchers have indicated that measuring heart rate from the back may yield better results due to reduced breathing interaction.

In this experiment, six different targets are simultaneously measured from the front and the back. The target is positioned in a stool, and the radars are placed between 0.5 and 1 m from the PUT. The errors between the HR sequence extracted with the radar and the ECG are listed in Table 3.1.

Table 3.1: Heart rate errors obtained from the front and back locations.

	Chest		Back	
Gender	$MAE_{\{HR\}}$ (bpm)	$AE_{\{\overline{HR}\}}$ (bpm)	$MAE_{\{HR\}}$ (bpm)	$AE_{\{\overline{HR}\}}$ (bpm)
M	1.74	0.46	4.20	1.72
F	5.61	1.84	8.72	2.72
F	4.84	1.20	3.47	0.84
M	1.41	0.03	4.12	1.09
F	10.83	0.43	5.08	1.80
M	0.42	0.11	4.99	2.44

The results demonstrate that, in general, extracting the heart rate from the chest region

provides more accurate results. However, the heart rate extraction in females exhibits greater variability in the chest region compared to male subjects. By analyzing the radar performance for each gender separately, the results presented in Table 3.2 were obtained.

In conclusion, these results do not suggest that measuring from the back provides better results than measuring from the chest. However, greater errors in the heart rate extraction are obtained with female subjects. These discrepancies in accuracy can be attributed to variations in thoracic morphology. The thoracic region of men is comparatively flat, which facilitates the return of the displacement echo to the radar. Conversely, in women, this echo is more prone to scattering, particularly when measurements are conducted with a narrow beamwidth, as is the case with measurements conducted with dielectric lens.

Table 3.2: Heart rate errors obtained from the front and back locations: gender analysis.

	Chest		Back	
Gender	$MAE_{\{HR\}}$ (bpm)	$AE_{\{\overline{HR}\}}$ (bpm)	$MAE_{\{HR\}}$ (bpm)	$AE_{\{\overline{HR}\}}$ (bpm)
M	1,19	0,20	4,44	1,75
F	7,09	1,16	5,76	1,79

3.4.2 Carotid, chest, and wrist location analysis

The objective of this experiment is to analyze the extraction of heart rate exploring different body locations, with a particular focus on the potential benefits of utilizing higher-order heartbeat harmonics. This is due to the fact that at these frequencies, the influence of respiration is significantly reduced. For that purpose, a 3-node radar network, like the one presented in the PWV analysis, has been used. In this case, the carotid, the chest and the wrist locations have been monitored simultaneously.

Measurements were conducted on ten healthy PUT whose information is detailed in Table 3.3. The group consisted of eight males and two females participants, aged between 22 and 32 years (age: 25.3 ± 3.5 years) with different body mass indexes (BMI: 23.5 ± 3.4). During the measurements, all subjects were fully clothed and lying in a supine position, with the radars positioned at distances ranging between 0.3 and 0.5 meters from each location.

Regarding the analysis of the different locations, the spectrograms of the radar displacement at each location are presented in Fig. 3.30. The spectrogram of each location is adjusted to represent a 30 dB power range from the power of the first respiration harmonic. The frequency component related to respiratory activity is clearly visible at each location, with greater power observed in the chest displacement signal. It is worth noting that in some cases, there is an observable interaction between breathing and heart activity in the chest. This is represented by the signal with frequency $f_B + f_H$. The interaction is absent in both carotid and wrist measurements. Typically, this component is very close to the fundamental heartbeat harmonic, since the frequency of respiration is relatively low in comparison. This proximity can lead to distortion of the signal obtained by filtering in the heartbeat band.

Table 3.3: Overview of all subjects under test.

PUT	Age	Sex	Height (cm)	Weight (kg)	BMI	Duration (s)
1	22	M	178	78	24.6	780
2	22	F	153	53	22.6	780
3	22	M	172	90	30.4	780
4	28	M	177	65	20.7	780
5	22	M	173	61	20.4	360
6	25	M	181	87	26.6	780
7	26	M	182	62	18.7	660
8	32	M	176	75	24.2	660
9	29	F	165	68	25	660
10	25	M	182	72	21.7	660

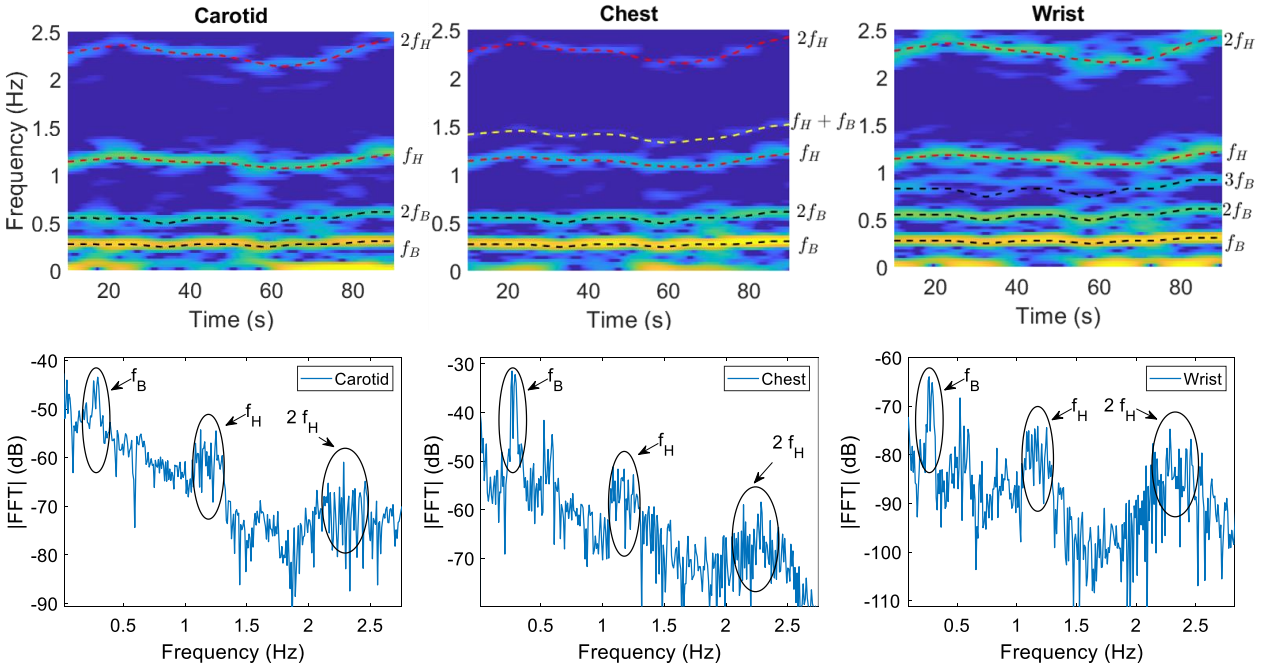

Figure 3.30: Spectrograms and spectra of the radar displacement signal for each location, where the main frequency components are identified.

Analyzing these signals in the respiratory frequency range, from 0.05 to 0.8 Hz, the results presented in Fig. 3.31 are obtained. Despite these signals are generated by the same phenomenon, the expansion and contraction of the chest due to the lung motion, the resulting waveforms differ in shape, but the frequency content coincides. These differences in shape are most clearly visible at the wrist location, since the movement associated to the respiration activity is transferred to the wrist by the movement of the shoulders, and not directly by the movement of the rib cage. This suggests that the separation of these signals is more

challenging in the chest region, given that the heartbeat is more susceptible to being masked by the respiratory activity.

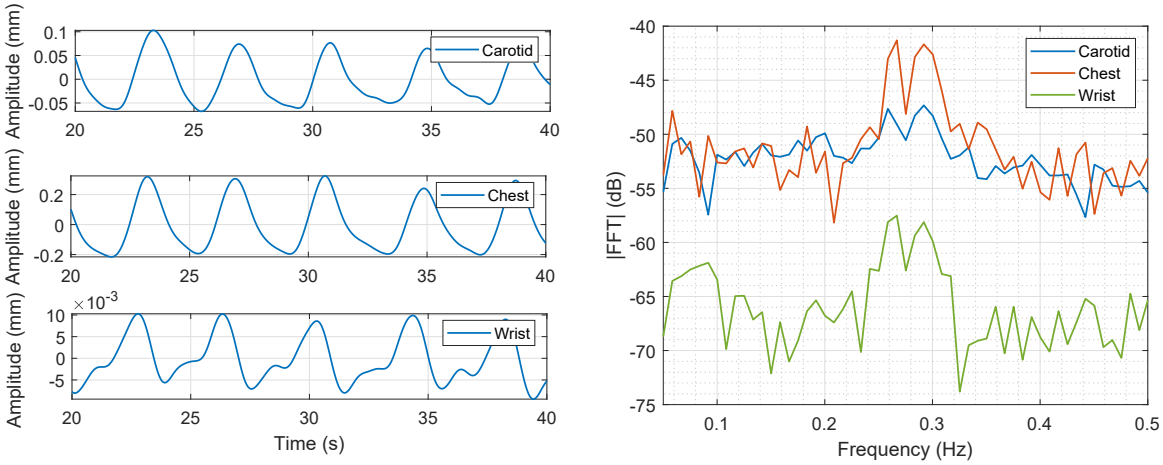

Figure 3.31: Radar displacement associated to the respiration activity for each location (carotid, chest and wrist). From left to right: radar displacement waveform, and spectrum of each radar signal.

When analyzing the heartbeat waveform extracted using linear filtering, it is observed that the heartbeat waveform extracted at the chest location is more modulated due to respiration compared to the carotid and wrist locations, as shown in Fig. 3.32. This modulation of the heartbeat signal affects its morphology, complicating the extraction of derived parameters such as HRV with maximum precision. Additionally, it is evident that the heartbeat strength is higher at the chest location.

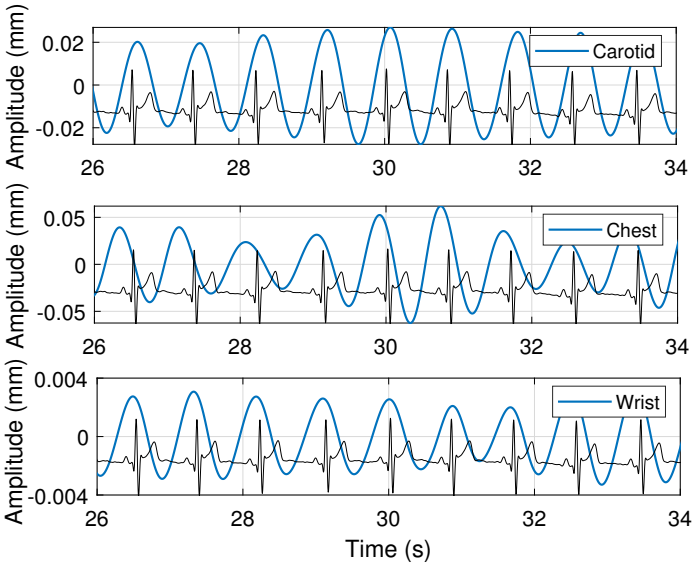

Figure 3.32: Radar displacement associated to the heart activity for each location (carotid, chest and wrist), using linear filtering.

Furthermore, upon revisiting Figs. **??** and 3.30, it becomes apparent that the SNR of the heart harmonics is higher at different locations compared to the chest. Thus, it is interesting to understand if the heart information extraction could be improved analyzing these harmonic frequencies. The resulting waveforms are displayed in Fig. 3.33. The heartbeat modulation due to the breathing activity is still visible at the chest, but it is negligible at the wrist. The results of extracting the heart rate and the HRV from the second harmonic are displayed in Table 3.4. The metrics used to analyze the heart extraction accuracy are defined in Appendix F.2. These metrics quantify the mean absolute error of the dynamic HR ($\text{MAE}_{\{\text{HR}\}}$), the mean absolute error of the HRV ($\text{MAE}_{\{\text{HRV}\}}$), and the absolute error of the mean HR ($\text{AE}_{\{\overline{\text{HR}}\}}$)[7].

Table 3.4: Heartbeat analysis performance comparing first and second harmonic information.

Focusing region	**$\text{MAE}_{\{\text{HR}\}}$ (bpm)**		**$\text{MAE}_{\{\text{HRV}\}}$ (ms)**	
	1^{st} harmonic	2^{nd} harmonic	1^{st} harmonic	2^{nd} harmonic
Carotid	3,63	3,22	5,22	5,26
Chest	4,21	7,80	6,11	11,36
Wrist	3,10	2,82	4,45	4,25

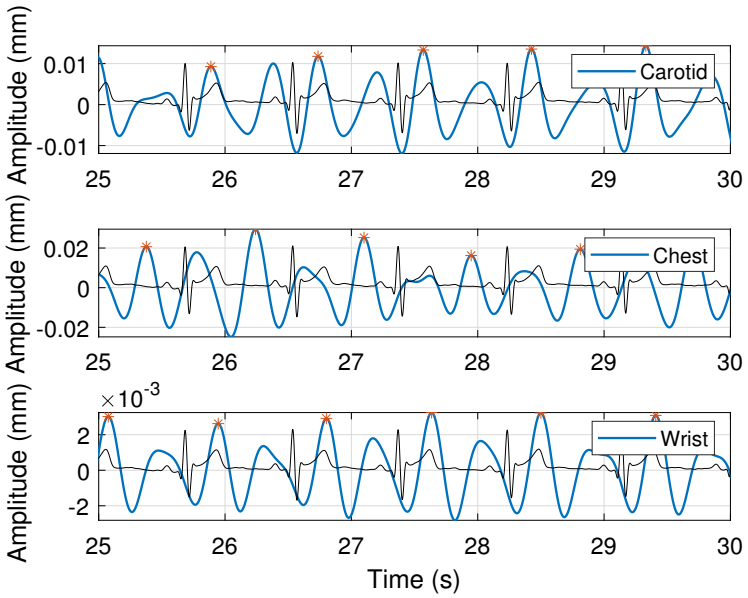

Figure 3.33: Radar displacement associated to the second heart harmonic for each location (carotid, chest and wrist), using linear filtering.

There is an improvement in the results when analyzing the second harmonic instead of the first one, as the impact of breathing is less significant. However, worse results are obtained at the chest location. This is because in some subjects, the second harmonic is not visible in the chest with a sufficient level of SNR, with only the first and third harmonics being visible.

[7]The mean HR is measured from the FFT, thus, loosing the time information.

Fig. 3.34 exemplifies this fact. If the third harmonic is analyzed for the chest location instead of the second one, the $\text{MAE}_{\{\text{HR}\}}$ is reduced from 7.80 bpm to 4.92 bpm.

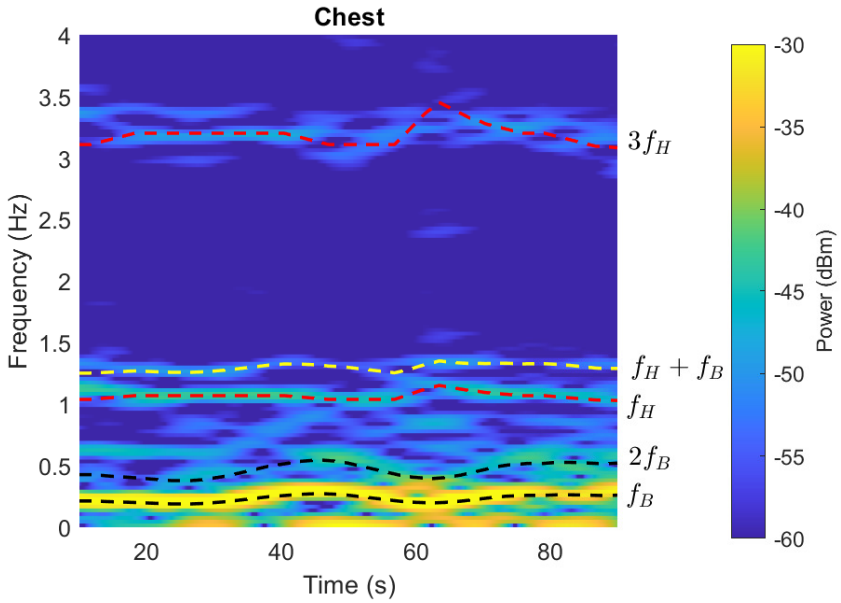

Figure 3.34: Spectrogram of the radar displacement signal at chest location.

In conclusion, the analysis of higher-order harmonics of the heart represents an interesting approach to reduce the impact of breathing activity on the heartbeat waveform, when compared with the traditional approach of analyzing the fundamental heartbeat frequency. Indeed, more accurate cardiac monitoring can be achieved by measuring the second harmonic when the radar is focused on the wrist. The main issue with this approach lies in the variability of the waveforms, as they depend on the measurement position, age, sex and constitution. These shape differences also lead to differences in the contribution of the harmonics. For example, in the case of the wrist, the first and second harmonics have a similar power level. Conversely, in the case of the chest, the power reduction of the second harmonic is more significant, as can be appreciated in Fig. 3.30. Additionally, these harmonics have reduced power levels as the order increases, making them more sensitive to noise.

3.5 Analysis of Cardiac Data Extraction: Optimal Location and Methods

The previous section has demonstrated that the most accurate cardiac monitoring is achieved when using the second harmonic focusing on the wrist. However, this analysis is limited to the heartbeat waveform. This section presents an analysis of the HR and HRV extraction, exploring the use of vital signs other than the heartbeat waveform. The HR and HRV sequences have been calculated from the heartbeat waveform, heart sounds, and skin acceleration. Moreover, these signals have been extracted using time-domain and time-frequency domain techniques: linear

filtering and wavelet transform, described in Section 2.4.1.2 and Section 2.4.3.2, respectively. In this analysis, the dataset presented in Section 3.4.2 is analyzed.

The IBIs are calculated following the procedure described in Section 3.3.2. However, so as to reduce the shape variability in the heartbeat waveform, a more restrictive filtering step is carried out. The heartbeat waveform is filtered in the frequency range of $[0.9f_{Hmin}$ $1.1f_{Hmax}]$ using a 4th-order Butterworth filter, the minimum and maximum heart rate (f_H) is estimated from the spectrogram. The heart rate extraction from the spectrogram is displayed in Fig. 3.35. An example of the time instants identified to calculate the IBIs and the extracted HR is displayed in Figs. 3.36 and 3.37, respectively.

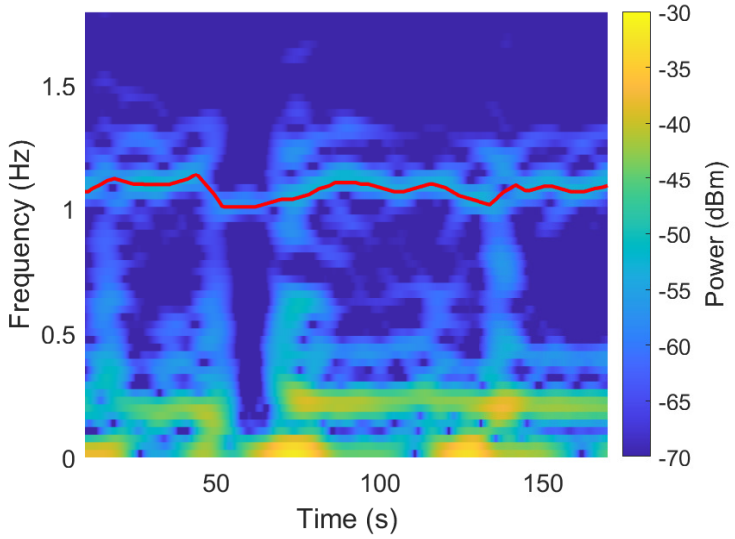

Figure 3.35: Heart rate extraction from the radar displacement signal (in red).

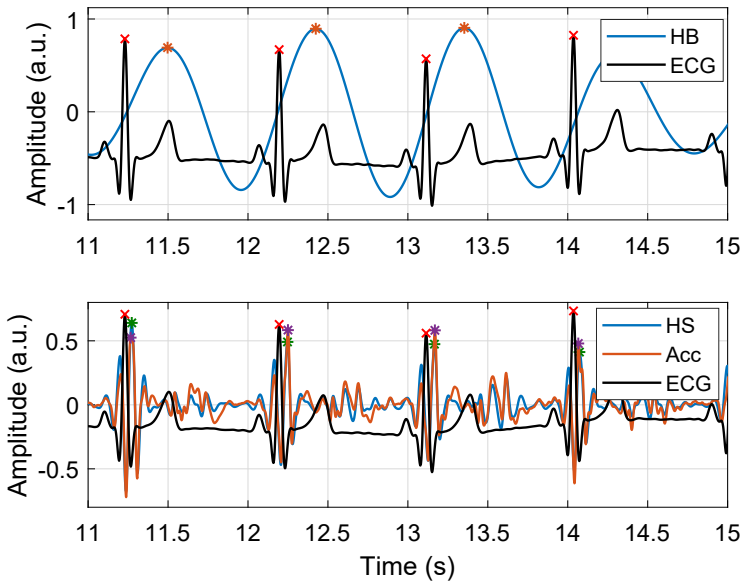

Figure 3.36: Time interval identification for HR and HRV extraction from the heartbeat, heart sounds and skin acceleration signals, focused on the chest location.

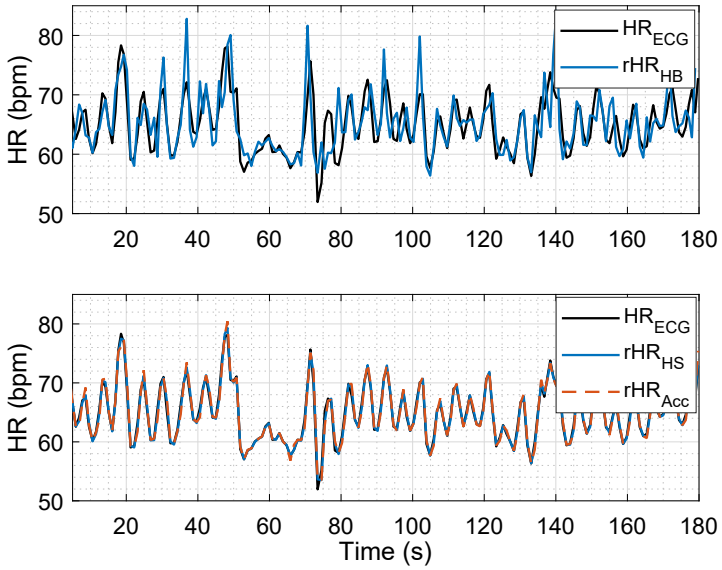

Figure 3.37: HR extraction from the heartbeat, heart sounds and skin acceleration signals, focused on the chest location.

Fig. 3.37 shows the variability of the HR throughout the measurement. This variation is primarily attributed to the respiration, the aforementioned RSA phenomenon, as can be seen in Fig. 3.38, where the breathing signal is superimposed to the HR. Additionally, the measurement captures instances where the PUT holds his breath, between the 50 and 70 seconds period, leading to reduced HR variation. However, the respiration is not the only factor which modulates the heart rate, as was explained in Section 3.3.2, the interaction between the sympathetic and parasympathetic nervous system can also influence the HR. Fig. 3.39 shows another example of the HR extraction, where the HR is not only modulated by the breathing, as can be appreciated between seconds 15 and 25, as well as between 35 and 40.

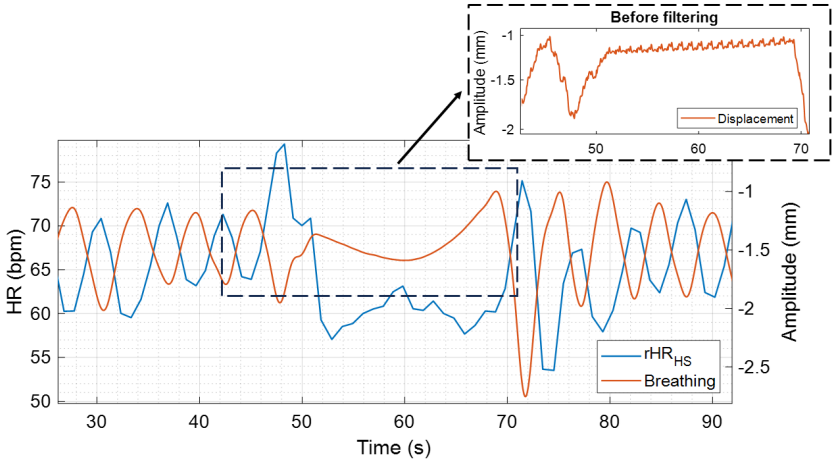

Figure 3.38: HR extraction from the heart sounds signal compared with the breathing waveform, showing the RSA phenomenon, focused on the chest location.

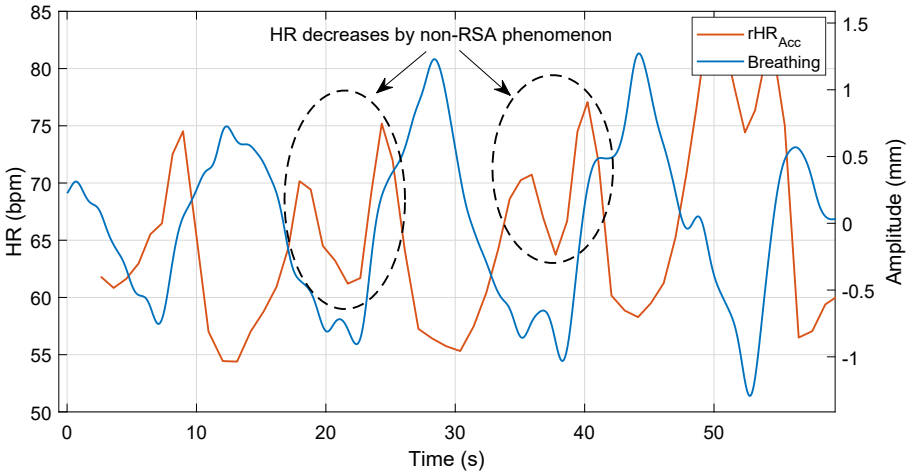

Figure 3.39: HR extraction from the heart sounds signal compared with the breathing waveform, showing that the HR is not only affected by the RSA phenomenon, focused on the chest location.

Results for each technique and location are summarized in Tables 3.5 and 3.6. These results are grouped by focusing region and processing technique used to extract the HR and HRV sequences. Table 3.5 shows the time-domain analysis of the heart activity focused on the carotid, chest and wrist. On the other hand, Table 3.6 shows the frequency-time-domain analysis of the heart activity using the optimal wavelet for each location. The analysis of the optimal wavelet for each location is carried out in Appendix G.

These results allow us to draw some conclusions:

- The mean HR can be extracted from the three locations analyzed with good agreement (>99% choosing the best waveform for each location).
- These results evidence the distortion that the heartbeat waveform suffers in the chest location due to the breathing activity. The worst results are observed at the wrist location, which are attributed to the attenuation of the heartbeat signal and the inherent challenges associated with radar focusing on this area.
- The results demonstrate that the optimal monitoring of cardiac activity is achieved by focusing on the chest region and extracting the heart sounds using the wavelet $fk4$. Indeed, the lowest errors are achieved using heart sounds or the acceleration signal, in both linear filtering and wavelets, as these signals are less susceptible to the effects of breathing coupling, which is coherent with the conclusions of Section 3.3.2. The impact of breathing harmonics is lower in the heart sounds band, and the double differentiation process used to extract the acceleration also attenuates these low-frequency components.
- Errors are slightly higher when focusing on the carotid than in the chest. This is due to the fact that the automatic identification of S1 at the carotid may prove challenging, as it is not always the loudest heart sound in each pulse, as stated in Section 3.2.3.

Table 3.5: Heartbeat analysis performance using linear filtering.

Waveform	**Focusing region**	**MAE$_{\{\text{HR}\}}$ (bpm)**	**MAE$_{\{\text{HRV}\}}$ (bpm)**	**AE$_{\{\overline{\text{HR}}\}}$ (bpm)**	**Relative MAE$_{\{\text{HR}\}}$ (%)**	**Relative AE$_{\{\overline{\text{HR}}\}}$ (%)**
Heartbeat	Carotid	3.63	5.22	0.79	5.35	1.17
Heart sounds	Carotid	**1.26**	1.91	0.27	1.85	0.38
Acceleration	Carotid	**1.33**	2.00	0.40	1.97	0.56
Heartbeat	Chest	4.21*	6.11	1.45	6.82	1.93
Heart sounds	Chest	**1.28**	2.01	0.53	1.92	0.72
Acceleration	Chest	**1.09**	1.74	0.32	1.65	0.43
Heartbeat	Wrist	3.10	4.45	0.70	4.44	0.99
Heart sounds	Wrist	6.67	8.77	2.86	9.42	3.83
Acceleration	Wrist	8.16	10.10	3.82	11.65	5.11

*The chest location for the heartbeat waveform demonstrates a greater degree of error due to the influence of respiration.

Table 3.6: Heartbeat analysis performance using wavelet decomposition.

Waveform	**Focusing region**	**Optimal wavelet**	**MAE$_{\{\text{HR}\}}$ (bpm)**	**MAE$_{\{\text{HRV}\}}$ (bpm)**	**AE$_{\{\overline{\text{HR}}\}}$ (bpm)**	**Relative MAE$_{\{\text{HR}\}}$ (%)**	**Relative AE$_{\{\overline{\text{HR}}\}}$ (%)**
Heartbeat	Carotid	fk8	3.41	5.13	1.10	4.99	1.62
Heart sounds	Carotid	haar/db1	2.44	3.64	0.75	3.62	1.10
Acceleration	Carotid	mb8.4	1.68	2.47	0.56	2.45	0.81
Heartbeat	Chest	haar/db1	5.76*	10.03	2.23	8.33	3.13
Heart sounds	Chest	fk4	**0.86**	1.63	0.21	1.28	0.30
Acceleration	Chest	mb8.4	**1.25**	1.83	0.44	1.78	0.63
Heartbeat	Wrist	coif1	3.52	5.53	0.96	5.13	1.43
Heart sounds	Wrist	mb8.3	5.89	7.49	2.52	8.37	3.52
Acceleration	Wrist	db2/sym2	8.79	10.73	4.00	12.47	4.81

*The chest location for the heartbeat waveform demonstrates a greater degree of error due to the influence of respiration.

A comparison of the accuracy in extracting IBI between the chest wall acceleration signal subjected to linear filtering and heart sounds extracted using the fk4 wavelet, both referenced against ECG, is illustrated in Figs. 3.40 and 3.41, respectively. The Bland-Altman method, which is presented in Appendix F.3, is employed to assess the agreement between the two aforementioned measurement techniques. In both cases, the Pearson's r^2-value exceeds 0.9. The Bland-Altman plots also show that there is a high degree of concordance between the ECG and radar data, with errors below 10% observed in over 95% of the extracted IBIs. This aligns with the maximum acceptable error described in the ANSI/AAMI EC13 [Asso 02] standard for HR monitoring (±10% or ±5 bpm).

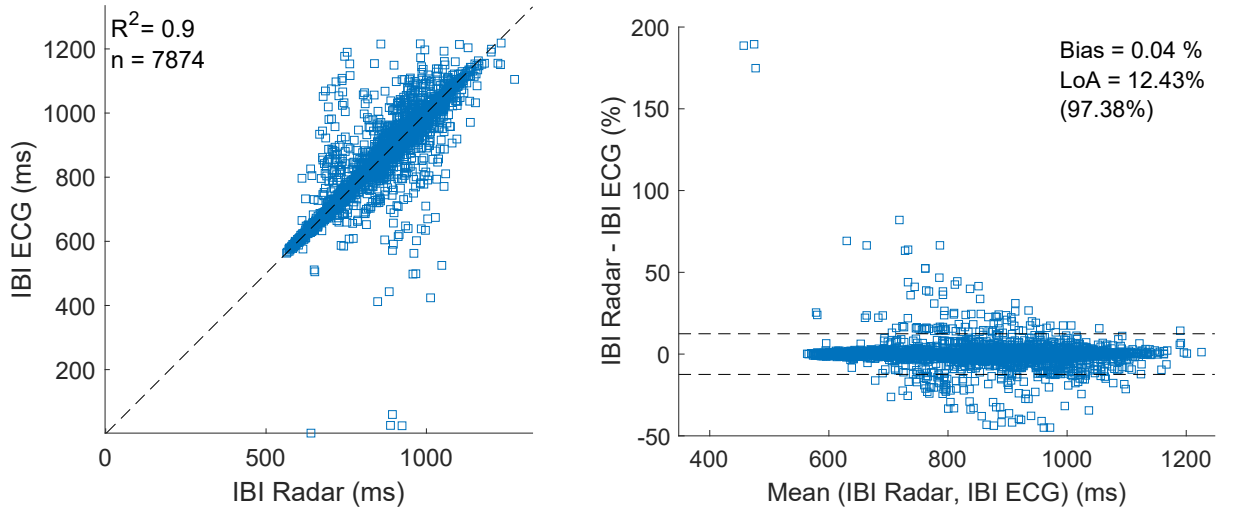

Figure 3.40: Correlation and Bland-Altman plots of the RR intervals measured using the chest wall acceleration.

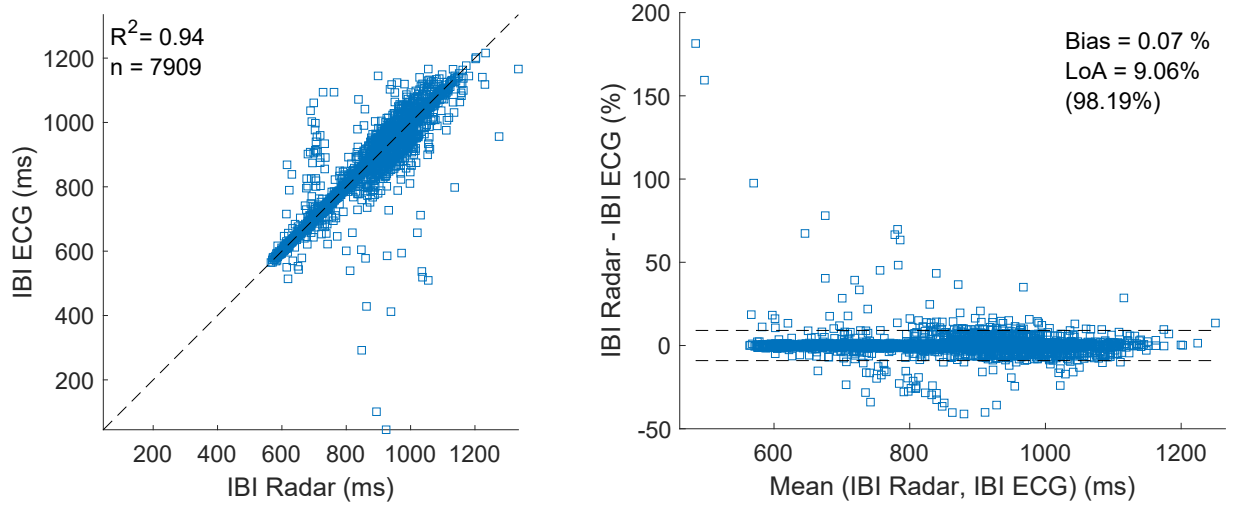

Figure 3.41: Correlation and Bland-Altman plots of the RR intervals measured using the heart sounds extracted using the fk4 wavelet focused on the chest.

The HRV sequences obtained have also been analyzed for each subject. The SDNN, RMSSD and pNN50 values are calculated analyzing each of the 60-seconds segments of each measurement. The mean values obtained for each subject with the radar and the ECG are listed in Table 3.7. It is important to highlight that ultra-short-term measurements (less than 5 min of data) are still being studied to prove its efficient use in clinical environments [Shaf 17]. Moreover, it is suggested that for healthy subjects 1 minute should be sufficient for estimating HR, SDNN or RMSSD as long as professionals carefully remove artifacts. On the other hand, the recording method used can also have a greater impact on ultra-short-term measurements than on longer recordings [Shaf 17].

In order to reduce the artifacts that can be presented in the HRV sequences extracted, the algorithm proposed in [Lipp 19] is applied. This algorithm is capable of identifying the abnormal beats (such as atrial and ventricular ectopic beats), correct missing and extra beats with good results. It is also important to note that the application of this algorithm is not optimal, since it requires 91 surrounding beats to reach the accuracy rates that presents in its research study.

Table 3.7 analyzes the HRV sequence extracted with the radar only at the carotid and chest locations, since these are the ones which present better results for the HRV extraction, as shown in Tables 3.5 and 3.6. Moreover, following the same criteria, only the HRV extracted from the heart sounds and skin acceleration signals is analyzed. The results presented in Table 3.7 show a strong correlation between HRV parameter extraction across the majority of PUT locations. However, it is important to note that this analysis was conducted on short-term and ultra-short-term measurements, which may be susceptible to artifacts such as missing beats and ectopic beats. These artifacts can be effectively removed by professionals to ensure the accuracy of the results.

Table 3.7: HRV sequence analysis for each PUT.

		SDNN (ms)			RMSSD (ms)			pNN50 (%)		
PUT		**HS**	**ACC**	**ECG**	**HS**	**ACC**	**ECG**	**HS**	**ACC**	**ECG**
1	Carotid	71,06	72,26	74,30	59,33	62,41	61,55	0,29	0,33	0,38
	Chest	73,63	73,75	74,30	59,84	60,26	61,55	0,37	0,37	0,38
2	Carotid	44,77	45,14	45,53	38,07	38,52	39,5	0,19	0,20	0,21
	Chest	59,14	69,56	45,53	67,07	81,93	39,50	0,45	0,44	0,21
3	Carotid	41,56	42,20	43,11	31,75	30,05	37,01	0,10	0,09	0,18
	Chest	42,40	42,46	43,11	33,48	33,76	37,01	0,14	0,15	0,18
4	Carotid	57,04	57,97	59,98	47,45	48,82	53,98	0,29	0,29	0,37
	Chest	60,87	62,51	59,98	54,62	57,93	53,98	0,39	0,41	0,37
5	Carotid	52,89	55,63	55,97	45,62	47,07	51,21	0,25	0,24	0,31
	Chest	55,35	54,60	55,97	50,19	49,29	51,21	0,30	0,29	0,31
6	Carotid	38,76	40,49	37,27	22,08	24,64	21,65	0,02	0,03	0,03
	Chest	43,07	41,98	37,27	29,59	31,72	21,65	0,07	0,07	0,03
7	Carotid	81,81	86,08	59,10	82,61	84,01	49,45	0,43	0,36	0,22
	Chest	57,64	59,22	59,10	46,97	49,93	49,45	0,21	0,22	0,22
8	Carotid	61,29	62,8	60,47	69,87	71,90	71,46	0,43	0,43	0,44
	Chest	58,94	60,45	60,47	64,19	66,05	71,46	0,40	0,41	0,44
9	Carotid[1]	-	-	-	-	-	-	-	-	-
	Chest	27,61	29,41	27,19	18,39	18,26	17,41	0,03	0,04	0,02
10	Carotid	64,74	70,96	62,31	48,39	59,23	46,37	0,24	0,26	0,26
	Chest	98,81	81,79	62,31	120,10	83,64	46,37	0,55	0,43	0,26

[1] The measurements taken for PUT 9 at the carotid location are not analyzed since they were not acquired properly due to a bad radar focusing.

In order to assess the radar's performance over longer periods, PUT number 4 has been monitored for one hour. The subject was positioned in a manner identical to that of the previous experiment, lying in a supine position with the radar directed towards his chest. The heart rate extracted with the radar using the 'fk4' wavelet transform its compared with the heart rate extracted with the reference ECG in Fig. 3.42. The $MAE_{\{HR\}}$ obtained is 0.83 bpm.

The HRV sequence extracted is also analyzed and the results are presented in Table 3.8, showing that the radar is capable of extracting results highly correlated with the reference ECG.

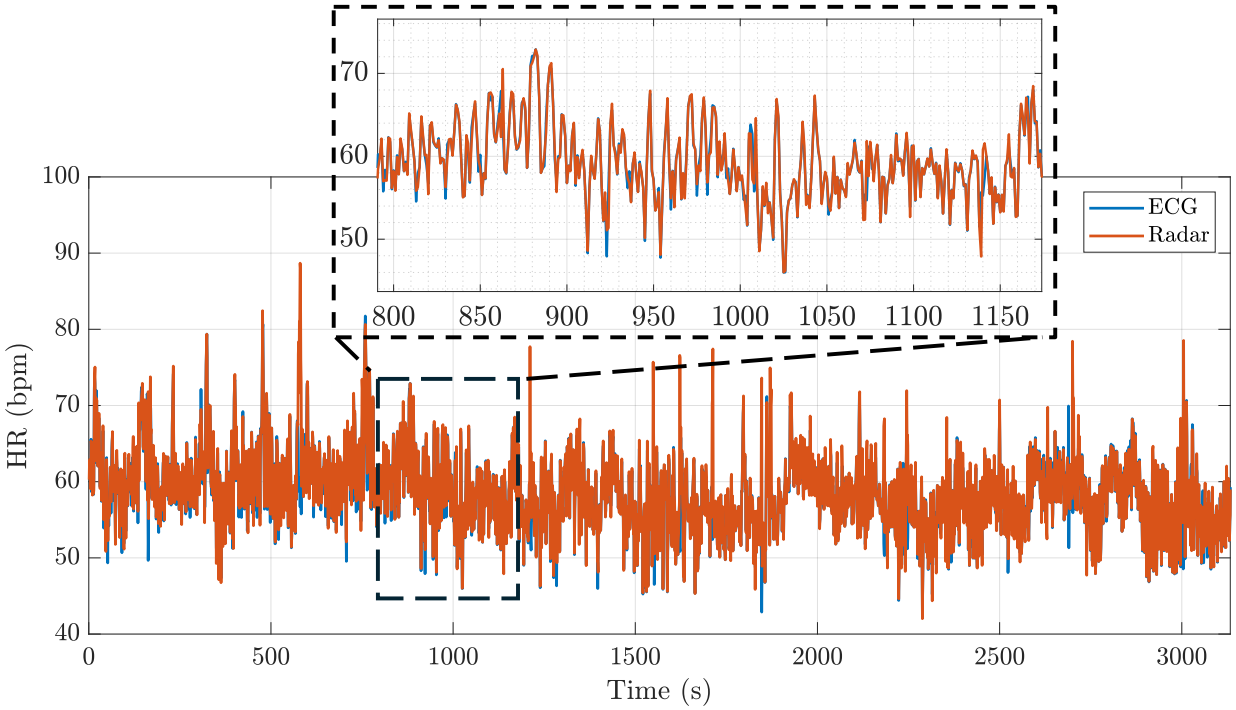

Figure 3.42: 1-hour HR monitoring measurement.

Table 3.8: 1-hour HRV sequence analysis for PUT number 4.

SDNN (ms)		RMSSD (ms)		pNN50 (%)	
Radar	**ECG**	**Radar**	**ECG**	**Radar**	**ECG**
87,86	84,24	72,64	66,44	0,44	0,41

Furthermore, the radar performance has been analyzed in a real-world scenario. For this experiment, a PUT was monitored for 40 minutes while working on a computer. The radar utilized is the AWR2243 Cascade, positioned at a distance of 0.75 meters from the target, as illustrated in Fig. 3.43, where other targets can be identified at 2 and 3 meters. This radar enables more precise target focusing, specially, when the target is not perpendicular to the radar. This will be discussed in further detail in Chapter 4, where the radar processing scheme followed will also be detailed. The extracted HR sequence is compared with an ECG in Fig. 3.44. The results obtained reveal that when the target is moving the HR extraction is more susceptible to errors (comparing with those obtained in the previous experiment, Fig. 3.42). However, a 4-s sliding window has been employed to reduce these outliers, demonstrating that the averaged dynamic HR extracted with the radar is consistent with the one measured with the ECG.

Indeed, an analysis of the $\text{MAE}_{\{\text{HR}\}}$ is presented in Fig. 3.45. The results indicate that approximately 60% of the time, the $\text{MAE}_{\{\text{HR}\}}$ is below 2 bpm, and 75% of the time, the error is below 6 bpm. Conversely, the $\text{MAE}_{\{\text{HR}\}}$ (after applying the 4-s sliding window) is below 2

bpm the 70% of the time, while a 95% of the time is below 6 bpm. Therefore, the radar is capable of accurately follow the averaged dynamic HR.

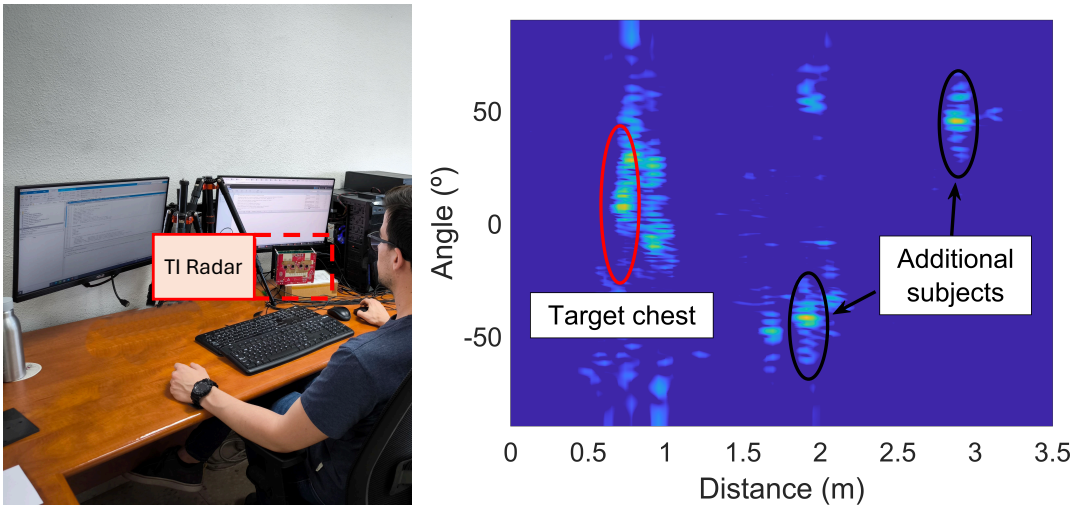

Figure 3.43: HR monitoring measurement in a real-world scenario. The radar is placed at 0.75 meters from the target.

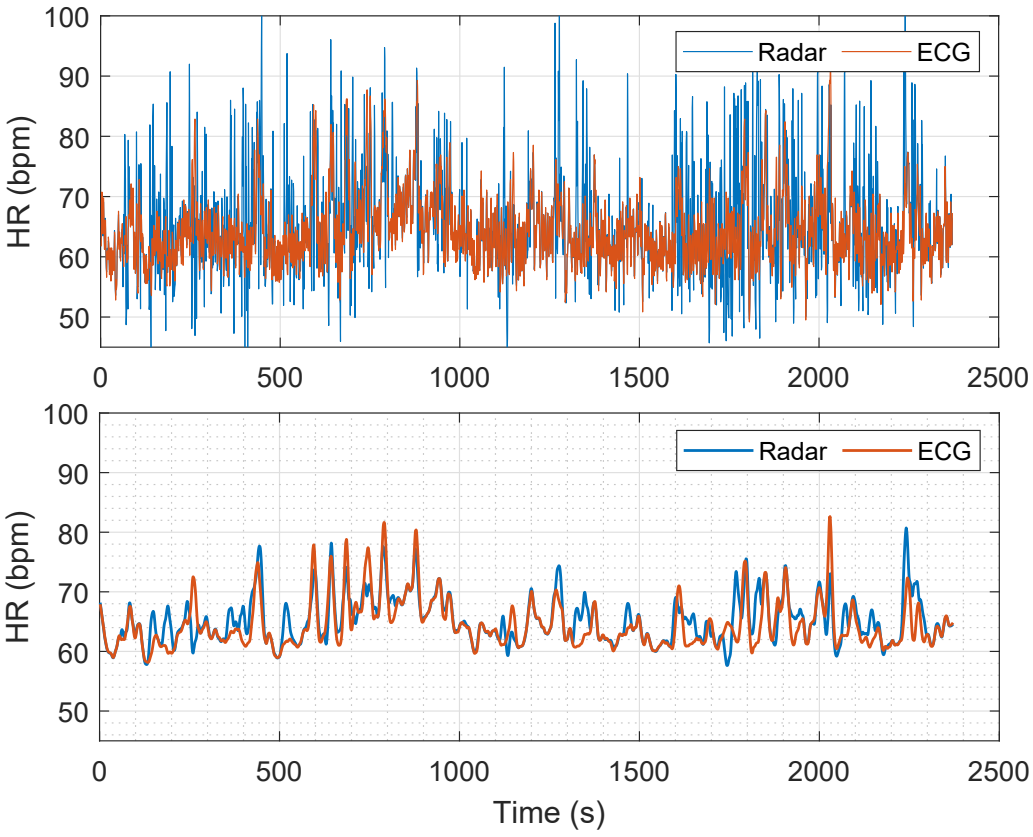

Figure 3.44: HR sequence extracted with the radar and the ECG. From top to bottom: the HR sequences extracted for each pulse, and the HR sequences averaged using a 4-s sliding window.

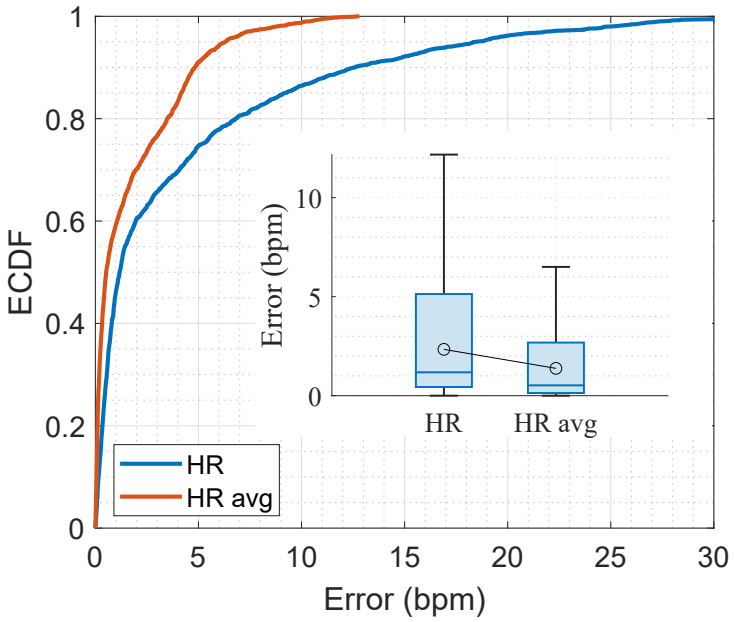

Figure 3.45: Comparison between the error distributions of the dynamic HR and the dynamic HR averaged (avg).

Chapter 4

Vital Sign Monitoring With Radar: Challenges

Despite the considerable advances made in radar technology in vital sign monitoring, there are still a number of challenges to be addressed if it is to be made practical for real-world applications [Sing 21, Isla 22a, Fior 23]. The majority of research is conducted in controlled scenarios where the target is carefully and accurately positioned facing the radar, at short distances, and at normal incidence. This research is usually limited to a single target and does not address multi-target scenarios. Additionally, the majority of solutions presented in the literature are performed offline and lack real-time implementation.

Thus, this chapter addresses some of these challenges currently facing the research field of vital sign signal monitoring using radar. The chapter is divided into the following sections:

- In Section 4.1, the simultaneous monitoring of multiple targets is described. This section presents the vital sign extraction using LFMCW single-input single-output (SISO)[1] radars and the advantages of using multiple-input multiple-output (MIMO) configurations in multi-target scenarios.
- Section 4.2 examines the robustness of the radar system with regard to the extraction of vital signs. It analyzes the scenarios in which the target is situated at different angles and distances. Furthermore, it presents the impact of the target movement on vital sign extraction.
- Finally, Section 4.3 presents a real-time implementation for multi-target monitoring. This application is capable of measuring simultaneously the breathing and heart activities of several targets. Moreover, it can detect apnea periods, representing a preliminary step towards OSA monitoring.

Unless otherwise indicated, all measurements presented in this section are conducted with the subject(s) seated on a stool facing the radar. In order to facilitate the understanding of the cardiac information extraction, we use the dynamic HR extraction instead of HRV; however, both parameters can be monitored accurately, given that both are calculated from the IBIs,

[1]For purposes of simplicity, the radar comprising a unique TX-RX pair is referred to as an SISO radar.

as presented in Chapter 3.

4.1 Multi-target Monitoring

Radar vital signal monitoring systems have showed promising results in controlled scenarios where the target is nearly static in the proximity of the radar sensor. However, in realistic scenarios, the system should be capable of addressing the presence of multiple targets in the same area.

The fundamental principle underlying the extraction of multiple vital signs is the localization and isolation of the target, followed by the detection of the heart and breathing activities for each subject. The target can be localized in a range domain or an angle-range domain:

- Range localization: The estimation of the target's range can be achieved by measuring the flight time of the radar signal as it travels from the radar device to the target and back. This can be accomplished using any radar, with the exception of CW radars, such as pulse-Doppler or FMCW radars.
- Angle localization: The estimation of the angle of arrival (AoA) is performed using an array antenna or a rotating radar. A common method for AoA estimation is through the use of multiple antennas combined with digital beamforming [Bech 16]. This method involves a digital combination of the receiving radar channels, which sum constructively at a specific direction. This increases the gain in that direction with respect to the rest of angles [Stey 88]. This allows for the separation of targets that are in the same range bin.

Consequently, beamforming is a signal processing technique based on the application of a phase shift to each receiving channel with the objective of steering the beam towards a specific angle. Consequently, these channels are multiplied by a steering vector, resulting in a single receive channel pointing to the desired angle. The steering vector for a uniform linear antenna array is calculated as [Vasa 20]:

$$\alpha_{steering}(k) = e^{-j2\pi kd/\lambda sin(\theta)}, \quad k \in [\,0,\, N-1] \tag{4.1}$$

where d stands for the constant separation between antennas, λ is the wavelength, θ represents the desired pointing direction, and N stands for the number of antennas.

Therefore, after applying the steering vector, the received signal pointing to the direction θ can be defined as:

$$x_{DBF}(\theta) = \sum_{k=0}^{N-1} r[k] e^{-j2\pi kd/\lambda sin(\theta)} \tag{4.2}$$

where $r[k]$ is the received signal at the k^{th} antenna. This equation is analogous to the definition of the DFT, which indicates that AoA estimation can be performed using a DFT when the antenna array is linearly equally spaced [Samm 11].

Thus, this section presents the structure of data captured by LFMCW radars with the objective of extracting both range and angle information, thereby enabling the localization

and separation of multiple targets. The working principle of LFMCW radars and the signal processing steps necessary to isolate the target in range were presented in Section 2.2.

Fig. 4.1 details how the range and angle information is obtained from the data acquired by the radar:

- Range information: The range-time spectrum is obtained by performing an FFT to the acquired data along the fast-time dimension. As previously described, the range resolution is determined by the transmitted bandwidth, which can be expressed as $\Delta R = c/2B$.
- Angle information: The angle-range spectrum is obtained by performing an FFT along the RX-channel dimension, if the antennas are equally spaced. The angle resolution is determined by the array size. The angle resolution can be enhanced through the use of MIMO radars [Broo 85], as larger virtual arrays can be obtained with the same number of antenna elements.

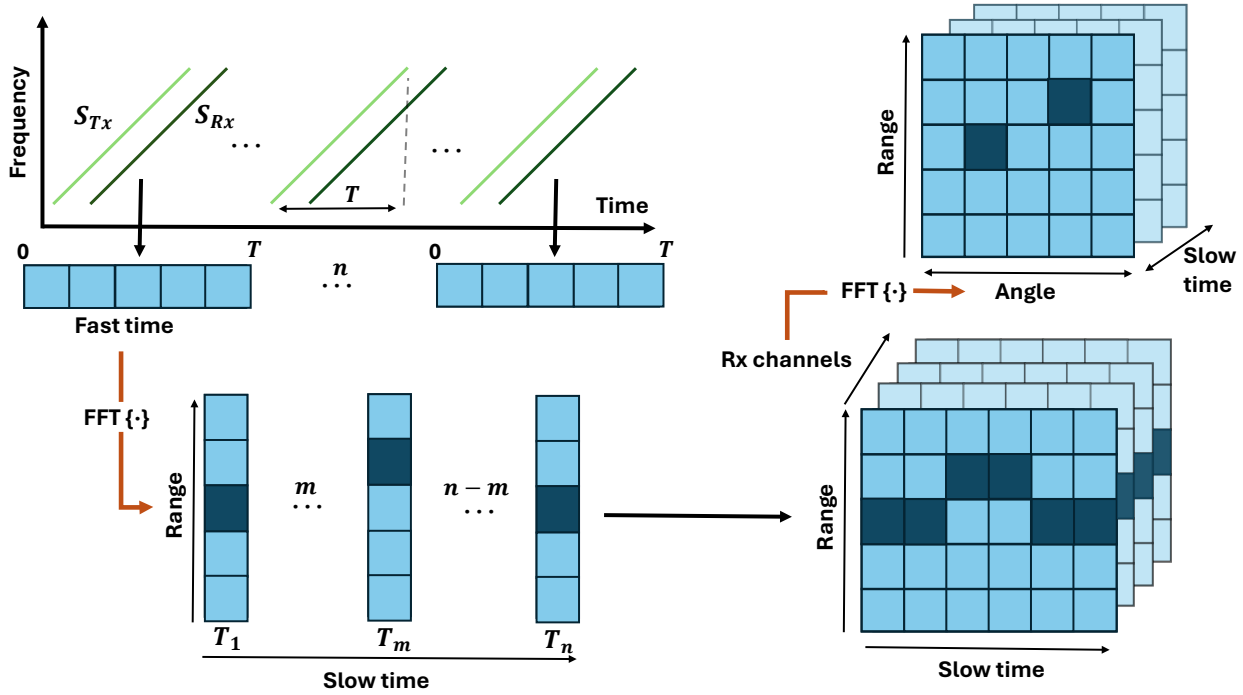

Figure 4.1: Flowchart with the data structure and information obtained with a multi-antenna LFMCW radar.

Consequently, LFMCW radars configured with a SISO architecture are capable of distinguishing between two targets in range if their separation is greater than the radar's range resolution. Nevertheless, a SIMO or MIMO configurations offer another degree of freedom because their improvement in cross-range resolution (angle resolution) compared to a SISO configuration.

4.1.1 Multi-target monitoring: LFMCW SISO radars

This section presents an experiment designed to show the LFMCW system's ability to measure the vital signs of multiple targets simultaneously. The experiment involves measuring two male subjects, aged 21 and 25 years, respectively, at distances of 1.2 and 1.6 meters from the radar setup (Fig. 4.2a). The radar used is the 134 GHz node from Silicon Radar, described in Section 2.1, and the signal processing flow used is described in Section 2.2.2 and Section 3.3.2.

Moreover, Fig. 4.2b shows that these two subjects can be clearly distinguished in range. Furthermore, the chest displacement waveforms captured and the dynamic heart rates computed for each subject are also displayed in Fig. 4.3.

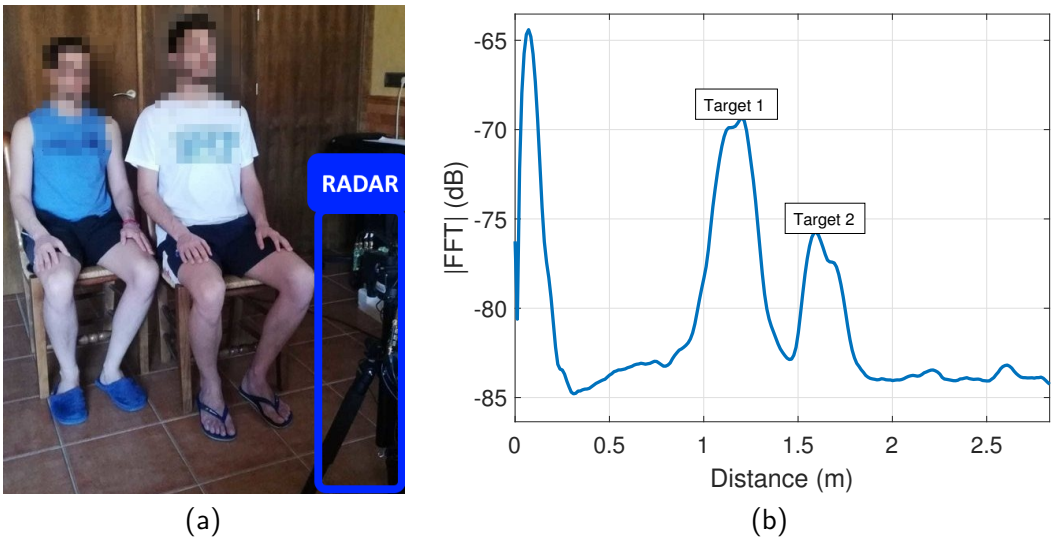

Figure 4.2: Multi-target scenario using a LFMCW SISO radar. (**a**) Photo of the radar setup. (**b**) Frequency spectrum of the captured radar signal, where the two targets are clearly separated at 1.2 and 1.6 m.

However, this configuration presents some limitations:

- It is necessary to utilize antennas with a wide beamwidth, as the targets must be located within the radar's FoV. Therefore, this implies a reduction in antenna gain due to the less directive nature of these antennas, which consequently affects the SNR.
- There is no AoA information.
- The process of radar focusing is notoriously challenging. In these scenarios, where the SNR is low, normal incidence to the targets is necessary to increase the radar cross section (RCS) and, consequently, the received power.

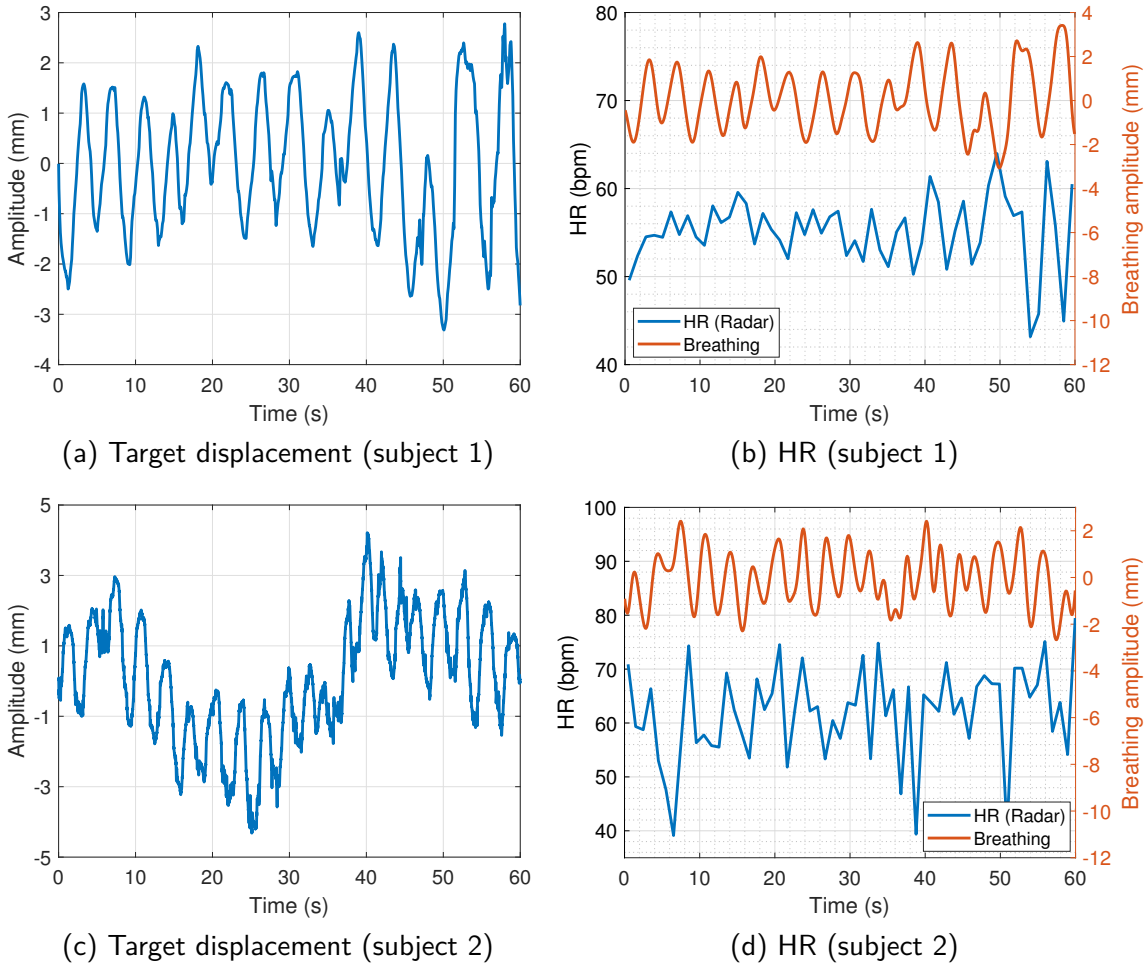

(a) Target displacement (subject 1)

(b) HR (subject 1)

(c) Target displacement (subject 2)

(d) HR (subject 2)

Figure 4.3: Vital signs extracted from the multi-target scenario using SISO radar. (**a**) Target displacement from subject 1. (**b**) Heart rate from the target located at 1.2 m. (**c**) Target displacement from subject 2. **(d)** Heart rate from the target located at 1.6 m.

4.1.2 Multi-target monitoring: LFMCW MIMO radars

This section describes the use of MIMO radars for target separation using angle and range information. The radars used in this section are the AWR2243BOOST and the AWR2243 Cascade from Texas Instruments, described in Section 2.1. The methodology employed to extract vital signs from multiple targets is illustrated in Fig. 4.4.

In this section, the localization of the target in the angle plane is achieved through the use of digital beamforming. As previously described, a steering vector is applied to the virtual channels in order to digitally steer the beam towards a specific angle. Digital beamforming offers a more flexible alternative to analog beamforming, as it is not subject to limitations regarding the number of directions that can be measured simultaneously.

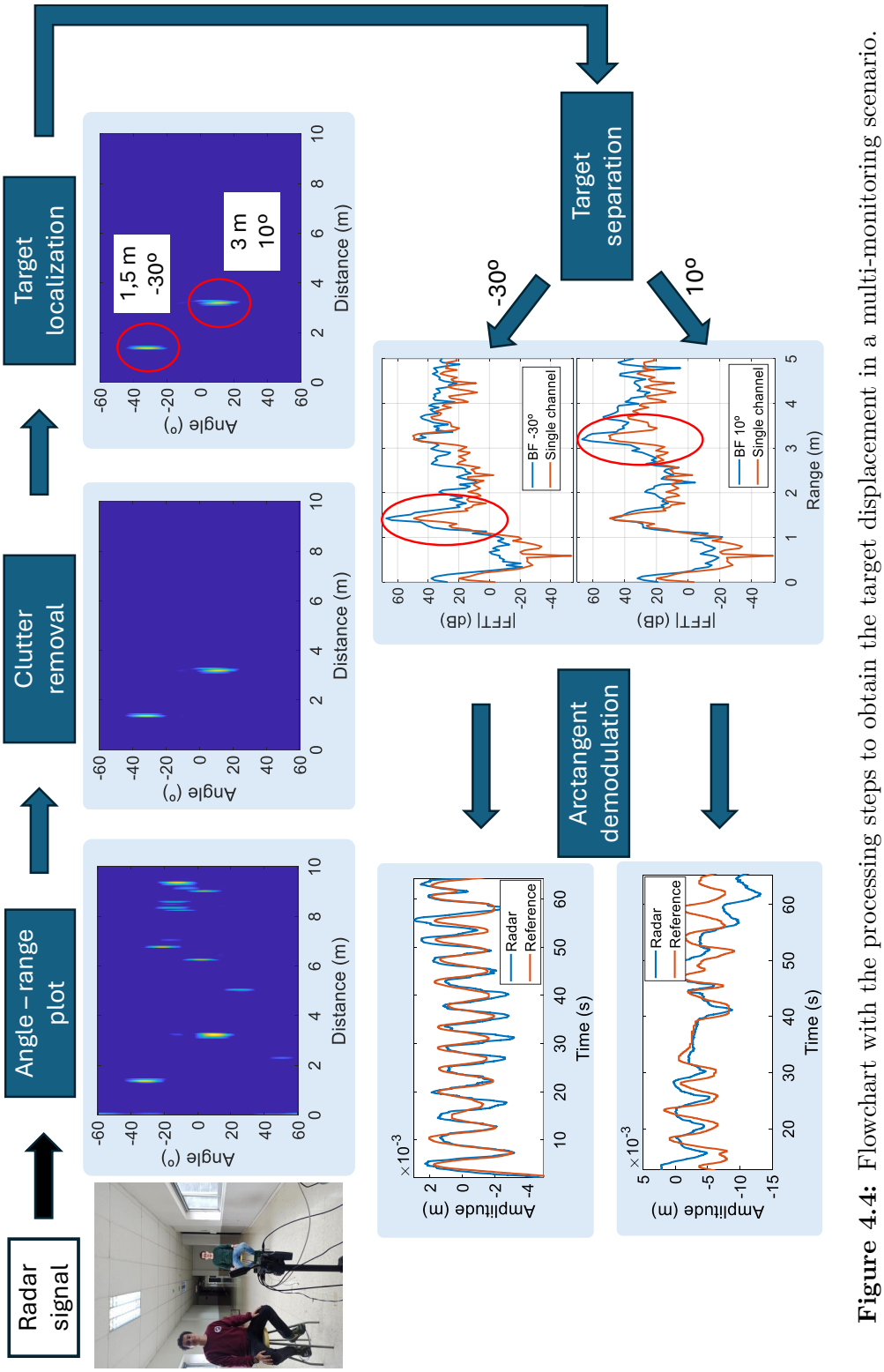

Figure 4.4: Flowchart with the processing steps to obtain the target displacement in a multi-monitoring scenario.

Therefore, the first step consists of performing a 2D-FFT in order to estimate the location of the targets in the angle-range domain. To enhance the target localization process, a static clutter removal step is conducted, which involves the utilization of a filter in the Doppler dimension. An FFT in slow time is then performed, wherein the targets exhibiting no Doppler velocity are filtered out [Ehrn 21]. Once the angle and range of each target have been identified, the displacement caused by heart and breathing activity is extracted in accordance with the procedure outlined in Section 2.2.2.

The following example illustrates how beam steering, in this case digital beam steering, enhances target displacement extraction in multi-target scenarios. Two targets are situated at approximately the same distance from the radar, approximately 1.2 meters, and at -15° and 20°, respectively. The radar employed is the AWR2243BOOST, using only the two transmitters that provide azimuth information (Tx1 and Tx3 in Fig. 2.9). The comparison between the range spectra of using a single channel radar (SISO configuration) and a TDM-MIMO configuration with digital beamforming is shown in Fig. 4.5a. Although these two targets are difficult to distinguish in range, they are clearly separated in the angle-range plot, as shown in Fig. 4.5b.

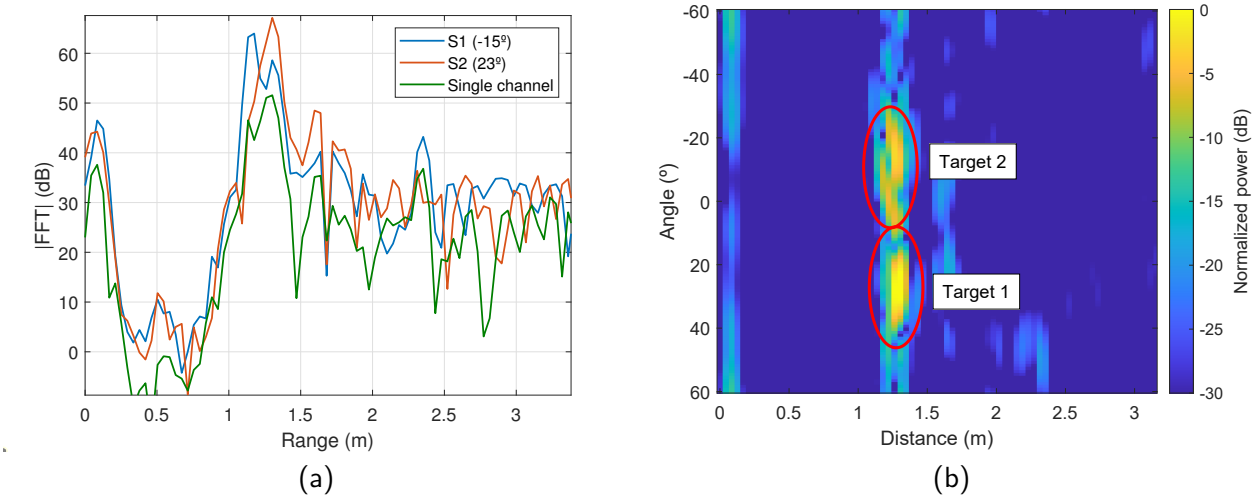

Figure 4.5: Muti-target location enhancement using the AWR2243BOOST and digital beamforming. (**a**) Range spectra comparison using a single channel (SISO configuration) and digital beamforming towards each subject (S1 and S2). (**b**) Angle-range plot where two targets which are in the same range bin can be separated.

Furthermore, Fig. 4.6 presents a comparison between the breathing waveforms obtained using a single channel of the radar (SISO configuration), and applying digital beamforming towards each target. It illustrates that the waveform extracted using a single channel is a combination of the breathing waveforms of the subjects. The signals obtained using digital beamforming are displayed below compared with the signal extracted using the Zephyr BioHarness sensor [Zeph 12].

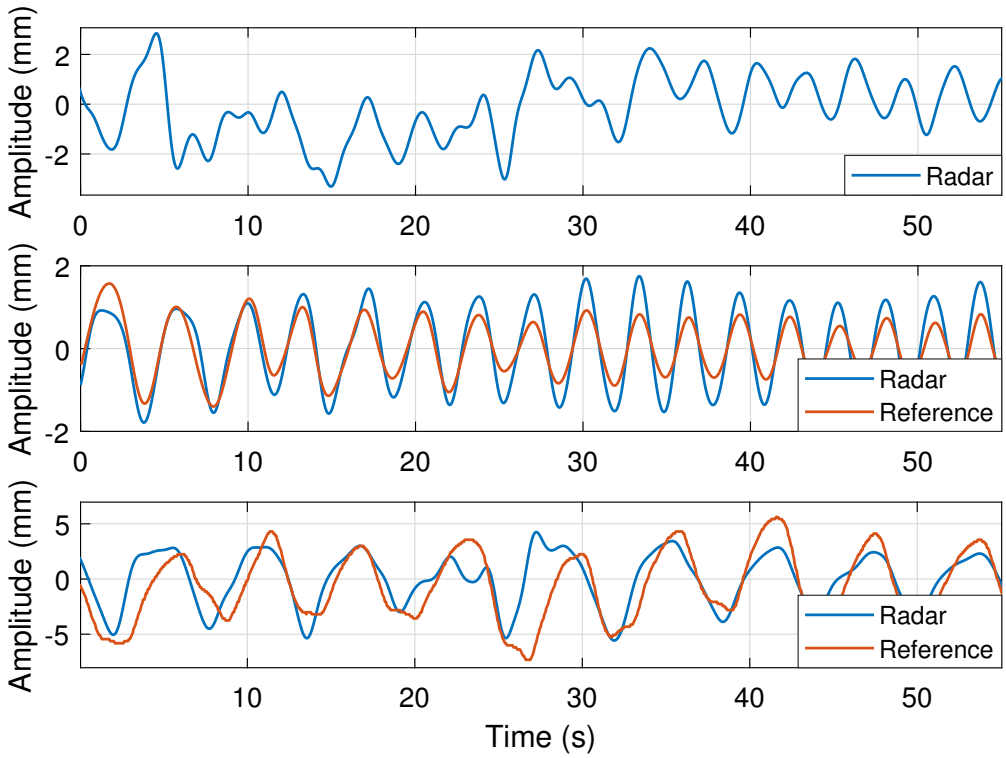

Figure 4.6: Comparison between the breathing waveform obtained using a SISO and TDM-MIMO configurations, compared with the external reference. From top to bottom, the target displacement using a single channel, using TDM-MIMO and beam steering towards -15°, and using TDM-MIMO and beam steering towards 23°.

It is important to note that, at these distances, this radar covers a wide FoV and the heart information is not accurately extracted. Indeed, the same experiment has been conducted using the AWR2243 Cascade in order to show the advantages of enhanced angle resolution in this type of application. This radar allows for a more precise radar pointing with a reduced field of view, allowing for a more accurate extraction of heart information. The enhanced angle resolution of the AWR2243 Cascade in comparison to the AWR2243BOOST was detailed in Section 2.1.

Therefore, the two targets are positioned approximately at a distance of 1.5 meters, with the first target at -10° and the second target at 15°. The angle-range plot and the maximum normalized power obtained at each direction are shown in Fig. 4.7. Comparing this plot with the obtained using the AWR2243BOOST (Fig. 4.5b), it can be observed the higher angular resolution of this setup compared to Fig. 4.5b. In Fig. 4.7, these two targets are clearly located analyzing the power distribution in each angle direction.

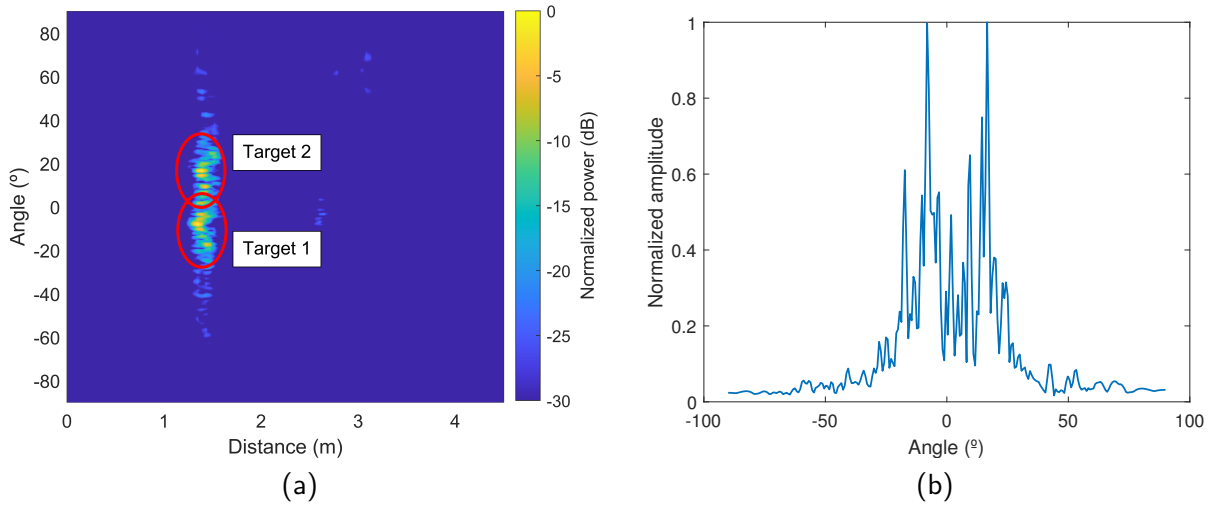

Figure 4.7: Multi-target location enhancement using the AWR2243 Cascade and digital beamforming. (**a**) Angle-range plot where two targets are located at 1.5 meters from the radar. (**b**) Maximum power received in each angle direction.

The extracted vital signs for each subject are displayed in Fig. 4.8. These experiments show that this radar is capable of extracting the vital signs of targets located at the same range bin using a TDM-MIMO configuration.

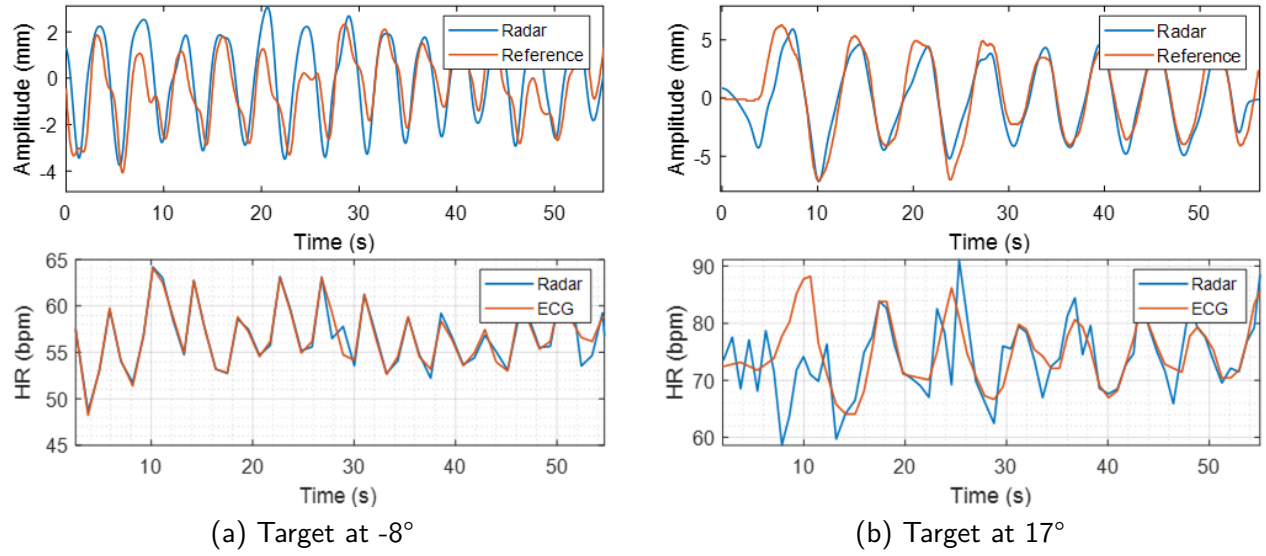

Figure 4.8: Multi-target vital sign extraction. From top to bottom: comparison between breathing waveforms and dynamic heart rates obtained with the radar and the external reference.

In conclusion, a radar system capable of providing a narrow beamwidth is necessary for the accurate extraction of cardiac information, such as the AWR2243 Cascade.

4.2 Robustness Analysis of the Vital Sign Extraction

This section analyzes the robustness of the radar system performance with respect to the following main aspects:

- Radar field of view: It analyzes whether the vital sign extraction is dependent on the FoV covered by the radar.
- Target location: It analyzes whether the vital sign extraction is dependent on the target distance to the radar or the angle at which the target is located from the radar.
- Interfering movements: It analyzes the extraction of vital signs when the target is not completely still. Two types of motion are described: random body movements (RBM) and large motions, such as those resulting from walking.

Furthermore, the robustness of the heart rate extraction was showed in Section 3.5, where the HR and HRV of a single target were monitored in two distinct scenarios: lying on a stretcher and seated while working on a PC.

4.2.1 Radar field of view

As was previously explained, the radar integrates all the movements within the illuminated area, referred to as the FoV. Fig. 4.9 illustrates this working principle, where a radar measures the displacement of the chest.

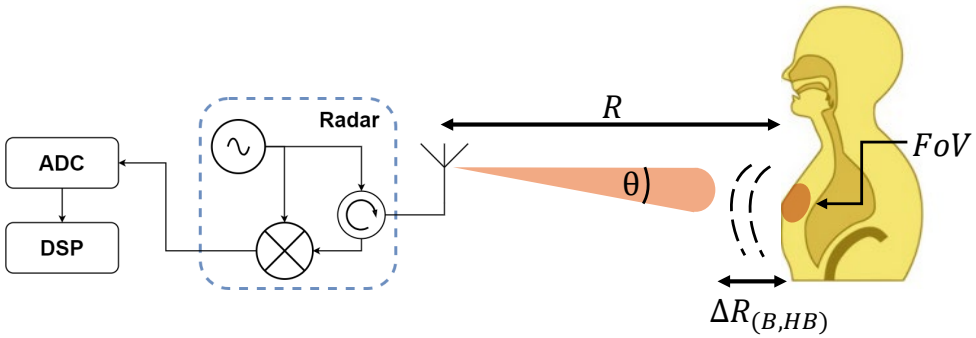

Figure 4.9: Diagram of the radar working principle for monitoring the chest displacement due to breathing and heart activity ($\Delta R_{(B,HB)}$).

In this figure, R represents the distance between the target and the radar, while θ denotes the antenna beamwidth. Thus, the FoV covered by the radar can be approximated by the following expression:

$$FoV \approx 2 \cdot R \cdot \tan(\theta/2) \tag{4.3}$$

It is evident that, in real-world applications where no prior information about the target position is available, the radar must cover a wide FoV to ensure the presence of the individual to be measured. However, the use of a wide FoV is not the most effective approach for vital sign extraction, as the radar integrates all the movements within its FoV. This is not a problem for

breathing monitoring, since the movement of the thoracic cage is uniform along a big surface (41.1 cm-wide in males and 36.7 cm-wide in females, attending to [McDo 09]). In contrast, the circulatory system can be defined as a distributed system, where the pressure wave, generated in the heart, travels along the body surface. This effect was shown in Section 3.2.2 (Fig. 3.9) and Section 3.3.3 (Fig. 3.26), where it was illustrated that the heartbeat waveform varies depending on the radar focusing region. Therefore, a wide FoV will integrate several pulses, distorting the time information of the desired waveform. Encompassing these questions regarding the radar field of view:

- It has to cover an area that is narrower or comparable in size to that of the heart (12 x 8 cm^2 [Vinc 13, Moha 16]) for an accurate monitoring of the dynamic changes of heart rate or extract HRV.
- Scanning techniques, such as digital beamforming, are required to search and locate different targets within a wide area. This is necessary to compensate for the use of an antenna with a narrow beamwidth.

Therefore, it is crucial to evaluate the performance of the vital sign extraction in relation to the FoV covered by the radar. For that reason, the AWR2243 Cascade radar is used for this experiment. The radar in question permits both wide and narrow FoVs, as it has approximately a beamwidth of 70° in H-plane [Texa 20a] for each receiver antenna, which provides a wide FoV. Conversely, it enables the beam to be "tightened" by approximately an order of N [Mail 17], where N is the number of virtual channels (86 azimuth channels). Consequently, with digital beamforming, a beamwidth of 0.8° can be achieved with this radar.

The experiment carried out compares the vital sign extraction of a single target sited at 1 meter from the radar pointing to its chest. The radar covers approximately a FoV of 140-cm wide using a SISO configuration, and 1.4-cm wide using digital beamforming. The person chest is 40-cm wide. Fig. 4.10 shows the breathing waveform and the heart rate extracted with two TX-RX pairs (SISO configuration) and using a radar configuration based on digital beamforming. With regard to the monitoring of breathing activity, both the SISO configuration and digital beamforming are capable of extracting accurate information. However, an accurate heart rate is only extracted with digital beamforming.

Therefore, it is advantageous to extract heart activity information using a reduced FoV. This is also reflected in Fig. 4.11, which compares the spectrum of the heartbeat waveforms used in Fig. 4.10. It shows that the fundamental heart frequency, which is 0.93 Hz (55.8 bpm), is clearly identified only with digital beamforming. Conversely, this frequency is masked by other frequency components in the two SISO configurations.

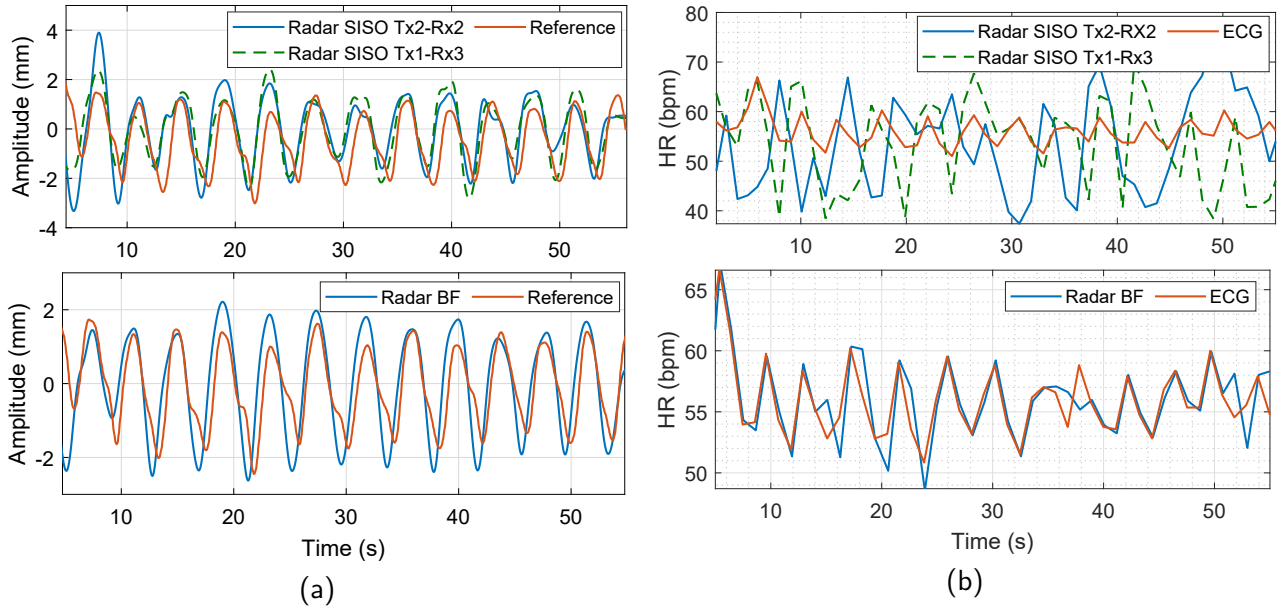

Figure 4.10: Comparison between the vital sign extracted using different radar configurations and the external reference. (**a**) Breathing waveform extracted using SISO configuration and digital beamforming. (**b**) HR extracted using SISO configuration and digital beamforming.

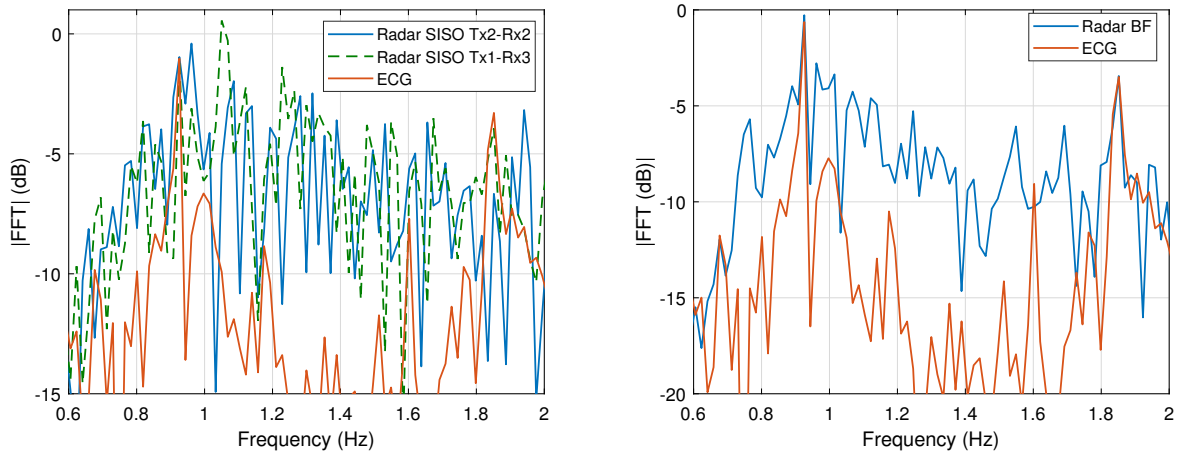

Figure 4.11: Comparison between the heartbeat spectrum using SISO configuration and digital beamforming and the external reference.

An additional experiment is performed to illustrate the extraction of cardiac activity from different locations within the target's chest. This experiment takes advantage of the small FoVs and improved angular resolution that can be achieved with large virtual arrays such as the AWR2243 Cascade. This experiment consists of a vertical chest exploration using digital beamforming, from the target's neck to its abdominal region, as presented in Fig. 4.12a. The target is lying on a stretcher in a horizontal position at a distance of 0.7 meters from the radar.

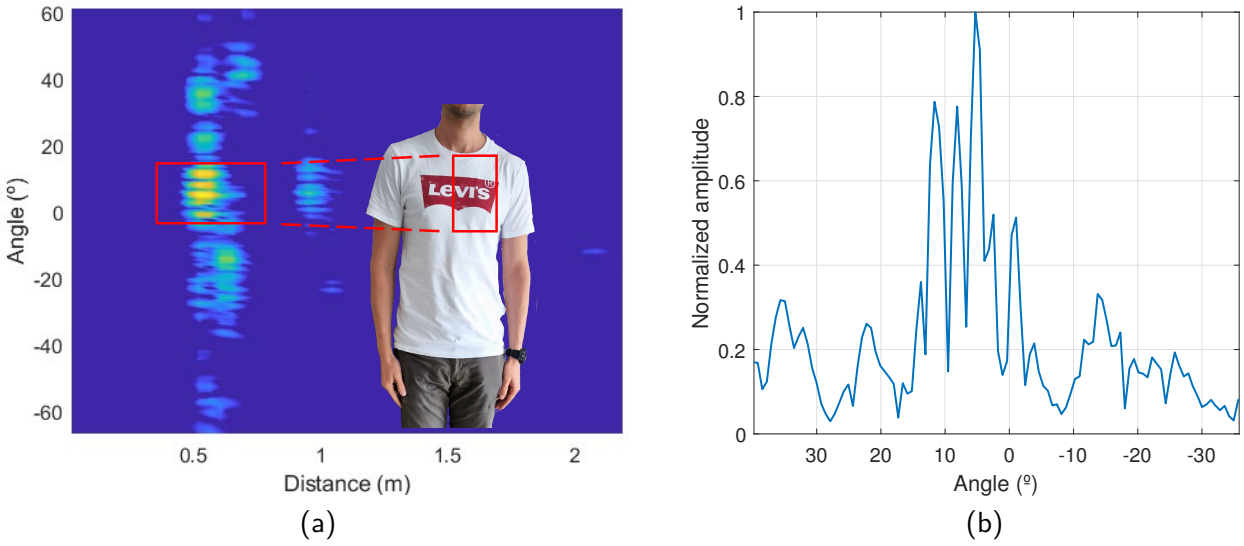

Figure 4.12: Radar pointing for the chest exploration for the target positioned horizontally on a stretcher at 0.7 meters from the radar. (**a**) Angle-range plot. (**b**) Maximum power received at each angle direction.

The $\text{MAE}_{\{\text{HR}\}}$ and the $\text{AE}_{\{\overline{\text{HR}}\}}$ are calculated for an angular sweep between -15° and 15°and shown in Fig. 4.13. Better results are obtained when the radar is focused on the region of the heart. On the other hand, the worst results are obtained in regions closer to the neck, since this region is more sensitive to random movements from the head (angles greater than 8° in Figs. 4.12 and 4.13).

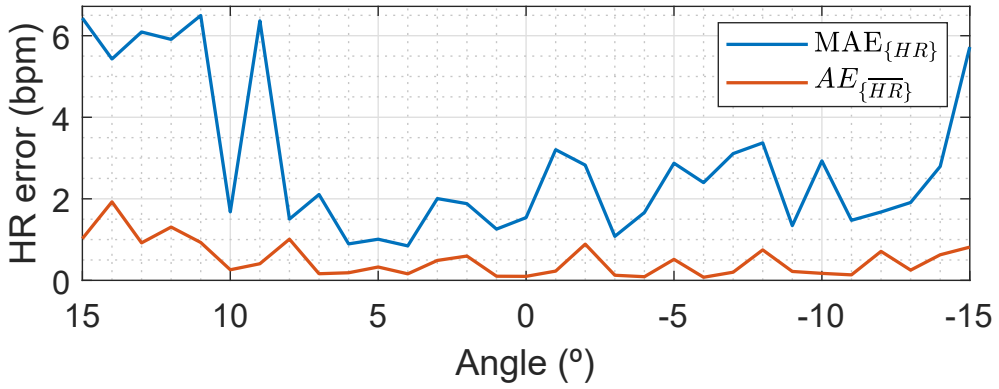

Figure 4.13: Errors obtained for each angle direction.

The findings presented in this section are consistent with the research conducted throughout this thesis. The optimal results have been achieved through the utilization of radars that provide a narrow FoV (e.g. in Table 2.7), such as the 134 GHz radar manufactured by Silicon Radar (with a dielectric lens) or the 24 GHz radar at short distances (less than 0.5 meters).

4.2.2 Target location

In real-world scenarios, vital sign monitoring requires the radar system to be able to extract these vital signs without target location constraints. Therefore, this section examines the extraction of vital signs at different target locations, where the target's distance and the angle between the normal direction to the radar and the target are varied. Measurements at varying distances and angles are provided to show that the system is not constrained by angle or distance (while the FoV is still comparable with the heart size). In this case, two targets are sited in front of the radar at 1 and 1.5 meters. The target localization is shown in Fig. 4.14, where targets are located at -3° and 16° with respect to the radar, and their vital signs are presented in Fig. 4.15.

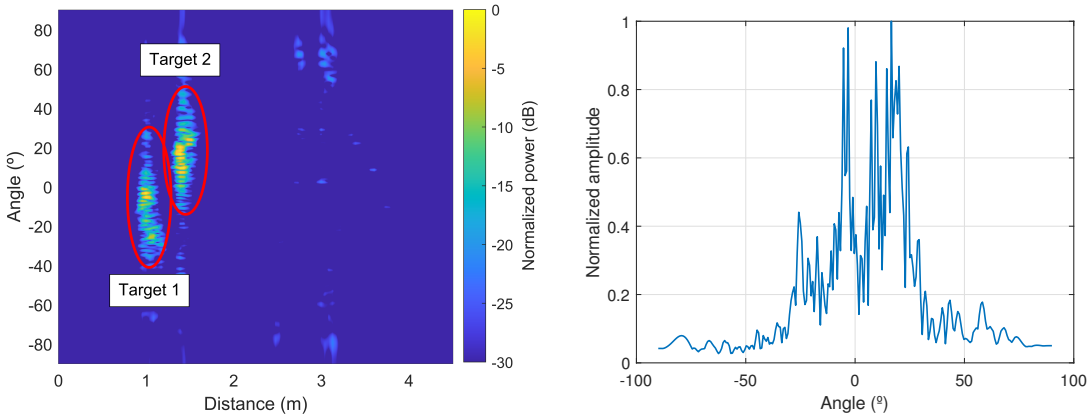

Figure 4.14: Multi-target location using the AWR2243 Cascade. (**a**) Angle-range plot where two targets are at 1 and 1.5 meters. (**b**) Maximum power received at each angle direction.

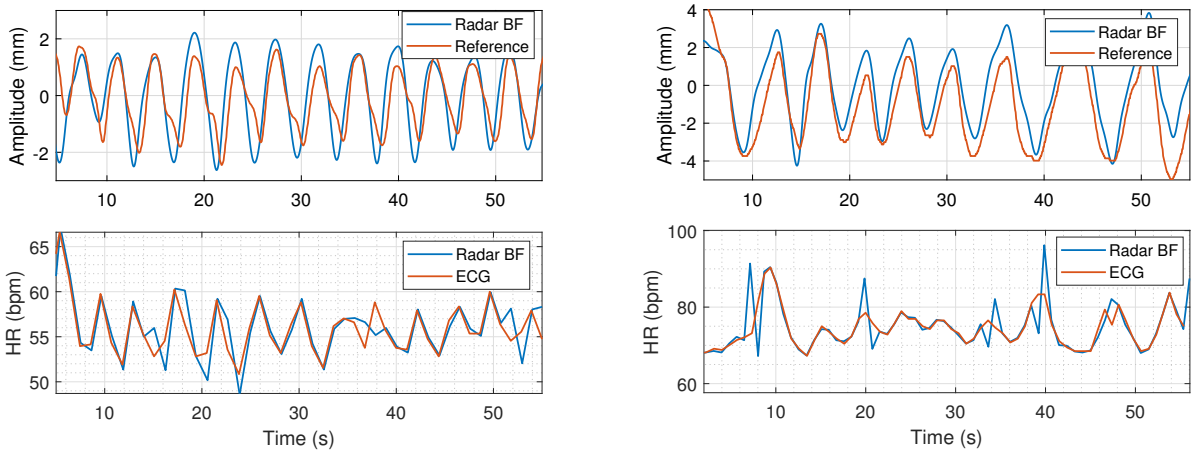

Figure 4.15: Multi-target vital sign extraction. From top to bottom: breathing waveform and dynamic heart rate obtained with the radar and the external reference.

In addition, vital signs can be monitored at longer distances. Indeed, the increasing in the gain due to digital beamforming allows for the measurement of targets at larger distances. For instance, Figs. 4.16 and 4.17 show the vital signs extracted for a target at 5.5 meters from the radar, where the extraction is also compared with a SISO configuration.

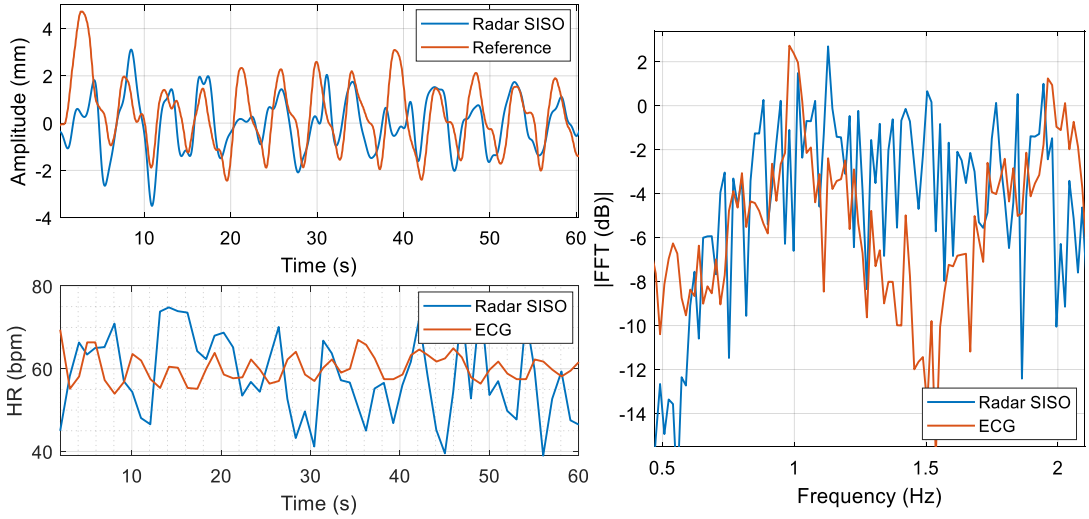

Figure 4.16: Vital sign extraction at 5.5 m using SISO configuration. From left to right: breathing waveform, dynamic heart rate, and heartbeat spectra.

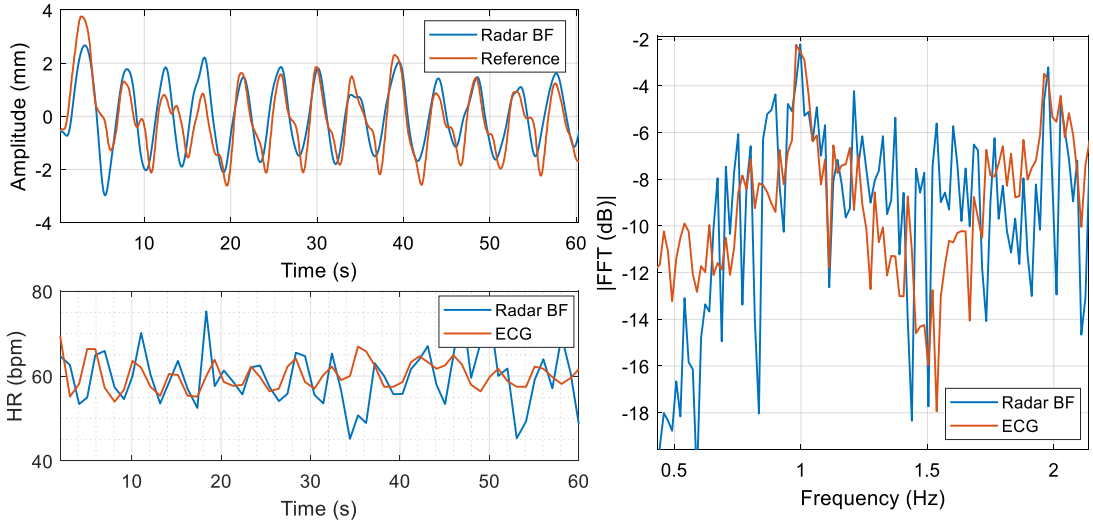

Figure 4.17: Vital sign extraction at 5.5 m using beamforming. From left to right: breathing waveform, dynamic heart rate, and heartbeat spectra.

These results show that the breathing activity can be monitored in both cases (with errors below 1 breath/min), although as anticipated, the cardiac activity cannot. At these distances, the FoV is still comparable with the dimensions of the heart (using digital beamforming), since the radar covers an area of approximately 7-cm-wide, so the dynamic heart rate can be extracted. However, extracting this biomarker becomes more challenging due to the reduction

in SNR as the distance increases. Nevertheless, the heartbeat spectrum plotted in Fig. 4.17 shows that the mean heart rate can still be measured with good accuracy, since the error obtained is below 1 bpm.

4.2.3 Interfering movements

One of the most significant challenges in vital sign monitoring using radar technology is the extraction of vital signs in the presence of target movements that interfere with the measurement process [Isla 22a]. These movements can be random body movements, such as shaking or postural sway, or voluntary movements during normal activities like walking.

4.2.3.1 Random Body Movements

It is important to note that certain body movements can occur within the amplitude and frequency range of the vital signs, which can make their accurate extraction challenging. One such example is postural sway during natural standing, which has been widely studied in the literature [Soam 82, Kim 12b]. It has been reported that the majority of the power of this signal occurs below 2 Hz, with an amplitude range that could be of the order of millimeters and centimeters [Kim 12b, Yama 15]. This signal is normally estimated with the single- and double-inverted pendulum model [Maur 05].

It can be seen that these movements can interfere with the vital sign extraction process. An experiment was conducted to measure a standing target at distances of 0.5 and 1 meter from the radar (AWR2234 Cascade). Fig. 4.18 shows the target displacement and the low-frequency component of the RBM obtained from the measurement at 0.5 meters. This signal is obtained using a 4th-order Butterworth low-pass filter with a cutoff frequency of 0.1 Hz (below the breathing frequency range). It is important to note that the RBM may have components in the breathing frequency range (0.1-0.6 Hz). Therefore, they cannot be separated from the breathing waveform and can distort it, as illustrated in the breathing waveform extracted in Figs. 4.19 and 4.20.

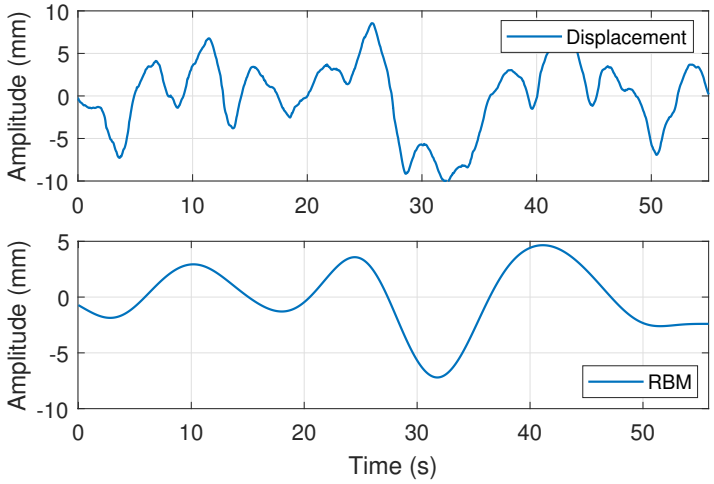

Figure 4.18: Random body motion caused by postural sway extracted from a target standing at 0.5 m from the radar.

Figs. 4.19 and 4.20 depict the breathing waveform and the heart rate extracted at 0.5 and 1 meters. In these cases, both vital signs are extracted with satisfactory results. However, as previously mentioned, the extracted vital signs for a person at one meter exhibit distortions caused by RBM within the breathing range.

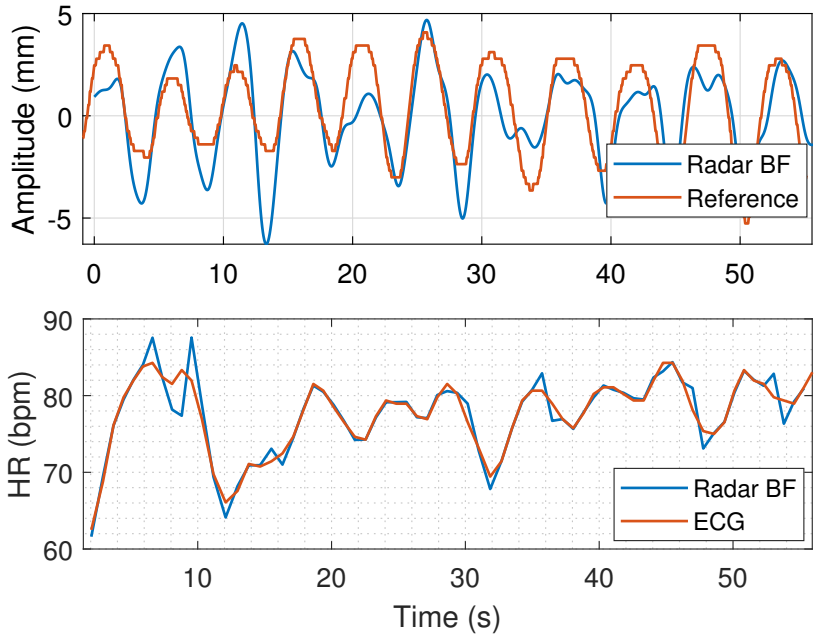

Figure 4.19: Vital sign extraction at 0.5 m using beamforming where the target is standing in front of the radar. From top to bottom: the breathing waveform and the heart rate.

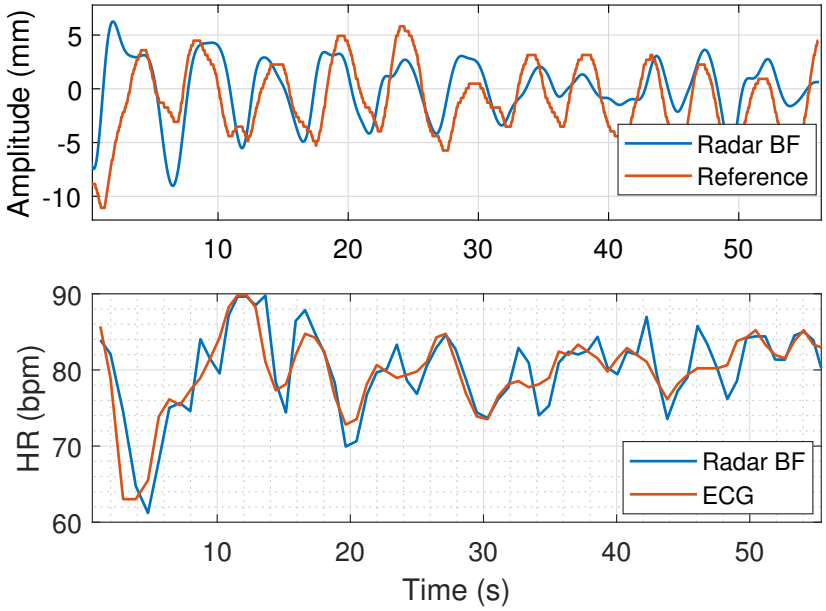

Figure 4.20: Vital sign extraction at 1 m using beamforming where the target is standing in front of the radar. From top to bottom: the breathing waveform and the heart rate.

4.2.4 Voluntary movements

Another challenging scenario for monitoring vital signs is when the subject is performing large-scale movements, such as walking, which significantly overshadow the displacements caused by vital signs because the movement itself may interfere with the extracted vital signs when its frequency content is within the vital signs range.

Therefore, the objective of this section is to minimize the impact of body movements and enhance the extraction of vital signs. For this purpose, a scenario where a target is simultaneously monitored from its front and back is proposed, see Fig. 4.21. This radar configuration exploits the fact that, if the target is moving towards one radar, it is moving away from the other, and this movement can be mitigated while vital sign contributions remain.

It is important to note that, as detailed in Section 3.1, due to the anatomy of the rib cage and sternum, breathing motion is not uniform throughout the entire thoracic cage, as detailed in Section 3.1, which implies that the same displacement cannot be measured from the front and the back. However, these movements are synchronous. In addition, with the proposed setup, a motion cancellation is only possible if the movement is performed in the straight line between both radars.

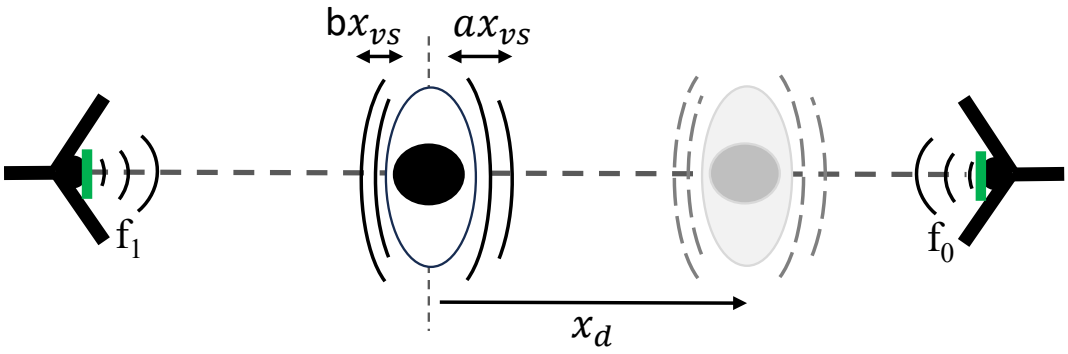

Figure 4.21: Scenario proposed for vital sign monitoring when the target is walking.

Assuming that $x_d(t)$ is the target displacement (including macro-movements such as walking and RBM) seeing from one radar[2], and x_{vs} is the target displacement because of vital sign activity, the displacement measured with each radar can be modeled as:

$$x_{front}(t) = a \cdot x_{vs}(t) + x_d(t) \tag{4.4}$$

$$x_{back}(t) = b \cdot x_{vs}(t) - x_d(t) \tag{4.5}$$

where a and b, which share sign, are the coefficients that model the aforementioned non-uniformity of the movement displacement. Thus,

$$x_{combined}(t) = x_{front}(t) + x_{back}(t) \approxeq (a+b) \cdot x_{vs}(t) \tag{4.6}$$

[2]Note that the movements performs towards a radar are against the other.

In this scenario, two experiments are carried out:

- The first experiment is conducted with a target sitting between two 134 GHz radar nodes, oriented towards the target's chest and back. The target is instructed to remain seated and to perform a motion involving movement towards and away from the radar.
- The second experiment involves a target positioned between two 24 GHz radar nodes, oriented towards the target's chest and back. In this case, the target is in a standing position and is instructed to walk towards and away from the line between the two radars.

In the first scenario, both radars are configured in different frequency bands to prevent mutual interference. The transmitted center frequencies of the radars (f_0 and f_1) are separated 10 MHz, being 134 GHz and 134.01 GHz, respectively. The radars are separated 1 meter. The extracted displacement for each radar is presented in Fig. 4.22, which shows the target's movement between the two radars and its combination. It shows that the majority of the movement's power lies in the low-frequency band (below 0.2 Hz).

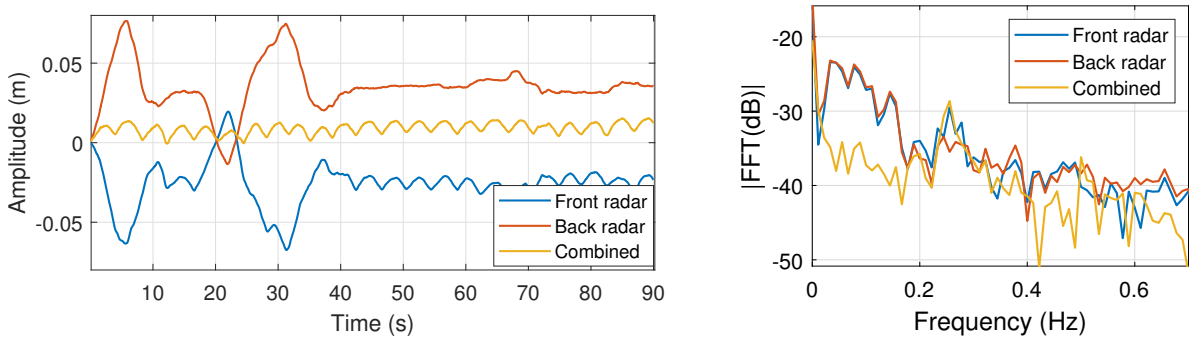

Figure 4.22: Target displacement measured from the front and back radars, and the combined displacement.

After that, each radar displacement is processed to extract the breathing information, which is compared with the Zephyr BioHarness. The results are presented in Figs. 4.23 and 4.24. It is important to note that the radar is unable to extract breathing information when the target is moving (0–40 seconds).

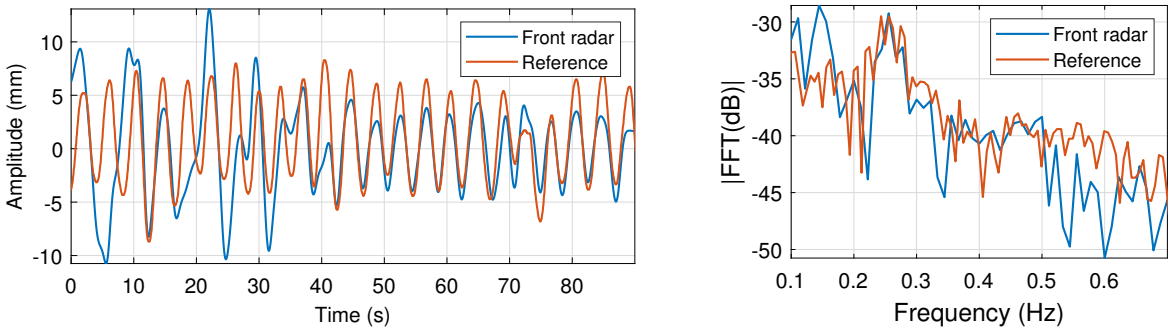

Figure 4.23: Breathing waveform and its spectrum from the front radar compared with the external reference.

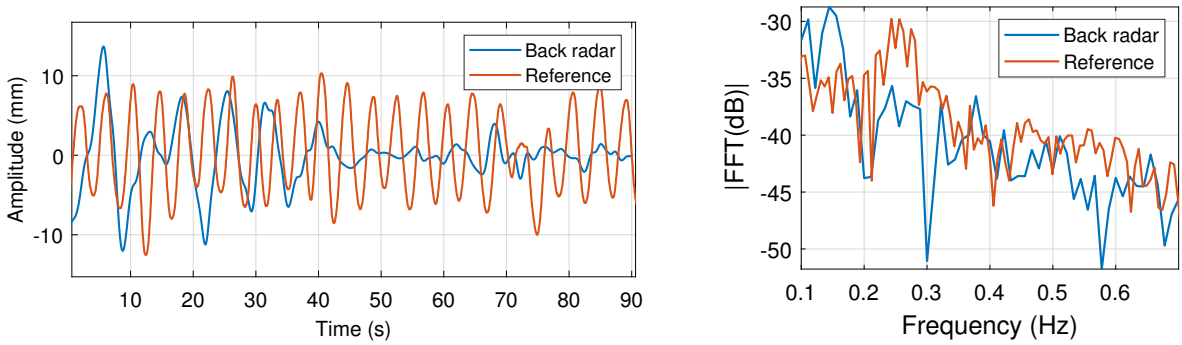

Figure 4.24: Breathing waveform and its spectrum from the back radar compared with the external reference.

Conversely, Fig. 4.25 illustrates the results after combining the extracted signal from both radars. In this case, breathing information is accurately extracted.

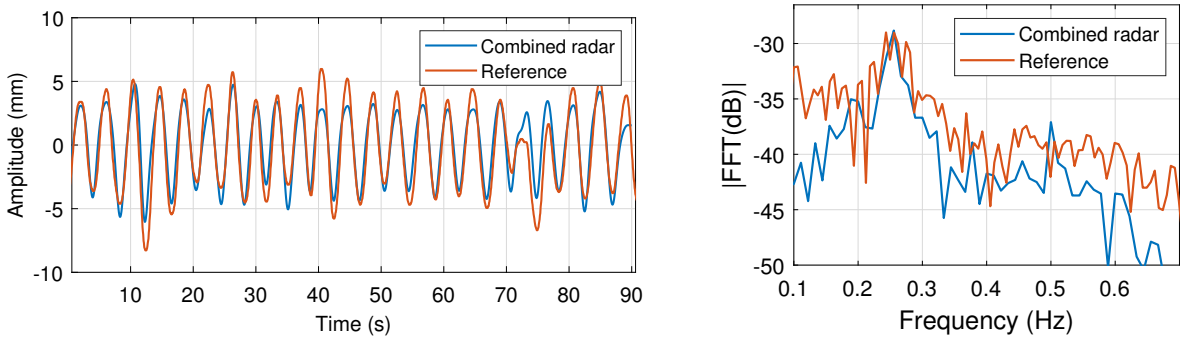

Figure 4.25: Breathing waveform and spectrum extracted from the combination of both radars compared with the external reference.

On the other hand, heart rate can be accurately extracted without combining the radar information, since the movement forced by the target does not introduces a significant distortion at higher frequencies (for the heart sounds extraction). Fig. 4.26 shows the heart rate extraction from the front radar.

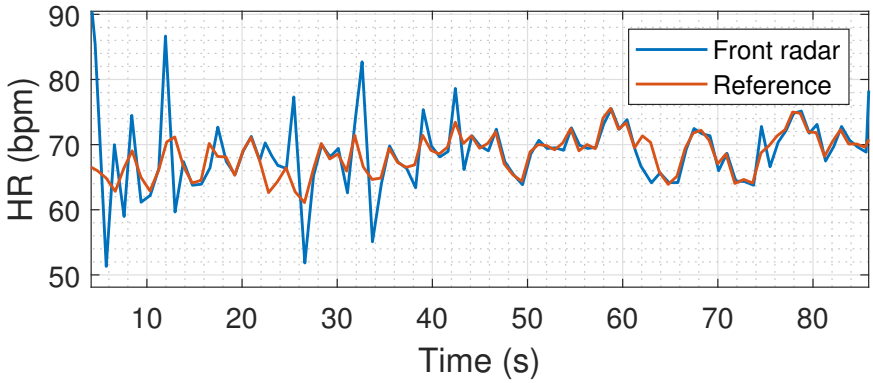

Figure 4.26: Heart rate extracted from the front radar using the heart sounds.

The issue with this second experiment is that the 134 GHz radar (with the lens) is highly sensitive to radar pointing. Therefore, conducting the same experiment carried out above while walking is practically unfeasible, as even minor changes in the target orientation can result in the loss of signal from the target. Thus, the experiment is carried out using two 24 GHz radars from Silicon Radar, which cover a broader FoV than the 134 GHz radar and are less sensitive to radar pointing, but the FoV covered is not suitable for an accurate heart rate extraction.

The experiment is conducted in a manner analogous to the previous one, in which both radars are configured in different frequency bands to prevent mutual interference between them (with center frequencies of 24.5 GHz and 24.51 GHz, in this case). The radars are separated by a distance of 2 meters. Fig. 4.27 illustrates the extracted displacement for each radar, where the movement's power also lies in the low-frequency band (below 0.2 Hz).

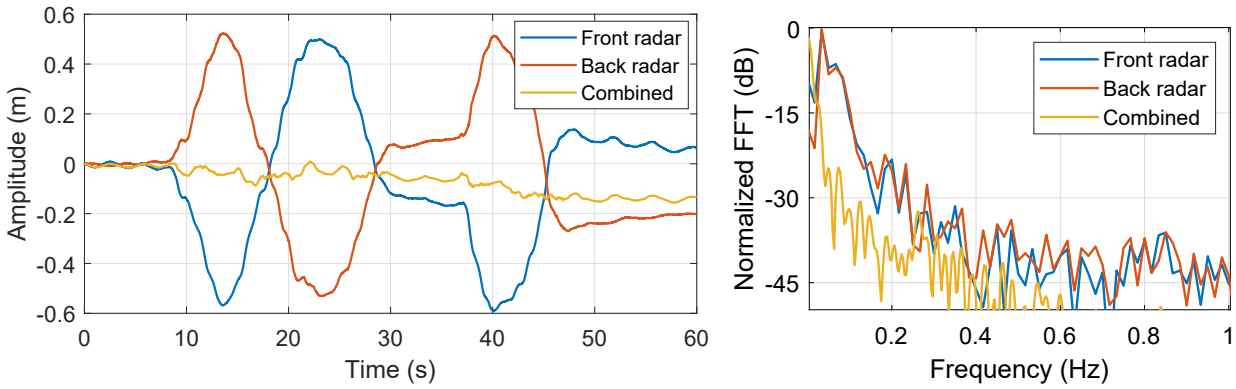

Figure 4.27: Target displacement measured from the front and back radars.

Analogously, each radar displacement is processed to extract the breathing information and it is compared with the reference. The results are presented in Figs. 4.28 and 4.29. It should be noted that the radar is not able to extract the breathing information.

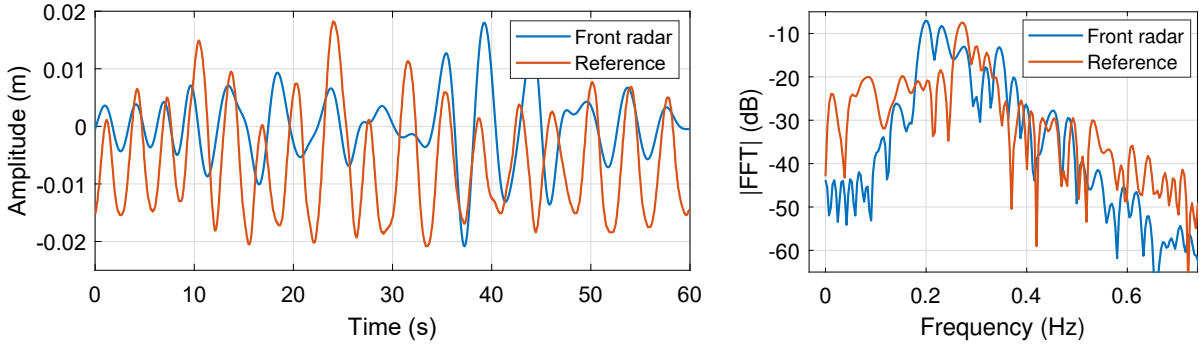

Figure 4.28: Breathing waveform and its spectrum from the front radar compared with the external reference.

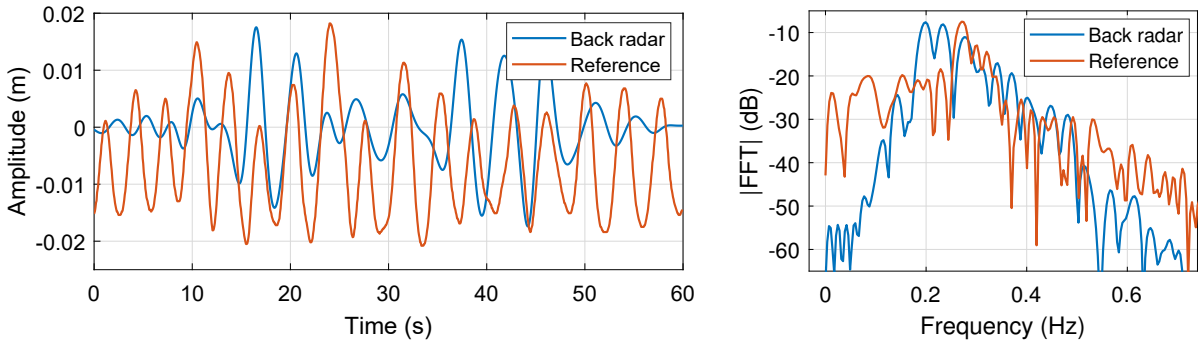

Figure 4.29: Breathing waveform and its spectrum from the back radar compared with the external reference.

On the other hand, Fig. 4.30 illustrates the results after combining the extracted signal from both radars. In this case, breathing information is accurately extracted.

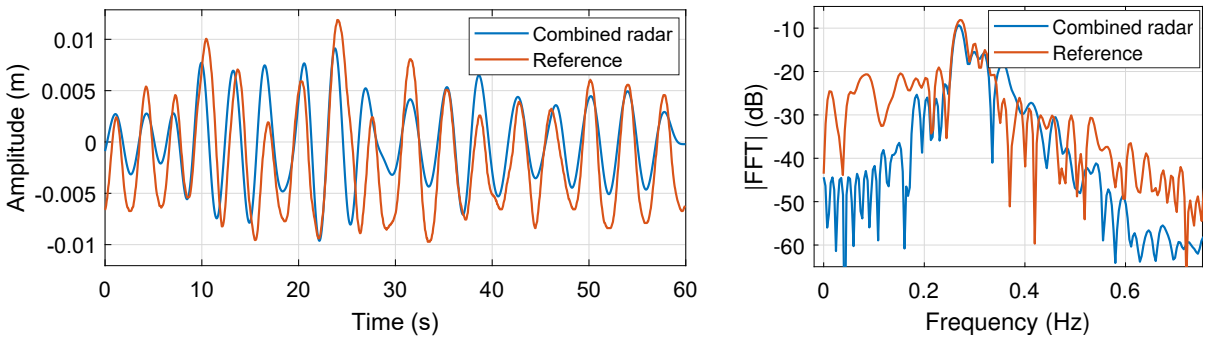

Figure 4.30: Breathing waveform and spectrum extracted from the combination of both radars compared with the external reference.

It is important to note that more complex networks are necessary to mitigate motion that does not occur in a straight line between the two radars. The use of MIMO radars, which permit digital beam steering, plays a pivotal role in these deployments, as they can provide angular trajectory information and focus the beam in a specific direction, enhancing the motion cancellation. This approach can be used for both type of interfering movements: random body movements and large scale movements.

4.3 Real-time vital sign extraction

Another challenge for vital signs monitoring using radar techniques is real-time monitoring. One of the main concerns regarding real-time implementations is the temporal lag between the occurrence of a physiological event and the subsequent reporting of that event by the system, which is referred to as latency. The most commonly utilized vital sign extraction algorithms are conducted in the frequency domain, which means that at least one period of these signals must be analyzed for accurate breathing and heart rate estimation. This

results in the use of analysis windows of, at least, 10 seconds to ensure the inclusion of at least one breathing cycle (to being able to measure the minimum normal breathing rate: 6 breaths/min [Bori 15]), which implies a minimum delay of 10 seconds for breathing rate extraction. Indeed, apnea events are defined as periods during which breathing activity ceases for a minimum of 10 seconds [McNi 08, Ishi 17].

Moreover, these techniques necessitate longer windows[3] to achieve a reasonable resolution for breathing and heart rate estimation. The combination of this delay and the filter group delay introduced during the processing steps may prove inadequate for certain applications that require a fast-acting protocol. Therefore, a time domain approach has to be used to deal with low latency protocols.

Thus, this section proposes a real-time implementation of a vital sign monitoring tool designed to extract the breathing and heartbeat waveforms, as well as the breathing and heart rates for multiple targets. Additionally, an apnea detector has been implemented, making it suitable for applications such as obstructive sleep apnea (OSA) detection or monitoring.

In the first instance, a general scheme of this application is outlined, which is designed to be independent of the radar device used. It only requires an interface block which defines the structure of the raw data transmitted by the radar. Subsequently, its implementation using the AWR2243BOOST is presented, due to its capacity of real-time raw data transfer through the DCA1000 board, as detailed in Section 2.1. However, as was concluded in Section 4.1 and Section 4.2, this radar is not suitable for an accurate heart activity extraction, since a reduced FoV is required for this purpose. Therefore, the real-time implementation with this radar is tested for multi-target breathing activity extraction and the apnea detection scenarios. The extracted signals are compared with the output of the Zephyr BioHarness, which serves as an external reference.

4.3.1 Real-time application implementation

A general overview of the real-time implementation is presented in Fig. 4.31. Firstly, the radar's raw samples are transmitted to an external PC, which implements an acquisition process to extract this data. Appendix H.1 details the acquisition process developed in C++ for the real-time application. Subsequently, the multiple target location and the subsequent extraction of their vital signs are implemented in MATLAB and Simulink. Additionally, they are compared with an external reference, whose signal conditioning and synchronization with the radar is implemented also in Simulink. Finally, a graphical user interface (GUI) presents the extracted data, including the target location, the radar vital signs extracted compared with the external reference, and an apnea indicator.

[3]To achieve resolutions of 1 breaths/min or bpm using the FFT, it is necessary to analyze a window of 60 seconds.

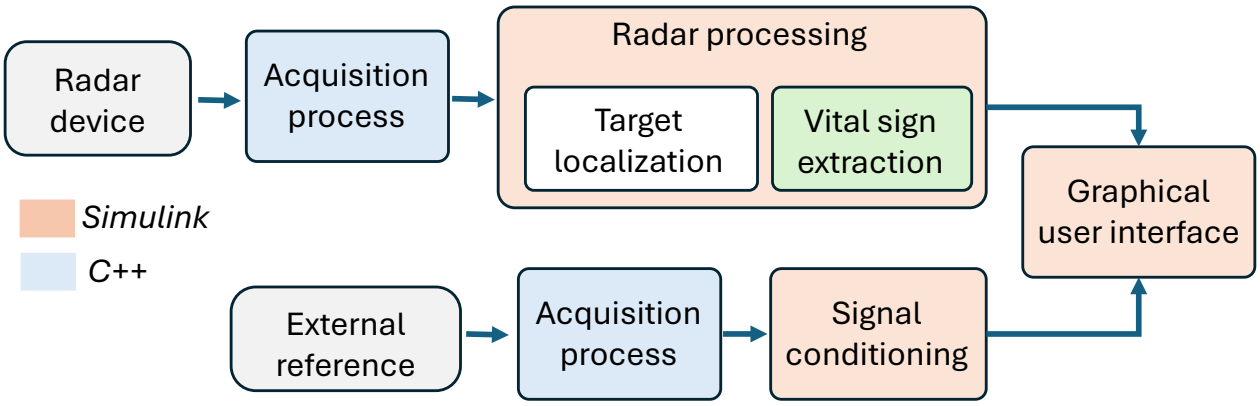

Figure 4.31: General real-time application overview.

Regarding the radar processing implemented, which is illustrated in Fig. 4.32 for the real-time monitoring of two targets, the same processing steps presented in Section 4.1.2 are followed.

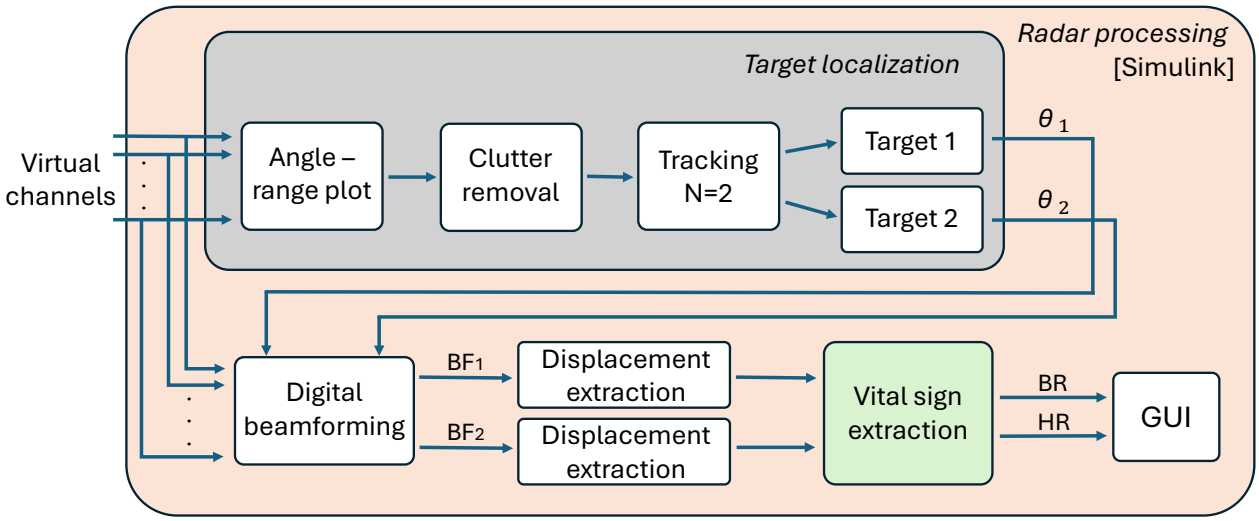

Figure 4.32: Flowchart with the real-time radar signal processing for a two-target scenario.

Firstly, the system processes the radar matrix, derived from the acquisition process, with the objective of identifying the angle-range location of each target. To this end, a 2D-FFT is employed to obtain the angle-range plot. Subsequently, a clutter removal step is applied, which consists of a process that averages the chirps of the previous 10 seconds, thereby enabling the system to adapt to new static clutter appearances in dynamic scenarios.

For target location, the cross-range plot[4] is calculated, and the two maxima in this plot are identified as targets. It is important to note that a bounding-box is defined around each

[4]2-D graphical representation, commonly used in SAR, for visualizing targets in the range, and cross-range (perpendicular to the range dimension) dimensions [Skol 80].

target, so the two regions cannot overlap. The region is selected to cover the mean chest width, measured between the shoulders (biacromial breadth [Garl 14]), which has been reported to be 41.1 cm in males and 36.7 cm in females [McDo 09]. The dimensions of this bounding box can be fixed in the cross-range representation, but it is not possible in the angle-range plot. This is because the same chest width covers a different number of angle bins depending on the target distance to the radar.

Once each target has been located in the cross-range plot, its angle direction is calculated and digital beamforming is applied to the output matrix of the acquisition process. The angle direction is updated each second with the mean angle during this period, in order to reduce the effect of small power variations on the angle direction, which would otherwise result in a flickering effect.

4.3.2 Real-time vital sign extraction

The processing steps which introduces more temporal lag between the occurrence of a physiological event and the subsequent reporting of that event by the system are concentrated in the vital sign extraction. Therefore, this section proposes an alternative processing algorithm to reduce the system's time response, which is illustrated in Fig. 4.33.

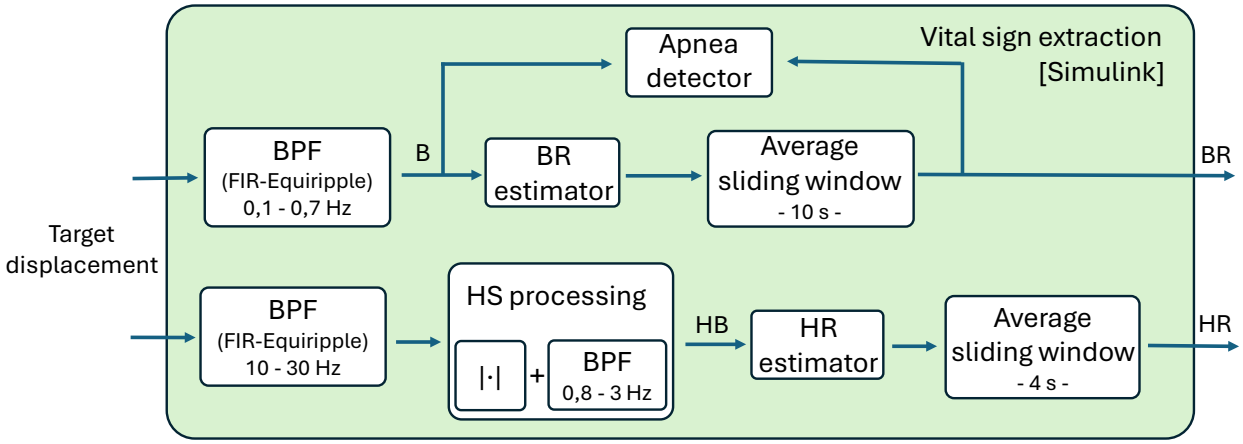

Figure 4.33: Flowchart with the real-time radar vital sign extraction.

Firstly, the breathing (B) and heartbeat (HB) waveforms are extracted from the target displacement. The breathing waveform is obtained directly through an equiripple FIR band-pass filter[5]. On the other hand, the heartbeat information is derived from the heart sounds in order to reduce the impact of breathing harmonics. An additional signal processing step is applied to the heart sounds before the heart rate estimation, which is detailed in Appendix H.2. Once the vital sign waveforms have been extracted, the breathing and heart rates are estimated. The rate estimation process and the apnea detector implemented are detailed in Appendix H.3.

[5]Simulink implements this filter using the Parks-McClellan algorithm [Park 72].

Finally, an average sliding window is implemented to stabilize the output signal rates, as the breathing and heart rate signal rates vary in accordance with the heartbeat and breathing instant frequency.

It is important to note that, although the system has been implemented, the cardiac monitoring tool has not yet been tested in real-time scenarios. This is due to the lack of a device capable of performing a real-time extraction of the raw data from the radars used for cardiac activity monitoring in this thesis (the 134 GHz radar from Silicon Radar and the AWR2243 Cascade). However, breathing monitoring has been tested using the AWR2243BOOST, as the DCA1000 board allows for real-time data extraction.

4.3.3 Case of use: AWR2234BOOST

This section presents the performance of the real-time monitoring application using the AWR2234BOOST. The radar is configured to utilize two transmitters and four receivers in a TDM-MIMO configuration. It is also configured to transmit chirps of 128 μs, sampled at a rate of 2 MHz. The pulse repetition frequency (PRF) is set to 100 Hz, which implies that the chirps are transmitted each 10 ms. The radar is connected to a PC through Ethernet, with a transmitted bitrate of 6.55 Mbps. The system presented in this section is run on a 2020 laptop[6] with Windows 10. The system have been tested in three scenarios:

- Single target scenario: The subject is seated on a stool at a distance of 0.7 meters from the radar, with an angle around 10° with respect to the radar. The subject is instructed to breathe normally and to perform a random apnea period during the three-minute measurement.
- Multiple target scenario: Two targets are seated on stools at distances of 1.6 and 2.4 meters, with an angle of -10° and 35°, respectively. The subjects are instructed to breathe normally and to perform a random apnea period during the three-minute measurement.
- Sleeping apnea monitoring scenario: The subject is positioned on a stretcher at a distance of 1.5 meters from the radar. The subject is instructed to breathe normally and to perform several apnea periods, each lasting between 10 and 15 seconds, during the measurement. This is done in order to simulate an obstructive sleep apnea monitoring.

In order to accurately visualize the different signals in the GUI, a processing block has been developed that measures the delay that each signal experiences during each processing stage. This system then compensates for these delays, providing an accurate synchronization. Fig. 4.34 shows a summary window that presents real-time data regarding the angle and distance at which the identified targets are located. Additionally, it displays the breathing rates measured with the radar and the external reference. Furthermore, each target's summary is accompanied by an apnea indicator, which illuminates in red when a period of apnea is identified. Finally, the targets are situated within the designated angle range.

It is important to note that the delay estimation is not constant and needs to be continuously evaluated. This is caused by the fact that the Windows operating system (OS) is not a

[6]All development and test were carried on an AMD Ryzen 7 4750U laptop.

real-time operating system [Chen 19]. Indeed, on Windows, all requests are processed on a best-effort basis, without any guarantee of a specific response time. Nevertheless, the principal factor contributing to the latency in the processing of the different waveforms is the group delay resulting from the filters implemented in the vital sign extraction stage. In summary, the time response between a physiological event is captured by the radar and the instant when it is displayed by the GUI is as follows[7]:

- Breathing waveform: 7.32±0.02 seconds.
- Breath rate: 9.82±0.02 seconds.

These latencies are consistent with the maximum alarm time specified in the ANSI/AAMI EC13 [Asso 02] standard for HR monitoring (≤10 s). For the visualization, all the signals are synchronized to compensate the maximum delay response.

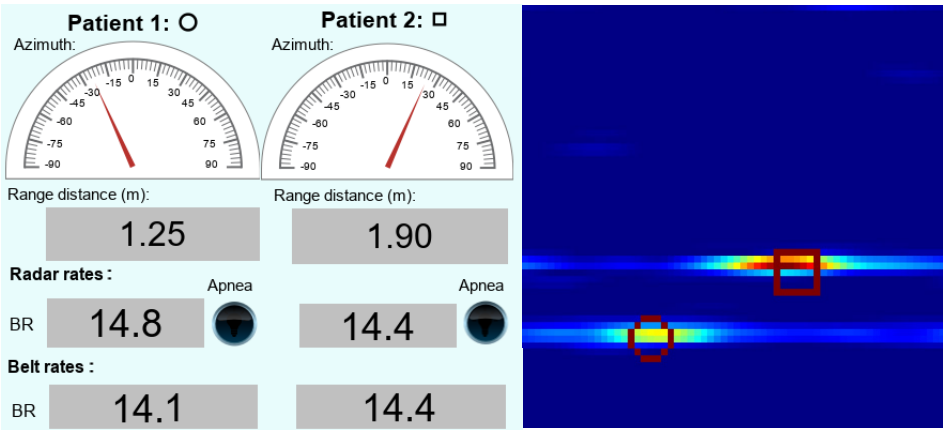

Figure 4.34: Target location window for the real-time application.

4.3.3.1 Single target scenario

The results obtained for this scenario are shown in Figs. 4.35 and 4.36, where the breathing information is accurately extracted, with a dynamic BR error of 0.5 breaths/min.

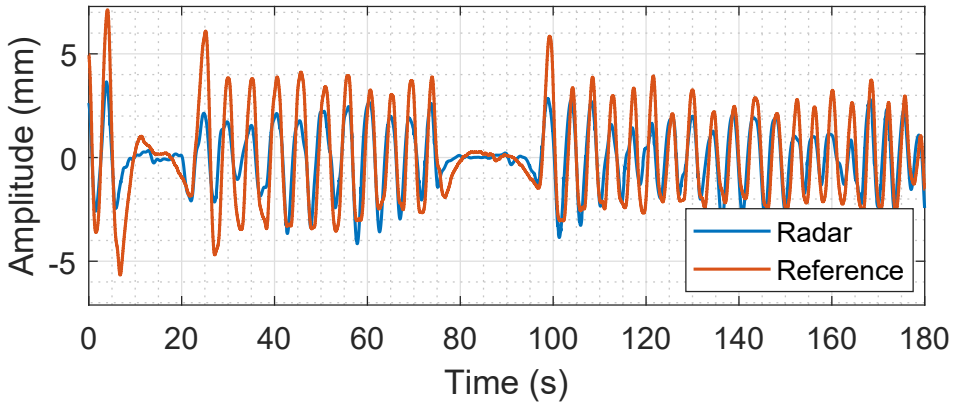

Figure 4.35: Real-time vital signs breathing waveform monitoring of a single target.

[7]It shows the mean delay for a 5-minute measurement.

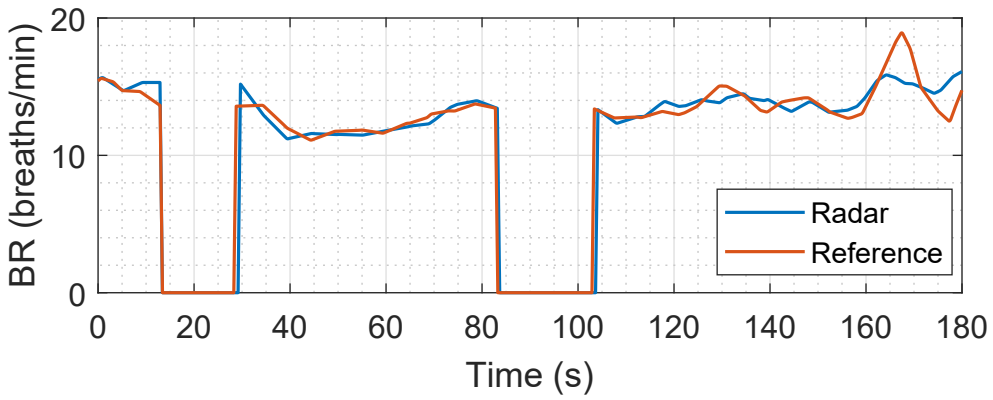

Figure 4.36: Real-time vital signs breathing rate monitoring of a single target.

4.3.3.2 Multiple-target scenario

The results obtained for this scenario are shown in Figs. 4.37 and 4.38, for the target located at 1.6 and 2.4 meters, respectively. Similarly to the previous scenario, the subjects are asked to perform some apnea period, randomly, during the measurement. These figures show a high correlation between the breathing waveforms extracted with the radar and the reference belt in both cases.

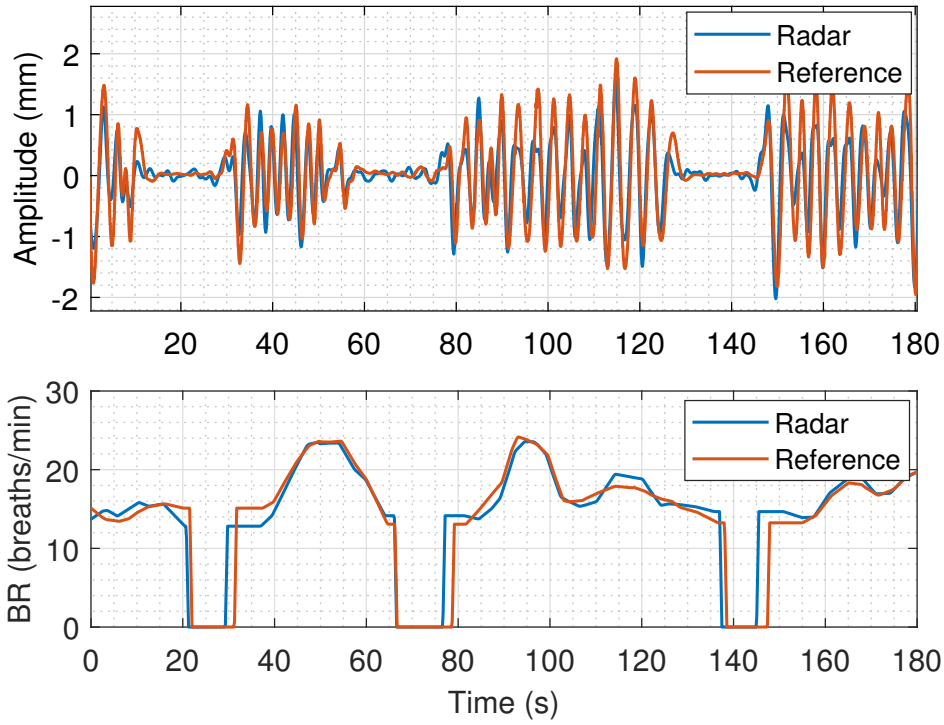

Figure 4.37: Real-time breathing waveform and rates extracted for the target at 1.6 meters.

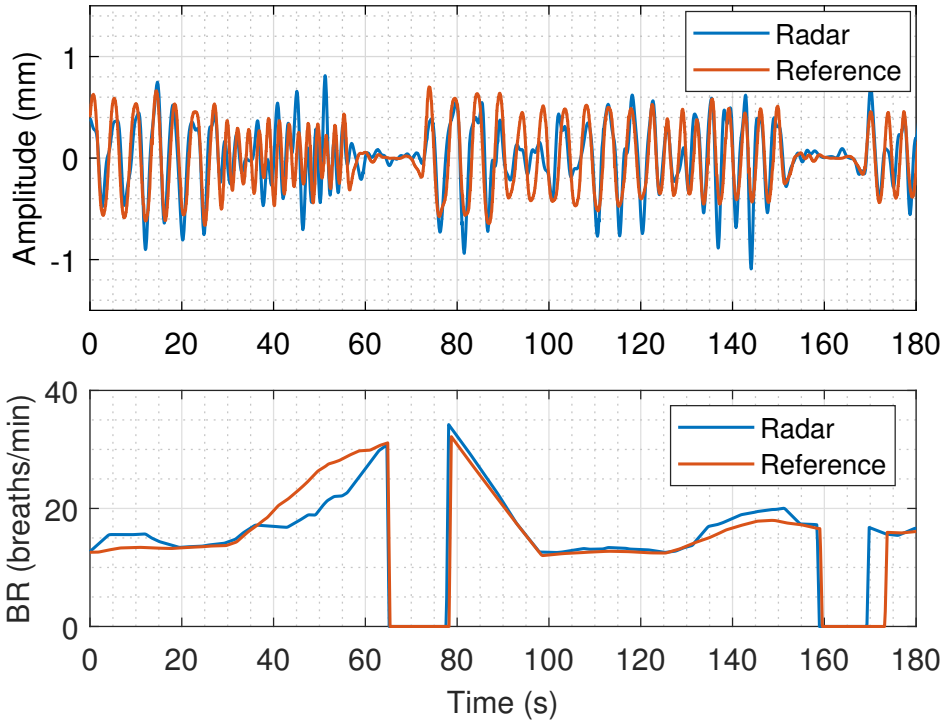

Figure 4.38: Real-time breathing waveform and rates extracted for the target at 2.4 meters.

The discrepancies observed in the rates can be attributed to the fact that the breathing waveforms measured with the radar and the BioHarness exhibit differences. These discrepancies can be attributed to random body movements, as can be seen in the 40–60 second interval in Fig. 4.38. Consequently, the reference and radar signals are not simultaneously triggered.

4.3.3.3 Sleeping apnea monitoring scenario

The target is under the radar in horizontal position and is asked to perform several apnea periods during a 4-minutes measurement. The results are illustrated in Fig. 4.39.

These results show that all apnea periods are accurately identified. The time lag between the apnea period and the system alert is within the estimated window (10 seconds)[8,9]. Therefore, this system is a promising tool for enhancing the monitoring of sleeping scenarios, as it does not require direct contact with the target, eliminating the discomfort of being wired, which could result in a less accurate diagnosis.

[8]An apnea period is defined as a cease of breathing for 10 seconds or longer.

[9]The cessation of respiration at 250 seconds is only observed for 8 seconds, and thus is not considered as an apnea period.

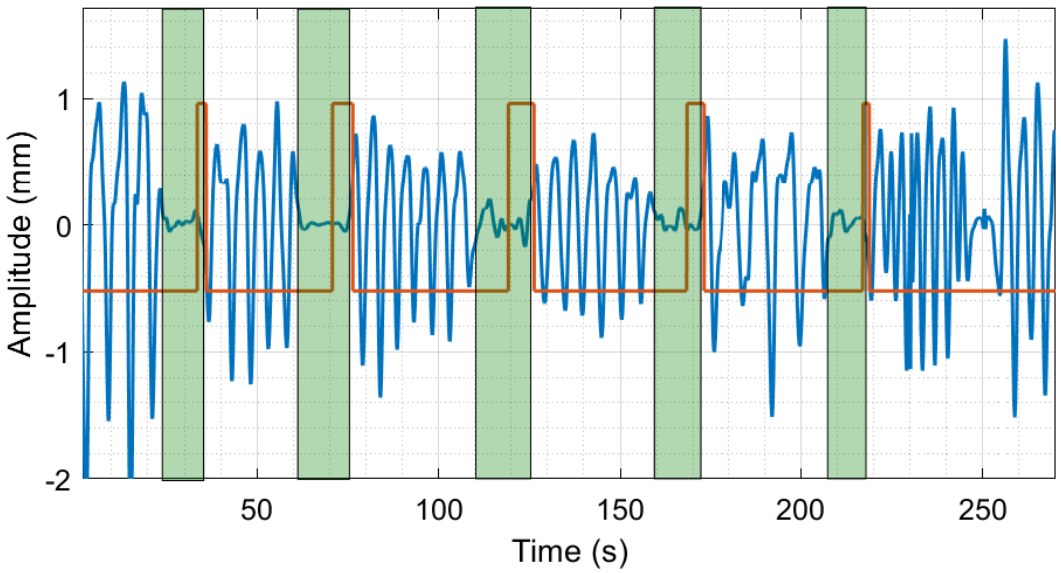

Figure 4.39: Breathing waveform extracted with the radar for the sleeping apnea scenario. The apnea periods are identified with green vertical bars, and the apnea detector trigger in red.

Although promising results have been obtained, this technology is still in the prototype phase and requires further development in certain areas:

- It is necessary to conduct measurement campaigns in clinical settings to validate the performance of the device in real scenarios.
- Additional efforts must be made to enhance the radar's robustness against interfering human motion. At least, it is necessary to identify the time intervals during which the radar quality is poor in order to extract the vital signs and biomarkers.
- It is also necessary to test the real-time cardiac monitoring implementation with a radar device that has a narrow beamwidth and is capable of real-time data extraction.
- This system can be implemented in a FPGA to optimize signal processing and reduce latencies in vital sign extraction.

Chapter 5

Conclusions and Future Work

This last chapter summarizes the main results and conclusions obtained during the development of this Ph.D. thesis. In addition, several research opportunities have been identified as a result of our findings. These possible approaches are suggested for future developments.

5.1 Conclusions

This thesis has been primarily focused on improving the performance of non-contact monitoring of vital signs using radar technology. To achieve this goal, the work carried out has focused on three main aspects:

1. Identification of the optimal radar configuration for vital sign extraction.
2. Analysis of the various vital signs and biomarkers that can be monitored with radar technology.
3. Analysis of the various aspects necessary to make this solution a viable tool for real-world scenarios, particularly in terms of robustness.

Apart from an initial introduction, the first part of this thesis is dedicated to an in-depth analysis of the radar configuration parameters, with the objective of achieving optimal radar performance for vital sign monitoring. In particular, the main analysis provides a comprehensive comparison between CW and LFMCW radars. This comparison is carried out at two different working frequencies, 24 and 134 GHz, in order to show that the conclusions are independent of this parameter. The results show that both configurations can be utilized with satisfactory outcomes for breathing monitoring. However, LFMCW radars are most robust in terms of low-frequency noise, IQ imbalances, and clutter suppression, which enables more accurate heart activity monitoring. Furthermore, the LFMCW configuration allows for multi-target monitoring, which is essential in real-world scenarios.

The second part of this thesis examines the different vital signs and biomarkers that can be extracted using radar technology to monitor breathing and heart activities. It provides a better understanding of the radar processing techniques used to monitor the dynamic changes in these signals. Indeed, it is showed that the optimal heart activity monitoring is obtained

with the information contained in the heart sounds, rather than in the heart fundamental frequency band. Furthermore, it has been showed that cardiac information can be extracted from distinctive locations within the body, including the neck, wrist, and leg. This has enabled the development of a radar network for the non-invasive monitoring of the carotid-femoral pulse wave velocity, which represents the gold standard for the evaluation of arterial stiffness.

The last part of the thesis is concerned with the challenges of deploying this technology in real-world scenarios. First, multi-target scenarios are analyzed, demonstrating the necessity of MIMO configurations to enhance target separation. Second, radar robustness is examined, concluding that the radar spot must cover a FoV comparable with the size of the heart or smaller to extract heart information accurately. It has been shown that vital sign extraction can be performed regardless of target location (angle and distance from the radar) if the aforementioned FoV condition is satisfied. Additionally, the difficulties encountered by the radar in monitoring vital signs in the presence of interfering target movements are presented. Finally, a real-time implementation of vital sign monitoring is detailed. This application enables multi-target breathing and heart rate monitoring, as well as apnea detection. This shows the feasibility of this application for indoor monitoring, as well as its potential as a complementary tool for sleep monitoring scenarios and obstructive sleep apnea diagnosis.

5.2 Future Work

During the development of this thesis, several potential future research directions were identified:

- **Target motion mitigation**. As previously outlined in Chapter 4, the extraction of vital signs in the presence of interference body movements, such as postural sway or walking, represents a significant challenge that must be addressed in order for radar technology to be considered a robust candidate for in-home monitoring. It has been shown that these movements cannot be effectively separated when they lie within the frequency band of vital signs using a simple radar source. Consequently, future research should focus on the development of more complex radar networks that can provide an accurate motion decomposition, particularly in the case of random trajectories, in order to mitigate these movements. The deployment of phased-array radars, which possess the capacity to direct the beam towards the target in conjunction with blind source separation signal processing techniques such as independent component analysis (ICA), could be an effective means of dealing with this problem [Li 23]. This technique can be used to isolate random body movements from vital signs, since the vital signs can be observed from all the sources, being highly correlated, while the interfering movements change between sources, since they are asymmetric.
- **Biometric authentication**. In addition to their applications in health sensing, radars have the potential to play a significant role in enhancing system security and privacy, particularly in the context of user authentication. Indeed, vital sign-based user identity authentication is one of the new trends with radar in the field of vital sign monitoring. Recent studies have proposed the use of ECG signals for this purpose due to their high inter-person variability [Melz 23]. The results obtained in Chapter 3 have proven

the accurate performance of radar technology to monitor different biomarkers such as HRV, PWV, or the different breathing and heart rates simultaneously. Thus, radar is a promising solution for biometric authentication with the advantage of being non-invasive and non-contact compared to other authentication systems.

- **Cardiopulmonary disease evaluation/detection**. Most of the results available in the literature on vital signs monitoring using radar are based on a limited human population, usually young healthy subjects. Throughout this thesis, especially in Chapters 3 and 4, it has become clear that radar systems can be a viable solution or supporting tool for medical assessment. However, more research is needed with real patients in realistic medical scenarios. Longer public datasets, combined with the advances in pattern recognition and machine learning, may be a promising area of research that could help in the early detection of medical complications. For example, the ability to detect arrhythmias or periods of apnea during sleep monitoring could alert the subject to consider medical evaluation [Kang 20].
- **Implementation in home-monitoring scenarios.** The integration of radar into our daily lives is one of the hot topics related to this technology, particularly for elderly care. Most efforts are directed towards the vital sign monitoring of individuals in their domestic environments. For example, [Hu 22] proposes a novel FMCW radar-based vital sign monitoring method for monitoring the vital signs of individuals while they are walking indoors. Nevertheless, vital sign monitoring is not the only research area in which radar is used for in-home monitoring. There is an increasing number of studies investigating the classification of human activity, with most of them focusing on fall detection [Fior 23]. Additionally, radar is also being employed for indoor gait monitoring with the objective of early Parkinson's disease detection [Lope 23].
- **Explore the extraction of other cardiovascular parameters.** In recent years, considerable effort has been directed towards the development of non-contact technology for blood pressure (BP) monitoring. Hypertension represents a significant cardiovascular risk factor associated with an increase in complications and mortality rates regardless of age group [Coll 02]. Thus, improving the monitoring of this parameter is a major health priority, since almost a third of adults suffers from hypertension [Worl 23]. Nevertheless, a method has not yet been developed that allows for monitoring without the need for an external reference, which is normally used to calibrate the system. The proposed devices are based on the underlying principle of the relationship between the time it takes for a volume of blood to travel from the heart to the peripheral organs. This can be calculated through the PTT or the pulse arrival time [Shar 17]. After that, several mathematical model have been proposed to optimize the regression process between the pulse travel time and the BP, some of them are listed in [Shar 17]. However, each of these studies necessitates the calibration of the relationship between BP and PTT. This calibration is specific to the individual subject. This gives rise to two principal issues: the manner in which to address scenarios involving multiple subjects and the circumstances under which recalibration may be required. It has been demonstrated that the PTT depends on factors such as age and weight, which introduces a degree of complexity when attempting to generalise the findings across different populations. New developments

in the field of machine learning have prompted the use of neural networks to address this issue. The radar signals are collected with calibration parameters, including age, gender, height, and weight [Vyso 23]. However the dataset and the network used were insufficient in size to provide accurate and concluding results.

Bibliography

[Abba 11] A. K. Abbas, K. Heimann, K. Jergus, T. Orlikowsky, and S. Leonhardt. "Neonatal non-contact respiratory monitoring based on real-time infrared thermography". *BioMedical Engineering OnLine*, Vol. 10, No. 1, p. 93, Oct. 2011.

[Abra 22] Abracon. *ABLNO Series - Ultra-Low Noise XO/VCXO*. 2022.

[ADLI 14] ADLINK Technology. *PCI-9816/9826/9846 Data Acquisition Cards Datasheet*. 2014.

[Ahma 18] A. Ahmad, J. C. Roh, D. Wang, and A. Dubey. "Vital Signs Monitoring of Multiple People using a FMCW Millimeter-Wave Sensor". In: *2018 IEEE Radar Conference (RadarConf18)*, pp. 1450–1455, IEEE, Oklahoma City, OK, USA, Apr 2018.

[Ahma 22] W. A. Ahmad and X. Yi. "How Will Radar Be Integrated Into Daily Life?: mm-Wave Radar Architectures for Modern Daily Life Applications". *IEEE Microwave Magazine*, Vol. 23, No. 5, pp. 30–43, Apr. 2022.

[Ahme 21] S. S. Ahmed. "Microwave Imaging in Security—Two Decades of Innovation". *IEEE Journal of Microwaves*, Vol. 1, No. 1, pp. 191–201, Jan. 2021.

[AlGh 12] M. AlGhatrif and J. Lindsay. "A brief review: history to understand fundamentals of electrocardiography". *Journal of Community Hospital Internal Medicine Perspectives*, Vol. 2, No. 1, p. 14383, Apr. 2012.

[Amin 16] M. G. Amin, Y. D. Zhang, F. Ahmad, and K. D. Ho. "Radar Signal Processing for Elderly Fall Detection: The future for in-home monitoring". *IEEE Signal Processing Magazine*, Vol. 33, No. 2, pp. 71–80, Mar. 2016.

[Amin 17] M. Amin. *Radar for Indoor Monitoring: Detection, Classification, and Assessment*. CRC Press, 2017.

[Amit 09] G. Amit, K. Shukha, N. Gavriely, and N. Intrator. "Respiratory modulation of heart sound morphology". *American Journal of Physiology-Heart and Circulatory Physiology*, Vol. 296, No. 3, pp. H796–H805, Mar. 2009.

[Amit 21] D. Amitrano, G. Di Martino, R. Guida, P. Iervolino, A. Iodice, M. N. Papa, D. Riccio, and G. Ruello. "Earth Environmental Monitoring Using Multi-Temporal Synthetic Aperture Radar: A Critical Review of Selected Applications". *Remote Sensing*, Vol. 13, No. 4, p. 604, Feb. 2021.

[Anal 10] Analog Devices. *ADXL335 Datasheet*. 2010.

[Anal 14] Analog Devices. *ADF4159 Datasheet*. 2014.

[Anse 19] J. M. Ansermino, G. Dumont, and A. S. Ginsburg. "How Uncertain Is Our Reference Standard for Respiratory Rate Measurement?". *American Journal of Respiratory and Critical Care Medicine*, Vol. 199, No. 8, pp. 1036–1037, Apr. 2019.

[Anto 18] L. Antognoli, P. Marchionni, S. Nobile, V. Carnielli, and L. Scalise. "Assessment of cardio-respiratory rates by non-invasive measurement methods in hospitalized preterm neonates". In: *2018 IEEE International Symposium on Medical Measurements and Applications (MeMeA)*, pp. 1–5, IEEE, Rome, Italy, Jun. 2018.

[Arno 18] P. Arnold, J. Moll, M. Mälzer, V. Krozer, D. Pozdniakov, R. Salman, S. Rediske, M. Scholz, H. Friedmann, and A. Nuber. "Radar-based structural health monitoring of wind turbine blades: The case of damage detection". *Wind Energy*, Vol. 21, No. 8, pp. 676–680, Aug. 2018.

[Arno 84] P. Arnott, G. Pfeiffer, and M. Tavel. "Spectral analysis of heart sounds: relationships between some physical characteristics and frequency spectra of first and second heart sounds in normals and hypertensives". *Journal of Biomedical Engineering*, Vol. 6, No. 2, pp. 121–128, Apr. 1984.

[Arth 19] K. Arthittayapiwat, P. Pirompol, and P. Samanpiboon. "Chest Expansion Measurement in 3-Dimension by Using Accelerometers". *Engineering Journal*, Vol. 23, No. 2, pp. 71–84, Mar. 2019.

[Asso 02] Association for the Advancement of Medical Instrumentation and others. "Cardiac monitors, heart rate meters, and alarms". *American National Standard (ANSI/AAMI EC13: 2002), Arlington, VA*, pp. 1–87, 2002.

[Atme 14] Atmel. *Attiny-167 Datasheet*. 2014.

[Bala 16] C. A. Balanis. *Antenna Theory: Analysis and Design*. John Wiley & Sons, 2016.

[Barb 20] M. Barbosh, P. Singh, and A. Sadhu. "Empirical mode decomposition and its variants: A review with applications in structural health monitoring". *Smart Materials and Structures*, Vol. 29, No. 9, p. 093001, Aug. 2020.

[Bech 16] J. Bechter, K. Eid, F. Roos, and C. Waldschmidt. "Digital Beamforming to Mitigate Automotive Radar Interference". In: *2016 IEEE MTT-S International Conference on Microwaves for Intelligent Mobility (ICMIM)*, pp. 1–4, IEEE, San Diego, CA, USA, May 2016.

[Bech 17] J. Bechter, F. Roos, and C. Waldschmidt. "Compensation of Motion-Induced Phase Errors in TDM MIMO Radars". *IEEE Microwave and Wireless Components Letters*, Vol. 27, No. 12, pp. 1164–1166, Dec. 2017.

[Bene 09] A. Beneduci. "Evaluation of the Potential In Vitro Antiproliferative Effects

of Millimeter Waves at Some Therapeutic Frequencies on RPMI 7932 Human Skin Malignant Melanoma Cells". *Cell Biochemistry and Biophysics*, Vol. 55, pp. 25–32, Jun. 2009.

[Beri 46] R. Beringer. "The Absorption of One-Half Centimeter Electromagnetic Waves in Oxygen". *Physical Review*, Vol. 70, No. 1-2, p. 53, Jul. 1946.

[Beta 14] J. Betancur. *Multimodal image registration for the characterization of the hypertrophic cardiomyopathy and the cardiac asynchronism*. PhD thesis, Université Rennes, May 2014.

[Bett 13] J. G. Betts, K. A. Young, J. A. Wise, E. Johnson, B. Poe, D. H. Kruse, O. Korol, J. E. Johnson, M. Womble, and P. DeSaix. *Anatomy and Physiology*. OpenStax, 2013.

[Bjar 04] J. Bjarnason, T. Chan, A. Lee, M. Celis, and E. Brown. "Millimeter-wave, terahertz, and mid-infrared transmission through common clothing". *Applied Physics Letters*, Vol. 85, No. 4, pp. 519–521, Jul. 2004.

[Blan 86] J. M. Bland and D. Altman. "Statistical methods for assessing agreement between two methods of clinical measurement". *The Lancet*, Vol. 327, No. 8476, pp. 307–310, Feb. 1986.

[Boas 15] B. Boashash. *Time-Frequency Signal Analysis and Processing: A Comprehensive Reference*. Academic Press, 2015.

[Boot 76] H. A. Boot and J. T. Randall. "Historical notes on the cavity magnetron". *IEEE Transactions on Electron Devices*, Vol. 23, No. 7, pp. 724–729, Jul. 1976.

[Bori 15] O. Boric-Lubecke, V. M. Lubecke, A. D. Droitcour, B.-K. Park, and A. Singh. *Doppler Radar Physiological Sensing*. John Wiley & Sons, 2015.

[Broo 85] E. Brookner. "Phased-Array Radars". *Scientific American*, Vol. 252, No. 2, pp. 94–103, Feb. 1985.

[Brus 15] C. Bruser, C. H. Antink, T. Wartzek, M. Walter, and S. Leonhardt. "Ambient and Unobtrusive Cardiorespiratory Monitoring Techniques". *IEEE Reviews in Biomedical Engineering*, Vol. 8, pp. 30–43, Mar. 2015.

[Butt 81] K. J. Button and J. C. Wiltse. *Infrared and Millimeter Waves: Millimeter Systems*. Vol. 4, Elsevier, 1981.

[Carr 95] W. G. Carrara, R. S. Goodman, and R. M. Majewski. *Spotlight Synthetic Aperture Radar : Signal Processing Algorithms*. Artech, 1995.

[Chah 11] N. Chahat, M. Zhadobov, R. Augustine, and R. Sauleau. "Human skin permittivity models for millimetre-wave range". *Electronics Letters*, Vol. 47, No. 7, pp. 427–428, Mar. 2011.

[Chan 13] W. Chan, M. Woldeyohannes, R. Colman, P. Arand, A. D. Michaels, J. D. Parker, J. T. Granton, and S. Mak. "Haemodynamic and structural correlates of the first and second heart sounds in pulmonary arterial hypertension: an acoustic

cardiography cohort study". *BMJ Open*, Vol. 3, No. 4, pp. 1–10, Mar. 2013.

[Chen 19] K. Chen, C. Du, J. Chen, and Z. Yuan. "Real-time Extension Technologies on the Windows Operation System". In: *2019 IEEE 8th Joint International Information Technology and Artificial Intelligence Conference (ITAIC)*, pp. 789–793, IEEE, Chongqing, China, May 2019.

[Chur 81] F. Churchill, G. Ogar, and B. Thompson. "The Correction of I and Q Errors in a Coherent Processor". *IEEE Transactions on Aerospace and Electronic Systems*, No. 1, pp. 131–137, Jan. 1981.

[Citi 11] L. Citi, M. T. Bianchi, E. B. Klerman, and R. Barbieri. "Instantaneous Monitoring of Sleep Fragmentation by Point Process Heart Rate Variability and Respiratory Dynamics". In: *2011 Annual International Conference of the IEEE Engineering in Medicine and Biology Society*, pp. 7735–7738, Boston, MA, USA, Sept. 2011.

[CNSy 23] CNSystems Medizintechnik GmbH. "Non-invasive, continuous blood pressure and hemodynamic measurement". https://www.cnsystems.com/. Accessed on Jan, 2023.

[Cohn 63] M. Cohn, F. Wentworth, and J. Wiltse. "High-Sensitivity 100-to 300-Gc Radiometers". *Proceedings of the IEEE*, Vol. 51, No. 9, pp. 1227–1232, Sept. 1963.

[Coll 02] P. S. Collaboration *et al.* "Age-specific relevance of usual blood pressure to vascular mortality: a meta-analysis of individual data for one million adults in 61 prospective studies". *The Lancet*, Vol. 360, No. 9349, pp. 1903–1913, Dec. 2002.

[Colo 14] M. A. Colominas, G. Schlotthauer, and M. E. Torres. "Improved complete ensemble EMD: A suitable tool for biomedical signal processing". *Biomedical Signal Processing and Control*, Vol. 14, pp. 19–29, Nov. 2014.

[Dark 08] A. Darkins, P. Ryan, R. Kobb, L. Foster, E. Edmonson, B. Wakefield, and A. E. Lancaster. "Care Coordination/Home Telehealth: The Systematic Implementation of Health Informatics, Home Telehealth, and Disease Management to Support the Care of Veteran Patients with Chronic Conditions". *Telemedicine and e-Health*, Vol. 14, No. 10, pp. 1118–1126, Dec. 2008.

[Dehk 19] P. Dehkordi, F. Khosrow-Khavar, M. Di Rienzo, O. T. Inan, S. E. Schmidt, A. P. Blaber, K. Sørensen, J. J. Struijk, V. Zakeri, P. Lombardi, *et al.* "Comparison of Different Methods for Estimating Cardiac Timings: A Comprehensive Multimodal Echocardiography Investigation". *Frontiers in Physiology*, p. 1057, Aug. 2019.

[Dokh 19] S. H. Dokhanchi, B. S. Mysore, K. V. Mishra, and B. Ottersten. "A mmWave Automotive Joint Radar-Communications System". *IEEE Transactions on Aerospace and Electronic Systems*, Vol. 55, No. 3, pp. 1241–1260, Jun. 2019.

[Dong 20] S. Dong, Y. Zhang, C. Ma, C. Zhu, Z. Gu, Q. Lv, B. Zhang, C. Li, and L. Ran. "Doppler Cardiogram: A Remote Detection of Human Heart Activities". *IEEE Transactions on Microwave Theory and Techniques*, Vol. 68, No. 3, pp. 1132–1141, Mar. 2020.

[Drak 09] R. Drake, A. W. Vogl, and A. W. Mitchell. *Gray's Anatomy for Students E-Book*. Elsevier Health Sciences, 2009.

[Droi 01] A. Droitcour, V. Lubecke, Jenshan Lin, and O. Boric-Lubecke. "A microwave radio for Doppler radar sensing of vital signs". In: *2001 IEEE MTT-S International Microwave Sympsoium Digest (Cat. No.01CH37157)*, pp. 175–178, IEEE, Phoenix, AZ, USA, May 2001.

[Duan 18] Z. Duan and J. Liang. "A Non-Contact Detection Method for Multi-Person Vital Signs Based on IR-UWB Radar". *IEEE Access*, Vol. 7, pp. 36888–36895, Aug. 2018.

[Eckb 83] D. L. Eckberg. "Human sinus arrhythmia as an index of vagal cardiac outflow". *Journal of Applied Physiology*, Vol. 54, No. 4, pp. 961–966, Apr. 1983.

[Ehrn 21] M. G. Ehrnsperger, M. Noll, U. Siart, and T. F. Eibert. "Background and Clutter Removal Techniques for Ultra Short Range Radar". In: *2020 17th European Radar Conference (EuRAD)*, pp. 78–81, IEEE, Utrecht, Netherlands, Jan. 2021.

[Espe 14] S. A. Esper and M. R. Pinsky. "Arterial waveform analysis". *Best Practice & Research Clinical Anaesthesiology*, Vol. 28, No. 4, pp. 363–380, Dec. 2014.

[Farl 21] J. Farlík and L. Gacho. "Researching UAV Threat – New Challenges". In: *2021 International Conference on Military Technologies (ICMT)*, pp. 1–6, IEEE, Brno, Czech Republic, Jun. 2021.

[Fila 94] I. Filanovsky and H. Baltes. "CMOS Schmitt Trigger Design". *IEEE Transactions on Circuits and Systems I: Fundamental Theory and Applications*, Vol. 41, No. 1, pp. 46–49, Jan. 1994.

[Fior 23] F. Fioranelli, R. G. Guendel, N. C. Kruse, and A. Yarovoy. "Radar Sensing in Healthcare: Challenges and Achievements in Human Activity Classification & Vital Signs Monitoring". In: *International Work-Conference on Bioinformatics and Biomedical Engineering*, pp. 492–504, Springer, Meloneras, Gran Canaria, Spain, Jul. 2023.

[Gand 10] Y. Gando, K. Yamamoto, H. Murakami, Y. Ohmori, R. Kawakami, K. Sanada, M. Higuchi, I. Tabata, and M. Miyachi. "Longer Time Spent in Light Physical Activity Is Associated With Reduced Arterial Stiffness in Older Adults". *Hypertension*, Vol. 56, No. 3, pp. 540–546, Jul. 2010.

[Gand 86] O. P. Gandhi and A. Riazi. "Absorption of Millimeter Waves by Human Beings and its Biological Implications". *IEEE Transactions on Microwave Theory and Techniques*, Vol. 34, No. 2, pp. 228–235, Feb. 1986.

[Garc 19] F. A. García Rial. *Technological contributions to imaging radars in the millimeter-wave band*. PhD thesis, E.T.S.I. Telecomunicación (UPM), Sept. 2019.

[Garl 14] T. Garlie and H. J. Choi. "Characterizing the Size of the Encumbered Soldier". Tech. Rep. NATICK/TR-14/019, Research, Development, and Engineering Center (NSRDEC), Natick, MA, USA, Aug. 2014.

[Gedd 91] L. A. Geddes. *Handbook of Blood Pressure Measurement*. Humana Press, Clifton, N.J, 1991.

[Geig 19] M. Geiger and C. Waldschmidt. "160-GHz Radar Proximity Sensor With Distributed and Flexible Antennas for Collaborative Robots". *IEEE Access*, Vol. 7, pp. 14977–14984, Jan. 2019.

[Gesc 12] H. Gesche, D. Grosskurth, G. Küchler, and A. Patzak. "Continuous blood pressure measurement by using the pulse transit time: comparison to a cuff-based method". *European Journal of Applied Physiology*, Vol. 112, No. 1, pp. 309–315, May 2012.

[Giar 04] N. D. Giardino, L. Chan, and S. Borson. "Combined Heart Rate Variability and Pulse Oximetry Biofeedback for Chronic Obstructive Pulmonary Disease: Preliminary Findings". *Applied Psychophysiology and Biofeedback*, Vol. 29, No. 2, pp. 121–133, Jun. 2004.

[Giav 15] D. Giavarina. "Understanding Bland Altman analysis". *Biochemia Medica*, Vol. 25, No. 2, pp. 141–151, Jun. 2015.

[Ginz 76] E. L. Ginzton. "The $100 idea". *IEEE Transactions on Electron Devices*, Vol. 23, No. 7, pp. 714–723, Jul. 1976.

[Gouv 20] C. Gouveia, A. Tomé, F. Barros, S. C. Soares, J. Vieira, and P. Pinho. "Study on the usage feasibility of continuous-wave radar for emotion recognition". *Biomedical Signal Processing and Control*, Vol. 58, p. 101835, Apr. 2020.

[Grim 16] C. E. Grim and C. M. Grim. "Auscultatory BP: still the gold standard". *Journal of the American Society of Hypertension*, Vol. 10, No. 3, pp. 191–193, Mar. 2016.

[Gu 13] C. Gu, T. Inoue, and C. Li. "Analysis and Experiment on the Modulation Sensitivity of Doppler Radar Vibration Measurement". *IEEE Microwave and Wireless Components Letters*, Vol. 23, No. 10, pp. 566–568, Mar. 2013.

[Gu 16] C. Gu. "Short-Range Noncontact Sensors for Healthcare and Other Emerging Applications: A Review". *Sensors*, Vol. 16, No. 8, Jul. 2016.

[Gurb 19] S. Z. Gurbuz and M. G. Amin. "Radar-Based Human-Motion Recognition With Deep Learning: Promising Applications for Indoor Monitoring". *IEEE Signal Processing Magazine*, Vol. 36, No. 4, pp. 16–28, Jun. 2019.

[Ha 21] U. Ha, S. Madani, and F. Adib. "WiStress: Contactless Stress Monitoring Using Wireless Signals". *Proceedings of the ACM on Interactive, Mobile, Wearable and Ubiquitous Technologies*, Vol. 5, No. 3, pp. 1–37, Sept. 2021.

[Hadd 58] F. Haddock. "Introduction to Radio Astronomy". *Proceedings of the IRE*, Vol. 46, No. 1, pp. 3–12, Jan. 1958.

[Hale 33] S. Hales, W. Innys, R. Manby, and T. Woodward. *Statical essays, containing haemastaticks, or, An account of some hydraulick and hydrostatical experiments made on the blood and blood vessels of animals : also an account of some*

experiments on stones in the kidneys and bladder : with an enquiry into the nature of those anomalous concretions : to which is added, an appendix, containing observations and experiments relating to several subjects in the first volume, the greater part of which were read at several meetings before the Royal Society : with an index to both volumes. Printed for W. Innys and R. Manby, at the west-end of St. Paul's, and T. Woodward, at the Half-Moon between Temple-Gate, Fleetstreet, 1733.

[He 17] M. He, Y. Nian, and Y. Gong. "Novel signal processing method for vital sign monitoring using FMCW radar". *Biomedical Signal Processing and Control*, Vol. 33, pp. 335–345, Mar. 2017.

[Heck 82] J. L. Heckman, G. H. Stewart, P. R. Lynch, and M. C. Ziskin. "Frequency analysis approach to the origin of the first and second heart sounds". *American Heart Journal*, Vol. 104, No. 6, pp. 1309–1318, Dec. 1982.

[Herz 22] L. Herzer, A. Muecke, R. Richer, N. C. Albrecht, M. Heyder, K. M. Jaeger, V. Koenig, A. Koelpin, N. Rohleder, and B. M. Eskofier. "Influence of Sensor Position and Body Movements on Radar-Based Heart Rate Monitoring". In: *2022 IEEE-EMBS International Conference on Biomedical and Health Informatics (BHI)*, pp. 1–4, IEEE, Ioannina, Greece, Sept. 2022.

[Hong 97] H. Hong. "Noninvasive detection of cardiovascular pulsations by optical Doppler techniques". *Journal of Biomedical Optics*, Vol. 2, No. 4, p. 382, Oct. 1997.

[Hu 13] W. Hu, Z. Zhao, Y. Wang, H. Zhang, and F. Lin. "Noncontact Accurate Measurement of Cardiopulmonary Activity Using a Compact Quadrature Doppler Radar Sensor". *IEEE Transactions on Biomedical Engineering*, Vol. 61, No. 3, pp. 725–735, Mar. 2013.

[Hu 22] Y. Hu and T. Toda. "Remote Vital Signs Measurement of Indoor Walking Persons Using mm-Wave FMCW Radar". *IEEE Access*, Vol. 10, pp. 78219–78230, Jul. 2022.

[Huan 98] N. E. Huang, Z. Shen, S. R. Long, M. C. Wu, H. H. Shih, Q. Zheng, N.-C. Yen, C. C. Tung, and H. H. Liu. "The empirical mode decomposition and the Hilbert spectrum for nonlinear and non-stationary time series analysis". *Proceedings of the Royal Society of London. Series A: Mathematical, Physical and Engineering Sciences*, Vol. 454, No. 1971, p. 903–995, Mar. 1998.

[Infi 13] Infineon. *BGT24ATR11 Silicon Germanium 24 GHz Transceiver MMIC*. 2013.

[Infi 14] Infineon. *BGT24ATR12 Silicon Germanium 24 GHz Transceiver MMIC*. 2014.

[Infi 23a] Infineon. *BGT60ATR24C 60 GHz radar sensor*. 2023.

[Infi 23b] Infineon. *BGT60UTR11AIP 60 GHz radar sensor with antennas in package*. 2023.

[Inte 20] International Commission on Non-Ionizing Radiation Protection and others. "Guidelines for limiting exposure to electromagnetic fields (100 kHz to 300 GHz)".

Health Physics, Vol. 118, No. 5, pp. 483–524, Oct. 2020.

[Inte 23] International Committee on Electromagnetic Safety (ICES). "IEEE Standard for Safety Levels with Respect to Human Exposure to Electric, Magnetic, and Electromagnetic Fields, 0 Hz to 300 GHz". *IEEE Std C95.7-2022 (Revision of IEEE Std C95.7-2014)*, Mar. 2023.

[Inte 98] International Commission on Non-Ionizing Radiation Protection and others. "Guidelines for limiting exposure to time-varying electric, magnetic, and electromagnetic fields (up to 300 GHz)". *Health Physics*, Vol. 74, No. 4, pp. 494–522, Oct. 1998.

[Ishi 17] T. Ishiwata, K. Tsushima, M. Fujie, K. Suzuki, K. Hirota, M. Abe, N. Kawata, J. Terada, and K. Tatsumi. "End-tidal capnographic monitoring to detect apnea episodes during flexible bronchoscopy under sedation". *BMC Pulmonary Medicine*, Vol. 17, pp. 1–5, Jan. 2017.

[Ishr 23] M. S. Ishrak, F. Cai, S. M. M. Islam, O. Borić-Lubecke, T. Wu, and V. M. Lubecke. "Doppler radar remote sensing of respiratory function". *Frontiers in Physiology*, Vol. 14, p. 1130478, Apr. 2023.

[Isla 21] S. M. Islam and V. M. Lubecke. "BreathID: Radar's New Role in Biometrics". *IEEE Aerospace and Electronic Systems Magazine*, Vol. 36, No. 12, pp. 16–23, Dec. 2021.

[Isla 22a] S. M. M. Islam. "Radar-based remote physiological sensing: Progress, challenges, and opportunities". *Frontiers in Physiology*, Vol. 13, p. 955208, Oct. 2022.

[Isla 22b] S. M. Islam, O. Boric-Lubecke, V. M. Lubecke, A.-K. Moadi, and A. E. Fathy. "Contactless Radar-Based Sensors: Recent Advances in Vital-Signs Monitoring of Multiple Subjects". *IEEE Microwave Magazine*, Vol. 23, No. 7, pp. 47–60, Jul. 2022.

[Isla 23] S. M. Islam, A. Droitcour, E. Yavari, V. M. Lubecke, and O. Boric-Lubecke. "Building occupancy estimation using microwave Doppler radar and wavelet transform". *Building and Environment*, Vol. 236, p. 110233, May 2023.

[Jame 89] R. J. James. "A history of radar". *IEE Review*, Vol. 35, No. 9, pp. 343–349, Oct. 1989.

[Janb 18] P. Janbakhshi and M. B. Shamsollahi. "ECG-derived respiration estimation from single-lead ECG using gaussian process and phase space reconstruction methods". *Biomedical Signal Processing and Control*, Vol. 45, pp. 80–90, Aug. 2018.

[Jeni 18] V. Jenik, P. Hudec, and P. Panek. "Extended Noise Analysis Model of CW-type Radar Sensors with IQ Down-Conversion". *Radioengineering*, Vol. 27, No. 2, Jun. 2018.

[Jens 11] B. S. Jensen, T. Jensen, V. Zhurbenko, and T. K. Johansen. "Noise Considerations for Vital Signs CW Radar Sensors". In: *Proceedings of the 5th European Conference on Antennas and Propagation (EUCAP)*, pp. 2805–2809, IEEE, Rome,

Italy, Apr. 2011.

[Kang 16] J. H. Kang, J. K. Kim, S. H. Hong, C. H. Lee, and B. Y. Choi. "Heart Rate Variability for Quantification of Autonomic Dysfunction in Fibromyalgia". *Annals of Rehabilitation Medicine*, Vol. 40, No. 2, p. 301, Apr. 2016.

[Kang 20] S. Kang, D.-K. Kim, Y. Lee, Y.-H. Lim, H.-K. Park, S. H. Cho, and S. H. Cho. "Non-contact diagnosis of obstructive sleep apnea using impulse-radio ultra-wideband radar". *Scientific Reports*, Vol. 10, No. 1, p. 5261, Mar. 2020.

[Kara 10] A. Karagiannis and P. Constantinou. "Noise-Assisted Data Processing With Empirical Mode Decomposition in Biomedical Signals". *IEEE Transactions on Information Technology in Biomedicine*, Vol. 15, No. 1, pp. 11–18, Nov. 2010.

[Kay 93] S. M. Kay. *Fundamentals of Statistical Signal Processing: Estimation Theory*. Prentice-Hall, Inc., 1993.

[Kebe 20] M. Kebe, R. Gadhafi, B. Mohammad, M. Sanduleanu, H. Saleh, and M. Al-Qutayri. "Human Vital Signs Detection Methods and Potential Using Radars: A Review". *Sensors*, Vol. 20, No. 5, p. 1454, Mar. 2020.

[Khan 09] A. H. Khandoker, H. F. Jelinek, and M. Palaniswami. "Identifying diabetic patients with cardiac autonomic neuropathy by heart rate complexity analysis". *BioMedical Engineering OnLine*, Vol. 8, No. 1, p. 3, Jan. 2009.

[Kim 12a] J.-H. Kim, R. Roberge, J. Powell, A. Shafer, and W. J. Williams. "Measurement Accuracy of Heart Rate and Respiratory Rate during Graded Exercise and Sustained Exercise in the Heat Using the Zephyr BioHarness". *International Journal of Sports Medicine*, pp. 497–501, Jun. 2012.

[Kim 12b] J. Kim, Y. Kwon, H.-Y. Chung, C.-S. Kim, G.-M. Eom, J.-H. Jun, and B. K. Park. "Relationship between Body Factors and Postural Sway during Natural Standing". *International Journal of Precision Engineering and Manufacturing*, Vol. 13, pp. 963–968, May 2012.

[King 16] T. Kinghorn, I. Scott, and E. Totten. "Recent Advances in Airborne Phased Array Radar Systems". In: *2016 IEEE International Symposium on Phased Array Systems and Technology (PAST)*, pp. 1–7, IEEE, Waltham, MA, USA, Oct. 2016.

[Koba 98] H. Kobayashi. "Normalization of Respiratory Sinus Arrhythmia by Factoring in Tidal Volume". *Applied Human Science*, Vol. 17, No. 5, pp. 207–213, Aug. 1998.

[Kons 12] M. A. Konstam. "Home Monitoring Should Be the Central Element in an Effective Program of Heart Failure Disease Management". *Circulation*, Vol. 125, No. 6, pp. 820–827, Feb. 2012.

[Krau 16] B. Krauss, S. Silvestri, J. L. Falk, and J. Grayzel. "Carbon dioxide monitoring (capnography)". *UpToDate. Retrieved from http://www. uptodate. com/contents/carbon-dioxide-monitoring-capnography H*, Vol. 14, 2016.

[Krol 54] N. Kroll and M. Bernstein. "Magnetron Research at Columbia Radiation Labo-

ratory". *Transactions of the IRE Professional Group on Microwave Theory and Techniques*, Vol. 2, No. 3, pp. 33–37, Sept. 1954.

[Kun 00] Kun-Mu Chen, Yong Huang, Jianping Zhang, and A. Norman. "Microwave Life-Detection Systems for Searching Human Subjects Under Earthquake Rubble or Behind Barrier". *IEEE Transactions on Biomedical Engineering*, Vol. 47, No. 1, pp. 105–114, Jan. 2000.

[Kuus 16] T. Kuusela. "Methodological Aspects of Heart Rate Variability Analysis". In: *Heart Rate Variability (HRV) Signal Analysis*, pp. 28–61, CRC press, 2016.

[Kwon 18] O. Kwon, J. Jeong, H. B. Kim, I. H. Kwon, S. Y. Park, J. E. Kim, and Y. Choi. "Electrocardiogram Sampling Frequency Range Acceptable for Heart Rate Variability Analysis". *Healthcare Informatics Research*, Vol. 24, No. 3, p. 198, Jul. 2018.

[Laur 20] S. Laurent and P. Boutouyrie. "Arterial Stiffness and Hypertension in the Elderly". *Frontiers in Cardiovascular Medicine*, Vol. 7, p. 544302, Oct. 2020.

[Laza 10] A. Lazaro, D. Girbau, and R. Villarino. "Analysis of Vital Signs Monitoring Using an IR-UWB Radar". *Progress In Electromagnetics Research*, Vol. 100, pp. 265–284, Jan. 2010.

[Le K 19] J. Le Kernec, F. Fioranelli, C. Ding, H. Zhao, L. Sun, H. Hong, J. Lorandel, and O. Romain. "Radar Signal Processing for Sensing in Assisted Living: The Challenges Associated With Real-Time Implementation of Emerging Algorithms". *IEEE Signal Processing Magazine*, Vol. 36, No. 4, pp. 29–41, Jul. 2019.

[Lee 14] Y. S. Lee, P. N. Pathirana, C. L. Steinfort, and T. Caelli. "Monitoring and Analysis of Respiratory Patterns Using Microwave Doppler Radar". *IEEE Journal of Translational Engineering in Health and Medicine*, Vol. 2, pp. 1–12, Oct. 2014.

[Lee 18] H. Lee, B.-H. Kim, and J.-G. Yook. "Path Loss Compensation Method for Multiple Target Vital Sign Detection with 24-GHz FMCW Radar". In: *2018 IEEE Asia-Pacific Conference on Antennas and Propagation (APCAP)*, pp. 100–101, IEEE, Auckland, New Zealand, Aug. 2018.

[Lehr 13] P. Lehrer. "How Does Heart Rate Variability Biofeedback Work? Resonance, the Baroreflex, and Other Mechanisms". *Biofeedback*, Vol. 41, No. 1, pp. 26–31, Mar. 2013.

[Lehr 97] P. Lehrer, R. E. Carr, A. Smetankine, E. Vaschillo, E. Peper, S. Porges, R. Edelberg, R. Hamer, and S. Hochron. "Respiratory Sinus Arrhythmia Versus Neck/Trapezius EMG and Incentive Inspirometry Biofeedback for Asthma: A Pilot Study". *Applied Psychophysiology and Biofeedback*, Vol. 22, No. 2, pp. 95–109, Jun. 1997.

[Li 06] C. Li, Y. Xiao, and J. Lin. "Experiment and Spectral Analysis of a Low-Power Ka-Band Heartbeat Detector Measuring From Four Sides of a Human Body". *IEEE Transactions on Microwave Theory and Techniques*, Vol. 54, No. 12,

pp. 4464–4471, Dec. 2006.

[Li 07] C. Li and J. Lin. "Optimal Carrier Frequency of Non-contact Vital Sign Detectors". In: *2007 IEEE Radio and Wireless Symposium*, pp. 281–284, IEEE, Long Beach, CA, USA, Jan. 2007.

[Li 08] J. Li and P. Stoica. *MIMO Radar Signal Processing*. John Wiley & Sons, 2008.

[Li 10] C. Li, J. Ling, J. Li, and J. Lin. "Accurate Doppler Radar Noncontact Vital Sign Detection Using the RELAX Algorithm". *IEEE Transactions on Instrumentation and Measurement*, Vol. 59, No. 3, pp. 687–695, Mar. 2010.

[Li 13] C. Li, V. M. Lubecke, O. Boric-Lubecke, and J. Lin. "A Review on Recent Advances in Doppler Radar Sensors for Noncontact Healthcare Monitoring". *IEEE Transactions on Microwave Theory and Techniques*, Vol. 61, No. 5, pp. 2046–2060, May 2013.

[Li 17] C. Li, Z. Peng, T.-Y. Huang, T. Fan, F.-K. Wang, T.-S. Horng, J.-M. Munoz-Ferreras, R. Gomez-Garcia, L. Ran, and J. Lin. "A Review on Recent Progress of Portable Short-Range Noncontact Microwave Radar Systems". *IEEE Transactions on Microwave Theory and Techniques*, Vol. 65, No. 5, pp. 1692–1706, May 2017.

[Li 19a] X. Li, Y. He, and X. Jing. "A Survey of Deep Learning-Based Human Activity Recognition in Radar". *Remote Sensing*, Vol. 11, No. 9, p. 1068, May 2019.

[Li 19b] Z. Li, C. Song, C. Yu, R. Xiao, L. Chen, H. Luo, K. Dai, D. Ge, Y. Ding, Y. Zhang, and Q. Zhang. "Application of Satellite Radar Remote Sensing to Landslide Detection and Monitoring: Challenges and Solutions". *Geomatics and Information Science of Wuhan University*, Vol. 44, No. 7, pp. 967–979, Jul. 2019.

[Li 23] Z. Li, T. Jin, Y. Dai, and Y. Song. "Motion-Robust Contactless Heartbeat Sensing Using 4-D Imaging Radar". *IEEE Transactions on Instrumentation and Measurement*, Sept. 2023.

[Lien 16] J. Lien, N. Gillian, M. E. Karagozler, P. Amihood, C. Schwesig, E. Olson, H. Raja, and I. Poupyrev. "Soli: Ubiquitous Gesture Sensing with Millimeter Wave Radar". *ACM Transactions on Graphics (TOG)*, Vol. 35, No. 4, pp. 1–19, Jul. 2016.

[Lin 16] J. C. Lin. "Human Exposure to RF, Microwave, and Millimeter-Wave Electromagnetic Radiation [Health Effects]". *IEEE Microwave Magazine*, Vol. 17, No. 6, pp. 32–36, Jun. 2016.

[Lin 75] J. Lin. "Noninvasive Microwave Measurement of Respiration". *Proceedings of the IEEE*, Vol. 63, No. 10, pp. 1530–1530, Oct. 1975.

[Lipp 19] J. A. Lipponen and M. P. Tarvainen. "A robust algorithm for heart rate variability time series artefact correction using novel beat classification". *Journal of Medical Engineering & Technology*, Vol. 43, No. 3, pp. 173–181, Jul. 2019.

[Liu 21] J. Liu, Y. Li, C. Li, C. Gu, and J.-F. Mao. "Accurate Measurement of Human Vital Signs With Linear FMCW Radars Under Proximity Stationary Clutters".

IEEE Transactions on Biomedical Circuits and Systems, Vol. 15, No. 6, pp. 1393–1404, Dec. 2021.

[Loga 06] M. K. Logani, I. Szabo, V. Makar, A. Bhanushali, S. Alekseev, and M. C. Ziskin. "Effect of Millimeter Wave Irradiation on Tumor Metastasis". *Bioelectromagnetics*, Vol. 27, No. 4, pp. 258–264, Apr. 2006.

[Lohm 02] B. Lohman, O. Boric-Lubecke, V. Lubecke, P. Ong, and M. Sondhi. "A digital signal processor for Doppler radar sensing of vital signs". *IEEE Engineering in Medicine and Biology Magazine*, Vol. 21, No. 5, pp. 161–164, Dec. 2002.

[Lope 23] I. E. López-Delgado, E. Antolinos, I. Sardinero-Meirás, M. Gómez-Bracamonte, J. D. Arias-Londoño, E. Luque-Buzo, F. Grandas, J. I. Godino-Llorente, and J. Grajal. "mm-Wave wireless radar network for early detection of Parkinson's Disease by gait analysis". In: *2023 IEEE Radar Conference (RadarConf23)*, pp. 1–6, IEEE, San Antonio, TX, USA, May 2023.

[Loug 18] P. C. Loughlin, F. Sebat, and J. G. Kellett. "Respiratory Rate: The Forgotten Vital Sign—Make It Count!". *Joint Commission Journal on Quality and Patient Safety*, Vol. 44, No. 8, pp. 494–499, Jun. 2018.

[Lu 11] L. Lu, C. Li, and J. A. Rice. "A Software-Defined Multifunctional Radar Sensor for Linear and Reciprocal Displacement Measurement". In: *2011 IEEE Topical Conference on Wireless Sensors and Sensor Networks*, pp. 17–20, IEEE, Phoenix, AZ, USA, Jan. 2011.

[Lube 02] O. B. Lubecke, P.-W. Ong, and V. Lubecke. "10 GHz Doppler Radar Sensing of Respiration and Heart Movement". In: *Proceedings of the IEEE 28th Annual Northeast Bioengineering Conference (IEEE Cat. No. 02CH37342)*, pp. 55–56, IEEE, Apr. 2002.

[Lube 23] V. Lubecke, O. Borić-Lubecke, M. S. Ishrak, T. Wu, and F. Cai. "Radar Monitoring in Sleep Medicine". In: *2023 16th International Conference on Advanced Technologies, Systems and Services in Telecommunications (TELSIKS)*, pp. 109–113, IEEE, Oct. 2023.

[Ludw 47] C. Ludwig. "Beiträge zur Kenntniss des Einflusses der Respirationsbewegungen auf den Blutlauf im Aortensysteme". *Archiv für Anatomie, Physiologie, und Wissenschaftliche Medicin*, Vol. 4, p. 242–302, 1847.

[Lv 21] W. Lv, W. He, X. Lin, and J. Miao. "Non-Contact Monitoring of Human Vital Signs Using FMCW Millimeter Wave Radar in the 120 GHz Band". *Sensors*, Vol. 21, No. 8, p. 2732, Apr. 2021.

[Mail 17] R. J. Mailloux. *Phased Array Antenna Handbook*. Artech, 2017.

[Maka 05] V. Makar, M. Logani, A. Bhanushali, M. Kataoka, and M. Ziskin. "Effect of Millimeter Waves on Natural Killer Cell Activation". *Bioelectromagnetic*, Vol. 26, No. 1, pp. 10–19, Dec. 2005.

[Mall 99] S. Mallat. *A wavelet tour of signal processing*. Academic Press, 1999.

[Maly 06] V. Malyavej, I. R. Manchester, and A. V. Savkin. "Precision missile guidance using radar/multiple-video sensor fusion via communication channels with bit-rate constraints". *Automatica*, Vol. 42, No. 5, pp. 763–769, May 2006.

[Mass 09] W. Massagram, V. Lubecke, A. Host-Madsen, and O. Boric-Lubecke. "Assessment of Heart Rate Variability and Respiratory Sinus Arrhythmia via Doppler Radar". *IEEE Transactions on Microwave Theory and Techniques*, Vol. 57, No. 10, pp. 2542–2549, Oct. 2009.

[Maur 05] C. Maurer and R. J. Peterka. "A New Interpretation of Spontaneous Sway Measures Based on a Simple Model of Human Postural Control". *Journal of Neurophysiology*, Vol. 93, No. 1, pp. 189–200, Jan. 2005.

[Mazl 09] S. J. Mazlouman, K. Tavakolin, A. Mahanfar, and B. Kaminska. "Contact-less Assessment of In-vivo Body Signals Using Microwave Doppler Radar". *Biomedical Engineering*, Vol. 13, pp. 239–260, Oct. 2009.

[McDo 09] M. A. McDowell, C. D. Fryar, and C. L. Ogden. "Anthropometric Reference Data for Children and Adults: United States, 1988-1994". *Vital and Health Statistics. Series 11, Data from the National Health Survey*, No. 249, pp. 1–68, Apr. 2009.

[McNi 08] W. T. McNicholas. "Diagnosis of Obstructive Sleep Apnea in Adults". *Proceedings of the American Thoracic Society*, Vol. 5, No. 2, pp. 154–160, Feb. 2008.

[Melz 23] P. Melzi, R. Tolosana, and R. Vera-Rodriguez. "ECG Biometric Recognition: Review, System Proposal, and Benchmark Evaluation". *IEEE Access*, Feb. 2023.

[Menc 14] B. Mencía Oliva. *Desarrollo y aplicaciones de radares de alta resolución en bandas milimétricas*. PhD thesis, E.T.S.I Telecomunicación (UPM), 2014.

[Moha 16] S. Mohammadi, A. Hedjazi, M. Sajjadian, N. Ghoroubi, M. Mohammadi, and S. Erfani. "Study of the normal heart size in Northwest part of Iranian population: a cadaveric study". *Journal of Cardiovascular and Thoracic Research*, Vol. 8, No. 3, p. 119, Sept. 2016.

[Morg 09] D. R. Morgan and M. G. Zierdt. "Novel signal processing techniques for Doppler radar cardiopulmonary sensing". *Signal Processing*, Vol. 89, No. 1, pp. 45–66, Jan. 2009.

[Mukh 15] S. C. Mukhopadhyay, M. A. Pimentel, P. H. Charlton, and D. A. Clifton. *Probabilistic Estimation of Respiratory Rate from Wearable Sensors*, Chap. 10, p. 243. Springer, 2015.

[Muño 17] J.-M. Muñoz-Ferreras, Z. Peng, R. Gómez-García, and C. Li. "Review on Advanced Short-Range Multimode Continuous-Wave Radar Architectures for Healthcare Applications". *IEEE Journal of Electromagnetics, RF and Microwaves in Medicine and Biology*, Vol. 1, No. 1, pp. 14–25, Jun. 2017.

[Naza 18] G. Nazari, P. Bobos, J. C. MacDermid, K. E. Sinden, J. Richardson, and A. Tang. "Psychometric properties of the Zephyr bioharness device: a systematic review". *BMC Sports Science, Medicine and Rehabilitation*, Vol. 10, pp. 1–8, Feb. 2018.

[NXP 19] NXP. *TEF810X 77GHz Automotive Radar Transceiver*. 2019.

[NXP 20] NXP. *TEF82xx 77GHz Automotive Radar Transceiver*. 2020.

[Oged 10] G. Ogedegbe and T. Pickering. "Principles and techniques of blood pressure measurement". *Cardiology Clinics*, Vol. 28, No. 4, pp. 571–586, Nov. 2010.

[Olin 84] A. Oliner. "Historical Perspectives on Microwave Field Theory". *IEEE Transactions on Microwave Theory and Techniques*, Vol. 32, No. 9, pp. 1022–1045, Sept. 1984.

[Open 16] OpenStax. *Anatomy and Physiology*. OpenStax CNX, 2016.

[Pan 85] J. Pan and W. J. Tompkins. "A Real-Time QRS Detection Algorithm". *IEEE Transactions on Biomedical Engineering*, No. 3, pp. 230–236, Mar. 1985.

[Park 07] B.-K. Park, O. Boric-Lubecke, and V. M. Lubecke. "Arctangent Demodulation With DC Offset Compensation in Quadrature Doppler Radar Receiver Systems". *IEEE Transactions on Microwave Theory and Techniques*, Vol. 55, No. 5, pp. 1073–1079, May 2007.

[Park 20] J.-H. Park and J.-R. Yang. "Multiphase Continuous-Wave Doppler Radar With Multiarc Circle Fitting Algorithm for Small Periodic Displacement Measurement". *IEEE Transactions on Microwave Theory and Techniques*, Vol. 69, No. 11, pp. 5135–5144, Dec. 2020.

[Park 24] J. Park, S. Yang, G. Chung, I. J. L. Zanghettin, and J. Han. "Ultra-Wideband Radar-Based Sleep Stage Classification in Smartphone Using an End-to-End Deep Learning". *IEEE Access*, Apr. 2024.

[Park 72] T. Parks and J. McClellan. "A program for the design of linear phase finite impulse response digital filters". *IEEE Transactions on Audio and Electroacoustics*, Vol. 20, No. 3, pp. 195–199, Aug. 1972.

[Paul 17] M. Pauli, B. Gottel, S. Scherr, A. Bhutani, S. Ayhan, W. Winkler, and T. Zwick. "Miniaturized Millimeter-Wave Radar Sensor for High-Accuracy Applications". *IEEE Transactions on Microwave Theory and Techniques*, Vol. 65, No. 5, pp. 1707–1715, May 2017.

[Pere 15] T. Pereira, C. Correia, and J. Cardoso. "Novel Methods for Pulse Wave Velocity Measurement". *Journal of Medical and Biological Engineering*, Vol. 35, No. 5, pp. 555–565, Oct. 2015.

[Petk 09] D. T. Petkie, C. Benton, and E. Bryan. "Millimeter Wave Radar for Remote Measurement of Vital Signs". In: *2009 IEEE Radar Conference*, pp. 1–3, Pasadena, CA, USA, May 2009.

[Pisa 21] T. Pisanu, G. Muntoni, L. Schirru, P. Ortu, E. Urru, and G. Montisci. "Recent Advances of the BIRALET System about Space Debris Detection". *Aerospace*, Vol. 8, No. 3, p. 86, Mar. 2021.

[Prat 19] A. Prat, S. Blanch, A. Aguasca, J. Romeu, and A. Broquetas. "Collimated

Beam FMCW Radar for Vital Sign Patient Monitoring". *IEEE Transactions on Antennas and Propagation*, Vol. 67, No. 8, pp. 5073–5080, Aug. 2019.

[Prat 87] V. Pratt. "Direct Least-Squares Fitting of Algebraic Surfaces". *ACM SIGGRAPH Computer Graphics*, Vol. 21, No. 4, pp. 145–152, Aug. 1987.

[Radz 04] A. Radzievsky, O. Gordiienko, I. Szabo, S. Alekseev, and M. Ziskin. "Millimeter Wave-Induced Suppression of B16 F10 Melanoma Growth in Mice: Involvement of Endogenous Opioids". *Bioelectromagnetics*, Vol. 25, No. 6, pp. 466–473, Sept. 2004.

[Raje 06] U. Rajendra Acharya, K. Paul Joseph, N. Kannathal, C. M. Lim, and J. S. Suri. "Heart rate variability: a review". *Medical and Biological Engineering and Computing*, Vol. 44, pp. 1031–1051, Dec. 2006.

[Rams 67] J. Ramsey. "Millimeter Wave Research In The 1890's". *IEEE Spectrum*, Vol. 4, p. 5, Dec. 1967.

[Rapp 19] T. S. Rappaport, Y. Xing, O. Kanhere, S. Ju, A. Madanayake, S. Mandal, A. Alkhateeb, and G. C. Trichopoulos. "Wireless Communications and Applications Above 100 GHz: Opportunities and Challenges for 6G and Beyond". *IEEE Access*, Vol. 7, pp. 78729–78757, Jun. 2019.

[Ream 93] R. E. Reamer, W. Stockton, and R. D. Stromfors. "New military uses for synthetic aperture radar (SAR)". In: *Airborne Reconnaissance XVI*, pp. 113–119, International Society for Optics and Photonics, SPIE, San Diego, CA, United States, Feb. 1993.

[Refe 10] Reference Values for Arterial Stiffness' Collaboration. "Determinants of pulse wave velocity in healthy people and in the presence of cardiovascular risk factors:'establishing normal and reference values"'. *European Heart Journal*, Vol. 31, No. 19, pp. 2338–2350, Oct. 2010.

[Ren 16] L. Ren, H. Wang, K. Naishadham, O. Kilic, and A. E. Fathy. "Phase-Based Methods for Heart Rate Detection Using UWB Impulse Doppler Radar". *IEEE Transactions on Microwave Theory and Techniques*, Vol. 64, No. 10, pp. 3319–3331, Oct. 2016.

[Rene 22] Renesas Electronics. *RAA270205 Automotive Radar Transceiver*. 2022.

[Rife 74] D. Rife and R. Boorstyn. "Single-Tone Parameter Estimation from Discrete-Time Observations". *IEEE Transactions on Information Theory*, Vol. 20, No. 5, p. 591–598, Sept. 1974.

[Rill 08] G. Rilling and P. Flandrin. "One or Two Frequencies? The Empirical Mode Decomposition Answers". *IEEE Transactions on Signal Processing*, Vol. 56, No. 1, pp. 85–95, Jan. 2008.

[Robe 04] F. C. Robey, S. Coutts, D. Weikle, J. C. McHarg, and K. Cuomo. "MIMO Radar Theory and Experimental Results". In: *Conference Record of the Thirty-Eighth Asilomar Conference on Signals, Systems and Computers, 2004*, pp. 300–304,

IEEE, Pacific Grove, CA, USA, Nov. 2004.

[Roja 98] M. Rojavin and M. Ziskin. "Medical application of millimetre waves". *QJM: An International Journal of Medicine*, Vol. 91, No. 1, pp. 57–66, Jan. 1998.

[Roma 14] S. Romagnoli, Z. Ricci, D. Quattrone, L. Tofani, O. Tujjar, G. Villa, S. M. Romano, and A. R. De Gaudio. "Accuracy of invasive arterial pressure monitoring in cardiovascular patients: an observational study". *Critical Care*, Vol. 18, No. 6, p. 644, Dec. 2014.

[Russ 97] D. M. Russell. "Error Measures for Comparing Transient Data: Part I: Development of a Comprehensive Error Measure". In: *Proceedings of the 68th Shock and Vibration Symposium*, pp. 175–184, Hunt Valley, MD, USA, Nov. 1997.

[Sadr 21] H. Sadreazami, M. Bolic, and S. Rajan. "Contactless Fall Detection Using Time-Frequency Analysis and Convolutional Neural Networks". *IEEE Transactions on Industrial Informatics*, Vol. 17, No. 10, pp. 6842–6851, Oct. 2021.

[Saka 24] T. Sakamoto, I. Iwata, T. Minami, and T. Matsumoto. "Review: Noncontact Sensing of Animals Using Radar". *IEICE Transactions on Electronics*, Sept. 2024.

[Samm 11] P. F. Sammartino, J. Fortuny-Guasch, and D. Tarchi. "Efficient signal processing in MIMO radars". In: *2011 8th European Radar Conference*, pp. 13–16, IEEE, Manchester, UK, Oct. 2011.

[Sant 18] A. Santra, R. V. Ulaganathan, and T. Finke. "Short-Range Millimetric-Wave Radar System for Occupancy Sensing Application". *IEEE Sensors Letters*, Vol. 2, No. 3, pp. 1–4, Sept. 2018.

[Sche 20] S. Schellenberger, K. Shi, T. Steigleder, A. Malessa, F. Michler, L. Hameyer, N. Neumann, F. Lurz, R. Weigel, C. Ostgathe, and A. Koelpin. "A dataset of clinically recorded radar vital signs with synchronised reference sensor signals". *Scientific Data*, Vol. 7, No. 1, pp. 1–11, Sept. 2020.

[Schw 20] A. R. Schwerdtfeger, G. Schwarz, K. Pfurtscheller, J. F. Thayer, M. N. Jarczok, and G. Pfurtscheller. "Heart rate variability (HRV): From brain death to resonance breathing at 6 breaths per minute". *Clinical Neurophysiology*, Vol. 131, No. 3, pp. 676–693, Mar. 2020.

[Seif 19] A.-K. Seifert, M. G. Amin, and A. M. Zoubir. "Toward Unobtrusive In-Home Gait Analysis Based on Radar Micro-Doppler Signatures". *IEEE Transactions on Biomedical Engineering*, Vol. 66, No. 9, pp. 2629–2640, Sept. 2019.

[Serm 03] M. Sermesant. *Modèle électromécanique du coeur pour l'analyse d'image et la simulation (Electromechanical Model of the Heart for Image Analysis and Simulation)*. PhD thesis, Université Nice Sophia Antipolis, May 2003.

[Shaf 17] F. Shaffer and J. P. Ginsberg. "An Overview of Heart Rate Variability Metrics and Norms". *Frontiers in Public Health*, p. 258, Sept. 2017.

[Shar 17] M. Sharma, K. Barbosa, V. Ho, D. Griggs, T. Ghirmai, S. K. Krishnan, T. K.

Hsiai, J.-C. Chiao, and H. Cao. "Cuff-Less and Continuous Blood Pressure Monitoring: A Methodological Review". *Technologies*, Vol. 5, No. 2, p. 21, May 2017.

[Shi 20] K. Shi, S. Schellenberger, C. Will, T. Steigleder, F. Michler, J. Fuchs, R. Weigel, C. Ostgathe, and A. Koelpin. "A dataset of radar-recorded heart sounds and vital signs including synchronised reference sensor signals". *Scientific Data*, Vol. 7, No. 1, p. 50, Feb. 2020.

[Shi 23] D. Shi, F. Liang, J. Qiao, Y. Wang, Y. Zhu, H. Lv, X. Yu, T. Jiao, F. Liao, K. Yan, *et al.* "A Novel Non-Contact Detection and Identification Method for the Post-Disaster Compression State of Injured Individuals Using UWB Bio-Radar". *Bioengineering*, Vol. 10, No. 8, p. 905, Jul. 2023.

[Sili 20] Silicon Radar. *TRA120045 120-GHz Wide-Band IQ Transceiver with Antennas on Chip*. 2020.

[Sili 22] Silicon Radar. "Radar Evaluation Kits for various Front Ends". https://siliconradar.com/evalkits/. Accessed on May, 2022.

[Sili 23a] Silicon Radar. *T4R4060096 60-GHz Highly Integrated MIMO Transceiver with four Receivers and four Transmitters*. 2023.

[Sili 23b] Silicon Radar. *TR2060095 60-GHz Highly Integrated IQ Transceiver with two Receivers*. 2023.

[Sili 23c] Silicon Radar. *TRA240091 EXB001 240-GHz Highly Integrated Radar Transceiver with Antenna on Chip*. 2023.

[Sili 23d] Silicon Radar. *TRX120067 120-GHz Highly Integrated IQ Transceiver with Antennas in Package in Silicon Germanium Technology*. 2023.

[Silv 24] M. Louro da Silva, C. Gouveia, D. F. Albuquerque, and H. Plácido da Silva. "Radar-Based Invisible Biometric Authentication". *Information*, Vol. 15, No. 1, p. 44, Jan. 2024.

[Sing 13] A. Singh, X. Gao, E. Yavari, M. Zakrzewski, X. H. Cao, V. M. Lubecke, and O. Boric-Lubecke. "Data-Based Quadrature Imbalance Compensation for a CW Doppler Radar System". *IEEE Transactions on Microwave Theory and Techniques*, Vol. 61, No. 4, pp. 1718–1724, Apr. 2013.

[Sing 21] A. Singh, S. U. Rehman, S. Yongchareon, and P. H. J. Chong. "Multi-Resident Non-Contact Vital Sign Monitoring Using Radar: A Review". *IEEE Sensors Journal*, Vol. 21, No. 4, pp. 4061–4084, 2021.

[Siyi 15] Siying Wang, A. Pohl, T. Jaeschke, M. Czaplik, M. Kony, S. Leonhardt, and N. Pohl. "A Novel Ultra-Wideband 80 GHz FMCW Radar System for Contactless Monitoring of Vital Signs". In: *2015 37th Annual International Conference of the IEEE Engineering in Medicine and Biology Society (EMBC)*, pp. 4978–4981, IEEE, Milan, Italy, Aug. 2015.

[Skol 62] M. I. Skolnik. *Radar Handbook*. McGraw-Hill Education, 1962.

[Skol 80] M. I. Skolnik. *Introduction to Radar Systems*. McGraw-Hill New York, 1980.

[Slep 54] D. Slepian. "Estimation of signal parameters in the presence of noise". *Transactions of the IRE Professional Group on Information Theory*, Vol. 3, No. 3, p. 68–89, Mar. 1954.

[Soam 82] R. Soames and J. Atha. "The spectral characteristics of postural sway behaviour". *European Journal of Applied Physiology and Occupational Physiology*, Vol. 49, pp. 169–177, Aug. 1982.

[Sobo 84] H. Sobol. "Microwave Communications - An Historical Perspective". *IEEE Transactions on Microwave Theory and Techniques*, Vol. 32, No. 9, pp. 1170–1181, Sept. 1984.

[Star 39] I. Starr, A. J. Rawson, H. A. Schroeder, and N. R. Joseph. "Studies on the estimation of cardiac output in man, and of abnormalities in cardiac function, from the heart's recoil and the blood's impact; the ballistocardiogram". *American Journal of Physiology-Legacy Content*, Vol. 127, No. 1, pp. 1–28, Jul. 1939.

[Stey 88] H. Steyskal. "Digital Beamforming". In: *1988 18th European Microwave Conference*, pp. 49–57, IEEE, Stockholm, Sweden, Sept. 1988.

[STMi 19] STMicroelectronics. *STRADA431 24 GHz Transceiver MMIC for Automotive Radar Sensor*. 2019.

[Stov 92] A. G. Stove. "Linear FMCW radar techniques". In: *IEE Proceedings F (Radar and Signal Processing)*, pp. 343–350, IET, Oct. 1992.

[Subo 22] M. Z. Suboh, R. Jaafar, N. A. Nayan, N. H. Harun, and M. S. F. Mohamad. "Analysis on Four Derivative Waveforms of Photoplethysmogram (PPG) for Fiducial Point Detection". *Frontiers in Public Health*, Vol. 10, p. 920946, Jun. 2022.

[Taba 21] A. Tabassum and M. A. R. Ahad. *Biomedical Radar and Antenna Systems for Contactless Human Activity Analysis*, pp. 213–241. Springer, 2021.

[Tadi 15] M. J. Tadi, E. Lehtonen, T. Koivisto, M. Pänkäälä, A. Paasio, and M. Teräs. "Seismocardiography: Toward Heart Rate Variability (HRV) Estimation". In: *2015 IEEE International Symposium on Medical Measurements and Applications (MeMeA) Proceedings*, pp. 261–266, IEEE, Turin, Italy, May. 2015.

[Taeb 17] A. Taebi and H. A. Mansy. "Time-Frequency Distribution of Seismocardiographic Signals: A Comparative Study". *Bioengineering*, Vol. 4, No. 2, p. 32, Apr. 2017.

[Taeb 19] A. Taebi, B. E. Solar, A. J. Bomar, R. H. Sandler, and H. A. Mansy. "Recent Advances in Seismocardiography". *Vibration*, Vol. 2, No. 1, pp. 64–86, Jan. 2019.

[Task 96] Task Force of the European Society of Cardiology and the North American Society of Pacing and Electrophysiology. "Heart rate variability: standards of measurement, physiological interpretation, and clinical use". *Circulation*, Vol. 93,

No. 5, pp. 1043–1065, Mar. 1996.

[Tata 18] A. B. Tataraidze, L. N. Anishchenko, L. S. Korostovtseva, M. V. Bochkarev, and Y. V. Sviryaev. "Non-contact Respiratory Monitoring of Subjects with Sleep-Disordered Breathing". In: *2018 IEEE International Conference "Quality Management, Transport and Information Security, Information Technologies" (IT&QM&IS)*, pp. 736–738, IEEE, St. Petersburg, Sept. 2018.

[Tere 12] L. G. Tereshchenko, I. Cygankiewicz, S. McNitt, R. Vazquez, A. Bayes-Genis, L. Han, S. Sur, J.-P. Couderc, R. D. Berger, A. B. de Luna, and W. Zareba. "Predictive Value of Beat-to-Beat QT Variability Index Across the Continuum of Left Ventricular Dysfunction: Competing Risks of Noncardiac or Cardiovascular Death and Sudden or Nonsudden Cardiac Death". *Circulation: Arrhythmia and Electrophysiology*, Vol. 5, No. 4, pp. 719–727, Aug. 2012.

[Texa 18] Texas Instruments. *DAC1000 EVM User's Guide*. 2018.

[Texa 20a] Texas Instruments. *AWR2243 Cascade User's Guide*. 2020.

[Texa 20b] Texas Instruments. *AWR2243 Evaluation Module (AWR2243BOOST) mmWave Sensing Solution*. 2020.

[Texa 20c] Texas Instruments. *AWR2243 single-chip 76-to 81-GHz FMCW transceiver*. 2020.

[Texa 20d] Texas Instruments. *MMWCAS-DSP-EVM User's Guide*. 2020.

[Texa 21] Texas Instruments. *AWR1642 Single-Chip 77- to 79-GHz FMCW Radar Sensor*. 2021.

[Texa 22a] Texas Instruments. *AWR1843 Single-Chip 77- to 79-GHz FMCW Radar Sensor*. 2022.

[Texa 22b] Texas Instruments. *AWR6443, AWR6843 Single-Chip 60- to 64-GHz mmWave Sensor*. 2022.

[Texa 24] Texas Instruments. *AWRL6432 Single-Chip 57- to 64GHz Automotive Radar Sensor*. 2024.

[Till 07] T. Tillin, J. Chambers, I. Malik, E. Coady, S. Byrd, J. Mayet, A. R. Wright, J. Kooner, A. Shore, S. Thom, *et al.* "Measurement of pulse wave velocity: site matters". *Journal of Hypertension*, Vol. 25, No. 2, pp. 383–389, Feb. 2007.

[Toft 20] S. Toften, S. Pallesen, M. Hrozanova, F. Moen, and J. Grønli. "Validation of sleep stage classification using non-contact radar technology and machine learning (Somnofy®)". *Sleep Medicine*, Vol. 75, pp. 54–61, Nov. 2020.

[Tsao 13] J. Tsao, S. Evans, L. Seidman, Lung, L. Zeltzer, and B. Naliboff. "Heart rate variability as a biomarker for autonomic nervous system response differences between children with chronic pain and healthy control children". *Journal of Pain Research*, p. 449, Jun. 2013.

[Van 01] L. M. Van Bortel, E. J. Balkestein, J. J. van der Heijden-Spek, F. H. Vanmolkot,

J. A. Staessen, J. A. Kragten, J. W. Vredeveld, M. E. Safar, H. A. S. Boudier, and A. P. Hoeks. "Non-invasive assessment of local arterial pulse pressure: comparison of applanation tonometry and echo-tracking". *Journal of Hypertension*, Vol. 19, No. 6, pp. 1037–1044, Jun. 2001.

[Van 59] B. Van Iperen. "Reflex klystrons for millimeter waves". In: *Proceedings of the Symposium on Millimeter Waves*, pp. 249–250, New York, NY, USA, Mar. 1959.

[Vari 12] B. J. van Varik, R. J. M. W. Rennenberg, C. P. Reutelingsperger, A. A. Kroon, P. W. de Leeuw, and L. J. Schurgers. "Mechanisms of arterial remodeling: lessons from genetic diseases". *Frontiers in Genetics*, Vol. 3, Dec. 2012.

[Vasa 02] R. Vasan, M. Larson, and E. Leip. "Impact of high-normal blood pressure on the risk of cardiovascular disease". *ACC Current Journal Review*, Vol. 11, No. 2, p. 31, Mar. 2002.

[Vasa 20] C. Vasanelli, F. Roos, A. Durr, J. Schlichenmaier, P. Hugler, B. Meinecke, M. Steiner, and C. Waldschmidt. "Calibration and direction-of-arrival estimation of millimeter-wave radars: A practical introduction". *IEEE Antennas and Propagation Magazine*, Vol. 62, No. 6, pp. 34–45, 2020.

[Viea 15] S. Vieau and P. A. Iaizzo. *Basic ECG Theory, 12-Lead Recordings, and Their Interpretation*, pp. 321–334. Springer International Publishing, 2015.

[Vinc 13] G. Vinci, S. Lindner, F. Barbon, S. Mann, M. Hofmann, A. Duda, R. Weigel, and A. Koelpin. "Six-Port Radar Sensor for Remote Respiration Rate and Heartbeat Vital-Sign Monitoring". *IEEE Transactions on Microwave Theory and Techniques*, Vol. 61, No. 5, pp. 2093–2100, May 2013.

[Vyso 23] N. Vysotskaya, C. Will, L. Servadei, N. Maul, C. Mandl, M. Nau, J. Harnisch, and A. Maier. "Continuous Non-Invasive Blood Pressure Measurement Using 60 GHz-Radar – A Feasibility Study". *Sensors*, Vol. 23, No. 8, p. 4111, Apr. 2023.

[Wan 14] Q. Wan, Y. Li, C. Li, and R. Pal. "Gesture Recognition for Smart Home Applications using Portable Radar Sensors". In: *2014 36th Annual International Conference of the IEEE Engineering in Medicine and Biology Society*, pp. 6414–6417, IEEE, Chicago, IL, USA, Aug. 2014.

[Wang 12] T. Wang, M. Zhang, Q. Yu, and H. Zhang. "Comparing the applications of EMD and EEMD on time–frequency analysis of seismic signal". *Journal of Applied Geophysics*, Vol. 83, pp. 29–34, Aug. 2012.

[Wang 13a] J. Wang, X. Wang, Z. Zhu, J. Huangfu, C. Li, and L. Ran. "1-D Microwave Imaging of Human Cardiac Motion: An Ab-Initio Investigation". *IEEE Transactions on Microwave Theory and Techniques*, Vol. 61, No. 5, pp. 2101–2107, May 2013.

[Wang 13b] Y. Wang, Q. Liu, and A. E. Fathy. "CW and Pulse–Doppler Radar Processing Based on FPGA for Human Sensing Applications". *IEEE Transactions on Geoscience and Remote Sensing*, Vol. 51, No. 5, pp. 3097–3107, May 2013.

[Wang 14a] G. Wang, J.-M. Muñoz-Ferreras, C. Gu, C. Li, and R. Gomez-Garcia. "Application

of Linear-Frequency-Modulated Continuous-Wave (LFMCW) Radars for Tracking of Vital Signs". *IEEE Transactions on Microwave Theory and Techniques*, Vol. 62, No. 6, pp. 1387–1399, Jun. 2014.

[Wang 14b] J. Wang, X. Wang, L. Chen, J. Huangfu, C. Li, and L. Ran. "Noncontact Distance and Amplitude-Independent Vibration Measurement Based on an Extended DACM Algorithm". *IEEE Transactions on Instrumentation and Measurement*, Vol. 63, No. 1, pp. 145–153, Jan. 2014.

[Wang 19] P. Wang, Y. Zhang, Y. Ma, F. Liang, Q. An, H. Xue, X. Yu, H. Lv, and J. Wang. "Method for Distinguishing Humans and Animals in Vital Signs Monitoring Using IR-UWB Radar". *International Journal of Environmental Research and Public Health*, Vol. 16, No. 22, p. 4462, Nov. 2019.

[Wang 21] Y. Wang, H. Liu, K. Cui, A. Zhou, W. Li, and H. Ma. "m-Activity: Accurate and Real-Time Human Activity Recognition Via Millimeter Wave Radar". In: *ICASSP 2021-2021 IEEE International Conference on Acoustics, Speech and Signal Processing (ICASSP)*, pp. 8298–8302, IEEE, Toronto, ON, Canada, Jun. 2021.

[Wang 24] C. Wang, T. S. Kumar, W. De Raedt, G. Camps, H. Hallez, and B. Vanrumste. "Eat-Radar: Continuous Fine-Grained Intake Gesture Detection Using FMCW Radar and 3D Temporal Convolutional Network With Attention". *IEEE Journal of Biomedical and Health Informatics*, Feb. 2024.

[Wart 77] W. Warters. "WT4 Millimeter Waveguide System: Introduction". *Bell System Technical Journal*, Vol. 56, No. 10, pp. 1825–1827, Dec. 1977.

[Will 17] C. Will, K. Shi, S. Schellenberger, T. Steigleder, F. Michler, R. Weigel, C. Ostgathe, and A. Koelpin. "Local Pulse Wave Detection Using Continuous Wave Radar Systems". *IEEE Journal of Electromagnetics, RF and Microwaves in Medicine and Biology*, Vol. 1, No. 2, pp. 81–89, Dec. 2017.

[Will 18] C. Will, K. Shi, S. Schellenberger, T. Steigleder, F. Michler, J. Fuchs, R. Weigel, C. Ostgathe, and A. Koelpin. "Radar-Based Heart Sound Detection". *Scientific Reports*, Vol. 8, No. 1, pp. 1–14, Jul. 2018.

[Wilt 84] J. C. Wiltse. "History of Millimeter and Submillimeter Waves". *IEEE Transactions on Microwave Theory and Techniques*, Vol. 32, No. 9, pp. 1118–1127, Sept. 1984.

[Worl] "World Health Organization Global Health Expenditure Database". apps.who.int/nha/database. Retrieved on April 7, 2023.

[Worl 20] World Health Organization. *World Health Statistics 2020: Monitoring Health for the SDGs, Sustainable Development Goals*. World Health Organization, Geneva, 2020. Licence: CC BY-NC-SA 3.0 IGO.

[Worl 23] World Health Organization. *Global Report on Hypertension: The Race Against a Silent Killer*. World Health Organization, September 2023.

[Wu 09] Z. Wu and N. E. Huang. "Ensemble empirical mode decomposition: a noise-

assisted data analysis method". *Advances in Adaptive Data Analysis*, Vol. 1, No. 01, pp. 1–41, Jan. 2009.

[Wu 12] H.-Y. Wu, M. Rubinstein, E. Shih, J. Guttag, F. Durand, and W. Freeman. "Eulerian Video Magnification for Revealing Subtle Changes in the World". *ACM Transactions on Graphics*, Vol. 31, No. 4, pp. 1–8, Aug. 2012.

[Wu 15] T. Wu, T. S. Rappaport, and C. M. Collins. "Safe for Generations to Come: Considerations of Safety for Millimeter Waves in Wireless Communications". *IEEE Microwave Magazine*, Vol. 16, No. 2, pp. 65–84, Mar. 2015.

[Xia 18] Z. Xia, M. M. H. Shandhi, O. T. Inan, and Y. Zhang. "Non-Contact Sensing of Seismocardiogram Signals Using Microwave Doppler Radar". *IEEE Sensors Journal*, Vol. 18, No. 14, pp. 5956–5964, Jul. 2018.

[Yama 15] T. Yamamoto, C. E. Smith, Y. Suzuki, K. Kiyono, T. Tanahashi, S. Sakoda, P. Morasso, and T. Nomura. "Universal and individual characteristics of postural sway during quiet standing in healthy young adults". *Physiological Reports*, Vol. 3, No. 3, p. e12329, Mar. 2015.

[Yan 22] J. Yan, H. Jiao, W. Pu, C. Shi, J. Dai, and H. Liu. "Radar sensor network resource allocation for fused target tracking: A brief review". *Information Fusion*, Vol. 86, pp. 104–115, Oct. 2022.

[Yao 22] Y. Yao, C. Liu, H. Zhang, B. Yan, P. Jian, P. Wang, L. Du, X. Chen, B. Han, and Z. Fang. "Fall Detection System Using Millimeter-Wave Radar Based on Neural Network and Information Fusion". *IEEE Internet of Things Journal*, Vol. 9, No. 21, pp. 21038–21050, Nov. 2022.

[Yeh 10] J.-R. Yeh, J.-S. Shieh, and N. E. Huang. "Complementary ensemble empirical mode decomposition: A novel noise enhanced data analysis method". *Advances in Adaptive Data Analysis*, Vol. 2, No. 02, pp. 135–156, Apr. 2010.

[Yin 23] M. Yin, R. Ma, H. Luo, J. Li, Q. Zhao, and M. Zhang. "Non-contact sensing technology enables precision livestock farming in smart farms". *Computers and Electronics in Agriculture*, Vol. 212, p. 108171, Sept. 2023.

[Zane 91] J. Zanetti and D. Salerno. "Seismocardiography: a technique for recording precordial acceleration". In: *[1991] Computer-Based Medical Systems@m_-Proceedings of the Fourth Annual IEEE Symposium*, pp. 4–9, IEEE Comput. Soc. Press, Baltimore, MD, USA, May 1991.

[Zeph 12] Zephyr Technology. *BioHarness 3 User Manual*. 2012.

[Zhad 11] M. Zhadobov, N. Chahat, R. Sauleau, C. Le Quement, and Y. Le Drean. "Millimeter-wave interactions with the human body: State of knowledge and recent advances". *International Journal of Microwave and Wireless Technologies*, Vol. 3, No. 2, pp. 237–247, Mar. 2011.

[Zhan 23] J. Zhang, X. Na, R. Xi, Y. Sun, and Y. He. "mmHawkeye: Passive UAV Detection with a COTS mmWave Radar". In: *2023 20th Annual IEEE International*

Conference on Sensing, Communication, and Networking (SECON), pp. 267–275, IEEE, Madrid, Spain, Sept. 2023.

[Zhao 16] M. Zhao, F. Adib, and D. Katabi. "Emotion recognition using wireless signals". In: *Proceedings of the 22nd Annual International Conference on Mobile Computing and Networking*, pp. 95–108, New York City, NY, USA, Oct. 2016.

Appendix A

Radar Working Principle

This appendix provides the mathematical formulation behind the two types of radar waveforms utilized in this thesis: continuous-wave (CW) and linear-frequency-modulated continuous-wave (LFMCW) configurations.

A.1 CW radars

The ideal CW transmitted signal can be defined with the following expression:

$$s_{tx}(t) = A\exp\left(j(2\pi f_0 t + \phi)\right) \tag{A.1}$$

where f_0 is the transmitted frequency and ϕ is the initial phase. The received signal for a point scatterer at a range $R(t)$ can be expressed as:

$$s_{rx}(t) = \sigma s_{tx}\left(t - \frac{2R(t)}{c}\right) \tag{A.2}$$

where σ is the reflection coefficient of the target and $\frac{2R(t)}{c}$ is the round trip delay, being c, the light velocity. The received signal is mixed with the transmitted one, thus:

$$\begin{aligned} s_b(t) =& s_{tx}(t)\cdot s_{rx}^*(t) = \\ & A\exp\left(j(2\pi f_0 t+\phi)\right)\cdot \sigma A\exp\left(-j\left(2\pi f_0\left(t-\frac{2R(t)}{c}\right)+\phi\right)\right) = \\ & A^2\sigma\exp\left(j\left(2\pi f_0 t+\phi-2\pi f_0 t+\frac{4\pi f_0 R(t)}{c}-\phi\right)\right) \end{aligned} \tag{A.3}$$

Therefore, the radar baseband signal can be expressed as:

$$s_b(t) = A_b\exp\left(j\frac{4\pi f_0 R(t)}{c}\right) \tag{A.4}$$

where A_b is the signal amplitude. Thus, the displacement information is contained in the phase of $s_b(t)$.

A.2 LFMCW radar

Analogously to CW radars, the LFMCW transmitted signal can be defined as:

$$s_{tx}(t) = A\exp\left(j\left(2\pi f_0 t + \pi\frac{B}{T}t^2\right)\right), \qquad t \in [0, T] \tag{A.5}$$

where f_0 stands for the initial transmitted frequency, B is the transmitted bandwidth and T is the sweep time. Similarly, the received signal is the transmitted signal that has been delayed in time by the round-trip propagation time, which is given by the ratio of the target range to the speed of light, $2R(\tau)/c$, where the range is assumed constant for each sweep time[1], and τ is the so-called *slow time*:

$$s_{rx}(t, \tau) = \sigma s_{tx}\left(t - \frac{2R(\tau)}{c}\right) \tag{A.6}$$

In the demodulation process, a replica of the transmitted signal, Eq. A.5, is mixed with the received signal, Eq. A.6, which is the so-called *beat signal*. The beat signal is given by:

$$\begin{aligned} &s_b(t, \tau) = s_{tx}(t) \cdot s^*_{rx}(t) = \\ &A\exp\left(j\left(2\pi f_0 t + \pi\frac{B}{T}t^2\right)\right) A\sigma\exp\left(-j\left(2\pi f_0\left(t - \frac{2R(\tau)}{c}\right) + \pi\frac{B}{T}\left(t - \frac{2R(\tau)}{c}\right)^2\right)\right) = \\ &A^2\sigma\exp\left(j\left(2\pi f_0 t + \pi\frac{B}{T}t^2 - 2\pi f_0 t + 4\pi f_0\frac{R(\tau)}{c} - \pi\frac{B}{T}t^2 + 4\pi\frac{BR(\tau)}{Tc}t - 4\pi\frac{BR(\tau)^2}{Tc^2}\right)\right) \end{aligned} \tag{A.7}$$

Simplifying,

$$s_b(t, \tau) = A_b\exp\left(j(2\pi f_b(\tau)t + \phi(\tau) + \phi_2(\tau)\right) \tag{A.8}$$

Therefore, the beat signal follows a sinusoidal waveform with a frequency known as beat frequency $f_b(\tau) = \frac{2B}{Tc}R(\tau)$, $\phi(\tau) = 4\pi f_0 R(\tau)/c$, and $\phi_2(\tau) = -\frac{4\pi BR^2(\tau)}{Tc^2}$. $\phi_2(\tau)$ represents the residual video phase (RVP) [Carr 95], which is found to be negligible and can be ignored, since it is proportional to $1/c^2$.

[1]This is known as the *stop and go assumption* [Carr 95].

Appendix B

IQ imbalance influence in phase extraction

B.1 CW case

The phase extraction in CW radars is carried out by performing the arctangent demodulation of the beat signal. The beat signal defined in Section 2.2 (Eq. 2.2) can also be expressed as:

$$s_b(t) = I(t) + jQ(t) \tag{B.1}$$

where $I(t)$ and $Q(t)$ are the in-phase and quadrature signal components, respectively. Non-ideal systems induce amplitude and phase imbalances between both channels which have to be calibrated. Additionally, there are dc-offset problems that have to be addressed in the I/Q demodulation. Therefore, the I- and Q-channels have the following expressions:

$$\begin{aligned} I(t) =& A_I \cos\left(\frac{4\pi f_c}{c} R(t) + \phi_I\right) + DC_I = \\ & A_I \cos\left(\Theta_I(t)\right) + DC_I \end{aligned} \tag{B.2}$$

$$Q(t) = A_Q \sin\left(\frac{4\pi f_c}{c} R(t) + \phi_Q\right) + DC_Q \tag{B.3}$$

where A_I and A_Q are the component amplitude, ϕ_I and ϕ_Q are the initial phase-shift, and DC_I and DC_Q are the signal bias. It is also possible to redefine $Q(t)$ in terms of the amplitude imbalance, $A_\epsilon = A_Q/A_I$, and the phase imbalance, $\phi_\epsilon = \phi_Q - \phi_I$, the resulting expressions are [Hu 13]:

$$I(t) = A_I \cos(\Theta_I(t)) + DC_I \tag{B.4}$$

$$Q(t) = A_I A_\epsilon \sin(\Theta_I(t) + \phi_\epsilon) + DC_Q \tag{B.5}$$

Therefore, the phase extracted from the beat signal has the following expression:

$$\begin{aligned} & \phi_{meas}(t) = arg(s_b(t)) = \tan^{-1}\left(\frac{Q(t)}{I(t)}\right) = \\ & \tan^{-1}\left[\frac{A_\epsilon[\sin(\Theta_I(t))\cos(\phi_\epsilon) + \cos(\Theta_I(t))\sin(\phi_\epsilon)] + \frac{DC_Q}{A_I}}{\cos(\Theta_I(t)) + \frac{DC_I}{A_I}}\right] \end{aligned} \tag{B.6}$$

This result implies that all the channel imbalances and dc-offset affect the phase extraction and have to be previously calibrated.

B.2 LFMCW case

The phase extraction in LFMCW radars is carried out by performing the arctangent demodulation of the beat signal, but unlike in CW systems, it is done in the frequency domain. $I(t,\tau)$ and $Q(t,\tau)$ are the phase and quadrature signal components, respectively. Taking into account the non-ideal components aforementioned in the CW case, the I- and Q-channels have the following expressions:

$$I(t,\tau) = A_I \cos\left(2\pi f_b(\tau)t + \frac{4\pi f_c}{c}R(\tau) + \phi_I\right) + DC_I \tag{B.7}$$

$$Q(t,\tau) = A_Q \sin\left(2\pi f_b(\tau)t + \frac{4\pi f_c}{c}R(\tau) + \phi_Q\right) + DC_Q \tag{B.8}$$

The beat signal is windowed to enhance the dynamic range and to reduce the interference of unwanted components. Being $w(t)$ the window response, the beat signal can be written as

$$s_b(t,\tau) = (I(t,\tau) + jQ(t,\tau)) \cdot w(t) \tag{B.9}$$

Performing the Fourier Transform of the beat signal, it follows the next expression:

$$\begin{aligned} S_b(f,\tau) = \frac{A_I}{2}\Bigg[&\delta(f-f_b)\exp\left(j\left(\frac{4\pi f_c}{c}R(\tau)+\phi_I\right)\right)+ \\ &+\delta(f+f_b)\exp\left(-j\left(\frac{4\pi f_c}{c}R(\tau)+\phi_I\right)\right)\Bigg] * W(f)+ \\ &+DC_I\delta(f) * W(f)+ \\ &+\frac{A_Q}{2}\Bigg[\delta(f-f_b)\exp\left(j\left(\frac{4\pi f_c}{c}R(\tau)+\phi_Q\right)\right)+ \\ &-\delta(f+f_b)\exp\left(-j\left(\frac{4\pi f_c}{c}R(\tau)+\phi_Q\right)\right)\Bigg] * W(f)+ \\ &+jDC_Q\delta(f) * W(f) \end{aligned} \tag{B.10}$$

Analyzing Eq. B.10 at $f = f_b$, it is obtained that:

$$\begin{aligned} &S_b(f_b,\tau) = \\ &\frac{A_I}{2}[1 + A_\epsilon \exp(j\phi_\epsilon)]\exp\left(j\left(\frac{4\pi f_c}{c}R(\tau)+\phi_I\right)\right)W(0)+ \\ &+\frac{A_I}{2}[1 - A_\epsilon \exp(j\phi_\epsilon)]\exp\left(j\left(\frac{4\pi f_c}{c}R(\tau)+\phi_I\right)\right)W(2f_b)+ \\ &+[DC_I + jDC_Q]W(f_b) \end{aligned} \tag{B.11}$$

Therefore, since the selected window has side lobe levels higher than 30 dB, the phase extracted can be approximated as

$$arg(S_b(f_b,\tau)) \simeq \frac{4\pi f_c}{c}R(\tau) + tan^{-1}\left(\frac{A_\epsilon sin(\phi_\epsilon)}{1+A_\epsilon cos(\phi_\epsilon)}\right) \tag{B.12}$$

where it can be observed that the imbalance due to dc-offset does not significantly modify the extracted phase. On the other hand, if the phase and amplitude imbalances do not vary with time, they can also be ignored, since they are constant. In summary, from Eqs. B.6 and B.12, it can be concluded that dc-offset only affects in the phase extraction in CW radars. Additionally, amplitude and phase imbalances have a higher impact in CW configurations.

B.2.1 Phase correction: LFMCW case

The beat signal, already defined in (2.3), follows this expression:

$$s_b(t,\tau) = \exp j(2\pi f_b(\tau)t + \phi(\tau)) \tag{B.13}$$

where $\phi(\tau) = \frac{4\pi f_c R(\tau)}{c}$. Performing an L-point FFT of the beat signal ($s_b(t,\tau)$), the phase measured evaluating a single bin can be expressed as:

$$\phi_{meas}(\tau) = \phi(\tau) + \phi_{error} \tag{B.14}$$

where ϕ_{error} represents the phase error since the frequency of the signal $s_b(t)$ does not match with FFT bin. The insertion phase of the filter bank implemented via an L-point FFT is linear from $\frac{-\pi}{2}$ to $\frac{+\pi}{2}$, as displayed in Fig. B.1, so this insertion phase can be model as:

$$\phi_{error} = \frac{\pi}{\Delta f}(f_b - f_{bin}) \tag{B.15}$$

where $\Delta f = f_s/L$ is the bin separation in an L-point FFT, and f_s represents the sampling frequency.

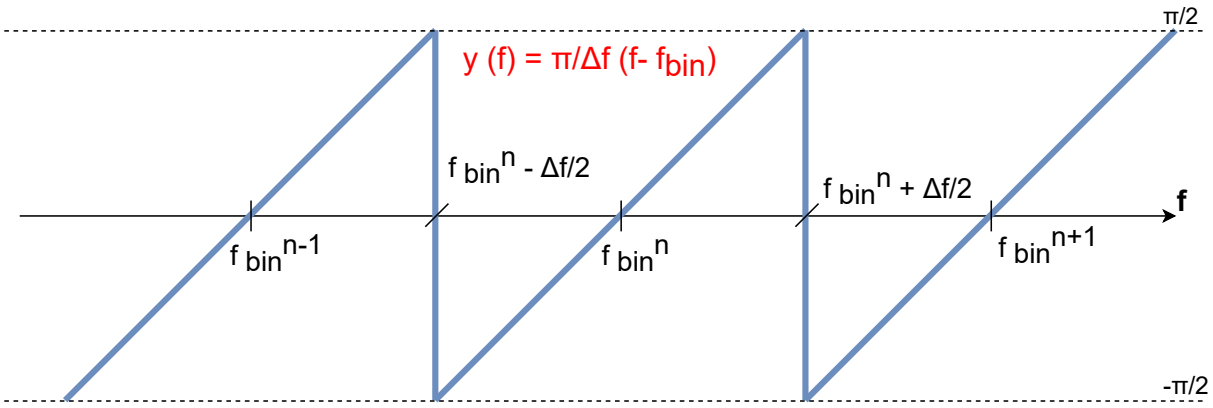

Figure B.1: Insertion phase for the filter bank developed with an FFT.

Thus, after performing the L-point FFT, ϕ_{meas} can be model as:

$$\begin{aligned}\phi_{meas}(\tau) =& \frac{4\pi f_c R(\tau)}{c} + \frac{\pi}{\Delta f}(f_b(\tau) - f_{bin}(\tau)) = \\ & \frac{4\pi f_c R(\tau)}{c} + \frac{\pi L}{f_s}\left(\frac{2BR(\tau)}{Tc} - f_{bin}(\tau)\right) = \\ & \frac{4\pi f_c R(\tau)}{c} + \frac{2\pi BLR(\tau)}{f_s Tc} - \frac{\pi L f_{bin}(\tau)}{f_s}\end{aligned} \tag{B.16}$$

Thus, the chest displacement can be expressed by the following equation:

$$R(\tau) = \frac{\phi_{meas}(\tau) + \frac{\pi L f_{bin}(\tau)}{f_s}}{\frac{4\pi f_c}{c} + \frac{2\pi BL}{f_s Tc}} \tag{B.17}$$

It is also important to highlight that the measured phase from the FFT is wrapped in the $[-\pi,+\pi]$ range, so an unwrapping algorithm has to be applied.

Moreover, the Cramér-Rao lower bound (CRLB) has been calculated. The new approach proposed is compared with the most used methods in the literature to extract the range information from the phase: arctangent demodulation (ATAN) and the differentiate and cross multiply (DACM) algorithm. Results are displayed in Fig. B.2, showing that our algorithm reaches the Cramér-Rao bound.

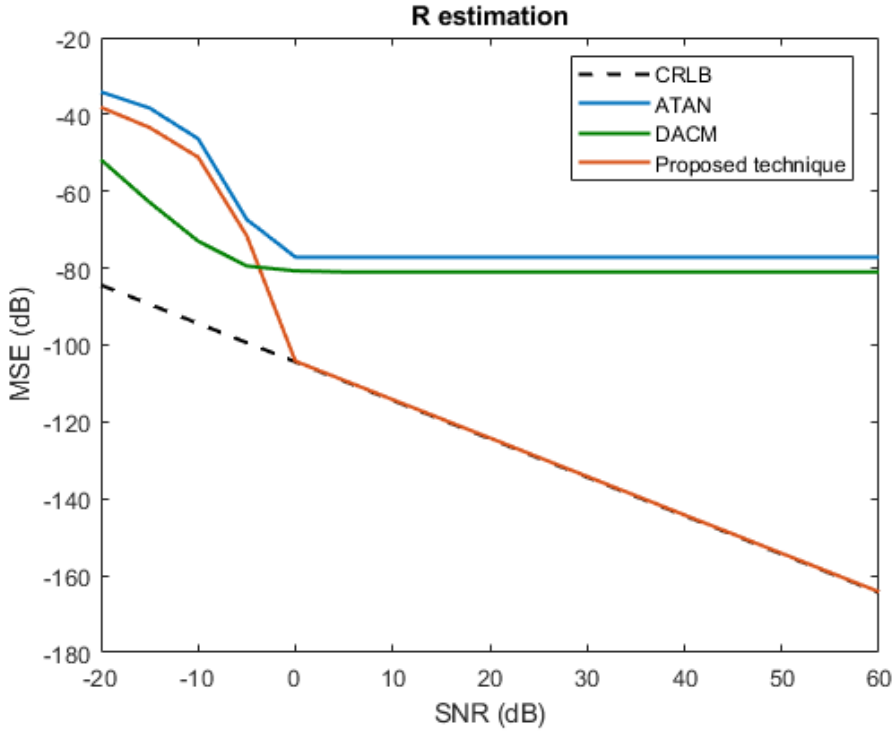

Figure B.2: Range estimation simulation results. The proposed technique (in orange) is compared with the arctangent demodulation (in blue), and the DACM algorithm (in green).

Appendix C

Optimal Working Frequency Band

It is necessary to analyze which working frequency band is more suitable to perform the detection of vital signs. For that purpose, the modulation sensitivity [Gu 13] of CW and LFMCW radar is analyzed. This analysis takes into account the signal's nature described in Chapter 3: breathing amplitudes between 4 and 12 mm and heartbeat amplitudes below 0.5 mm. Two scenarios has been analyzed:

- Best working frequency to detect a vibrational movement (the chest displacement).
- Best working frequency to detect the heartbeat signal, taking into account the breathing coupling.

C.1 Scenario 1: No Coupling

This scenario analyze the optimal frequency to detect a vibrational movement in CW and LFMCW radars. The chest displacement is simplified to a single movement $R(t) = R_0 + Asin(\omega t)$, being R_0 the target initial position, A the displacement amplitude and ω the angular frequency. This scenario does not take into account the coupling between breathing and heartbeat signals.

C.1.1 CW radar

Using the target displacement simplification, the CW radar baseband can be expressed as:

$$s_b(t) = \exp\left(j\left(\frac{4\pi f_c R_0}{c} + \frac{4\pi f_c A}{c} sin(\omega t)\right)\right) \tag{C.1}$$

Applying that $\exp(jzsin(\theta)) = \sum_{k=-\infty}^{\infty} J_k(z)\exp(k\theta)$:

$$s_b(t) = \sum_{k=-\infty}^{\infty} J_k\left(\frac{4\pi f_c A}{c}\right)\exp\left(j\left(\frac{4\pi f_c R_0}{c} + k\omega t\right)\right) \tag{C.2}$$

where $J_k(z)$ stands for the Bessel function of order k of the first kind.

The term $|J_1(\frac{4\pi f_c A}{c})|$ contains the information of the desired chest displacement, simplifying it as the fundamental (k=±1) modulation tone (breathing or heartbeat). Fig. C.1 shows the sensitivity of the system in terms of the working frequency and vibration amplitude that is pretended to be detected.

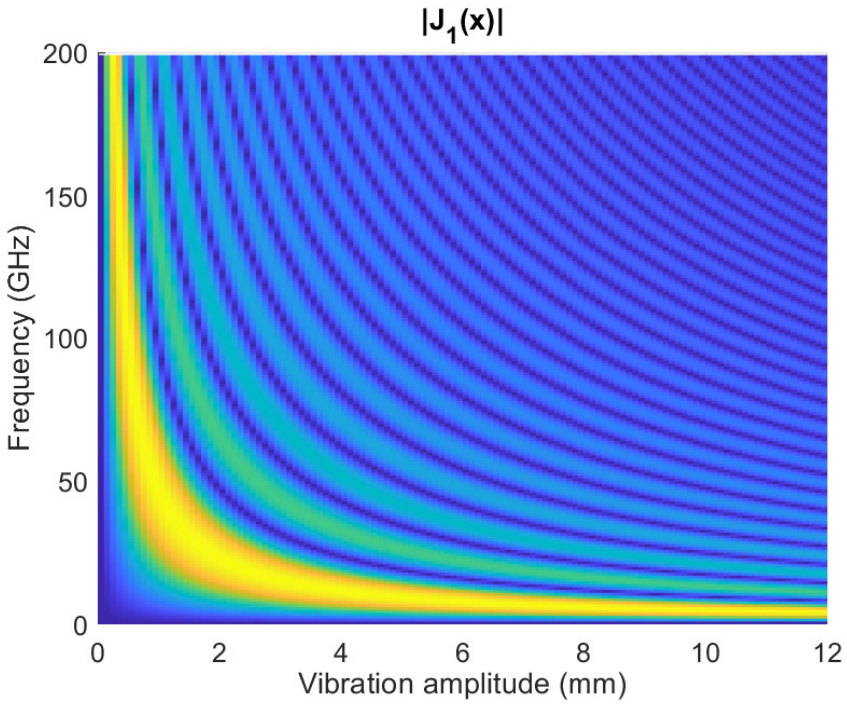

Figure C.1: Detection strength ($|J_1(\frac{4\pi f_c A}{c})|$) depending on chest displacement amplitude and frequency.

The maximum detection strength for each amplitude displacement along the frequency range is represented in Fig. C.2:

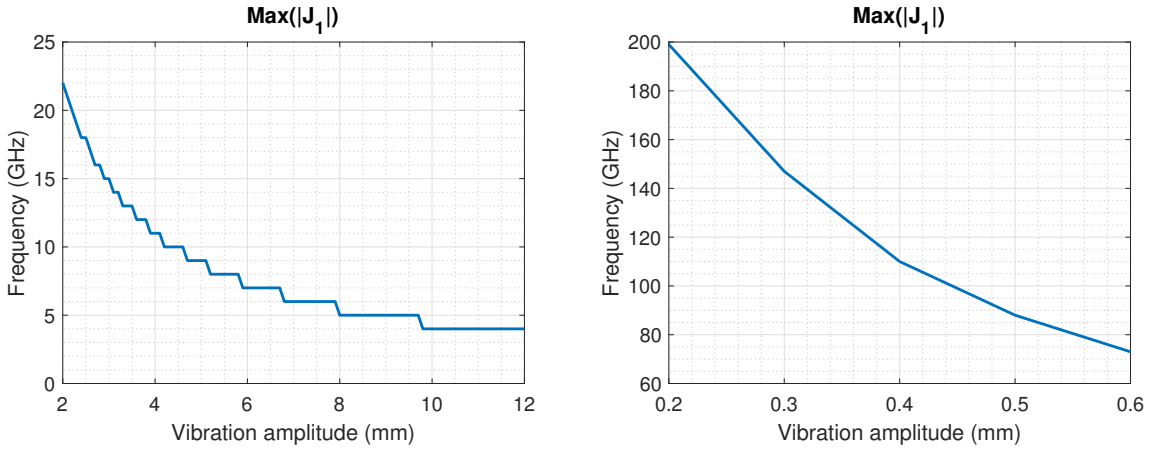

Figure C.2: Optimum frequency depending on the chest displacement amplitude. From left to right: breathing and heartbeat amplitude ranges.

It shows an optimum frequency to detect a vibrational movement in the range of the heartbeat amplitude of needs to be higher than 80 GHz, while the optimum frequency to detect amplitudes in the range of the breathing should be below 20 GHz. These results suggest to use a working frequency higher than 80 GHz to maximize the heartbeat detection, since it is more challenging that the breathing detection.

Conversely, it is important to consider that this is from a detection point of view. Given that the displacement information measured is derived from the argument of the beat signal ($s_b(t)$), it is evident that the higher the transmitted frequency, the greater the precision obtained. This is due to the fact that the phase change is proportional to the transmitted frequency for a given displacement, as can be derived from Eq. C.1.

C.1.2 LFMCW radar

In the LFMCW case, the same steps carried out in the CW case can be applied to define the beat signal as follows:

$$s_b(t,\tau) = \exp\left(j\left(\frac{4\pi B}{Tc}(R_0 + Asin(\omega\tau))t + \frac{4\pi f_0}{c}(R_0 + Asin(\omega\tau))\right)\right), \qquad t \in [0,T] \quad \text{(C.3)}$$

where B stands for the transmitted bandwidth, f_0 is the initial transmitted frequency, T is the sweep time, and τ stands for the slow time.

Applying the equivalence of $\exp(jzsin(\theta)) = \sum_{k=-\infty}^{\infty} J_k(z)\exp(k\theta)$:

$$\begin{aligned} s_b(t,\tau) = &\exp\left(j\left(\frac{4\pi BR_0}{Tc}t + \frac{4\pi f_0 R_0}{c}\right)\right)\cdot \\ &\left(\sum_{k=-\infty}^{\infty} J_k\left(\frac{4\pi BA}{Tc}t\right)\exp(jk\omega\tau)\right)\cdot\left(\sum_{n=-\infty}^{\infty} J_n\left(\frac{4\pi f_0 A}{c}\right)\exp(jn\omega\tau)\right) \end{aligned} \quad \text{(C.4)}$$

Simplifying,

$$s_b(t,\tau) = \sum_{k=-\infty}^{\infty}\sum_{n=-\infty}^{\infty} J_k\left(\frac{4\pi BA}{Tc}t\right)J_n\left(\frac{4\pi f_0 A}{c}\right)\exp\left(j\left(\frac{4\pi BR_0}{Tc}t + \frac{4\pi f_0 R_0}{c} + (k+n)\omega\tau\right)\right) \quad \text{(C.5)}$$

The terms $k = \pm 1$ with $n = 0$, and $n = \pm 1$ with $k = 0$ contain the information of the desired breathing or heartbeat vibrations. In this case, there are two Bessel functions, one which modulates $s_b(t,\tau)$ along the fast time, t, and the other which modulates it along the transmitted frequency. The optimum frequency have been calculated measuring the maximum of $S_b(f,\tau)$, which stands for the FFT of $s_b(t,\tau)$ along the fast-time dimension. Fig. C.3 shows the sensitivity of the system in terms of working frequency band and amplitude that is pretended to be detected. The simulation was conducted using standard values of bandwidth and sweep time: 12 GHz and 1 ms, respectively. Moreover, from Eq. C.5, it is appreciated that the bandwidth also affects the vibration modulation. Therefore, the optimum working frequency obtained for the breathing and heartbeat frequency bands, for different transmitted bandwidths, are illustrated in Fig. C.4.

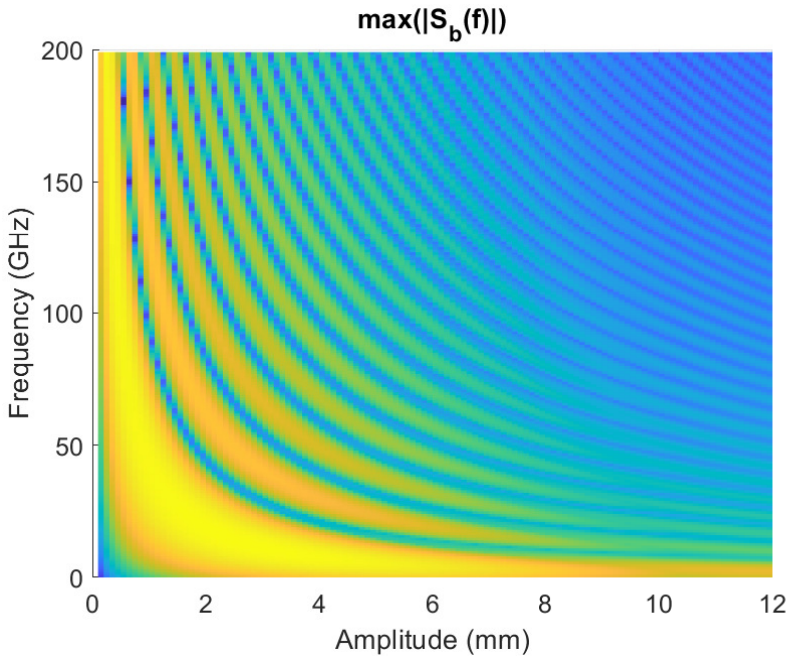

Figure C.3: Detection strength $\max(|S_b(f,\tau)|)$ depending on chest displacement amplitude and frequency.

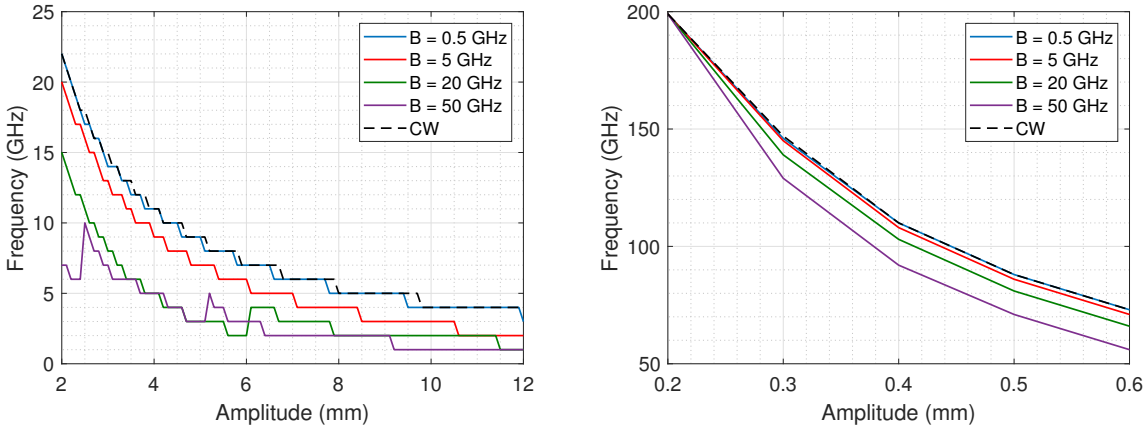

Figure C.4: Optimum frequency depending on the chest displacement amplitude. From left to right: breathing and heartbeat amplitude ranges.

The maximum detection strength for each amplitude displacement along the frequency range is also compared with the CW case presented in Fig. C.2, showing that transmitting higher bandwidths a lower working frequency is needed for an optimal vibration detection.

C.2 Scenario 2: Coupling

This scenario analyzes a more realistic case regarding to vital sign monitoring, since the body movement to be detected is caused by the sum of breathing and heartbeat. Therefore, the chest

displacement is modeled as the sum of two sinusoidal movements: one belonging to the breathing and other one for the heartbeat. In this case, $R(t) = R_0 + A_R sin(\omega_R \tau) + A_H sin(\omega_H \tau)$, where A_R and A_H are the breathing and heartbeat amplitudes, and ω_R and ω_H are the breathing and heartbeat angular frequencies.

C.2.1 CW radar

Using this target displacement model, the CW radar baseband can be expressed as:

$$s_b(t) = \exp\left(j\left(\frac{4\pi f_c R_0}{c} + \frac{4\pi f_c A_R}{c} sin(\omega_R t) + \frac{4\pi f_c A_H}{c} sin(\omega_H t)\right)\right) \tag{C.6}$$

Applying that $\exp(jzsin(\theta)) = \sum_{k=-\infty}^{\infty} J_k(z)\exp(k\theta)$:

$$s_b(t) = \sum_{k=-\infty}^{\infty}\sum_{n=-\infty}^{\infty} J_k\left(\frac{4\pi f_c A_R}{c}\right) J_n\left(\frac{4\pi f_c A_H}{c}\right) \exp\left(j\left(\frac{4\pi f_c R_0}{c} + k\omega_R t + n\omega_H t\right)\right) \tag{C.7}$$

It can be observed that there is a coupling between breathing and heartbeat signals. The impact of breathing signal on the heartbeat detection is analyzed, since the heartbeat extraction is the most challenging one. The terms $k = 0$ and $n = \pm 1$ contains this information. Fig. C.5 shows the sensitivity of the system in terms of working frequency and the breathing amplitude (for a heartbeat signal of 0.5 mm amplitude). It shows that selecting an optimal frequency is not trivial, since it varies with all the aforementioned parameters: breathing and heartbeat amplitudes and working frequency. Fig. C.5 shows that there are certain frequencies where the heartbeat strength is not null, but these gaps are filled with a finer breathing amplitude sweep.

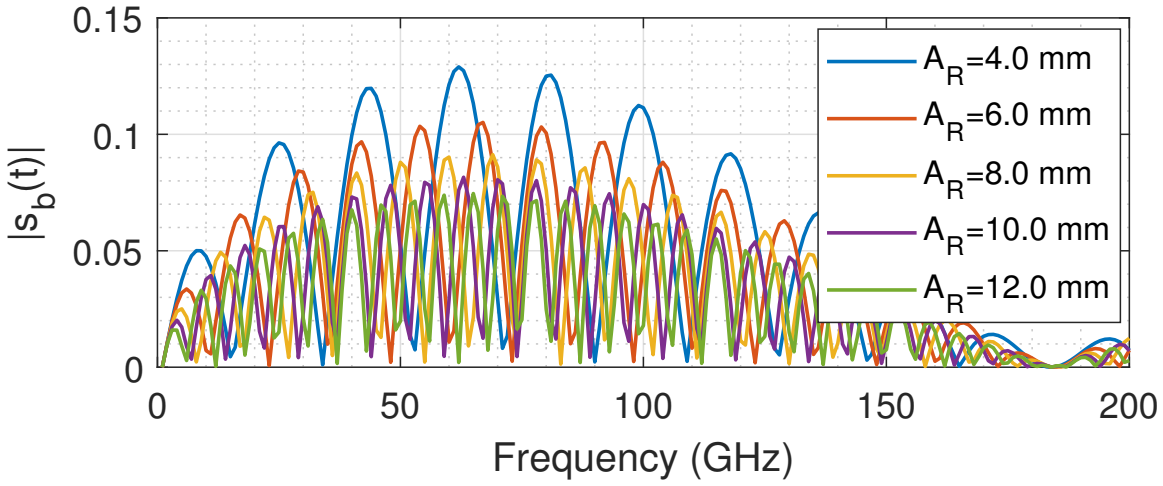

Figure C.5: Sensitivity depending on breathing amplitude and frequency for a heartbeat amplitude of 0.5 mm.

Fig. C.6 shows the frequency where heartbeat strength reaches its maximum for different breathing and heartbeat amplitudes. It also shows that there is not an optimum frequency for the desired application, since the breathing and heartbeat amplitudes vary with the time and with the body location where they are measured.

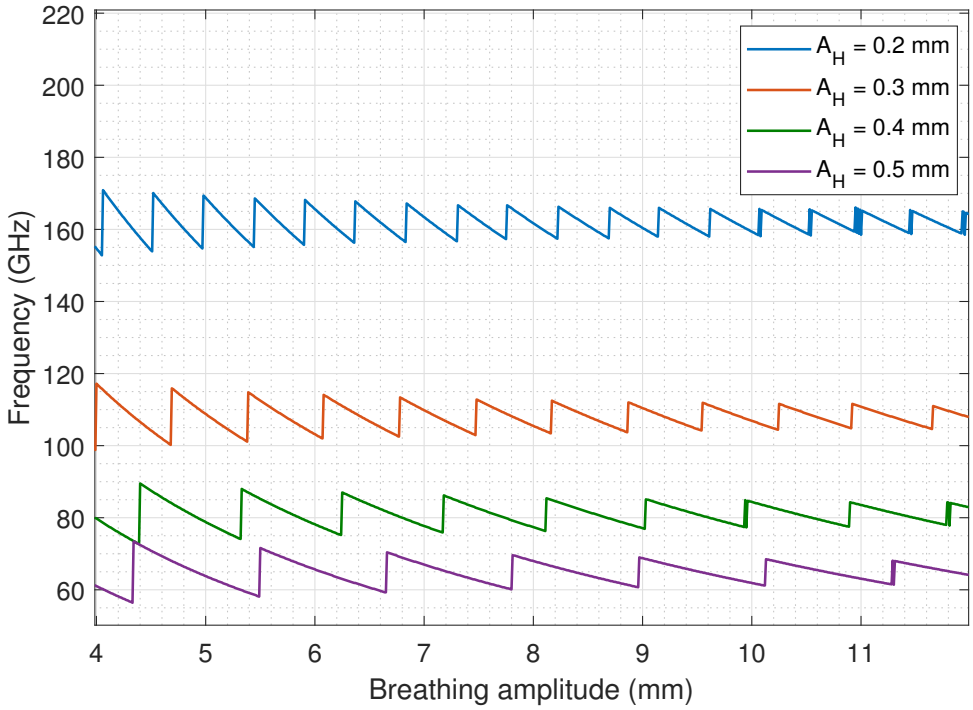

Figure C.6: Optimum frequency to detect the heartbeat signal depending on the breathing and heartbeat amplitudes.

C.2.2 LFMCW radar

Analogously to the CW case, the beat signal can be defined as:

$$s_b(t,\tau) = \exp\left(j\left(\frac{4\pi BR_0}{Tc}t + \frac{4\pi BA_R}{Tc}sin(\omega_R\tau)t + \frac{4\pi BA_H}{Tc}sin(\omega_H\tau)t + \frac{4\pi f_0R_0}{c} + \frac{4\pi f_0A_R}{c}sin(\omega_R\tau) + \frac{4\pi f_0A_H}{c}sin(\omega_H\tau)\right)\right) \tag{C.8}$$

Applying that $\exp(jzsin(\theta)) = \sum_{k=-\infty}^{\infty} J_k(z)\exp(k\theta)$, and simplifying:

$$s_b(t,\tau) = \sum_{k=-\infty}^{\infty}\sum_{l=-\infty}^{\infty}\sum_{m=-\infty}^{\infty}\sum_{n=-\infty}^{\infty} J_k\left(\frac{4\pi BA_R}{Tc}t\right)J_l\left(\frac{4\pi BA_H}{Tc}t\right)J_m\left(\frac{4\pi f_0A_R}{c}\right)J_n\left(\frac{4\pi f_0A_H}{c}\right) \cdot \exp\left(j\left(\frac{4\pi BR_0}{Tc}t + \frac{4\pi f_0R_0}{c} + (k+m)\omega_R\tau + (l+n)\omega_H\tau\right)\right) \tag{C.9}$$

The terms $k = 0$, $m = 0$, $l = \pm 1$ and $n = \pm 1$ contains the information of the desired heartbeat first harmonic. Fig. C.7 shows the sensitivity of the system in terms of working frequency and amplitude that is pretended to be detected.

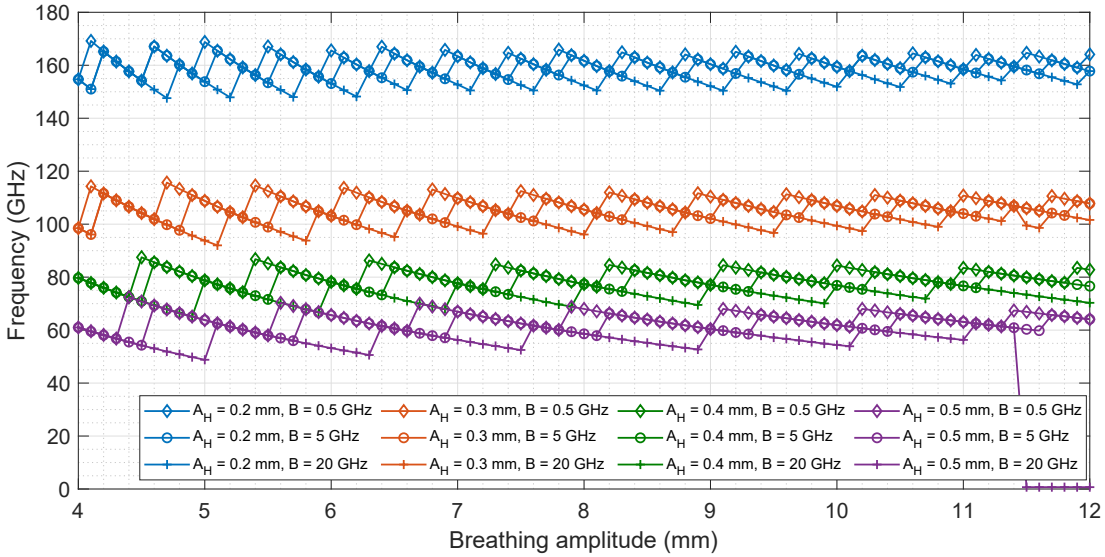

Figure C.7: Optimum frequency for heartbeat detection depending on breathing amplitude and working frequency. Different heartbeat amplitudes and transmitted bandwidths are analyzed.

Fig. C.7 presents results comparable to the CW case, with the addition of modulation due to the transmitted bandwidth described in the no-coupling scenario. Consequently, there is no optimal frequency for vital sign monitoring that maximizes detection. However, using higher operating frequencies proves to be the most advantageous. Simulations indicate that higher frequencies enhance the detection of lower amplitude vibrational motions. Additionally, at higher frequencies, small displacements result in significant phase changes, antenna sizes are reduced, and beamwidths become narrower.

Appendix D

Complex-Tone Parameter Estimation

This section discusses the estimation method chosen for determining the amplitude and range from a complex-tone embedded in noise for radar applications.

The estimation of the parameters of a complex tone in additive white Gaussian noise is a well-studied problem in communications and signal processing systems. It was previously formulated by Slepian in the first half of the 1950s [Slep 54]. However, this section follows the approach carried out by Rife in [Rife 74], since he analyzed the problem of estimating the tone parameters from noisy discrete-time observations. Unlike Rife's approach, this analysis seeks to estimate the range in radar applications, specifically, in LFMCW radar. Therefore, the parameters of interest in the estimation problem are the tone amplitude A, and the target range, R, which is derived from the beat frequency and phase.

In an estimation problem, it is important to determine the best estimation that can be made. This threshold is obtained computing the Cramér-Rao lower bound (CRLB), providing a benchmark of the minimum variance that an estimator can attain. This bound is given by the inverse of the Fisher information matrix, I, whose typical element for a parameter θ is:

$$I(\theta) = -E\left[\frac{\partial^2 ln\ p(x;\theta)}{\partial\theta^2}\right] \tag{D.1}$$

where $p(x;\theta)$ is the probability density function parameterized by the unknown parameter θ. Therefore, the CRLB sets that:

$$var(\theta) \geq \frac{1}{-E\left[\frac{\partial^2 \ln p(x;\theta)}{\partial\theta^2}\right]} \tag{D.2}$$

Taking the complex Gaussian probability density function [Kay 93]:

$$p(\tilde{x},\theta) = \frac{1}{\pi^N det(C_{\tilde{x}}(\theta))}\exp[-(\tilde{x}-\tilde{\mu}(\theta))^H C_{\tilde{x}}^{-1}(\theta)(\tilde{x}-\tilde{\mu}(\theta))] \tag{D.3}$$

where $\tilde{x}$ is the complex signal, $C_{\tilde{x}}$ its covariance matrix and θ is the parameter vector to be estimated. In [Kay 93] it is also derived the Fisher information matrix expression:

$$[I(\xi)]_{ij} = tr\left[C_{\tilde{x}}^{-1}(\xi)\frac{\partial C_{\tilde{x}}(\xi)}{\partial\xi_i}C_{\tilde{x}}^{-1}(\xi)\frac{\partial C_{\tilde{x}}(\xi)}{\partial\xi_j}\right] + 2\Re\left[\frac{\partial\tilde{\mu}^H(\xi)}{\partial\xi_i}C_{\tilde{x}}^{-1}(\xi)\frac{\partial\tilde{\mu}(\xi)}{\partial\xi_i}\right] \tag{D.4}$$

where xi is a vector of real parameters (it is assumed that θ is purely complex).

D.1 CW

Applying these concepts to the CW radar beat signal, we consider the estimation of the amplitude A and the range R. We define the complex data $\tilde{x}$ as:

$$\tilde{x}[n] = s_b[n] + \tilde{w}[n] \qquad 0 \leq n \leq N-1 \tag{D.5}$$

where $\tilde{w}[n] \sim CN(0, \sigma^2)$ and the beat signal is:

$$s_b[n] = A \exp\left(j\left(\frac{4\pi f_0 R[n]}{c}\right)\right) \tag{D.6}$$

The parameter vector to be estimated is $\xi = [AR]^T$. Moreover, the covariance matrix, $C_{\tilde{x}} = \sigma^2 I$ does not depend on ξ, thus, the Fisher information matrix, from Eq. D.4, can be expressed as:

$$[I(\xi)]_{ij} = 2\Re\left[\frac{\partial \tilde{\mu}^H(\xi)}{\partial \xi_i} C_{\tilde{x}}^{-1}(\xi) \frac{\partial \tilde{\mu}(\xi)}{\partial \xi_j}\right] = 2\Re\left[\sum_{n=0}^{N-1} \frac{\partial s_b^*[n]}{\partial \xi_i} \frac{\partial s_b[n]}{\partial \xi_j}\right] \tag{D.7}$$

The partial derivatives are:

$$\frac{\partial s_b}{\partial A} = \exp\left(j\left(\frac{4\pi f_0 R}{c}\right)\right) \tag{D.8}$$

$$\frac{\partial s_b}{\partial R} = jA\frac{4\pi f_0}{c} \exp\left(j\left(\frac{4\pi f_0 R}{c}\right)\right) \tag{D.9}$$

Therefore, the resulting Fisher information matrix is:

$$I(\xi) = \frac{2}{\sigma^2}\begin{bmatrix} N & 0 \\ 0 & (\frac{4\pi f_0}{c})^2 A^2 N \end{bmatrix} \tag{D.10}$$

Upon inversion and knowing that N=1:

$$var(\hat{A}) \geq \frac{\sigma^2}{2} \tag{D.11}$$

$$var(\hat{R}) \geq \left(\frac{c}{4\pi f_0}\right)^2 \frac{\sigma^2}{2A^2} \tag{D.12}$$

where the signal-to-noise ratio is A^2/σ^2.

D.2 LFMCW

The same procedure carried out in Section D.1 can be followed to obtain the CRLB for the LFMCW radar. In this case, the LFMCW radar beat signal is:

$$s_b(t) = A \exp\left(j\left(\frac{4\pi BR}{Tc} t + \frac{4\pi f_0 R}{c}\right)\right) \tag{D.13}$$

Calculating the partial derivatives:

$$\frac{\partial s_b}{\partial A} = \exp\left(j\left(\frac{4\pi BR}{Tc}t + \frac{4\pi f_0 R}{c}\right)\right) \tag{D.14}$$

$$\frac{\partial s_b}{\partial R} = jA\left(\frac{4\pi B}{Tc}t + \frac{4\pi f_0}{c}\right)\exp\left(j\left(\frac{4\pi BR}{Tc}t + \frac{4\pi f_0 R}{c}\right)\right) \tag{D.15}$$

Therefore, the resulting Fisher information matrix is:

$$I(\xi) = \frac{2}{\sigma^2}\begin{bmatrix} N & 0 \\ 0 & A^2(\frac{4\pi}{c})^2\sum_{n=0}^{N-1}(\frac{4\pi B}{Tc}t + \frac{4\pi f_0}{c}) \end{bmatrix} \tag{D.16}$$

Knowing that $t = (n_0 + n)T$, assuming $n_0 = 0$, and using the following expressions:

$$\sum_{n=0}^{N-1} n = \frac{N(N-1)}{2} \tag{D.17}$$

$$\sum_{n=0}^{N-1} n^2 = \frac{N(N-1)(2N-1)}{6} \tag{D.18}$$

The CRLB bounds are:

$$var(\hat{A}) \geq \frac{\sigma^2}{2N} \tag{D.19}$$

$$var(\hat{R}) \geq \left(\frac{c}{4\pi}\right)^2 \frac{\sigma^2}{2A^2}\frac{1}{Nf_0^2 + Bf_0(N-1) + \frac{B^2(2N-1)(N-1)}{6N}} \tag{D.20}$$

Appendix E

Noise in radars

This appendix analyzes the impact of different sources of noise in radar systems. Three sources of noise can be highlighted [Jens 11, Jeni 18]:

- Thermal noise: Thermal noise is typically additive noise, also known as white noise. It arises from the random motion of electrons and is characterized by a uniform distribution of energy over the frequency spectrum, following a Gaussian distribution.
- Phase noise: Phase noise is the noise that arises from the rapid and random phase fluctuations that occur in a signal. It describes how much the phase of the signal deviates from a perfect periodic signal over a given bandwidth.
- Flicker noise: Flicker noise is an electronic noise that has a power spectral density that is inversely proportional to the frequency of the signal. This noise is common in oscillators.

The working principle behind of CW and LFMCW radars is detailed in Appendix A, however, this analysis is carried out for the ideal case. In these sections, the different sources of noise are added to the ideal $s_b(t)$ (Eqs. 2.4 and 2.5). These types of noise are illustrated in Fig. E.1.

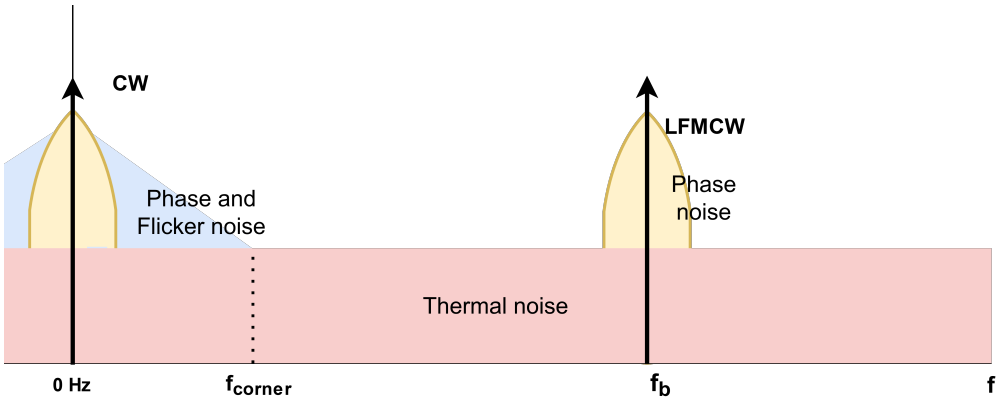

Figure E.1: Main sources of noise affecting a radar system: thermal noise, phase noise and flicker noise.

E.1 Thermal noise

E.1.1 Radar signal models

1. CW radars transmit and receive a sinusoidal waveform of frequency f_0. After the demodulation and filtering processes, the radar baseband signal can be expressed as:

$$s_b(t) = A\exp(j\phi(t)) + w(t) \tag{E.1}$$

where A is the signal amplitude, and $\phi(t) = \frac{4\pi f_0}{c}R(t)$. Being c, the light velocity; and $R(t)$, the target range, and $w(t)$ the complex white noise, where $w(t) \sim CN(0, \sigma^2)$.

2. The working principle of LFMCW is based on transmitting a linear modulated RF signal, which is reflected by the target. A replica of the transmitted signal is mixed with the received echoes, obtaining the beat signal. Under the "stop and go assumption" [Carr 95], which states that the target does not change its position during the radar sweep time, the beat signal for a point-scatterer at a range $R(\tau)$ (where τ is the so-called slow time[1]) can be formulated as:

$$s_b(t,\tau) = A\exp(j(2\pi f_b(\tau)t + \phi(\tau) + \phi_2(\tau))) + w(t) \tag{E.2}$$

The beat signal follows a sinusoidal waveform with a frequency known as beat frequency $f_b(\tau) = \frac{2B}{T\cdot c}R(\tau)$, $\phi(\tau) = 4\pi f_0 R(\tau)/c$, and $\phi_2(\tau) = -\frac{4\pi B_W R^2(\tau)}{T\cdot c^2}$. $\phi_2(\tau)$ represents the residual video phase (RVP) [Carr 95], which is found to be negligible and can be ignored, since it is proportional to $1/c^2$.

E.1.2 CW analysis

The displacement estimation in CW radars is performed for each sample, therefore, N=1. The CRLB bound that can be attained follows Eq. E.3, the whole mathematical analysis can be found in Appendix D.1:

$$var(\hat{R}) \geq \left(\frac{c}{4\pi f_0}\right)^2 \frac{\sigma^2}{2A^2} \tag{E.3}$$

where A^2/σ^2 is the signal-to-noise ratio.

The maximum likelihood estimator (MLE) for the CW case is analyzed in [Kay 93], resulting that:

$$\hat{R}[n] = \frac{c}{4\pi f_0}\tan^{-1}\left(\frac{\Im(s_b(t))}{\Re(s_b(t))}\right) = \frac{c}{4\pi f_0}\tan^{-1}\left(\frac{Q[n]}{I[n]}\right) \tag{E.4}$$

[1]Mathematically, the slow time can be expressed as $\tau_i = i \cdot T$, with $i \in \mathbb{Z}$, so it is a sampled version of the fast time t

E.1.3 LFMCW analysis

The analysis of the LFMCW radar signal embedded in white noise is equal to the parameter estimation of a sinusoid, when its parameters are assumed unknown, carried out by Kay in [Kay 93]. However, since the displacement information can be found in the beat frequency and the signal phase, it is possible to perform an estimation using both parameters simultaneously. The whole mathematical analysis has been detailed in Appendix D.2. The CRLB that can be attained using this approach has the following expression:

$$var(\hat{R}) \geq \left(\frac{c}{4\pi f_0^2}\right)^2 \frac{\sigma^2}{2A^2} \frac{1}{N + \frac{B(N-1)}{f_0} + \frac{B^2(2N-1)(N-1)}{6Nf_0^2}} \tag{E.5}$$

where A^2/σ^2 is the signal-to-noise ratio and N is the signal length.

The MLE for the LFMCW case is analyzed by Kay in [Kay 93], resulting that:

$$\hat{\phi}[n] = \tan^{-1}\left(\frac{-\sum_{n=0}^{N-1} x[n]\sin(2\pi\hat{f}_b n)}{\sum_{n=0}^{N-1} x[n]\cos(2\pi\hat{f}_b n)}\right) = \tan^{-1}\left(\frac{Imag\{X[n]\}}{Re\{X[n]\}}\right) \tag{E.6}$$

where the frequency has been previously estimated. Thus,

$$\hat{R}[n] = \left(\frac{c}{4\pi f_0}\right)\tan^{-1}\left(\frac{Imag\{X[n]\}}{Re\{X[n]\}}\right) \tag{E.7}$$

where $X[n]$ is the Fourier Transform of $x[n]$, and $x[n]$ is the beat signal.

E.1.4 Comparison

The main difference between the two aforementioned estimation problems defined is associated to the number of samples used to perform the estimation:

- In the CW case, the estimation is performed for each sample, thus, N_{CW}=1.
- In the LFMCW case, the estimation of the displacement is performed for each transmitted ramp, thus, $N_{LFMCW}=f_sT$, assuming that the target does not change its position during each ramp ("stop and go assumption").

Therefore, the relation between the estimation of the target displacement of both configurations is:

$$\frac{Var\left(\hat{R}_{LFMCW}\right)}{Var\left(\hat{R}_{CW}\right)} \propto \frac{1}{N_{LFMCW}} \tag{E.8}$$

Thus, a higher accuracy can be obtained with LFMCW radars.

E.2 Phase noise

This noise is added to the phase of the beat signal as the difference between the transmitted and received phase noise:

$$s_b(t,\tau) = \sigma \exp(j(2\pi f_b(\tau)t + \phi(\tau) + \phi_2(\tau) + \theta_{pn}(t) - \theta_{pn}(t - \tau_{delay}(\tau)))) \tag{E.9}$$

where $\theta_{pn}(t)$ is the phase noise in transmission and τ_{delay} is the delay that the transmitted signals suffers before being received $(2R(\tau)/c)$.

Since it is used for short-range applications, τ_{delay} is very small, which means that the phase noise transmitted is practically cancelled. It is possible to calculate the correlation factor of the phase noise as a function of the distance to the target (due to the delay between the transmitted and received signal) [Menc 14]:

$$C = 4\sin^2(\pi f_{b_{offset}} \tau_{delay}) \tag{E.10}$$

where $f_{b_{offset}}$ is the frequency offset with the beat signal.

E.3 Flicker noise

Flicker noise is more significant at lower frequencies and has a $1/f$ characteristic curve (drops 10 dB/decade). In terms of formulation, it is an additive noise such as thermal noise:

$$s_b(t) = A\exp(j\phi(t)) + s_f(t) \tag{E.11}$$

where $s_f(t)$ stands for the flicker noise of the system.

E.4 Noise simulation

This section analyzes the impact of noise in target displacement estimation, R. For that purpose, different scenarios are simulated, where the three aforementioned sources of noise are added to an ideal CW and LFMCW waveform. For these simulations, where the displacement estimation is carried out for different SNR values, it is important to note that the signal power is fixed and only the noise power varies.

E.4.1 Thermal noise

Fig. E.2 shows the Cramér-Rao lower bounds derived from Appendix D for CW and LFMCW configurations and the displacement estimation for CW and LFMCW configurations. The utilized configuration parameters are as follows:

- The target is located 0.5 meters from the transmitter and describes a sinusoidal motion of 8 mm amplitude and a frequency of 0.5 Hz.

- Transmitted center frequency 134 GHz.
- Sampling frequency 1 MHz.
- No imbalance between I and Q channels.
- LFMCW parameters: B = 6 GHz, T = 1 ms.

In Fig. E.2, the Cramér-Rao lower bounds for the CW and LFMCW cases are presented. These are given by Eqs. 2.9 and 2.10, respectively. Additionally, estimates of R in the presence of complex white noise (WN) are shown.

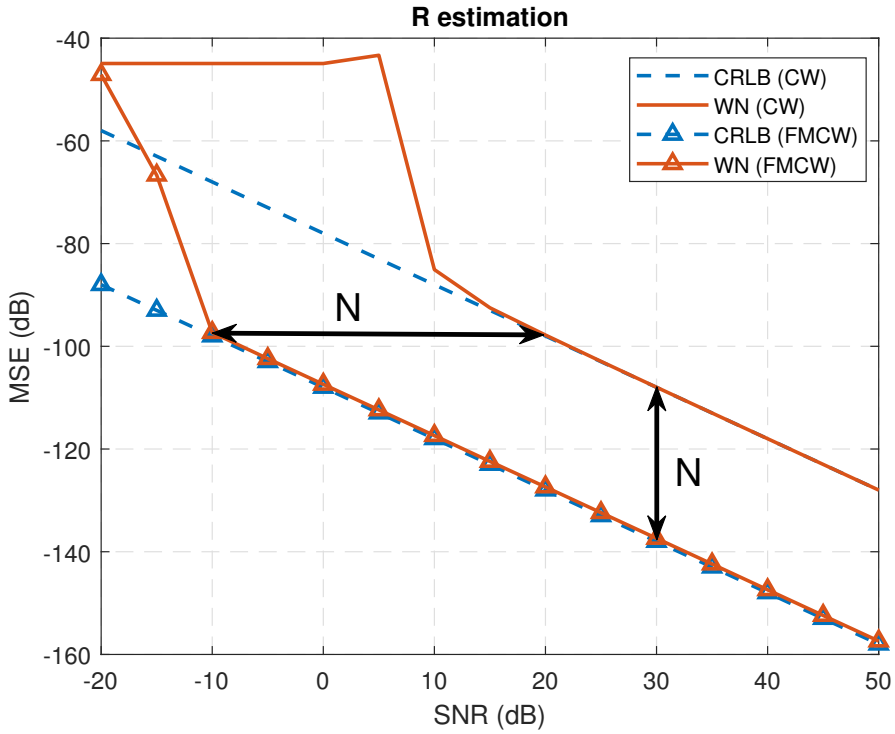

Figure E.2: Displacement estimation as a function of signal SNR for CW and LFMCW configurations: white noise.

In order to generate thermal noise, the signal amplitude has been fixed and the noise power has been swept to generate the different SNR values. As can be observed in Fig. E.2, in the case of LFMCW, an improvement of $10log_{10}(N_{LFMCW}) = 10log_{10}(1000) = 30$ dB is obtained.

E.4.2 Phase noise

The phase noise simulation is generated using a mask with the phase noise values provided by the manufacturer, Silicon Radar. The mask chosen is shown in Fig. E.3 (mask 1). On the other hand, Fig. E.4 shows the displacement estimation in the presence of phase and white noise for the different mask noise generated in Fig. E.3. Subsequently, Fig. E.5 shows the displacement estimation for the CW and LFMCW cases in the presence of phase noise

(mask 1). It is important to note that the CRLB bounds are obtained for a scenario that considers only the presence of white noise. Therefore, it is not feasible to attain these limits in alternative noise environments; nevertheless, they are employed as a point of comparison.

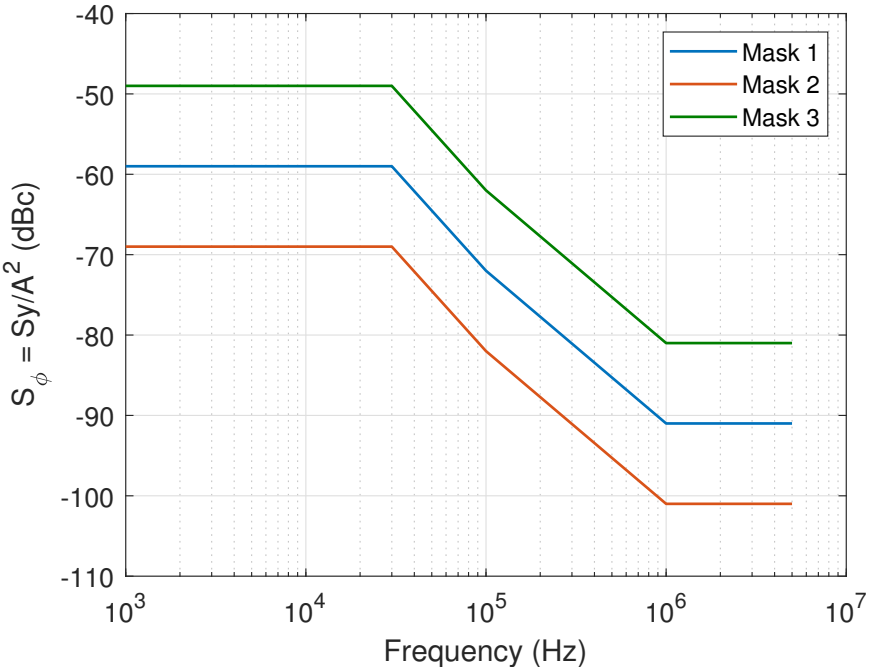

Figure E.3: Noise masks provided by the manufacturer.

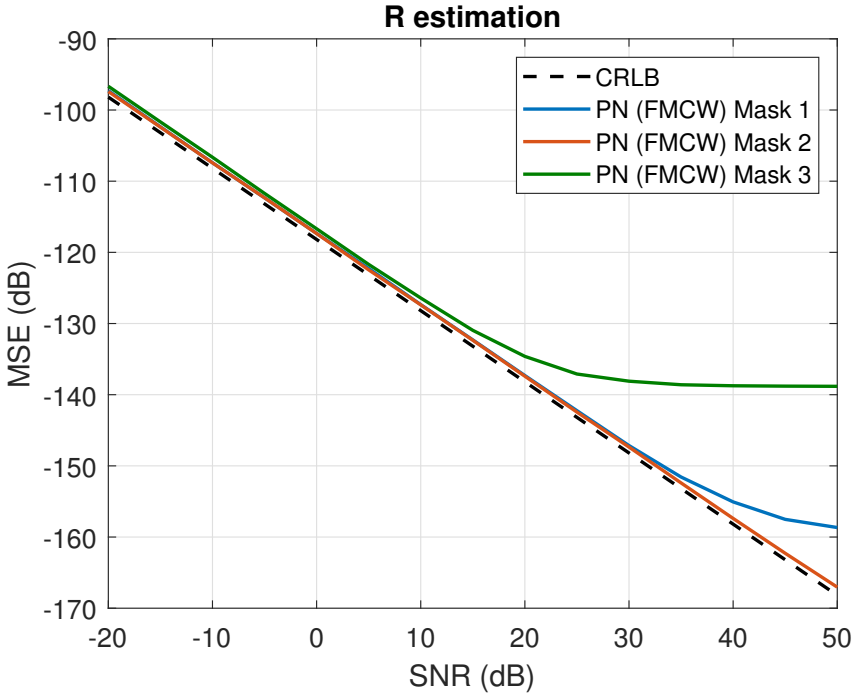

Figure E.4: Displacement estimation as a function of signal SNR for LFMCW configuration using different noise masks.

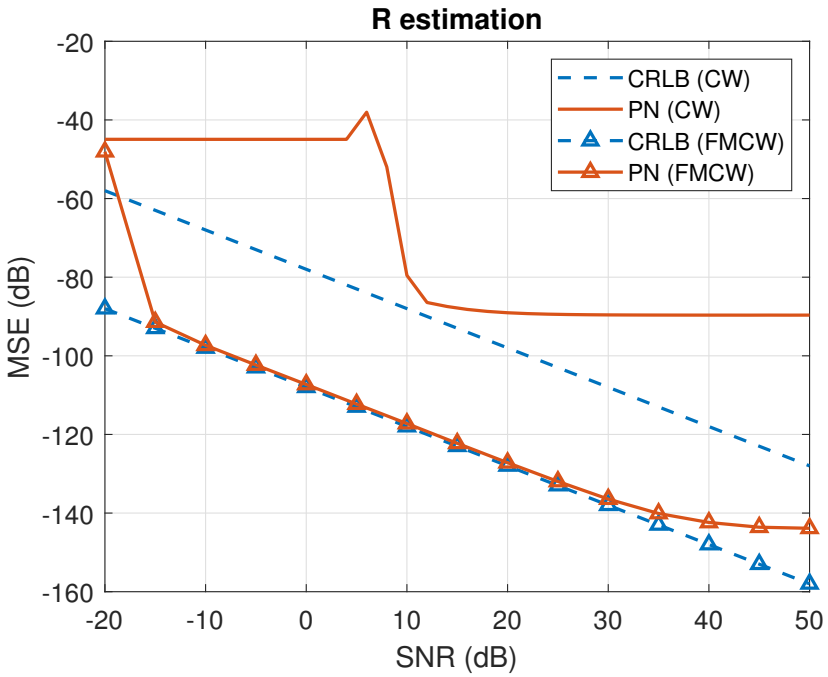

Figure E.5: Displacement estimation as a function of signal SNR for CW and LFMCW configurations: phase noise (using mask 1).

E.4.3 Ruido flicker

Fig. E.6 shows the displacement estimation in the presence of flicker noise.

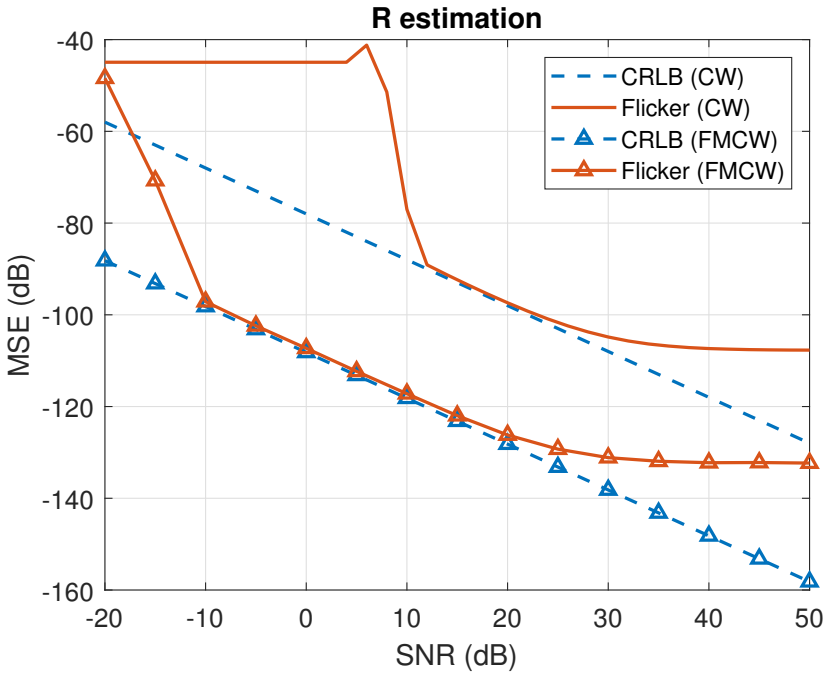

Figure E.6: Displacement estimation as a function of signal SNR for CW and LFMCW configurations: white noise and flicker noise.

Additionally, Fig. E.7 illustrates that the influence of flicker noise is amplified when the beat frequency approaches the dc-component. Moreover, Fig. E.8 depicts the cumulative effect of all noise sources on the beat signal, demonstrating that flicker noise has the greatest impact at low frequencies, particularly in the CW configuration.

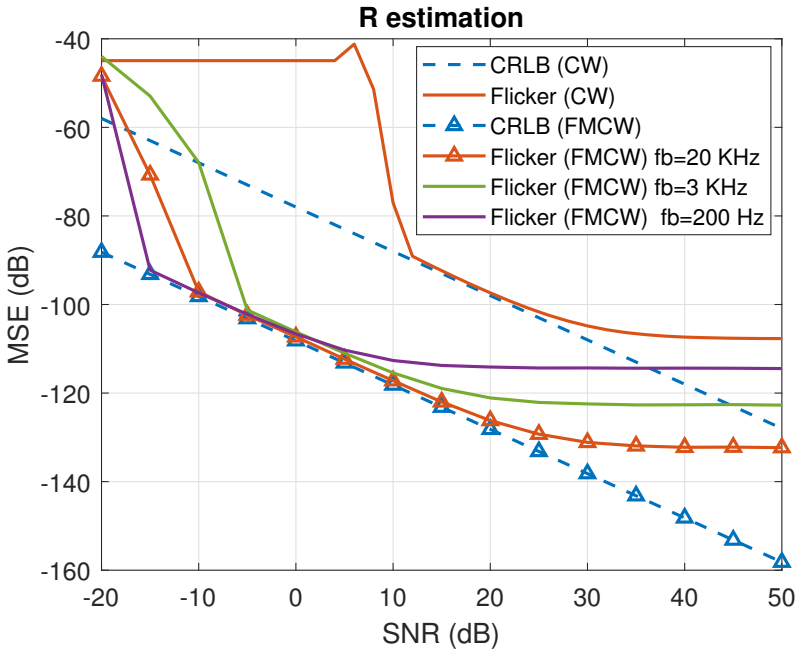

Figure E.7: Displacement estimation as a function of signal SNR for LFMCW configurations for different beat frequencies in the presence of flicker noise and thermal noise.

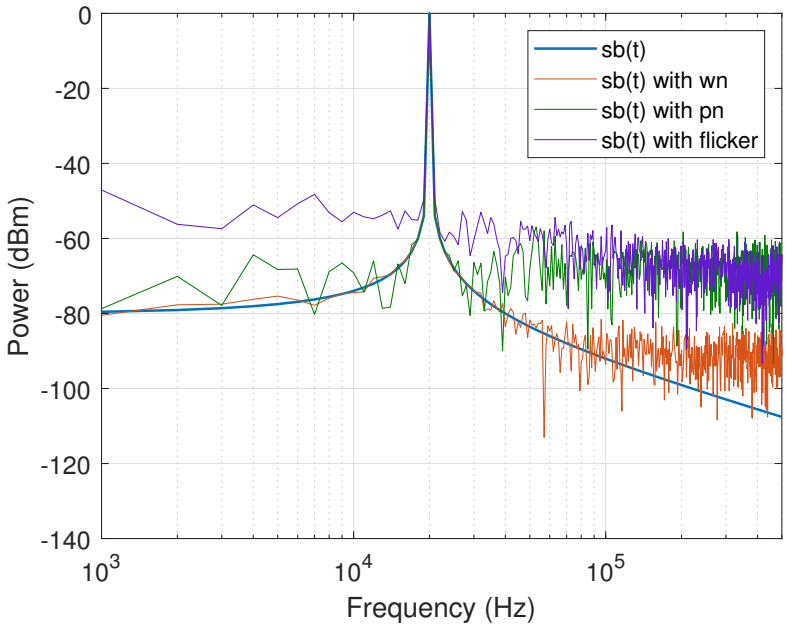

Figure E.8: Spectra of the beat signal and of the different noises affecting the system: white, phase (mask 1) and flicker.

Appendix F

Metrics

This appendix enumerates the different metrics and analytical tools employed for the examination and comparison of the results extracted in this thesis.

F.1 Russell's Metric

This metric [Russ 97] provides robust means for quantifying the magnitude and phase differences between two time histories separately, and the comprehensive error. For two time series $s1$ and $s2$, with energy E_{s1} and E_{s2}, and length N, the magnitude error is defined as:

$$\sigma_M = sign(rme) log_{10}(1 + |rme|) \tag{F.1}$$

where rme represents the relative magnitude error, which is defined as the following expression:

$$rme = \frac{E_{s_1} - E_{s_2}}{\sqrt{E_{s_1} \cdot E_{s_2}}} \tag{F.2}$$

The following equation represents the phase error:

$$\sigma_P = \frac{1}{\pi} \cos^{-1} \left(\frac{\sum_{i=1}^{N} s_{1i} \cdot s_{2i}}{\sqrt{E_{s_1} \cdot E_{s_2}}} \right) \tag{F.3}$$

And the comprehensive error results in the next equation:

$$\sigma_C = \sqrt{\frac{\pi}{4}(\sigma_M^2 + \sigma_P^2)} \tag{F.4}$$

F.2 Error metrics for cardiac activity analysis

The HR and HRV extraction has been evaluated using five error metrics:

- Mean absolute HR error ($\text{MAE}_{\{\text{HR}\}}$): It represents the mean absolute error between the dynamic HR extracted with the radar and the ECG reference.

$$\text{MAE}_{\{\text{HR}\}}\ (\text{bpm}) = \frac{1}{N}\sum_{i=1}^{N}|\text{HR}_{\text{radar},i} - \text{HR}_{\text{ECG},i}| \tag{F.5}$$

  where $\text{HR}_{\text{radar},i}$ and $\text{HR}_{\text{ECG},i}$ represents the HR for the radar and ECG for the ith-instant.

- Absolute mean HR error ($\text{AE}_{\{\overline{\text{HR}}\}}$): It represents the absolute error between the mean HR extracted with the radar and the ECG reference.

$$\text{AE}_{\{\overline{\text{HR}}\}}\ (\text{bpm}) = \left|\overline{\text{HR}}_{\text{radar}} - \overline{\text{HR}}_{\text{ECG}}\right| \tag{F.6}$$

  where $\overline{\text{HR}}_{\text{radar}}$ and $\overline{\text{HR}}_{\text{ECG}}$ represent the mean HR value for the radar and ECG measurements.

- Mean absolute HRV error ($\text{MAE}_{\{\text{HRV}\}}$): It represents the mean absolute error between the HRV value extracted with the radar and the ECG reference.

$$\text{MAE}_{\{\text{HRV}\}}\ (\text{ms}) = \frac{1}{N}\sum_{i=1}^{N}|\text{HRV}_{\text{radar},i} - \text{HRV}_{\text{ECG},i}| \tag{F.7}$$

  where $\text{HRV}_{\text{radar},i}$ and $\text{HRV}_{\text{ECG},i}$ represent the HRV for the radar and ECG for the ith-instant.

- Relative mean absolute HR error: It represents the mean relative absolute error between the HR extracted with the radar and the ECG reference, expressed as a percentage.

$$\text{Relative MAE}_{\{\text{HR}\}}\ (\%) = \frac{1}{N}\sum_{i=1}^{N}\left|\frac{HR_{\text{radar},i} - HR_{\text{ECG},i}}{HR_{\text{ECG},i}}\right| \cdot 100 \tag{F.8}$$

- Relative mean HR error: It represents the mean relative error between the mean heart rate extracted with the radar and the ECG reference, expressed as a percentage.

$$\text{Relative AE}_{\{\overline{\text{HR}}\}}\ (\%) = \left|\frac{\overline{\text{HR}}_{\text{radar}} - \overline{\text{HR}}_{\text{ECG}}}{\overline{\text{HR}}_{\text{ECG}}}\right| \cdot 100 \tag{F.9}$$

F.3 Bland Altman Analysis

Comparing two methods of measurement to determine their level of agreement is common practice in healthcare research. To assess the degree of agreement, it is crucial to select an appropriate statistical method. Although the correlation and linear regression are commonly used to evaluate agreement between two measurement methods, it is important to note these methods measure the linear relationship between two set of data but no their agreement. Therefore, it is not recommended for assessing comparability between methods [Giav 15].

In 1983, Altman and Bland proposed a method for comparing two measurement methods. They highlighted the problems of using metrics, such as correlation, for this purpose [Blan 86]:

- High agreement can only be achieved if the points lie along the line of equality, while high correlation can be achieved if the points lie along any straight line.
- Changing the scale of measurement does not affect the correlation, but it does affect the agreement.

The proposed method is based on quantifying the agreement between two quantitative measurements by establishing statistical limits of agreement. These limits are determined using the mean and standard deviation of the differences between the measurements.

The Bland-Altman (B&A) plot illustrates the difference between the two methods on the Y-axis and their mean on the X-axis. Additionally, it assumes that the variances are normally distributed, meaning that 95% of the differences will fall within the range of $[\overline{d}-1.96s, \overline{d}+1.96s]$, where $\overline{d}$ is the bias estimated by the mean difference and s stands for the standard deviation [Blan 86]. The differences can be expressed also as percentage, which is helpful when the variability of differences increases with the magnitude of the measurement [Giav 15]. It is important to note that the B&A plot only defines the limits of agreement (LoA) and does not indicate whether these limits are acceptable for the desired application. These limits should be defined beforehand based on the needs or requirements of the application. An example of the B&A plot is presented in Figs. F.1 and F.2.

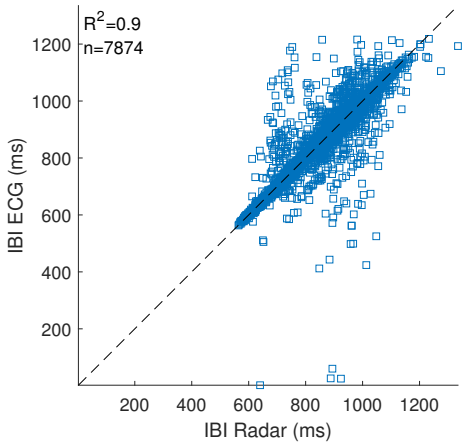

Figure F.1: Comparison between the two measurements using correlation. R^2 stands for the Pearson coefficient and n is the number of samples. The line $y = x$ is also plotted.

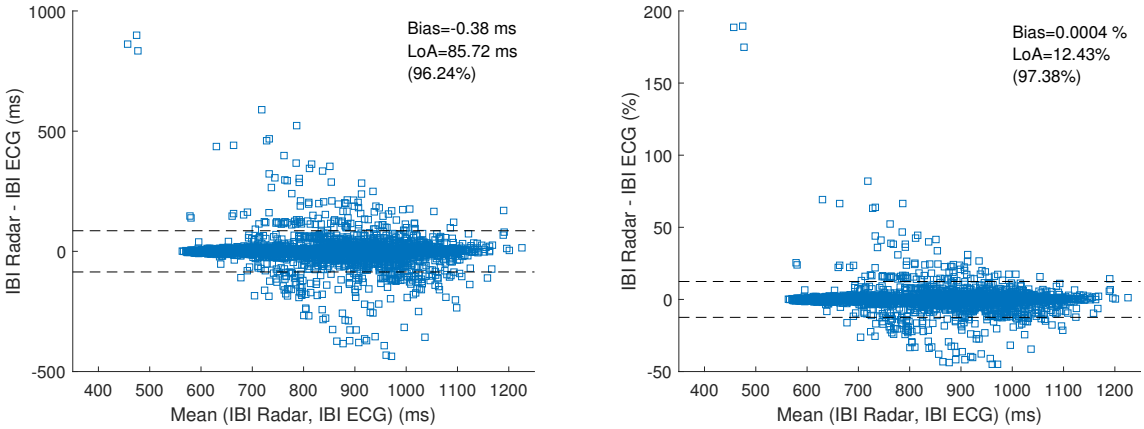

Figure F.2: Bland-Altman plot for the comparison between the two measurements. From left to right: the B&A plot expressed in natural units and the the B&A plot in percentages. LoA are marked using a dashed line.

This example compares two methods for the IBI extraction with an ECG and radar. Firstly, Fig. F.1 show the relation between both using the correlation, with a result of R^2 of 0.9. However, this plot does not give information about the level of agreement of both methods. On the other hand, Fig. F.2 shows the B&A representation, where the differences between both methods are represented against their mean, (method A + method B)/2. This figure shows the bias, the LoAs and the percentage of points which are within the LoAs.

Appendix G

Database wavelet decomposition analysis

This appendix presents the analysis conducted to determine which is the best wavelet for each waveform (heartbeat, heart sounds and skin wall acceleration) at each location (carotid, chest and wrist). The analysis utilizes the database outlined in Section 3.5.

The wavelet decomposition is performed using the following 60 orthogonal wavelet transforms:

- *Best-localized Daubechies: {7, 9, 10}*
- *Beylkin*
- *Coiflets: {1–5}*
- *Daubechies: {1–20}*
- *Fejér-Korovkin: {4, 6, 8, 14, 18, 22}*
- *Haar*
- *Han linear-phase moments*[1]: $\{2, 3\}.3$, $\{4, 5\}.5$
- *Morris minimum-bandwitdth*[2]: 4.2, $\{8, 10, 12, 14, 16, 18, 24, 32\}.3, 8.4$
- *Symplets: {$2 - 8$}*
- *Vaidyanathan*

The vital sign waveforms were reconstructed after the wavelet decomposition following this criteria:

- Heartbeat waveform: It selects the modes which frequency range lies between 0.8 and 3 Hz. The resulting waveform is filtered with a 4th-order Butterworth high-pass filter, so as to reduce the influence of breathing and random body movements. The cutoff frequency selected is $0.9 f_{Hmin}$.
- Heart sounds: It selects the modes with frequencies ranging between 10 and 30 Hz.
- Skin acceleration waveform: In contrast to previous cases where the radar displacement signal was decomposed, this analysis focuses on the acceleration signal, specifically selecting the modes characterized by frequencies ranging between 10 and 30 Hz.

[1] Han linear-phase moments $SR.LP$, where SR is the sum rules and LP is the order of linear-phase moments.

[2] Morris minimum-bandwidth $N.L$, where N is the number of filter coefficients (taps) and L is the level of the discrete wavelet transform used in the optimization.

The criteria followed to determine the best wavelet transform is the one that minimizes the $MAE_{\{HR\}}$ (see Appendix F.2), using the ECG as reference. The overall results are displayed in Table G.1, showing the mean error obtained with all the wavelets and its standard deviation.

Table G.1: Analysis of the optimal wavelet decomposition: summary results.

Waveform	**Focusing region**	**$MAE_{\{HR\}}$ (bpm)**	**Optimal wavelet**
Heartbeat	Carotid	3.61 ± 0.18	fk8
Heart sounds	Carotid	2.86 ± 0.10	haar/db1
Acceleration	Carotid	1.85 ± 0.08	mb8.4
Heartbeat	Chest	6.32 ± 0.16	haar/db1
Heart sounds	Chest	1.83 ± 0.31	fk4
Acceleration	Chest	1.31 ± 0.07	mb8.4
Heartbeat	Wrist	3.75 ± 0.13	coif1
Heart sounds	Wrist	7.25 ± 0.33	mb8.3
Acceleration	Wrist	8.94 ± 0.08	db2/sym2

Appendix H

Real-time Application Implementation

This appendix details some of the processes developed for the real-time implementation of the vital sign monitoring tool using radar.

H.1 Radar Acquisition Process

This section presents the radar acquisition process implemented, which is exemplified with the AWR2243BOOST case. As previously stated, the radar system transmits the unprocessed data to the PC via the Ethernet connection, which is situated on the DCA1000 board. This data is transmitted using the UDP protocol. The radar data stream is queued into a UDP buffer, which is implemented by the Windows operating system (OS). The queued packages are extracted by an UDP server implemented in C++. This server obtains the UDP packages from the OS buffer, verifying the sequence number of the radar package to identify any losses and replacing them with zeros, thus ensuring signal rate integrity. Subsequently, the extracted payload of each packet is queued into a circular buffer, which is read at a sample rate of 100 Hz (PRF of the system) by an external process implemented in Simulink.

The UDP client implemented in Simulink is also responsible for the separation of the data stream into chirps and virtual channels. The flowchart, which illustrates the radar acquisition process, is presented in Fig. H.1.

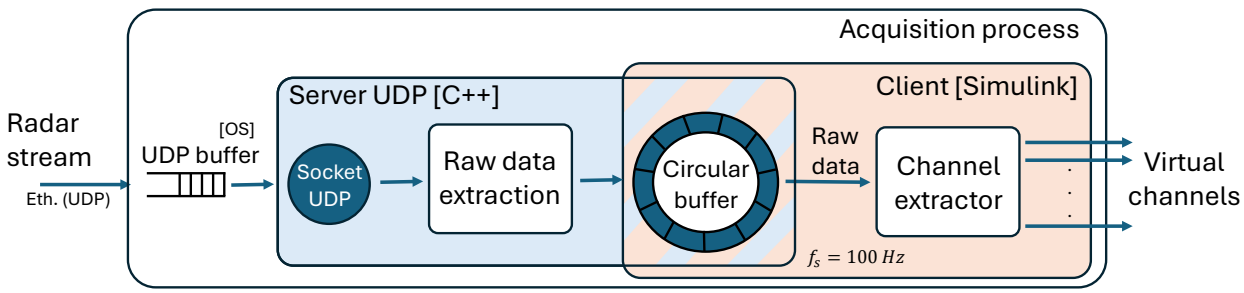

Figure H.1: Flowchart with the real-time acquisition process.

Furthermore, the variability in the delay estimation is a consequence of this block. As previously stated, this is due to the fact that the Windows operating system is not a real-time OS. Consequently, all requests are processed on a best-effort basis, without any guarantee of a specific response time. Consequently, the delay resulting from the UDP buffer is variable and it is estimated based on the circular buffer filling, given that the bitrate is known (for the latter synchronization with the external reference).

H.2 Heartbeat Waveform Extraction from Heart Sounds

Section 3.5 has demonstrated that the most accurate heart activity extraction is obtained from the heart sounds. Therefore, this signal is chosen for the heart rate estimation. With the aim of applying a Schmitt trigger block, such as in the breathing rate estimator, the heart sounds has to be processed.

For that purpose, an additional processing step is applied, which is inspired by the Pan & Tompkins algorithm developed for the QRS complex detection in ECG [Pan 85]. The extracted displacement is filtered within the heart sounds frequency band. Subsequently, the heart sounds signal is squared to make all the values positive and enhance the peaks. Then, a moving window integrator is applied to the squared signal to sum the values over a short period, smoothing the signal. Finally, the resulting waveform is filtered in the heartbeat frequency range. An example of this process is illustrated in Fig. H.2.

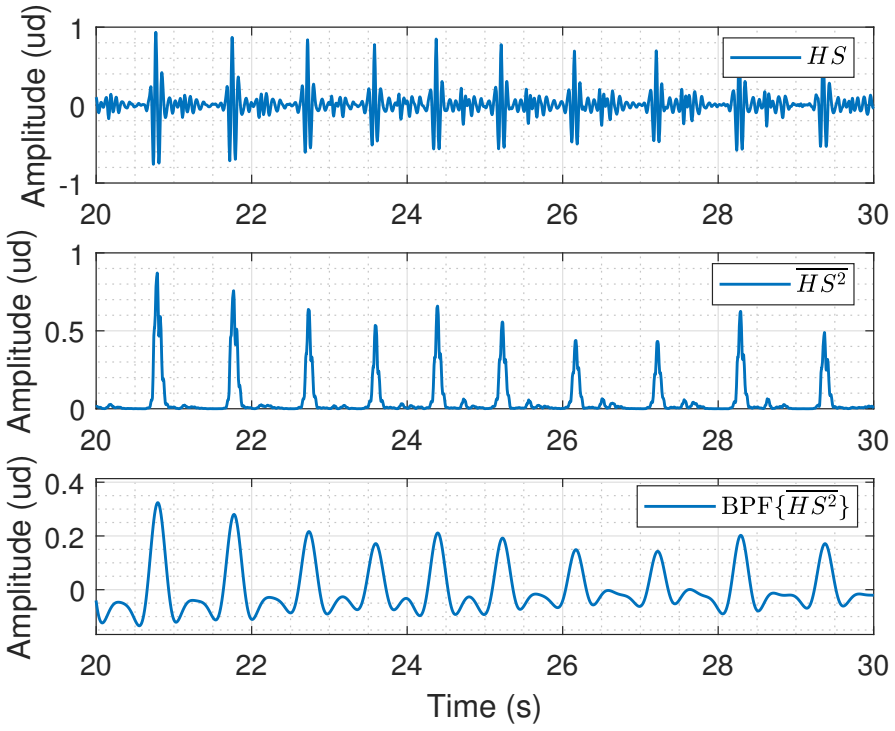

Figure H.2: Heartbeat waveform extracted from the heart sounds. From top to bottom: heart sound signal, output of the average moving integrator, and resulting waveform after bandpass filtering.

H.3 Vital Signs Rate Estimation and Apnea Detector

As previously stated, the vital signs rate estimation is carried out in the time domain. The breathing and heartbeat waveforms are processed using a processing equivalent to a Schmitt trigger [Fila 94], obtaining a digital signal from which the rate is calculated, as shown in Fig. H.3. This is achieved by measuring the time difference between rising edges. The amplitude threshold in the breathing rate estimator has been set to 0.5 mm, as the maximum heartbeat amplitude is below 0.5 mm [Bori 15], thus, the apnea episodes do not generate a trigger. In contrast, the threshold for the heart rate has been set to detect zero crosses. It is also important to note that if the measured breathing and heart rates fall outside the normal ranges (between 6 and 42 breaths/min, and between 48 and 180 bpm), the rates are not updated and the previous rate is maintained. In the case of apnea, the breathing rate is set to 0 breaths/min.

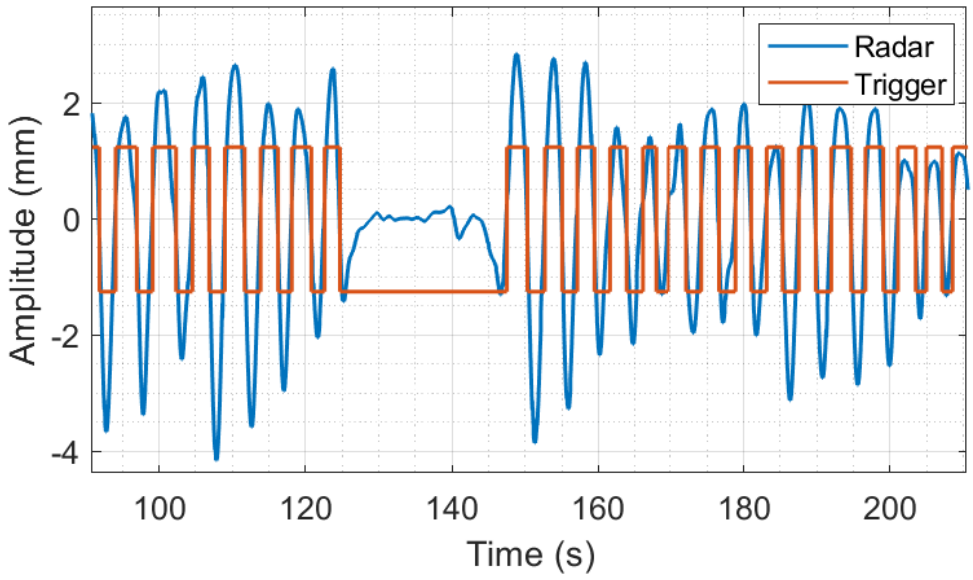

Figure H.3: Breathing waveform acquired with the radar and trigger signal generated.